PHYSIK

AG MAGNETISMUS

Annual Report 2014

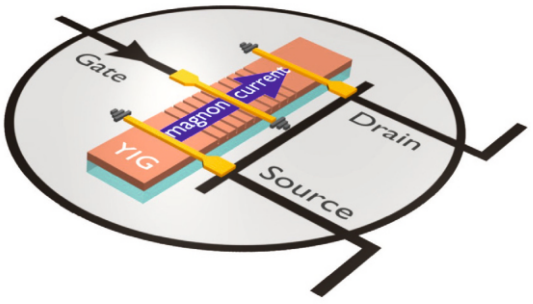

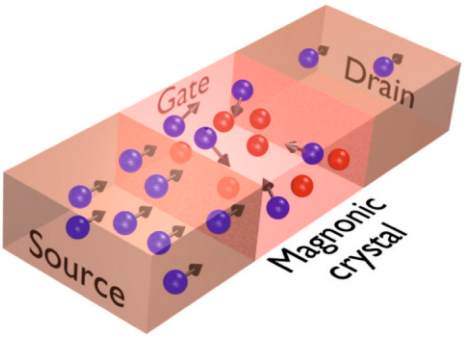

AG MAGNETISMUS
TU KAISERSLAUTERN

OPTIMAS

TECHNISCHE UNIVERSITÄT
KAISERSLAUTERN

Front page: Schematic of a magnon transistor and its operational principle. The transistor is based on a magnonic crystal designed in the form of an yttrium iron garnet film with an array of parallel grooves at its surface. The magnons are injected into the transistor's source and gate, and are detected at its drain using identical microstrip antennas. A magnon transistor allows for the suppression of the source-to-drain magnon current (shown with blue spheres in the right figure) via the injection of the gate magnons (red spheres) into the gate region. A nonlinear four-magnon scattering mechanism is responsible for the transistor's operational principle: When magnons from the transistor's source enter the gate region they are scattered by the gate magnons and, thus, reach the transistor's drain with attenuation. The high degree of gate magnon localization inside the transistor's gate is provided by the magnonic crystal formed by the periodic array of grooves and leads to high scattering probabilities. For more details see Section 4.11 of this Report.

Annual Report 2014

AG MAGNETISMUS
TU KAISERSLAUTERN

Address: Prof. Dr. Burkard Hillebrands
Fachbereich Physik
Landesforschungszentrum OPTIMAS
Technische Universität Kaiserslautern
Erwin-Schrödinger-Straße 56
67663 Kaiserslautern, Germany
Tel.: +49-(0)631-205-4228
Fax.: +49-(0)631-205-4095

Postal address: Postfach 3049
67653 Kaiserslautern, Germany

Internet: http://www.physik.uni-kl.de/hillebrands/
E-Mail: hilleb@physik.uni-kl.de

This Annual Report can be downloaded from:
http://www.physik.uni-kl.de/hillebrands/publications/annual-reports/

Our Group

From left to right:

Dmytro Bozhko, Dr. Milan Agrawal, Tobias Fischer, Stefan Klingler, Dr. Britta Leven, Sascha Keller, Peter Clausen, Laura Mihalceanu, Dr. Alexander Serga, Lisa Gareis, Thomas Langner, Jochen Greser, Dr. Philipp Pirro, Dr. Andrés Conca Parra, JProf. Dr. Evangelos Papaioannou, Ana Ruiz Calaforra, Thomas Brächer, Frank Heussner, Thomas Meyer, Dr. Vitaliy Vasyuchka, Viktor Lauer, Prof. Dr. Burkard Hillebrands

(The picture was taken at our group retreat in Annweiler in September 2014.)

Not on the picture: Dr. Andrii Chumak, Moritz Geilen, Björn Heinz, Philipp Jaeger, Martin Kewenig, Sibylle Müller, Donata Passarello, Dr. Isabel Sattler, Michael Schneider, Matthias Schweizer, Dieter Weller

Contents

Chapter 1: Preface

Dear Colleagues and Friends,

we are happy to present our Annual Report 2014 covering the period November 2013 to October 2014.

In the last year we achieved several research highlights: In the field of magnon gases and condensates we discovered an anomalous contribution to the dynamics of a magnon Bose-Einstein condensate, which is likely due to the excitation of a phase induced magnon supercurrent in a thermal gradient. We also found that a magnon Bose-Einstein condensate contributes to spin pumping and can generate an electric voltage in an adjacent Pt layer by the inverse spin Hall effect. This voltage has a contribution due to the coherency of the magnon condensate and thus can be used as an electric fingerprint of magnon Bose-Einstein condensates. We also found that short-wavelength magnons can generate an electric DC voltage by the planar Hall effect mechanism. We succeeded in establishing a microstructured local amplifier for spin waves using local parametric pumping. There was big progress in the studies of magnon-based data processing. We have realized the first magnon transistor-device in which a current of magnons from the source to the drain of the transistor is controlled by magnons at the gate. We regard this device as a key element for future all-magnon processors. A further big step towards magnon spintronics is the first demonstration of a realistic micron-sized spin-wave majority gate. Here, micro-magnetic simulations show the full functionality of a majority gate. And, finally, we developed a novel type of dynamic magnonic crystal and use it for the realization of a conceptually new spin-wave logic gate, which is not anymore using a Mach-Zehnder interferometer geometry. In the field of spin-caloric transport we present our new concept of efficient control of spin-wave properties by optically induced thermal landscapes. Almost any two-dimensional pattern can be used, and, as an example we show the transition from a one-dimensional magnonic crystal into a two-dimensional one. Our activities in the field of Heusler and other novel compounds continue fruitfully. Specifically we found evidence for a new non-Gilbert damping mechanism, which is important for Heusler compounds due to their low Gilbert-damping and high magnetization. In the field of applied spintronics the systematic magnetic characterization of the technologically relevant materials CoFeB and NiFe for multilayer sensor applications has been carried out.

Concerning our project portfolio, the prolongation of the DFG Priority Programme SPP 1538 “Spincaloric Transport - SpinCaT” is important news. In this program we have two projects (“Magnon Seebeck effect” and “Magnon mediated heat and spin transport in magnetic insulators”). We are also very happy to have started two new EU-funded projects, the FET-Open Xtrack project “Insulator spintronics (InSpin)” together with the Coordinator Arne Brataas (Norwegian University of Science and Technology, Trondheim), and Bart van Wees (Zernike Institute of Advanced Materials, Groningen), Gerrit Bauer (TU Delft), and Mathias Kläui (U Mainz), as well as the M-Era project “Heusler compounds for future magnetic memory and logic (HeuMem)” with Claudia Felser (Max Planck Institute for the Chemical Physics of Solids, Dresden) and Günter Reiss (U Bielefeld) in the DFG-framework and Mairbek Chshiev; Jean-Pierre Nozières; Ricardo Sousa from CEA/Spintec in Grenoble as our French partners. An important success of TU Kaiserslautern as a whole was the approval for a new Research Building “Laboratory for Advanced Spin Engineering (LASE)”. LASE will provide about $3,000\,\mathrm{m}^2$ of working space and is expected to be finished at the end of 2019. The investment of 39.4 million Euro (including large equipment) is shared between federal sources and the State of Rhineland-Palatinate.

Again, there have been several changes in our group. We are happy to welcome Tobias Fischer, Frank Heussner, Stefan Klingler, and Laura Mihalceanu as new diploma students and Sascha Keller as new PhD student. Several group members have left us during 2014: Florin Ciubotaru, Benjamin Jungfleisch, Roland Neb, Björn Obry, Katrin Schultheiß (née Vogt) and Thomas Sebastian (in alphabetical order). Milan Agrawal, Roland Neb and Philipp Pirro finished their PhD. Our postdoc Evangelos Papaioannou accepted a call for the Junior-Professorship "Magnetic Heterostructures" that has been applied for by OPTIMAS from the Carl-Zeiss Foundation. A personal change has been the end of my term as Vice President for Research, Technology and Innovation at the University of Kaiserslautern. This provides me with new degrees of freedom for science, teaching and public service, to which I am looking forward to.

We would like to extend our congratulations to two awardees closely related to our group: Our former PhD student Benjamin Jungfleisch (now postdoc at Argonne National Laboratories, USA) received the PhD award by the Foundation of the Kreissparkasse Kaiserslautern 2014. Our close collaborator Prof. Andrei Slavin (Oakland University, Rochester, MI, USA) was awarded a prestigious Visiting Professorship by the Graduate School of Excellence MAINZ.

Our work would not have been possible without valuable collaborations with people all over the world. They are too many to list them here all. In particular we would like to thank, in alphabetical order, Johan Åkerman, Yasuo Ando, Christian Back, Gerrit Bauer, Arne Brataas, Frederick Casper, Russell Cowburn, Sergej Demokritov, Bernard Dieny, Marco Doms, Rembert Duine, Carsten Dubs, Ursula Ebels, Hajo Elmers, Jürgen Fassbender, Gerhard Fecher, Claudia Felser, Albert Fert, Sebastian Goennenwein, John Gregg, Hubert Grimm, Dirk Grundler, Gianluca Gubbiotti, Konstantin Gusliyenko, Jaroslav Hamrle, Uwe Hartmann, Michel Hehn, Jos Heremans, Axel Hoffmann, Koichiro Innomata, Gerhard Jakob, Xiaofeng Jin, Martin Jourdan, Gleb Kakazei, Boris Kalinikos, Alexy Karenowska, Sang-Koog Kim, Akihiro Kirihara, Olivier Klein, Mathias Kläui, Peter Kopietz, Mikhail Kostylev, Volodymyr Kruglyak, Takahide Kubota, Ronald Lehndorff, Luis Lopez Diaz, Jörg Lösch, Wolfram Maaß, Sadamichi Maekawa, Stéphane Mangin, Gennadiy Melkov, Claudia and Tim Mewes, Shuichi Murakami, Hiroshi Naganuma, Ulrich Nowak, Jean-Pierre Nozières, Kevin O'Grady, Mikihiko Oogane, Yoshichika Otani, Stuart Parkin, Johannes Paul, Marco Rahm, Günter Reiss, Sergio Rezende, Bernhard Reuscher, Caroline Ross, Manfred Rührig, Eiji Saitoh, John R. Sandercock, Rudi Schäfer, Gerd Schönhense, Andrei Slavin, Rolf Slatter, Bob Stamps, Yoshishige Suzuki, Koki Takanashi, Vasyl Tiberkevich, Simon Trudel, Yaroslav Tserkovnyak, Ken-ichi Uchida, Alexey Ustinov, Ben Van de Wiele, Bart van Wees, Arne Vansteenkiste, and Mingzhong Wu.

Collaborations within the Fachbereich Physik at the University of Kaiserslautern (in particular Martin Aeschlimann, James Anglin, Sebastian Eggert, Michael Fleischhauer, Georg von Freymann, Jochen Kuhn, Herwig Ott, Hans-Christian Schneider, Volker Schünemann, and Arthur Widera and their groups), Michael Kopnarski and his team from the Institut für Oberflächen- und Schichtanalytik, as well as Sandra Wolff and her team from the Nano Structuring Center have been very stimulating. We are very grateful to be a member of the State Research Center for Optics and Material Sciences OPTIMAS.

I would also like to thank all our sponsors, which are the Deutsche Forschungsgemeinschaft (DFG), the Bundesministerium für Bildung und Forschung (BMBF), the Deutscher Akademischer Austauschdienst (DAAD), the European Community (EFRE, INTAS, INTERREG), the Carl Zeiss Foundation, the State of Rhineland Palatinate and the University of Kaiserslautern. Concerning our projects in applied research, I would like to express my gratitude to Sensitec GmbH and Singulus Technologies AG as our strong partners in R&D on spintronic sensors.

My special thanks go to Thomas Langner, Dieter Weller and Sibylle Müller for their help in preparing this report, and to the team from Photo-Repro-Druck, TU Kaiserslautern.

It is my special pleasure to greet all former group members. May this report help to stay in touch. If you are interested in our work I would be happy to hear from you.

With all my best wishes for Christmas, and a Happy New Year,

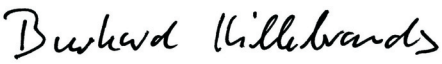

Kaiserslautern, November 2014

Vorwort

Liebe Kolleginnen und Kollegen, Freundinnen und Freunde unserer Arbeitsgruppe,

Wir freuen uns, Ihnen unseren Jahresbericht 2014 zu präsentieren, welcher den Zeitraum von November 2013 bis Oktober 2014 abdeckt.

Einige Höhepunkte unserer Forschungsaktivitäten aus dem genannten Zeitraum: Auf dem Gebiet der Magnonengase haben wir einen anormalen Beitrag zur Dynamik der Bose-Einstein Kondensate entdeckt, der mit der Erzeugung eines phaseninduzierten magnonischen Suprastroms in einem thermischen Gradienten erklärt werden kann. Wir konnten auch nachweisen, dass ein Bose-Einstein Kondensat von Magnonen zum Spinpumpen beiträgt und durch den inversen Spin-Hall-Effekt eine elektrische Spannung in einer angrenzenden Platinschicht hervorruft. Diese Spannung besitzt einen Beitrag, welcher durch die Kohärenz des Magonenkondensates hervorgerufen wird und kann deshalb als elektrischer Fingerabdruck des Bose-Einstein Kondensates angesehen werden. Wir haben auch herausgefunden, dass kurzwellige Magnonen eine elektrische Gleichspannung durch den planaren Hall-Effekt hervorrufen können. Des Weiteren ist uns gelungen, basierend auf einem lokalen parametrischen Pumpprozess einen mikrostrukturierten Verstärker für Spinwellen zu realisieren. Große Fortschritte konnten auf dem Gebiet der Magnon-basierten Datenverarbeitung gemacht werden. Wir haben den ersten Magnonentransistor realisiert, in welchem ein Magnonenfluss vom Eingang (“source”) zum Ausgang (“drain”) des Transistors durch Magnonen am Steuereingang (“gate”) kontrolliert werden kann. Dieses Bauteil stellt ein Schlüsselelement für zukünftige, rein magnonische Prozessoren dar. Ein weiterer großer Schritt in Richtung Magnon-Spintronik ist die Demonstration eines realistischen Spinwellen-Majoritätsgatters mit Abmessungen im Mikrometerbereich, dessen volle Funktionalität mit Hilfe mikromagnetischer Simulationen gezeigt werden konnte. Außerdem haben wir einen neuartigen, dynamischen magnonischen Kristall entwickelt, welchen wir in einem konzeptuell fortgeschrittenen Spinwellenlogikelement einsetzen, das ohne Mach-Zehnder Interferometer auskommt. Auf dem Gebiet des spinkalorischen Transports präsentieren wir ein neues Konzept, um die Eigenschaften von Spinwellen effizient mit Hilfe von thermischen Verteilungen zu kontrollieren, welche rein optisch induziert werden. Hierbei kann eine fast beliebige zweidimensionale Verteilung genutzt werden - beispielhaft zeigen wir den Übergang von einem eindimensionalen zu einem zweidimensionalen magnonischen Kristall. Unsere Aktivitäten auf dem Feld der Heusler- und anderer neuartiger Verbindungen konnten erfolgreich fortgesetzt werden. Hier wurde ein nicht-viskoser Dämpfungsmechanismus gefunden, welcher für Heusler-Verbindungen auf Grund ihrer geringen Gilbert-Dämpfung und ihrer hohen Magnetisierung eine große Rolle spielt. Auf dem Gebiet der angewandten Spintronik wurde eine systematische Charakterisierung der magnetischen Eigenschaften der technologisch relevanten Materialien CoFeB und NiFe im Hinblick auf ihre Anwendung in Sensoren auf der Basis von Vielschichtsystemen durchgeführt.

Bezüglich unserer Drittmittel geförderten Projekte war für uns die Verlängerung des DFG Schwerpunktprogramms “Spincaloric Transport - SpinCaT” (SPP 1538) besonders wichtig. In diesem Programm, das wir mit-initiiert hatten, sind wir mit zwei Projekten vertreten: (Magnon Seebeck Effect und Magnon mediated heat and spin transport in magnetic insulators). Wir freuen uns auch über zwei neue Projekte mit EU-Förderung: Das FET-Open Xtrack Projekt “Insulator spintronics (InSpin)”, mit Arne Brataas (Norwegian University of Science and Technology, Trondheim) als Koordinator, sowie Bart van Wees (Zernike Institute of Advanced Materials, Groningen), Gerrit Bauer (TU Delft) und Mathias Kläui (U Mainz) sowie das M-Era Projekt “Heusler compounds for future magnetic memory and logic (HeuMem)” zusammen mit Claudia Felser (Max-Planck-

Institut für Chemische Physik fester Stoffe, Dresden) und Günter Reiss (U Bielefeld) seitens der DFG, sowie Mairbek Chshiev; Jean-Pierre Nozières; Ricardo Sousa von CEA/Spintec in Grenoble als französische Partner. Ein besonderer Erfolg für die TU Kaiserslautern als Ganzes, ist die Bewilligung des neuen Forschungsgebäudes "Laboratory for Advanced spin Engineering (LASE)". LASE wird ungefähr 3.000 m^2 Arbeitsfläche bieten und soll Ende 2019 bezugsfertig sein. Die Investition in Höhe von 39,4 Millionen Euro (einschließlich Großgeräten) teilen sich der Bund und das Land Rheinland-Pfalz.

Erneut gab es einige Veränderungen in unserer Gruppe. Wir freuen uns, Tobias Fischer, Frank Heussner, Stefan Klingler, und Laura Mihalceanu als neue Diplom-Studierende und Sascha Keller als neuen Doktoranden in unserer Gruppe zu haben. Mehrere Mitglieder unser Arbeitsgruppe haben uns in 2014 verlassen: Florin Ciubotaru, Benjamin Jungfleisch, Roland Neb, Björn Obry, Katrin Schultheiß (geb. Vogt) und Thomas Sebastian (in alphabetischer Reihenfolge). Milan Agrawal, Roland Neb und Philipp Pirro haben 2014 ihre Promotionen abgeschlossen. Unser Postdoc Evangelos Papaioannou hat die Juniorprofessur "Magnetische Heterostrukturen" angetreten, die von OPTIMAS bei der Carl-Zeiss-Stiftung eingeworben wurde. Eine persönliche Veränderung war die Beendigung meines Amtes als Vizepräsident unsere Universität (Forschung, Technologie und Innovation). Dies gibt mir neue Freiräume für Forschung, Lehre und Funktionsaufgaben, auf die ich mich freue.

Wir möchten zwei Preisträgern aus dem Umfeld unserer Gruppe herzlich gratulieren: unser früherer Doktorand Benjamin Jungfleisch (jetzt Argonne National Laboratories, USA) erhielt den Doktorandenpreis der Kreissparkassen-Stiftung Kaiserslautern. Unser enger Kooperationspartner Prof. Andrei Slavin (Oakland University, Rochester, MI, USA) erhielt die angesehene "Visiting Professorship" der Graduiertenschule der Exzellenz MAINZ.

Unsere Arbeit wäre nicht ohne wertvolle Kooperationen mit Partnern aus der ganzen Welt möglich gewesen. Es sind zu viele um sie alle an dieser Stelle aufzulisten. Insbesondere möchten wir, in alphabetischer Reihenfolge, danken: Johan Åkerman, Yasuo Ando, Christian Back, Gerrit Bauer, Arne Brataas, Frederick Casper, Russell Cowburn, Sergej Demokritov, Bernard Dieny, Marco Doms, Rembert Duine, Carsten Dubs, Ursula Ebels, Hajo Elmers, Jürgen Fassbender, Gerhard Fecher, Claudia Felser, Albert Fert, Sebastian Goennenwein, John Gregg, Hubert Grimm, Dirk Grundler, Gianluca Gubbiotti, Konstantin Gusliyenko, Jaroslav Hamrle, Uwe Hartmann, Michel Hehn, Jos Heremans, Axel Hoffmann, Koichiro Innomata, Gerhard Jakob, Martin Jourdan, Gleb Kakazei, Boris Kalinikos, Alexy Karenowska, Sang-Koog Kim, Akihiro Kirihara, Olivier Klein, Mathias Kläui, Peter Kopietz, Mikhail Kostylev, Volodymyr Kruglyak, Takahide Kubota, Ronald Lehndorff, Luis Lopez Diaz, Jörg Lösch, Wolfram Maaß, Sadamichi Maekawa, Stéphane Mangin, Gennadiy Melkov, Claudia and Tim Mewes, Shuichi Murakami, Hiroshi Naganuma, Ulrich Nowak, Jean-Pierre Nozières, Kevin O'Grady, Mikihiko Oogane, Yoshichika Otani, Stuart Parkin, Johannes Paul, Marco Rahm, Günter Reiss, Sergio Rezende, Bernhard Reuscher, Caroline Ross, Manfred Rührig, Eiji Saitoh, John R. Sandercock, Rudi Schäfer, Gerd Schönhense, Andrei Slavin, Rolf Slatter, Bob Stamps, Yoshishige Suzuki, Koki Takanashi, Vasyl Tiberkevich, Simon Trudel, Yaroslav Tserkovnyak, Ken-ichi Uchida, Alexey Ustinov, Ben Van de Wiele, Bart van Wees, Arne Vansteenkiste, und Mingzhong Wu.

Die Zusammenarbeit mit dem Fachbereich Physik der Technischen Universität Kaiserslautern (insbesondere mit Martin Aeschlimann, James Anglin, Sebastian Eggert, Michael Fleischhauer, Georg von Freymann, Jochen Kuhn, Herwig Ott, Hans-Christian Schneider, Volker Schünemann und Arthur Widera und ihren Arbeitsgruppen), Michael Kopnarski und seinem Team des Instituts für Oberflächen- und Schichtanalytik sowie Sandra Wolff und ihrem Team des Nano Structuring Cen-

ters waren sehr stimulierend. Wir sind sehr dankbar, Mitglied des Landesforschungszentrums für Optik und Materialwissenschaften (OPTIMAS) zu sein.

Ich möchte außerdem unseren Geldgebern danken: der Deutschen Forschungsgemeinschaft (DFG), dem Bundesministerium für Bildung und Forschung (BMBF), dem Deutschen Akademischen Austauschdienst (DAAD), der Europäischen Gemeinschaft(EFRE, INTAS, INTERREG), der Carl Zeiss-Stiftung, dem Land Rheinland-Pfalz und der Technischen Universität Kaiserslautern. In Bezug auf unsere Projekte in der angewandten Forschung möchte ich meine Dankbarkeit gegenüber der Sensitec GmbH und der Singulus Technologies AG, unseren starken Partnern in R&D von spintronischen Sensoren, zum Ausdruck bringen.

Mein besonderer Dank geht an Thomas Langner, Dieter Weller und Sibylle Müller für ihre Hilfe beim Erstellen dieses Berichtes und an das Team von Photo-Repro-Druck, TU Kaiserslautern.

Es ist mir eine besondere Freude, hiermit auch allen ehemaligen Gruppenmitgliedern einen Gruß zu senden. Möge dieser Bericht uns helfen, im Kontakt zu bleiben. Wenn Sie an unserer Arbeit interessiert sind, würde ich mich freuen, von Ihnen zu hören.

Mit den besten Wünschen für ein frohes Weihnachtsfest und ein gutes Neues Jahr

Burkard Hillebrands

Kaiserslautern, im November 2014

Chapter 2: Personnel

2.1 Members of the group

Group leader:

Prof. Dr. Burkard Hillebrands

Senior scientists:

Dr. Andrii Chumak
Dr. Andrés Conca Parra
Dr. Britta Leven, Akad. Oberrätin
Jun. Prof. Dr. Evangelos Papaioannou
Dr. habil. Alexander Serga
Dr. Vitaliy Vasyuchka

Postdocs and long-term guest scientists:

Dr. Milan Agrawal	since 02/14
Dr. Florin Ciubotaru	until 08/14
Dr. Benjamin Jungfleisch	until 12/13
Akihiro Kirihara	until 04/14
Dr. Roland Neb	02/14 - 08/14
Dr. Björn Obry	until 08/14
Dr. Philipp Pirro	since 07/14
Dr. Katrin Schultheiß	until 12/13
Dr. Thomas Sebastian	until 12/13

Ph.D. students:

M.Sc.	Milan Agrawal	until 02/14
M.Sc.	Dmytro Bozhko	
Dipl.-Phys.	Thomas Brächer	
Dipl.-Phys.	Peter Clausen	
Dipl.-Phys.	Sascha Keller	since 10/14
Dipl.-Phys.	Thomas Langner	
Dipl.-Phys.	Viktor Lauer	
Dipl.-Phys.	Thomas Meyer	
Dipl.-Phys.	Roland Neb	until 02/14
M.Sc.	Donata Passarello (IBM Research lab)	
Dipl.-Phys.	Philipp Pirro	until 07/14
M.Sc.	Ana Ruiz Calaforra	

Diploma Students:

Tobias Fischer	since 05/14
Frank Heussner	since 01/14
Stefan Klingler	since 11/13
Laura Mihalceanu	since 07/14

Student Assistants:

Tanita Eichert	until 06/14
Lisa Gareis	since 12/13
Moritz Geilen	
Jochen Greser	
Björn Heinz	
Philipp Jaeger	
Martin Kewenig	since 10/14
Michael Schneider	since 10/14
Matthias Schweizer	

Engineers and Technicians

Dipl.-Ing. (FH) Dieter Weller

Administration:

Sibylle Müller
Dr. Isabel Sattler

2.2 Visiting scientists, postdoctoral fellows and exchange students

(sorted by date of first arrival in our group)

Akihiro Kirihara, NEC Corporation, Tsukuba Japan — 05.04.2013 - 12.04.2014

Akihiro Kirihara is a visiting researcher, belonging to Smart Energy Research Laboratories of NEC Corporation. In NEC, he works on the development of thermoelectric devices using the spin-Seebeck effect (SSE). He stayed in our group until mid of April and joined experimental projects related to the SSE and spin pumping.

Robert L. Stamps, University of Glasgow United Kingdom — 02.12. - 07.12.2013

Prof. Dr. Robert L. Stamps is a professor at Glasgow University and an internationally highly regarded expert in the theory of magnetization dynamics and magnetism at the nanoscale in general. We collaborate with him since more than 25 years. He visited our laboratory for six days to discuss new directions in magnon physics.

Boris Kalinikos, Department of Physical Electronics and Technology, St. Petersburg Electrotechnical University, St. Petersburg Russia — 16.12. - 17.12.2013

The visit of Prof. Kalinikos has been performed in the frame of the German-Russian project "Coherent nonlinear spin-wave states in ferromagneticfims and ferromagnetic/ferroelectronic layered structures" (DFG RUS 113/644/0). We discussed our joint results on a width-modulated dynamic magnonic crystal. As well we finished the project report and worked on the preparation of a new cooperative project.

Yoichi Shiota, Osaka University, Osaka Japan — 28.01 - 14.02.2014

Dr. Yoichi Shiota finished his PhD studies in the group of Prof. Y. Suzuki and is now a postdoc in National Institute of Advanced Industrial Science and Technology (AIST), Ibaraki, Japan. Our collaboration is long-standing and refers to the anisotropy-mediated coupling between magnetization dynamics and electric field in multilayered structures. During this visit, we performed joint experimental studies of spin-wave generation by electric field using Brillouin light scattering spectroscopy.

YochiChika Otani, ISSP, The University of Tokyo and Center for Emergent Matter Science, RIKEN Japan — 17.02 - 19.02.2014

Prof. Otani visited our group to participate in the PhD defense of Milan Agrawal as the second supervisor. During his stay, he delivered a talk about his cutting-edge research on the spin Hall effect. He enjoyed the PhD celebration function very much and wrote about it on his group web-page.

Aleksandra Trzaskowska, Adam Mickiewicz University, UAM, Poznan Poland — 28.04 - 14.05.2014

In 2008 Dr. Aleksandra Trzaskowska worked with us six month in frame of her DAAD fellowship. During her current stay, which was supported by the Adam Mickiewicz University, Alexandra performed BLS measurements of phonon and magnon excitations in multilayered magnetic structures.

Andrei Slavin, Oakland University, Rochester, Michigan USA — 14.05 - 15.05.2014

Prof. Slavin spend with us a few days fruitfully discussing the recent experimental results on magnon gases and condensates.

Benjamin Jungfleisch, Materials Science Division, Argonne National Laboratory, Argonne, Illinois USA — 09.06 - 13.06.2014

Benjamin Jungfleisch has finished his PhD studies in our group and is now a postdoc at Argonne National Laboratories, USA. During his visit in Kaiserslautern we have spent some very useful days discussing the perspectives, trends and problems of the field of magnon spintronics as well as perspectives for future joint studies.

Eiji Saitoh, Institute of Materials Research, Tohoku University, Sendai Japan — 11.07 - 13.07.2014

Prof. Dr. Eiji Saitoh, a professor at Institute for Materials Research at Tohoku University, Sendai, Japan is an experimentalist in the field of spin-caloric phenomena with excellent international reputation. We collaborate with him on the field of magnon caloritronics. He visited us for three days to discuss results and new research ideas.

Gennadii A. Melkov, National Taras Shevchenko University, University of Kyiv
Ukraine — 14.07 - 24.08.2014

This year the regular visit of Prof. Melkov to our group was supported by the Deutsche Forschungsgemeinschaft in the frame of the SFB/Transregio 49 "Condensed Matter Systems with Variable Many-Body Interactions". During his stay Prof. Melkov was mainly working on different aspects of phonon-magnon interactions in parametrically and thermally driven magnetic insulators.

Yaroslav Tserkovnyak, University of California (UCLA), Los Angeles
USA — 20.07 - 27.07.2014

Prof. Yaroslav Tserkovnyak worked with us on the theoretical description of our experimental results on the dynamics of Bose-Einstein magnon condensate in thermal gradients and on the enhanced Spin-Hall Effect voltage from the magnon Bose-Einstein condensate in YIG/Pt bilayers.

Ken-ichi Uchida, Institute of Materials Research, Tohoku University, Sendai, and PRESTO, Japan Science and Technology
Japan — 07.10 - 01.11.2014

Assoc. Prof. Ken-ichi Uchida visited our group in the frame of our research collaboration. During his visit, we experimentally studied the magnonic transport in ferrimagnetic spin-wave waveguides treated using a laser micro-processing system, and we investigated interactions between magnons and plasmon resonances in hybrid structures. The combination of Brillouin light scattering spectroscopy and microwave technique was used in these investigations.

2.3 Guest seminars

Abdelmadjid Anane 02.12.2013	Unité Mixte de Physique CNRS/Thales, Palaiseau et Université de Paris-Sud, Orsay, France *PLD grown thin YIG films for magnonics, spintronics and more* Special group seminar
Robert L. Stamps 04.12.2013	University of Glasgow, United Kingdom *Dynamics of spin configurations and textures* Special seminar
Adekunle Adeyeye 16.12.2013	National University of Singapore, Singapore *Artificial ferromagnetic nanostructures: An experimental platform for magnonics* Physics Kolloquium
Yoichi Shiota 10.02.2014	Osaka University, Osaka, Japan *Spin dynamics excited by voltage-effect in ferromagnetic metals* Special group seminar
Dr. Rolf Slatter 11.02.2014	Sensitec GmbH, Mainz, Germany *Wir stellen uns vor - Magnetische Mikro- und Nanotechnologie für robuste Sensorlösungen* Special seminar
YochiChika Otani 17.02.2014	ISSP, The University of Tokyo and Center for Emergent Matter Science, RIKEN, Japan *Static and dynamic measurements of spin Hall effects* Special group seminar
Aleksandra Trzaskowska 11.05.2014	Adam Mickiewicz University, UAM, Poznań, Poland *Periodic nanostructures on silicon surfaces* Special group seminar
Uwe Hartmann 02.06.2014	Universität des Saarlandes, Saarbrücken, Germany *Giant Magnetoimpedance* Physics Kolloquium
Benjamin Jungfleisch 11.06.2014	Materials Science Division, Argonne National Laboratory, Argonne, Illinois, USA *Spin pumping and inverse spin Hall effect in metallic ferromagnet structures* Special seminar
Christoph Becker 03.07.2014	Institut für Laserphysik, Universität Hamburg, Germany *High spin at low temperatures* TR49 Kolloquium

Yaroslav Tserkovnyak 21.07.2014	University of California (UCLA), Los Angeles, USA *Bosonic condensation and spin superfluidity in solid state* Physics Kolloquium
Julian Hüser 28.07.2014	Institut für Theoretische Physik, Universität Münster, Germany *Bose-Einstein condensation of magnons: A theoretical study of magnon-magnon and magnon-phonon interactions* Special group seminar
Yu-Ming Hung 15.09.2014	New York University, New York City, USA *I Current-induced switching and properties of Ta/CoFeB/MgO for spin logic device* *II Investigation of spin pumping in YIG/Cu/Py using ferromagnetic resonance* Special seminar
Ken-ichi Uchida 27.10.2014	Institute of Materials Research, Tohoku University, Sendai, and PRESTO, Japan Science and Technology, Japan *1. Experiments in Kaiserslautern* *2. Experimental progress on spin Seebeck effect* Special group seminar

2.4 Visits of group members at other laboratories

Tobias Fischer	Department of Chemistry, University of Calgary, Alberta, Canada 03.09.2013 - 28.02.2014 Host: Dr. Simon Trudel
Evangelos Papaioannou	Uppsala Universitet, Uppsala, Sweden 17.02.2014 - 21.02.2014 Host: Prof. Björgvin Hjörvarsson
Lisa Gareis	Center for Materials for Information Technology (MINT), University of Alabama, Tuscaloosa, USA 02.06. - 01.08.2014 Host: Prof. Dr. Tim Mewes
Thomas Meyer	Tohoku University, Sendai, Japan 09.06.2014 - 19.06.2014 Host: Prof. Yasuo Ando

2.5 Group member photo gallery

Dr. Milan Agrawal
Postdoc

Dmytro Bozhko
Ph.D. student

Thomas Brächer
Ph.D. student

Dr. Andrii Chumak
Senior scientist

Dr. Florin Ciubotaru
Postdoc

Peter Clausen
Ph.D. student

Dr. Andrés Conca Parra
Senior scientist

Tanita Eichert
Student assistant

Tobias Fischer
Diploma student

Lisa Gareis
Student assistant

Moritz Geilen
Student assistant

Jochen Greser
Student assistant

Björn Heinz
Student assistant

Frank Heussner
Diploma student

Prof. Dr. Burkard Hillebrands
Group leader

Philipp Jaeger
Student assistant

Dr. Benjamin Jungfleisch
Postdoc

Sascha Keller
Ph.D. student

Martin Kewenig
Student assistant

Akihiro Kirihara
Guest scientist

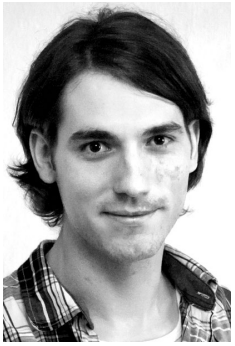

Stefan Klingler
Diploma student

Thomas Langner
Ph.D. student

Viktor Lauer
Ph.D. student

Dr. Britta Leven
Senior scientist

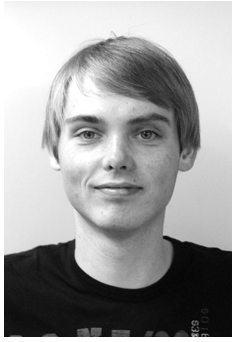

Thomas Meyer
Ph.D. student

Laura Mihalceanu
Diploma student

Sibylle Müller
Secretary

Dr. Roland Neb
Postdoc

Dr. Björn Obry
Postdoc

JProf. Dr. Evangelos Papaioannou
Senior scientist

Donata Passarello
Ph.D. student

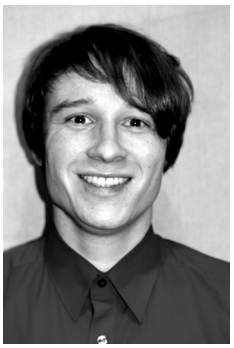

Dr. Philipp Pirro
Postdoc

Ana Ruiz Calaforra
Ph.D. student

Dr. Isabel Sattler
Administration

Michael Schneider
Student assistant

Dr. Katrin Schultheiß (née Vogt)
Postdoc

Matthias Schweizer
Student assistant

Dr. Thomas Sebastian
Postdoc

Dr. Alexander Serga
Senior scientist

Dr. Vitaliy Vasyuchka
Senior scientist

Dieter Weller
Mechanical engineer

Chapter 3: Methods

3.1 Brillouin light scattering spectroscopy (BLS)

Brillouin light scattering (BLS) spectroscopy is one of the key techniques in our laboratory to investigate the dynamic properties of magnetic materials and devices. It is based on the interaction of photons with the fundamental excitations of a solid such as magnons, the quanta of magnetic excitations. The interaction can be understood as an inelastic scattering process of the incident photons with magnons, taking into account energy and momentum conservation as indicated in Fig. 1.

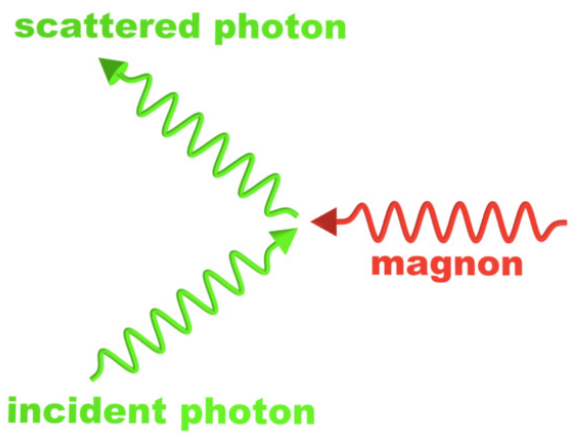

Fig. 1: Scheme of inelastic scattering of an incident photon by a magnon.

The detection of the inelastically scattered photons, i.e. the separation from the elastically scattered photons and the determination of the transferred energy, requires an interferometric technique with extremely high contrast and sensitivity. In our laboratory we implemented the (3+3) Tandem-Fabry-Perot-Interferometer, designed by John R. Sandercock and schematically shown in Fig. 2. It consists of two Fabry-Perot interferometers (FPI), each one passed three times by the inelastically scattered light. This approach results in a contrast better than 10^{10} for the separation of the elastically and inelastically scattered photons in a frequency range from 500 MHz up to 1 THz.

In the last decade we made significant progress in the improvement of BLS spectroscopy. The spatial resolution was pushed to the fundamental limit of classical optics by constructing a BLS-microscope (Fig. 3) with sophisticated active stabilization methods. Spin-wave transport phenom-

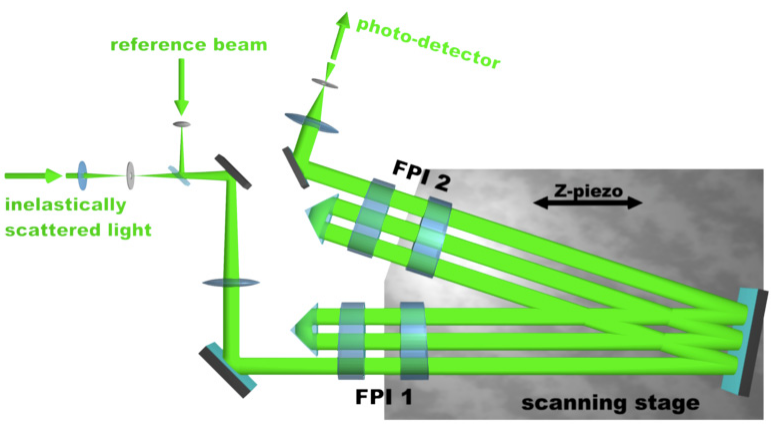

Fig. 2: Scheme of a (3+3) tandem Fabry-Perot interferometer, designed and build by John R. Sandercock (JRS Scientific Instruments, Zürich)

ena can be investigated by time, phase- and wave-vector resolution. The following list gives an overview of the different BLS setups available in our group:

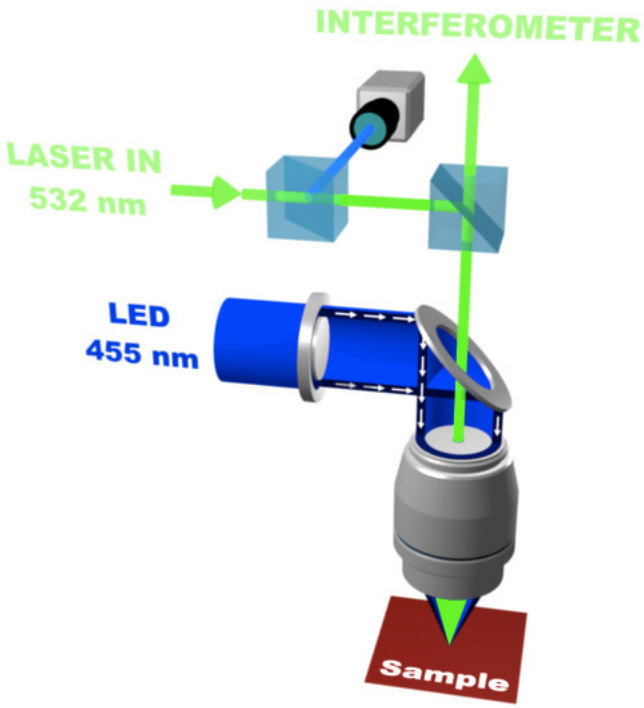

Fig. 3: Schematic setup of a BLS-microscope. The LED light is used to monitor the position of the laser focus on the sample by a CCD camera and to apply active position control to the sample stage.

BLS1: High-field electromagnet (1.2 T), standard BLS spectroscopy equipment. Time resolution, phase resolution, space resolution (50 µm), wave-vector resolution.

BLS2: High-field electromagnet (1.2 T), standard BLS spectroscopy equipment. Microscope stage with 250 nm spatial resolution and build-in time and phase resolution.

BLS3: High-field electromagnet (1.2 T), standard BLS spectroscopy equipment. Microscope stage with 250 nm spatial resolution and build-in time and phase resolution.

BLS4: Electromagnet (0.1 T), standard BLS spectroscopy equipment. Microscope stage with 250 nm spatial resolution and build-in time and phase resolution.

3.2 Microwave techniques

Brillouin light scattering (BLS) spectroscopy described in the previous section is indeed a powerful tool for the detection of spin waves and measurement of their characteristics. Nevertheless, it allows no spin-wave excitation. Thus, in many of our experiments BLS spectroscopy is combined with microwave techniques which ensure high-efficient generation of spin waves in magnetic structures. Spin waves are emitted by nano- and micro-sized microstip antennas placed on the surface of magnetic thin films and is driven by a microwave signal in the GHz frequency range [1]. Microwave sources in our laboratories generate signals of up to 67 GHz providing access to spin-waves in a very wide range of frequencies and wavenumbers. Furthermore, large powers (up to 100 W) provided by microwave amplifiers allow the study of strongly nonlinear spin-wave dynamics as well as quantum effects in parametrically-driven magnon gases. The microwave technique allows for the excitation of both, continuous spin waves as well as short spin-wave packets. Among

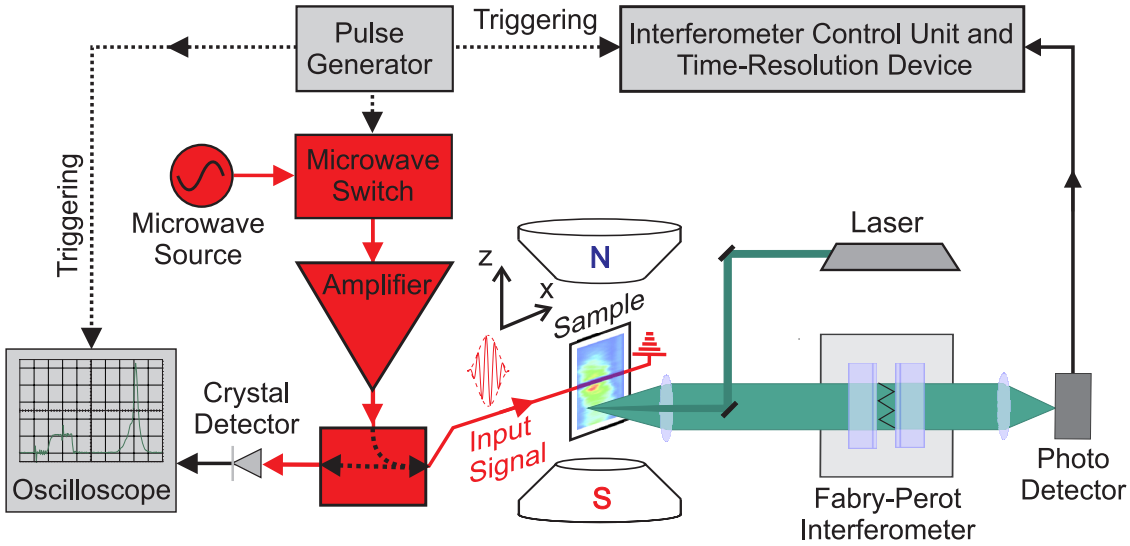

Fig. 1: Scheme of the microwave-assisted time- and space-resolved BLS setup

other advantages, the pulsed technique enables the realization of time resolved (resolution down to 250 ps) BLS spectroscopy [2] shown in Fig. 1. The continuous microwave excitation, by-turn, allows realization of phase-resolved BLS spectroscopy [3, 4].

Besides the excitation of spin waves, the microwave technique is intensively used for high-sensitive (10^{-13} W) detection. Using the same antennas the magnetization precession is converted into microwave currents. These currents are amplified by low-noise amplifiers and analyzed using wide-band oscilloscopes, vector network analyzers or a spectrum analyzer [1]. A vector network analyzer is also used for the ferromagnetic resonance (FMR) measurements allowing determination of such characteristics of the magnetic thin films as magnetization saturation, exchange constant, and damping.

Our microwave techniques are amended by detection of spin waves using the inverse spin Hall effect [5] and were used recently for investigations of microwave-induced spin currents in a ferromagnetic-insulator | normal-metal bilayer system [6]. Furthermore, we have realized a magnon transistor [7], where the magnon-by-magnon control principle is demonstrated using the microwave technique.

References

[1] A.A. Serga, A.V. Chumak, B. Hillebrands, *YIG magnonics*, J. Phys. D **43**, 264002 (2010).
[2] O. Büttner, M. Bauer, S.O. Demokritov, B. Hillebrands, Yu.S. Kivshar, V. Grimalsky, Yu. Rapoport, A.N. Slavin, *Linear and nonlinear diffraction of dipolar spin waves in yttrium iron garnet films observed by space- and time-resolved Brillouin light scattering*, Phys. Rev. B **61**, 11576 (2000).
[3] A.A. Serga, T. Schneider, B. Hillebrands, S.O. Demokritov, M.P. Kostylev, *Phase-sensitive Brillouin light scattering spectroscopy from spin-wave packets*, Appl. Phys. Lett. **89**, 063506 (2006).
[4] K. Vogt, H. Schultheiss , S.J. Hermsdoerfer, P. Pirro , A.A. Serga, B. Hillebrands, *All-optical detection of phase fronts of propagating spin waves in a $Ni_{81}Fe_{19}$ microstripe*, Appl. Phys. Lett. **95**, 182508 (2009).
[5] A.V. Chumak, A.A. Serga, M.B. Jungeisch, R. Neb, D.A. Bozhko, V.S. Tiberkevich, B. Hillebrands, *Direct detection of magnon spin transport by the inverse spin Hall effect*, Appl. Phys. Lett. **100**, 082405 (2012).
[6] M. Agrawal, A.A. Serga, V. Lauer, E.Th. Papaioannou, B. Hillebrands, V.I. Vasyuchka, *Microwave-induced spin currents in ferromagnetic-insulator\normal-metal bilayer system*, Appl. Phys. Lett. **105**, 092404 (2014).
[7] A.V. Chumak, A.A. Serga, B. Hillebrands, *Magnon transistor for all-magnon data processing*, Nat. Commun. **5**, 4700 (2014).

3.3 Magneto-optic Kerr effect magnetometry and microscopy (MOKE)

The magneto-optical Kerr effect (MOKE) is a well established technique to study magnetization properties. The effect is based on the fact, that the plane of polarization of light is rotated when the light is reflected from a magnetic material [1]. The physical origin of MOKE is the magnetic circular dichroism effect: exchange and spin-orbit coupling in a magnetic material lead to different absorption spectra for left- and right-circularly polarized light. Measuring the change of the polarization of the reflected beam (often referred to as Kerr angle Θ_{Kerr}) provides access to the magnetization state of the sample.

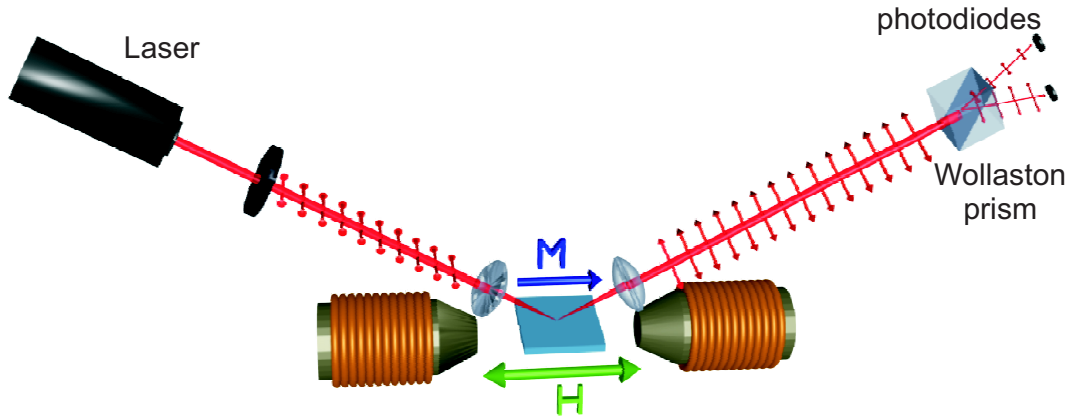

Fig. 1: Schematic setup of a longitudinal Kerr magnetometer.

With MOKE it is possible to study quasi-static magnetization reversal properties and magnetic anisotropies. When using a pulsed laser system it is also possible to study the time dependence of the magnetization under the influence of, e.g., a pulsed magnetic field or a microwave field. Since it is an optical technique it is non invasive, and the spatial resolution is only limited by the optical resolution. Thus, we are able to study the static and dynamic properties of magnetic thin films and magnetic structures with lateral dimension down to 1 µm.

Our group uses four different MOKE setups, all of them using the same principle. The light of a laser source is s-polarized through a thin-film polarizer. The beam is focused onto the sample. The polarization of the reflected light is analyzed by a detector unit that was developed and is built in our laboratory. A Wollaston prism divides the beam into two orthogonally polarized beams, which are monitored by a pair of photodiodes. The detector works as an opto-electrical bridge circuit to increase the signal-to-noise ratio. The obtained normalized differential signal $(I_1 - I_2)/(I_1 + I_2)$ is directly proportional to the Kerr angle Θ_{Kerr}.

Four experimental setups are available to investigate different scientific aspects:

Longitudinal Kerr magnetometer: Longitudinal MOKE geometry to probe quasi-static properties of magnetic thin films. Optical resolution $\sim 100\,\mu$m, magnetic field up to 2 T, automated sample positioning and rotation.

Microfocus Kerr microscope with rotation unit: Longitudinal MOKE geometry to probe quasi-static properties of micro-structured magnetic elements. Optical resolution $< 1\,\mu$m, magnetic field up to 0.6 T, automated sample positioning, rotation and stabilization.

Dual MOKE magnetometer: Two combined MOKE magnetometers working in parallel, one in longitudinal and one in polar geometry to study the quadratic MOKE effects on magnetic thin

films. Optical resolution $\sim 100\,\mu$m, two orthogonal pairs of magnet coils to provide any in-plane field direction up to 0.25 T, automated sample positioning and rotation.

Time resolved scanning Kerr microscope: Longitudinal or polar MOKE geometry to study dynamic magnetization reversal properties of micro-structured elements. Optical resolution $<$ 500 nm, time resolution ~ 60 ps, magnetic field up to 150 mT, automated sample positioning and stabilization.

References

[1] J. Kerr, *On rotation of the plane of polarization by reflection from the pole of a magnet*, Phil. Mag. **4** (5), 321 (1877).

3.4 Molecular beam epitaxy (MBE)

The molecular beam epitaxy (MBE) technique involves highly controlled evaporation of materials in an ultra-high vacuum chamber (pressure in the low 10^{-11} mbar region). This deposition from the vapor phase can lead to single crystal film growth. For this reason MBE possesses a dominant role in the world of nanotechnology regarding fabrication of materials for high performance applications.

Our group operates two molecular beam epitaxy (MBE) growth clusters. Both systems are equipped with tools for cleaning the substrates, controlling the evaporation from the sources and the film deposition, *in-situ* structural and chemical characterization, as well as for sample storage.

One of them is displayed in Fig. 1 and it is named MDA (Multidepositionsanlage). The MDA has been upgraded this year with new pumps, valves and new automated growth procedures. The linear construction of the sample holder reduces the total time for sample preparation drastically. It contains two Knudsen cells and one electron gun with 5 crucibles that are used to heat and evaporate the materials. The growth procedure is controlled *in-situ* by a quartz crystal. Additionally *in-situ* Low-Energy Electron Diffraction (LEED) and Auger analytics can be performed.

Our second cluster, named MBE, contains two Knudsen cells and one electron gun with 5 crucibles. The growth procedure is also controlled *in-situ* by a quartz crystal. One of the great advantages of our MBE system is the capability to control the *in-situ* growth by means of reflection of high-energy electron diffraction (RHEED). The characteristics of the RHEED technique is not to interfere with the deposition. An example of layer by layer deposition controlled by RHEED is shown in Fig. 2. This renders it as a unique tool for real-time structural characterization of the sample during the growth process. There is also here the option for low-energy electron diffraction (LEED) and Auger analytics.

In addition to the aforementioned techniques and linked to the MBE, a scanning tunneling microscope (STM) set-up is used for *in-situ* atomic probing. This increases further the capabilities of our MBE chamber. STM is a unique tool for surface investigation of the evaporated samples. The cluster includes furthermore a load chamber for inserting samples in vacuum and preparation chamber. The latter is used for cleaning the samples since there is the possibility to heat them up to 800 °C. Furthermore, there is an option for optical coatings. The ionization chamber is equipped with a fine-focus noble gas keV ion source. A transfer chamber connects all the parts of the growth cluster while a repository chamber is also available. The MBE chamber has another unique feature: that of *in-situ* magnetic characterization with Brillouin light scattering (BLS) spectroscopy

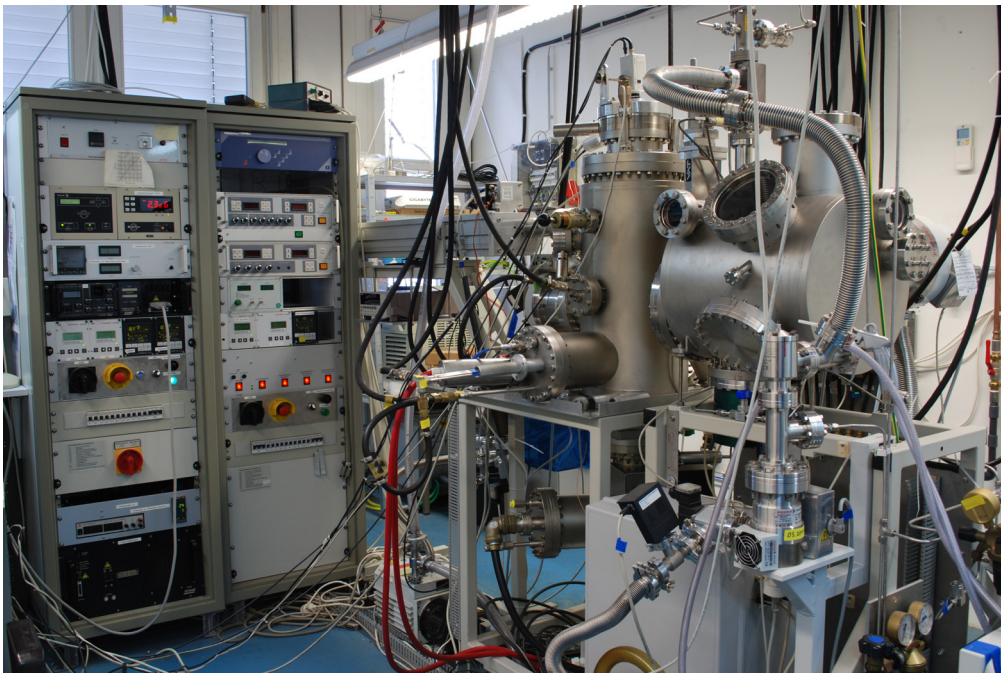

Fig. 1: A photo of our MDA growth cluster. One can see to the right the linear manipulator with the sample holder, the growth chamber and connected to that an oxidation chamber. On the left, the rack with the control units can be seen.

and Kerr effect magnetometry. The applied magnetic field can reach up to 1.2 T. There is an option for implementation of a cryostat.

The MBE evaporation technique offers unique advantages for the fabrication of patterned samples. The good control of the film growth and the directionality of the beam render MBE suitable to grow materials on patterned masks. Patterned samples of extreme quality can be produced either with pre- or post-treatment techniques.

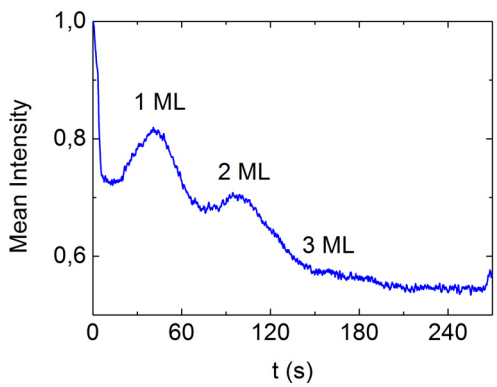

Fig. 2: RHEED oscillation observed for the growth of 3 ML Cr on top of Fe. RHEED offers unique advantages in controlling the growth procedure of the grown samples.

The sample production in 2014 included high structural quality samples like Fe, Py films and Fe/Pt, Fe/Au, Co/Pd, Co/Au bilayers for studies in magnetisation dynamics. Furthermore, the growth of insulating layers like MgO has been successfully tested.

Chapter 4: Reports on Experimental Results

A. Magnon Gases and Condensates

In ferromagnetic materials atoms having unpaired electrons act as individual magnets. Their magnetism is mostly caused by the magnetic moments of the uncompensated electron spins. Since these atomic magnets tend to be oriented in the same direction due to quantum-mechanical exchange interaction, a macroscopic magnetic moment appears. As the atoms strongly interact, a reversal of a single atomic magnetic moment is not spatially localized but spreads through the solid as a wave of discrete magnetic momentum transfer. This wave is known as a spin wave, and in frame of the second quantization it is associated with a quasi-particle called magnon. Weakly interacting magnons can be considered as a gas of magnetic bosonic quasi-particles and, therefore, this is called a magnon gas.

Recently magnon gases have been recognized as an excellent model environment for the experimental investigation of collective classical and quantum macroscopic properties of bosonic systems. Its potential is due to the wide controllability of the magnon density as well as of the spectral properties influencing the magnon-magnon interaction. For example, the dispersion branch of a magnon gas can be frequency shifted or otherwise modified by change in the strength or orientation of a bias magnetic field. The magnon population density can be effectively controlled by means of electromagnetic parametric pumping (see Gurevich and Melkov, Magnetization Oscillation and Waves, CRC, Cleveland, 1996). In the simplest case one photon of the pumping electromagnetic field excites two magnons with half the energy/frequency that propagate in opposite directions. Such a mechanism creates a huge quantity of phase correlated magnons, which are called a condensate of photon-coupled magnon pairs. The behavior of parametrically created magnon condensates, of gaseous magnon phases, and of Bose-Einstein condensates (BEC), which can be formed at the lowest energy state of a magnon gas, constitutes a hot research topic. The main goal of our work is to study the phase transition processes resulting in the formation of quantum macroscopic states of a magnon gas and to understand the role of magnon-magnon and magnon-phonon interactions in the properties of these correlated states of matter in comparison with the dynamics of ultra-cold quantum gases and quantum spin systems. We investigate the dynamics of the magnon system in a low-damping magnetic insulator (yttrium-iron-garnet, YIG) using wavevector- and time-resolved Brillouin light scattering (BLS) spectroscopy with special attention on the pump-free evolution of the magnetic medium after pumping. A focus lies on transport phenomena in magnon condensates including phase induced supercurrents.

Several very interesting recent experimental findings are presented this year.

In Report 4.1 “Magnetoelastic modes and lifetime of magnons in thin yttrium iron garnet films” a rigorous theoretical investigation of the influence of spin-lattice coupling on the magnon spectrum of thin YIG films is supported by experimental measurements of the wavenumber dependent damping of dipole-exchange magnons. Due to coupling to a transverse acoustic phonon the condensate of magnons has a finite group velocity.

In Report 4.2 “Full electric detection of a Bose-Einstein condensate via the spin-pumping effect” we present further evidence of the macroscopic coherence of a magnon BEC, which is responsible for the observed enhancement in the amplitude of the spin Hall effect induced voltage in the moment when the condensate is formed.

In Report 4.3 “Stimulated thermalization of a parametrically driven magnon gas and Bose-Einstein

condensation of dipole-exchange magnons" we demonstrate that at high pumping powers the external pumping magnetic field has a determining influence on the four-magnon process of thermalization of a parametrically driven magnon gas. This influence brakes the initial orthogonality between the wavevectors of the parametrically injected magnons and the lowest energy state of a magnon gas, and thus allows for the formation of the magnon BEC.

In Report 4.4 "Anomalous dynamics of a Bose-Einstein magnon condensate in a thermal gradient" we present first evidence of the existence of a magnon supercurrent excited in a magnon BEC by a laser-light induced thermal gradient. Such current, which leads to a magnon leakage from the focal point of the BLS probing laser beam, can be responsible for the enhanced decay of the freely evolving magnon condensate observed in our BLS experiments.

In Report 4.5 "Parallel parametric amplification of coherently excited propagating spin waves in a microscopic $Ni_{81}Fe_{19}$ waveguide" and in Report 4.6 "A localized spin-wave amplifier on the micrometer scale realized by parallel pumping" we further investigate the technique and physics of the parallel parametric amplification of spin waves propagating in microsized metal stripes. Specifically, in Report 4.6 a micro-sized parametric amplifier is realized and the ability of a steady-state amplification regime is demonstrated.

In Report 4.7 "Planar Hall effect induced dc voltage generation by short-wavelength microwave magnons" we show experimentally and theoretically that the phase correlation between parametrically populated magnon states permits the rectification of a microwave current induced by dipole-exchange magnons in a thin-film Permalloy sample.

A. Magnonengase und -kondensate

In ferromagnetischen Materialien treten Atome, die ungepaarte Elektronen haben, als einzelne Magnete auf. Ihr Magnetismus wird in der Regel durch die magnetischen Momente des nicht kompensierten Elektronenspins verursacht. Diese atomaren Magnete richten sich häufig aufgrund der quantenmechanischen Austauschwechselwirkung in einem Ferromagneten parallel zueinander aus. Daher beobachtet man ein makroskopisches magnetisches Moment. Da die Atome stark miteinander wechselwirken, wird das Umklappen eines einzelnen atomaren magnetischen Moments nicht räumlich lokalisiert sein, sondern breitet sich als Welle mit einem diskreten magnetischen Moment über den gesamten Festkörper aus. Diese Welle wird als Spinwelle bezeichnet und ist im Rahmen der zweiten Quantisierung mit einem Quasiteilchen, dem so genannten Magnon, verbunden. Schwach miteinander wechselwirkende Magnonen können als Gas von magnetischen bosonischen Quasiteilchen angesehen werden. Daher werden sie auch als Magnonengas bezeichnet.

Magnonengase sind unlängst als hervorragendes Modellsystem erkannt worden und dienen zur Untersuchung von korrelierten bosonischen Systemen mit sowohl klassischen Eigenschaften als auch mit makroskopischen Quanteneigenschaften. Ihr Potenzial liegt dabei in der guten Kontrollierbarkeit der Magnonendichte und den Eigenschaften des Spektrums, welches die Magnon-Magnon-Wechselwirkung beeinflusst. Zum Beispiel kann durch die Änderung der Richtung oder der Stärke eines externen Magnetfelds das Spektrum des Magnonengases in der Frequenz verschoben oder auch stark verändert werden. Der wirkungsvollste Mechanismus, die Dichte eines Magnonengases zu erhöhen, ist parametrisches Pumpen mittels Mikrowellen (s. Gurevich and Melkov, Magnetization Oscillation and Waves, CRC, Cleveland, 1996). Im einfachsten Fall erzeugt ein Photon des elektromagnetischen Pumpfeldes zwei Magnonen mit je der Hälfte der Energie des Photons, die sich in entgegengesetzte Richtungen ausbreiten. Dieser Mechanismus erzeugt eine

große Anzahl von phasenkorrelierten Magnonen, ein sogenanntes Kondensat von photonengekoppelten Magnonenpaaren. Die Verhaltensweisen parametrisch erzeugter Magnonenkondensate, gasförmiger Magnonenzustände, und von magnonischen Bose-Einstein-Kondensaten (BEC), welche im Zustand niedrigster Energie des Magnonengases erzeugt werden können, bilden ein heisses Forschungsthema. Das Hauptziel unserer Forschung ist die Untersuchung der Phasenübergänge, die zu der Bildung von Zuständen mit makroskopischen Quanteneigenschaften in Magnonengasen führen, und das Verständnis der Funktion der Viel-Magnonen-Wechselwirkungen in diesen korrelierten Zuständen der Materie im Vergleich mit der Dynamik von ultrakalten Quantengasen und Quanten-Spinsystemen. Wir untersuchen die Dynamik des Magnonensystems in einem Isolator mit niedriger Dämpfung (Yttrium-Eisen-Granat, YIG) mit Hilfe von wellenvektor- und zeitaufgelöster Brillouin-Lichtstreuspektroskopie mit besonderem Augenmerk auf die pumpfreie Entwicklung des magnetischen Mediums nach dem Pumpprozess. Die besondere Aufmerksamkeit konzentriert sich auf Transportphänomene in Magnonenkondensaten, die phaseninduzierte Supraströme einbeziehen.

Dieses Jahr werden einige sehr interessante neue experimentelle Ergebnisse vorgestellt.

In Bericht 4.1 “Magnetoelastic modes and lifetime of magnons in thin yttrium iron garnet films” wird eine theoretische Untersuchung des Einflusses einer Spin-Gitter-Kopplung von experimentellen Messungen der wellenzahlabhängigen Dämpfung dipolarer Austauschmagnonen begleitet.

In Bericht 4.2 “Full electric detection of a Bose-Einstein condensate via the spin-pumping effect” zeigen wir weitere Hinweise auf die makroskopische Kohärenz eines magnonischen Bose-Einstein-Kondensates, welches verantwortlich ist für die beobachtete Verstärkung der Amplitude der Spin-Hall-Effekt-induzierten Spannung in dem Augenblick, wenn das Kondensat entsteht.

In Bericht 4.3 “Stimulated thermalization of a parametrically driven magnon gas and Bose-Einstein condensation of dipole-exchange magnons” zeigen wir, dass das externe Pumpfeld bei hohen Pumpstärken einen messbaren Einfluss auf den Vier-Magnonen-Prozess der Thermalisierung eines parametrisch erzeugten magnonischen Bose-Einstein-Kondensates hat.

In Bericht 4.4 “Anomalous dynamics of a Bose-Einstein magnon condensate in a thermal gradient” präsentieren wir den ersten Hinweis auf die Existenz eines magnonischen Suprastroms, die in dem magnonischen Bose-Einstein-Kondensat durch einen Laserlicht-induzierten thermischen Gradienten erzeugt wird. Solch ein Strom, der zu einem Abfluss von Magnonen aus dem Fokuspunkt des BLS Probestrahls führt, kann verantwortlich sein für den verstärkten Zerfall des frei entstehenden Magnonenkondensates, der in unseren BLS-Experimenten beobachtet wird.

In Bericht 4.5 “Parallel parametric amplification of coherently excited propagating spin waves in a microscopic $Ni_{81}Fe_{19}$ waveguide” und Bericht 4.6 “A localized spin-wave amplifier on the micrometer scale realized by parallel pumping” untersuchen wir weiter die Physik und die Technik der parallelen parametrischen Verstärkung von Spinwellen, die sich in mikrometerskalierten Metallstreifen ausbreiten. In Bericht 4.6 wird insbesondere ein parametrischer Verstärker realisiert und es werden die Möglichkeiten eines stationären Verstärkungsregimes aufgezeigt.

In Bericht 4.7 “Planar Hall effect induced dc voltage generation by short-wavelength microwave magnons” zeigen wir experimentell und theoretisch, dass die Phasenkorrelationen zwischen parametrisch bevölkerten Magnonenzuständen einen Gleichrichtungseffekt des Mikrowellenstromes erlaubt, der durch dipolare Austauschmagnonen in einer dünnen Permalloy-Film-Probe bedingt wird.

4.1 Magnetoelastic modes and lifetime of magnons in thin yttrium iron garnet films

D.A. Bozhko, A.A. Serga, and B. Hillebrands

In collaboration with A. Rückriegel and P. Kopietz, Institut für Theoretische Physik, Universität Frankfurt, 60438 Frankfurt, Germany

The spin-lattice interactions in magnetic insulators can often be ignored. In some cases, however, the coupling between the spin degrees of freedom and the lattice vibrations (phonons) plays a crucial role. For example, in ultrasound experiments one uses the spin-lattice coupling to study the properties of the spin degrees of freedom from the measurement of the propagation and the attenuation of sound waves [2]. The theory of magneto-elastic effects in magnetic insulators has been developed more than half a century ago by Abrahams and Kittel [3,4], and by Kaganov and Tsukernik [5]. While in the past decades a few theoretical studies of magneto-elastic effects have appeared [6–11], recent experimental progress in the field of spintronics has revived the interest in the interactions between spin and lattice degrees of freedom [12]. In this work we calculate the effects of the spin-lattice coupling on the magnon spectrum of thin ferromagnetic films consisting of the magnetic insulator yttrium-iron garnet and present experimental results for the magnon damping in the dipolar regime, which have been obtained by means of time- and wave-vector-resolved Brillouin light scattering (BLS) spectroscopy [14].

It is generally established that the magnetic properties of YIG at room temperature can be obtained from the following effective quantum spin Hamiltonian [15–17]

$$\mathscr{H} = -\frac{1}{2}\sum_{ij}\sum_{\alpha\beta}(J_{ij}\delta_{\alpha\beta} + D_{ij}^{\alpha\beta})S_i^\alpha S_j^\beta - h\sum_i S_i^z \quad , \tag{1}$$

where the spin operators $\mathbf{S}_i = \mathbf{S}(\mathbf{R}_i)$ are localized at the sites $\mathbf{R}_i$ of a cubic lattice with lattice spacing $a \approx 1.2376\,\mathrm{nm}$, the exchange couplings $J_{ij} = J(\mathbf{R}_i - \mathbf{R}_j)$ connect the spins at nearest neighbour sites $\mathbf{R}_i$ and $\mathbf{R}_j$, and $h = \mu H$ is the Zeemann energy due to an external magnetic field H along the z axis (where $\mu = 2\mu_B$, and μ_B is the Bohr magneton). The dipole-dipole interaction is

$$D_{ij}^{\alpha\beta} = (1-\delta_{ij})\frac{\mu^2}{|\mathbf{R}_{ij}|^3}\left[3\hat{R}_{ij}^\alpha\hat{R}_{ij}^\beta - \delta_{\alpha\beta}\right] \quad , \tag{2}$$

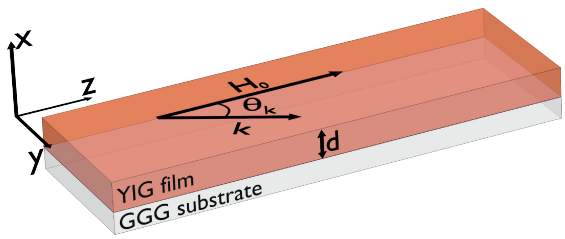

Fig. 1: Thin YIG stripe of thickness d in a magnetic field $\mathbf{H} = H\mathbf{e}_z$ along the direction $\mathbf{e}_z$ of the long axis. We consider magnons with wave vector $\mathbf{k} = |\mathbf{k}|\cos\theta_\mathbf{k}\mathbf{e}_z + |\mathbf{k}|\sin\theta_\mathbf{k}\mathbf{e}_y$ in the stripe-plane.

This work has been recently published in Physical Review B [1].

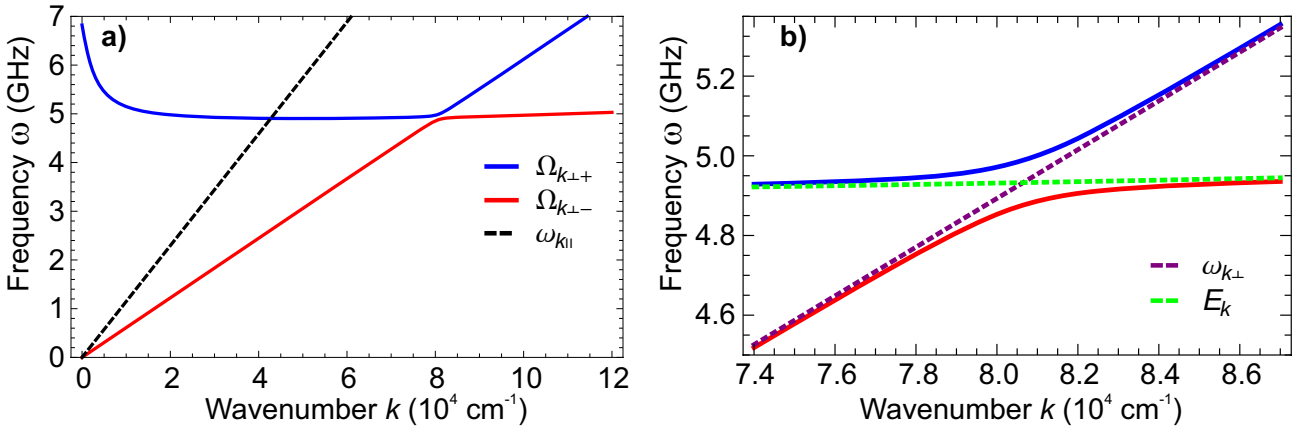

Fig. 2: a) Dispersions of the magneto-elastic modes of a thin YIG stripe with thickness $d = 6.7\,\mu$m in an external magnetic field $H = 1710\,$Oe, for $\mathbf{k} = k\mathbf{e}_z$ parallel to the in-plane magnetic field; b) A magnified view of the hybridisation at the crossing of magnon and transverse phonon dispersions.

where $\mathbf{R}_{ij} = \mathbf{R}_i - \mathbf{R}_j$ and $\hat{\mathbf{R}}_{ij} = \mathbf{R}_{ij}/|\mathbf{R}_{ij}|$. Within the framework of the usual expansion in inverse powers of the spin S the low-energy magnon spectrum of YIG can be quantitatively described if one chooses $J \approx 3.19\,$K and $S = M_s a^3/\mu \approx 14.2$, where the saturation magnetization of YIG is given by $4\pi M_s = 1750\,$G. Due to the large value of the effective spin S we may use the Holstein-Primakoff transformation [18] to express the spin operators in terms of canonical boson operators b_i and $b_i^\dagger$. To describe a thin stripe we can work with an effective two-dimensional model, as explained in Ref. [17]. We consider geometry shown in Fig. 1.

One source of the spin-phonon coupling is the dependence of the true positions $\mathbf{r}_i = \mathbf{R}_i + \mathbf{X}_i$ of the spins on the phonon displacements $\mathbf{X}_i = \mathbf{X}(\mathbf{R}_i)$ at the lattice sites $\mathbf{R}_i$. The resulting magnon phonon interaction can be derived from the effective spin-model (1) by expanding the exchange couplings $J_{ij} = J(\mathbf{R}_i - \mathbf{R}_j + \mathbf{X}_i - \mathbf{X}_j)$ in powers of the phonon displacements [19]. However, in collinear magnets such a procedure does not take into account the dominant source of the magnon-phonon interaction, which is generated by relativistic effects such as dipole-dipole interactions and spin-orbit coupling [10]. These effects involve the charge degrees of freedom so that they cannot be simply included in our effective spin model (1). To derive the proper quantized interaction between magnons and phonons in YIG, we therefore follow the semi-phenomenological approach pioneered by Abrahams and Kittel [3], which relies on the quantization of the phenomenological expression for the classical magneto-elastic energy [1, 3–5, 8, 10]:

$$E_{me}[\mathbf{M},\mathbf{X}] = \frac{n}{M_s^2}\int d^3r \sum_{\alpha\beta}\left[B_{\alpha\beta}M_\alpha(\mathbf{r})M_\beta(\mathbf{r}) + B'_{\alpha\beta}\frac{\partial\mathbf{M}(\mathbf{r})}{\partial r_\alpha}\cdot\frac{\partial\mathbf{M}(\mathbf{r})}{\partial r_\beta}\right]X_{\alpha\beta}(\mathbf{r}) \quad , \tag{3}$$

After quantization of magneto-elastic energy it becomes possible to calculate the energy dispersion of the magneto-elastic modes (for details, see Ref. [1]). The energy dispersion of these modes is shown graphically in Fig. 2 for $\mathbf{k} = k\mathbf{e}_z$ parallel to the in-plane magnetic field. Note that for this propagation direction the longitudinal phonon does not hybridise with the magnon dispersion because for $k_y = 0$ (corresponding to $\theta_{\mathbf{k}} = 0$) the relevant hybridisation function [1] vanishes.

The Brillouin light scattering intensity is proportional to the transverse spin structure factor [21,22]

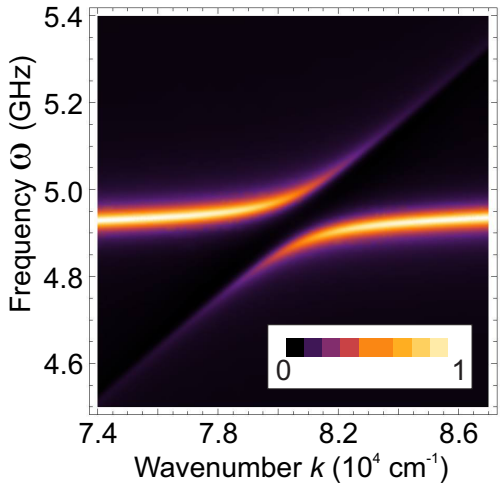

Fig. 3: Transverse spin dynamic structure factor of a thin YIG stripe at temperature $T = 300\,\mathrm{K}$, with thickness $d = 6.7\,\mu\mathrm{m}$ in an external magnetic field $H = 1710\,\mathrm{Oe}$, for $\mathbf{k} = k\mathbf{e}_z$ parallel to the in-plane magnetic field. The Dirac distributions were artificially broadened with a lifetime of 10 ns.

$$S_\perp(\mathbf{k},\omega) = \int_{-\infty}^{\infty} \frac{dt}{2\pi} e^{i\omega t} \langle S^x_{-\mathbf{k}}(0) S^x_{\mathbf{k}}(t) + S^y_{-\mathbf{k}}(0) S^y_{\mathbf{k}}(t) \rangle \quad . \tag{4}$$

The Fourier transform of the spin-operator is defined as $\mathbf{M}(\mathbf{k}) \to g\mu_B \sqrt{N}\mathbf{S}_\mathbf{k} = g\mu_B \sum_i e^{-i\mathbf{k}\cdot\mathbf{R}_i}\mathbf{S}_i$, where $n = N/V = 1/a^3$ is the unit cell number density.

An intensity plot of the transverse dynamic structure factor is shown in Fig. 3.

The damping $\gamma(\mathbf{k})$ of magnons with wave vector $\mathbf{k}$ and energy $E_\mathbf{k}$ can be obtained from the imaginary part of the self-energy $\Sigma(K) = \Sigma(\mathbf{k}, i\omega)$ after analytic continuation to the real frequency axis,

$$\gamma(\mathbf{k}) = -Im\Sigma(\mathbf{k}, i\omega \to E_\mathbf{k} + i\eta) \quad . \tag{5}$$

After carrying out the frequency sum we obtain [1]

$$\begin{aligned}\Sigma_2(\mathbf{k}, i\omega) = \frac{1}{N}\sum_{\mathbf{k}'\lambda} \Bigg\{ & \frac{|\Gamma^{\bar\beta\beta}_{\mathbf{k},\mathbf{k}',\lambda}|^2}{2m\omega_{\mathbf{k}-\mathbf{k}'\lambda}} \left[\frac{b(\omega_{\mathbf{k}-\mathbf{k}'\lambda}) - b(E_{\mathbf{k}'})}{i\omega + \omega_{\mathbf{k}-\mathbf{k}'\lambda} - E_{\mathbf{k}'}} + \frac{1 + b(\omega_{\mathbf{k}-\mathbf{k}'\lambda}) + b(E_{\mathbf{k}'})}{i\omega - \omega_{\mathbf{k}-\mathbf{k}'\lambda} - E_{\mathbf{k}'}} \right] \\ & - \frac{|\Gamma^{\beta\beta}_{\mathbf{k},\mathbf{k}',\lambda}|^2}{2m\omega_{\mathbf{k}+\mathbf{k}'\lambda}} \left[\frac{1 + b(\omega_{\mathbf{k}+\mathbf{k}'\lambda}) + b(E_{\mathbf{k}'})}{i\omega + \omega_{\mathbf{k}+\mathbf{k}'\lambda} + E_{\mathbf{k}'}} + \frac{b(\omega_{\mathbf{k}+\mathbf{k}'\lambda}) - b(E_{\mathbf{k}'})}{i\omega - \omega_{\mathbf{k}+\mathbf{k}'\lambda} + E_{\mathbf{k}'}} \right] \Bigg\}.\end{aligned} \tag{6}$$

Here $b(\omega) = 1/(e^{\omega/T} - 1)$ is the Bose function. Since the experiments of interest to us are performed at room temperature which is large compared with all other energy scales, we may use the high temperature expansion of the Bose functions, $b(\omega) \approx T/\omega$. Setting now $\omega = E_\mathbf{k}$ we obtain for the magnon damping on resonance at high temperatures,

$$\begin{aligned}\gamma_2(\mathbf{k}) = \frac{\pi T E_\mathbf{k}}{2mN}\sum_{\mathbf{k}'\lambda} \Bigg\{ & \frac{|\Gamma^{\bar\beta\beta}_{\mathbf{k},\mathbf{k}',\lambda}|^2}{E_{\mathbf{k}'}\omega^2_{\mathbf{k}-\mathbf{k}'\lambda}} \left[\delta(E_\mathbf{k} - E_{\mathbf{k}'} + \omega_{\mathbf{k}-\mathbf{k}'\lambda}) + \delta(E_\mathbf{k} - E_{\mathbf{k}'} - \omega_{\mathbf{k}-\mathbf{k}'\lambda}) \right] + \\ & \frac{|\Gamma^{\beta\beta}_{\mathbf{k},\mathbf{k}',\lambda}|^2}{E_{\mathbf{k}'}\omega^2_{\mathbf{k}+\mathbf{k}'\lambda}} \delta(E_\mathbf{k} + E_{\mathbf{k}'} - \omega_{\mathbf{k}+\mathbf{k}'\lambda}) \Bigg\} = \gamma^{Che}_{2a}(\mathbf{k}) + \gamma^{Che}_{2b}(\mathbf{k}) + \gamma^{con}_2(\mathbf{k}),\end{aligned} \tag{7-a}$$

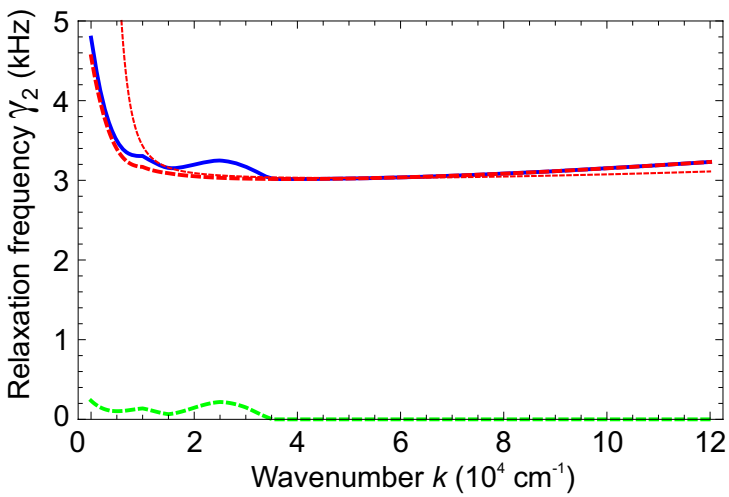

Fig. 4: Numerical evaluation of our result (7-a) for the damping rate of magnons in a thin YIG stripe at temperature $T = 300\,\mathrm{K}$, in the dipolar momentum regime. The plot is for a thin stripe of thickness $d = 6.7\,\mu\mathrm{m}$ in an external magnetic field $H = 1710\,\mathrm{Oe}$, for $\mathbf{k} = k\mathbf{e}_z$ parallel to the in-plane magnetic field. Solid lines correspond to the total damping rate, while the dashed and the dotted lines are the contribution from the Cherenkov and the confluent processes, respectively. The corresponding thin dotted line is the approximation in the dipolar momentum regime.

where,

$$\gamma_{2a}^{Che}(\mathbf{k}) = \frac{\pi T E_{\mathbf{k}}}{2mN} \sum_{\mathbf{q}\lambda} \frac{|\Gamma^{\bar{\beta}\beta}_{\mathbf{k},\mathbf{k}+\mathbf{q},\lambda}|^2}{E_{\mathbf{k}+\mathbf{q}}\omega^2_{\mathbf{q}\lambda}} \delta(E_{\mathbf{k}} - E_{\mathbf{k}+\mathbf{q}} + \omega_{\mathbf{q}\lambda}), \tag{7-b}$$

$$\gamma_{2b}^{Che}(\mathbf{k}) = \frac{\pi T E_{\mathbf{k}}}{2mN} \sum_{\mathbf{q}\lambda} \frac{|\Gamma^{\bar{\beta}\beta}_{\mathbf{k},\mathbf{k}-\mathbf{q},\lambda}|^2}{E_{\mathbf{k}-\mathbf{q}}\omega^2_{\mathbf{q}\lambda}} \delta(E_{\mathbf{k}} - E_{\mathbf{k}-\mathbf{q}} - \omega_{\mathbf{q}\lambda}), \tag{7-c}$$

$$\gamma_{2}^{con}(\mathbf{k}) = \frac{\pi T E_{\mathbf{k}}}{2mN} \sum_{\mathbf{q}\lambda} \frac{|\Gamma^{\beta\beta}_{\mathbf{k},-\mathbf{k}+\mathbf{q},\lambda}|^2}{E_{-\mathbf{k}+\mathbf{q}}\omega^2_{\mathbf{q}\lambda}} \delta(E_{\mathbf{k}} + E_{-\mathbf{k}+\mathbf{q}} - \omega_{\mathbf{q}\lambda}). \tag{7-d}$$

The contributions $\gamma_{2a}^{\mathrm{Che}}(\mathbf{k})$ and $\gamma_{2b}^{\mathrm{Che}}(\mathbf{k})$ are due to the Cherenkov type process where a magnon with energy $E_{\mathbf{k}}$ emits or absorbs a phonon with energy $\omega_{\mathbf{q}}$ and decays into a magnon with energy $E_{\mathbf{k}\pm\mathbf{q}}$. The last contribution $\gamma_2^{\mathrm{con}}(\mathbf{k})$ describes a confluent scattering process where two magnons with energies $E_{\mathbf{k}}$ and $E_{-\mathbf{k}+\mathbf{q}}$ decay into a phonon with energy $\omega_{\mathbf{q}}$.

In the long-wavelength regime where the exchange energy $\rho_s\mathbf{k}^2$ is much less then the characteristic dipolar energy Δ (i.e. $|\mathbf{k}| \lesssim \sqrt{\Delta/\rho_s}$), the behavior of the magnon damping (7-a) strongly depends on the size $v(\mathbf{k}) = |\mathbf{v}(\mathbf{k})|$ of the group velocity $\mathbf{v}(\mathbf{k}) = \nabla_{\mathbf{k}} E_{\mathbf{k}}$ of the magnons in comparison with the phonon velocities. In the regime around the minima of the dispersion, the velocity $v(\mathbf{k})$ is small compared with the phonon velocities, while at very small wave vectors $v(\mathbf{k}) > c_\lambda$. In this regime around the minima of the dispersion the decay rate of the magnons is dominated by the confluent process given in Eq. (7-d) because the Cherenkov processes are kinematically suppressed. In fact, in a substantial regime around the dispersion minima the quasi-particle velocity is small compared with the phonon velocities, so that we may approximate $E_{-\mathbf{k}+\mathbf{q}} \approx E_{\mathbf{k}} - \mathbf{v}(\mathbf{k}) \cdot \mathbf{q}$ and expand the decay rate in powers of $v(\mathbf{k})/c_\lambda$. The momentum integration in Eq. (7-d) can then be carried out and we obtain the confluent contribution to the high-temperature damping rate in the dipolar regime which is shown graphically as the thin dotted line in Fig. 4.

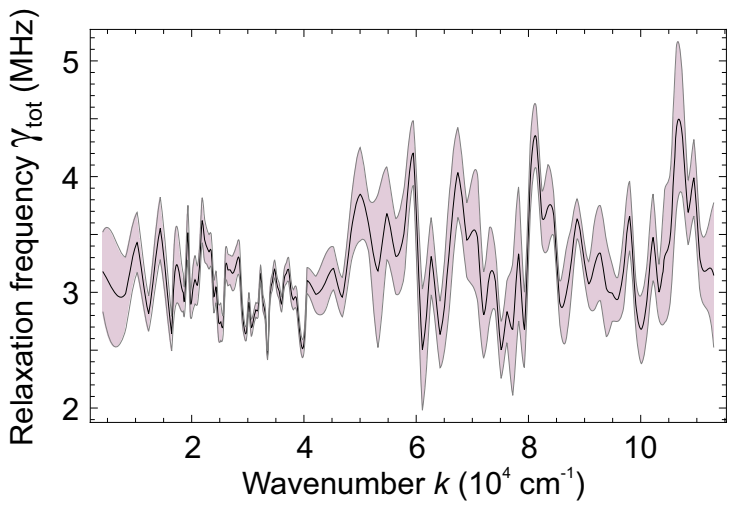

Fig. 5: Experimentally determined dependence of the total magnon damping γ_{tot} on the in-plane wave vector in the dipolar regime where the magnon dispersion is dominated by the competition between the dipole-dipole and the exchange interaction. The shaded regions represent the estimated experimental uncertainties.

For a comparison of our calculation with experiments one should keep in mind that we have only considered the contribution from the magnon-phonon interactions on the damping of the magnons. Of course, in the real system there are other sources leading to magnon decay, such as magnon-magnon interactions or the elastic scattering of magnons by impurities. We therefore expect that the magnon damping due to magnon-phonon interactions is a lower limit to the experimentally observed magnon damping rate. In fact, our experimental data presented below show that in the dipolar regime magnon-phonon interactions are not the dominant source of magnon damping.

In order to determine the relaxation time of different groups of magnons, a measurements of the spectral distribution of magnon gas densities as a function of the frequency and wave vector using time- and wave-vector-resolved BLS spectroscopy [14] has been performed. Due to technical reasons only in-plane wave vectors from 0 up to the $k_z^{\max} = 11 \times 10^4\,\mathrm{cm}^{-1}$ are accessible. The measurements were performed using a YIG film with thickness 6.7 µm, which was liquid-phase epitaxialy grown on a 500 µm thick gallium gadolinium garnet substrate.

The magnon spectrum was populated by intensive thermalization [20, 23, 24] of magnons, which were injected using the parallel parametric pumping technique [25] at half of the pumping frequency $f_p = 13.62\,\mathrm{GHz}$. The bias magnetic field of $H = 1710\,\mathrm{Oe}$ was tuned to provide the excitation of parametric magnons at the ferromagnetic resonance frequency. In this case the direct transition of magnons to the bottom of the spin wave spectrum is prohibited by conservation laws. This ensures high efficiency of multi-stage four-magnon scattering which is necessary for thermalization and thus population of the spectrum.

We have measured the redistribution of thermalized magnons along the fundamental backward-volume magnetostatic spin wave mode as a function of time and wave vector. After switching off the pumping, the magnons are allowed to relax freely. By fitting the relaxation times for different groups of thermalized magnons we were able to extract the damping rates. The obtained dependence of the measured total damping rate γ_{tot} on the in-plane wave vector for dipolar-exchange spin waves is shown in Fig. 5. Obviously, the value of relaxation rate is roughly three orders of magnitude larger than our calculated relaxation rate due to magnon-phonon interactions shown in Fig. 4. We thus conclude that in the long-wavelength dipolar regime other relaxation channels (in particular two-magnon scattering processes [26–29]) dominate the magnon damping. The rather irregular behavior of the measured damping rate in Fig. 5 suggests that elastic scattering of magnons by impurities might play an important role in this regime. Note that within the tolerance limits of the experiment the measured relaxation rate has a rather weak dependence on the in-plane wave

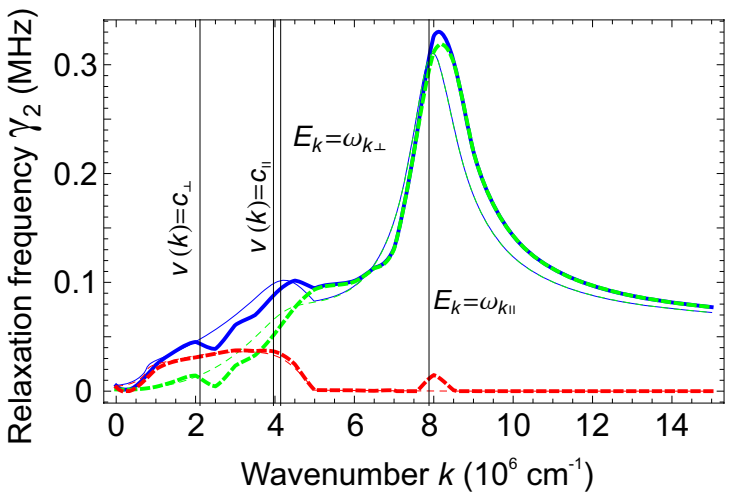

Fig. 6: Numerical evaluation of our result (7-a) for the damping rate of magnons in a thin YIG stripe at temperature $T = 300\,\mathrm{K}$, in the exchange momentum regime. The plot is for the same parameters as in Fig. 4. Solid lines correspond to the total damping rate, while the dashed and the dotted lines are the contribution from the Cherenkov and the confluent processes, respectively. The corresponding thin lines are the approximations in the exchange momentum regime.

vectors in the entire accessible range of wave vectors. In this respect the experimental results agree with our prediction of a momentum-independent damping rate in this regime.

Unfortunately, microscopic calculations of the magnon decay rates at room temperature, taking magnon-impurity and magnon-magnon interactions into account, are not available in the momentum range relevant for our experiment. One should keep in mind, however, that magnon-impurity scattering can only explain the momentum-relaxation of the magnon gas; for the equilibration of the different temperatures of the magnon and the phonon systems magnon-phonon interactions are essential.

For wave vectors in the regime where the exchange energy $\rho_s \mathbf{k}^2$ exceeds the characteristic dipolar energy Δ we may ignore the dipole-dipole interactions in the magnon dispersion and approximate the long-wavelength magnon dispersion by $E_{\mathbf{k}} \approx h + \rho_s \mathbf{k}^2$. Then the evaluation of the integrals in Eqs. (7-b)–(7-d) simplifies. We obtain for the Cherenkov part

$$\gamma_2^{\mathrm{Che}}(\mathbf{k}) \equiv \gamma_{2a}^{\mathrm{Che}}(\mathbf{k}) + \gamma_{2b}^{\mathrm{Che}}(\mathbf{k}) = \frac{T E_{\mathbf{k}}}{2} \frac{m_s}{m} \sum_\lambda \frac{a^2}{c_\lambda^2} \times \int_0^{2\pi} \frac{d\varphi}{2\pi} \frac{U_\lambda^2(\hat{\mathbf{q}}_\varphi)}{E_{\mathbf{k}} + 2 m_s c_\lambda (c_\lambda - v(\mathbf{k}) \cos\varphi)} \quad . \tag{8}$$

where $v(\mathbf{k}) = |\mathbf{k}|/m_s$, the mass m_s is defined via $\rho_s = 1/(2m_s)$.

A graph of the Cherenkov and confluent contribution to the high-temperature damping rate in the exchange regime is shown as the thin dashed line and thin dotted line in Fig. 6 respectively. As one can see, the magnon damping is strongly $\mathbf{k}$-dependent. In particular, it exhibits peaks at the crossing points of magnon and phonon dispersions as well as velocities. It also increases by two orders of magnitude between dipolar and exchange regimes, which are dominated by confluence and Cherenkov processes, respectively. For the magnon lifetime $\tau(\mathbf{k}) = 1/(2\pi\gamma(\mathbf{k}))$, this implies values of the order of $50\,\mu\mathrm{s}$ in the dipolar momentum range, while it can be as low as $480\,\mathrm{ns}$ for exchange momenta.

In this work we have studied magneto-elastic interactions in experimentally relevant thin films of the magnetic insulator YIG. As the dominant sources of magneto-elastic interactions are due to relativistic effects [10] which cannot be taken into account within an effective model containing only spin degrees of freedom, we have used a semi-phenomenological approach [3], which relies on the quantization of a suitable phenomenological expression for the magneto-elastic energy. For the quantized theory we have then carefully derived the momentum dependence of the magneto-elastic interaction vertices within the framework of the conventional $1/S$-expansion for ordered

quantum spin systems. Using these vertices, we have explicitly calculated the leading contributions to the hybridisation between magnon and phonon modes, as well as the damping of the magnons due to spin-lattice coupling. The hybridisation has been shown to give rise to a characteristic minimum in the spin dynamic structure factor at the crossing point of magnon and transversal phonon dispersions, where the spectral weight is transferred from the magnons to the transverse phonon mode. The position of this minimum quantitatively agrees with the recent experimental observation of the magneto-elastic mode [30].

The damping at room temperature has been shown to be strongly momentum dependent. In the long-wavelength dipolar regime it is rather flat and almost exclusively driven by confluent magnon-phonon scattering processes where two magnons decay into a phonon or vice versa. In this regime, we have also presented new experimental results for the magnon damping obtained by wave-vector-resolved Brillouin light scattering spectroscopy. The fact that the experimental results for the magnon damping are roughly three orders of magnitude larger than our theoretical results indicate that in the dipolar regime magnon-phonon interactions are not the dominant source of magnon damping in our samples at room temperature. We suspect that in this regime the magnon damping is dominated by elastic scattering of magnons from impurities. On the other hand, in the short-wavelength exchange regime the damping is due to magnon-phonon scattering processes of the Cherenkov type and is two orders of magnitude larger than in the dipolar regime. The damping rate exhibits pronounced peaks at the crossing points of magnon and phonon dispersions and velocities. This agrees very well with the conclusions of the experiment [13] , where the authors suggested that the spin-lattice relaxation in the dipolar regime should be much slower than in the exchange regime in order to reconcile their results with earlier work on the spin Seebeck effect.

The present work can be extended in two directions: on the theoretical side, it would be useful to have quanitatively accurate calculations of the magnon damping due to magnon-impurity and magnon-magnon interactions in the dipolar regime; we expect that this can provide a better explanation for our experimental results shown in Fig. 5, which is three orders of magnitude larger than the damping due to magnon-phonon interactions in this regime. Note, however, that recently Chernyshev [31] has considered spontaneous magnon decays of the $\mathbf{k} = 0$ magnon in YIG due to magnon-magnon interactions in high magnetic fields. On the experimental side, it would be useful to measure magnon damping in the exchange regime and compare the data with our theoretical prediction shown in Fig. 6.

Financial support by the DFG within the SFB/TR49 and Graduate School Materials Science in Mainz is acknowledged.

References

[1] A. Rückriegel, P. Kopietz, D.A. Bozhko, A.A. Serga, B. Hillebrands, *Magnetoelastic modes and lifetime of magnons in thin yttrium iron garnet films*, Physical Review B **89**, 184413 (2014).

[2] See, for example, B. Lüthi, *Physical acoustics in the solid state* (Springer, Berlin, 2005).

[3] E. Abrahams, C. Kittel, *Spin-lattice relaxation in ferromagnets*, Phys. Rev. **88**, 1200 (1952); Rev. Mod. Phys. **25**, 233 (1953).

[4] C. Kittel, *Interaction of spin waves and ultrasonic waves in ferromagnetic crystals*, Phys. Rev. **110**, 836 (1958).

[5] M.I. Kaganov, V.M. Tsukernik, *Phenomenological theory of kinetic processes in ferromagnetic dielectrics. Pt. 2. Interaction of spin waves with phonons*, Sov. Phys. JETP **9**, 151 (1959).

[6] H.F. Tiersten, *Coupled magnetomechanical equations for magnetically saturated insulators* J. Math. Phys. **5**, 1298 (1964).

[7] C.M. Bandari, G.S. Verma, *Scattering of magnons and phonons in the thermal conductivity of yttrium iron garnet*, Phys. Rev. **152**, 731 (1966).

[8] A.E. Lord Jr., *Sound wave attenuation due to the magnon-phonon interaction*, Phys. kondens. Materie **7**, 232 (1968).

[9] T. Kobayashi, R.C. Barker, J.L. Bleustein, A. Yelon, *Ferromagnetoelastic resonance in thin films. I. Formal treatment*, Phys. Rev. B **7**, 3273 (1973).

[10] A.G. Gurevich, G.A. Melkov, *Magnetization oscillations and waves* (CRC Press, Boca Raton, 1996).

[11] L. Dreher, M. Weiler, M. Pernpeintner, H. Huebl, R. Gross, M.S. Brandt, S.T.B. Goennenwein, *Surface acoustic wave driven ferromagnetic resonance in nickel thin films: Theory and experiment*, Phys. Rev. B **86**, 134415 (2012).

[12] A. Kamra, G.E.W. Bauer, *Actuation, propagation, and detection of transverse magnetoelastic waves in ferromagnets*, arXiv:1306.6268v2 [cond-mat.mes-hall] 1 Nov 2013.

[13] M. Agrawal, V.I. Vasyuchka, A.A. Serga, A.D. Karenowska, G.A. Melkov, B. Hillebrands, *Direct measurement of magnon temperature: new insight into magnon-phonon coupling in magnetic insulators*, Phys. Rev. Lett. **111**, 107204 (2013).

[14] C.W. Sandweg, M.B. Jungfleisch, V.I. Vasyuchka, A.A. Serga, P. Clausen, H. Schultheiss, B. Hillebrands, A. Kreisel, P. Kopietz, *Wide-range wavevector selectivity of magnon gases in Brillouin light scattering spectroscopy* , Rev. Sci. Instrum. **81**, 073902 (2010).

[15] V. Cherepanov, I. Kolokolov, V. L'vov, *The saga of YIG: Spectra, thermodynamics, interaction and relaxation of magnons in a complex magnet*, Phys. Rept. **229**, 81 (1993).

[16] I.S. Tupitsyn, P.C.E. Stamp, A.L. Burin, *Stability of Bose-Einstein condensates of hot magnons in yttrium iron garnet films*, Phys. Rev. Lett. **100**, 257202 (2008).

[17] A. Kreisel, F. Sauli, L. Bartosch, P. Kopietz, *Microscopic spin-wave theory for yttrium-iron garnet films*, Eur. Phys. J. B **71**, 59 (2009).

[18] T. Holstein, H. Primakoff, *Field dependence of the intrinsic domain magnetization of a ferromagnet*, Phys. Rev. **58**, 1098 (1940).

[19] A. Kreisel, P. Kopietz, P.T. Cong, B. Wolf, M. Lang, *Elastic constants and ultrasonic attenuation in the cone state of the frustrated antiferromagnet Cs2CuCl4*, Phys. Rev. B **84**, 024414 (2011).

[20] J. Hick, T. Kloss, P. Kopietz, *Thermalization of magnons in yttrium-iron garnet: Nonequilibrium functional renormalization group approach*, Phys. Rev. B **86**, 184417 (2012).

[21] M.G. Cottam, D.J. Lockwood, *Light scattering in magnetic solids* (Wiley, New York, 1986).

[22] J. Jorzick, S.O. Demokritov, C. Mathieu, B. Hillebrands, B. Bartenlian, C. Chappert, F. Rousseaux, A.N. Slavin, *Brillouin light scattering from quantized spin waves in micron-size magnetic wires*, Phys. Rev. B **60**, 15194 (1999).

[23] S.O. Demokritov, V.E. Demidov, O. Dzyapko, G.A. Melkov, A.A. Serga, B. Hillebrands, A.N. Slavin, *Bose-Einstein condensation of quasi-equilibrium magnons at room temperature under pumping*, Nature **443**, 430 (2006)

[24] V.E. Demidov, O. Dzyapko, M. Buchmeier, T. Stockhoff, G. Schmitz, G.A. Melkov, S.O. Demokritov, *Magnon kinetics and Bose-Einstein condensation studied in phase space*, Phys. Rev. Lett. **101**, 257201 (2008).

[25] A.A. Serga, C.W. Sandweg, V.I. Vasyuchka, M.B. Jungfleisch, B. Hillebrands, A. Kreisel, P. Kopietz, M.P. Kostylev, *Brillouin light scattering spectroscopy of parametrically excited dipole-exchange magnons*, Phys. Rev. B **86**, 134403 (2012).

[26] M. Sparks, *Ferromagnetic-relaxation theory* (McGraw-Hill, 1964)

[27] A.V. Chumak, A.A. Serga, B. Hillebrands, G.A. Melkov, V. Tiberkevich, A.N. Slavin, *Parametrically stimulated recovery of a microwave signal using standing spin-wave modes of a magnetic film*, Phys. Rev. B **79**, 014405 (2009)

[28] A.V. Chumak, A.A. Serga, M.B. Jungfleisch, R. Neb, D.A. Bozhko, V.S. Tiberkevich, B. Hillebrands, *Direct detection of magnon spin transport by the inverse spin Hall effect*, Appl. Phys. Lett. **100**, 082405 (2012)

[29] M.J. Hurben, C.E. Patton, *Theory of two magnon scattering microwave relaxation and ferromagnetic resonance linewidth in magnetic thin films*, J. Appl. Phys. **83**, 4344 (1998).

[30] B. Hillebrands *et al.*, Annual Report 2012: http://www.physik.uni-kl.de/hillebrands/publications/annual-reports/annual-report-2012.

[31] A.L. Chernyshev, *Field dependence of magnon decay in yttrium iron garnet thin films*, Phys. Rev. B **86**, 060401(R) (2012).

4.2 Full electric detection of a Bose-Einstein condensate via the spin-pumping effect

D.A. Bozhko, A. Kirihara, A.V. Chumak, B. Hillebrands, and A.A. Serga*

In collaboration with Y. Tserkovnyak, Department of Physics and Astronomy, University of California, Los Angeles, California 90095, USA, and
G.A. Melkov, Faculty of Radiophysics, Taras Shevchenko National University of Kyiv, 01601 Kyiv, Ukraine

**A. Kirihara is affiliated with Smart Energy Research Laboratories, NEC Corporation, Tsukuba 305-8501, Japan*

It is well known, that magnons excited in an insulating magnetic medium can transfer their angular momenta to free electrons in an adjacent non-magnetic metal layer, and thus generate a spin current via the spin-pumping (SP) effect [1]. Due to the inverse spin Hall effect (ISHE) [2, 3], caused by spin-dependent scattering, this current is transformed into a charge current and is measured as an electric voltage. It is commonly believed that the magnitude of the ISHE voltage increases with the total number of magnons in a spin-wave system [4] as well as with the energy of these magnons [5]. The electric signal, which corresponds to the formation of a magnon Bose-Einstein condensate (BEC) by a freely evolving magnon gas after the termination of an external pumping [6], breaks with this rule: The transition of the thermalized gaseous magnons to the lowest energy states, which develops alongside with the process of the magnon decay, leads to a pronounced upward jump of the voltage magnitude. This unusual behavior can be understood as a result of a rectification of a coherent microwave current induced by the magnon BEC in the non-magnetic metal layer. Thus, the voltage signal contains a fingerprint of the coherency of the condensate.

The experiment is performed using an in-plane magnetized 6.7 µm thick single-crystal yttrium iron garnet film (YIG) covered with a 10 nm thick platinum layer (see Fig. 1) and placed on top of a 50 µm microstrip resonator. The resonator is fabricated on top of an alumina substrate, which was used due to its low dielectric losses and good thermal conductivity to avoid spurious heating effects which could be potentially caused by high microwave powers. A pumping circuit consisting

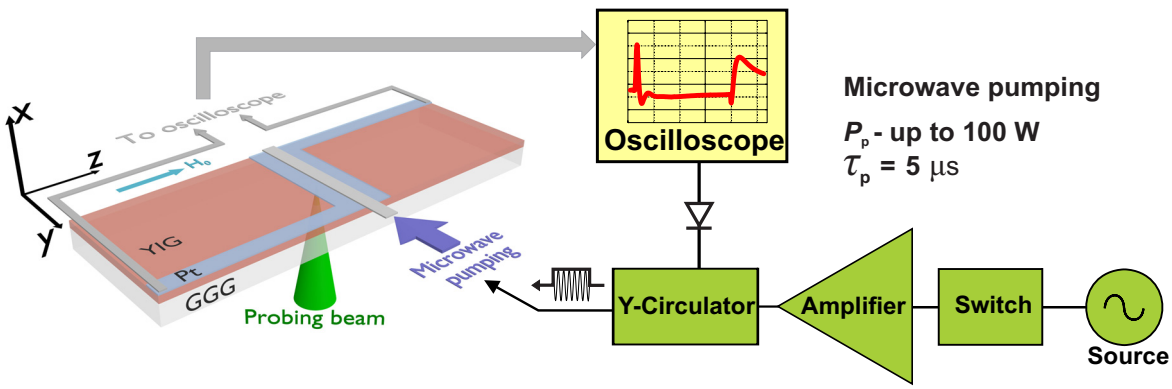

Fig. 1: Geometry of the experiment. An in-plane magnetized 6.7 µm thick YIG film covered with a 10 nm thick platinum layer. The geometry of the external bias magnetic field and the pumping area corresponds to the ISHE voltage generation along the Pt layer. The special shape of the Pt layer is designed to reduce losses of the ISHE voltage by short-cutting areas outside the pumped region under the microwave resonator.

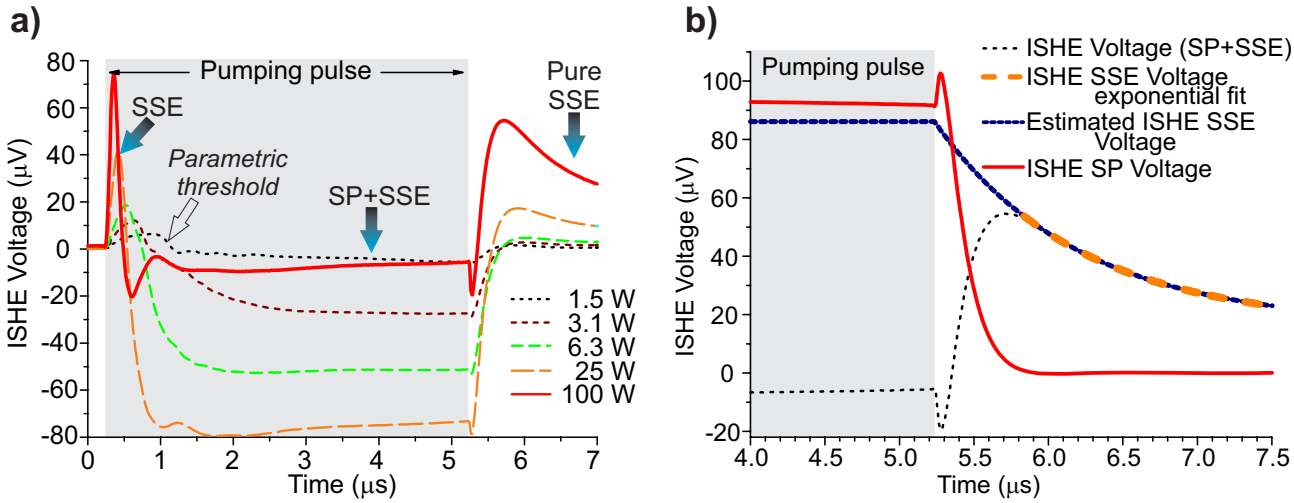

Fig. 2: a) The detected ISHE voltage profiles at different applied microwave powers; by arrows the SP and SSE contribution ranges are shown; b) Separation of the pure SSE and SP effect contributions to the total ISHE voltage.

of a microwave source, a switch, and a power amplifier feeds the resonator with $\tau_p = 5\,\mu\text{s}$ long microwave pulses at 13.6 GHz carrier frequency. An Y-circulator redirects the microwave power reflected from the resonator to a crystal detector and thus permits to monitor the efficiency of the parametric excitation process by an oscilloscope. The microstrip resonator induces a pumping Oersted field along the bias field $\mathbf{H}_0$. Thus, the geometry of parallel parametric pumping, when one pumping photon splits into two magnons at half of the pumping frequency [7], is realized. In all measurements the bias magnetic field is tuned to $H_0 = 1710\,\text{Oe}$ to excite magnons just above the ferromagnetic resonance (FMR) frequency. In this case direct scattering of the parametrically injected magnons to the bottom of the spin-wave spectrum is prohibited by conservation laws. As a result, the conditions for multistage four-magnon scattering processes, necessary for the effective thermalization of a magnon gas, are satisfied. The time evolution of the parametrically populated magnon gas is directly detected by the wavenumber- and time-resolved Brillouin light scattering (BLS) technique [8]. Simultaneously, the voltage picked up from the Pt layer is detected by an oscilloscope (see Fig. 2a).

The microwave pumping pulse produces not only an Oersted field but an Ohmic heating of the thin Pt layer as well. Thus, a thermal gradient is established in the direction from the Pt layer to YIG. This case corresponds to the transversal spin-Seebeck effect (SSE) observation geometry [9]. The combined contributions of the SSE and the pure SP effect explain the complicated shape of the observed voltage pulses. When the pumping pulse is applied, the heating of the Pt layer starts, causing the SSE voltage to rise. But after some delay (depending on the applied microwave power) the parametric process develops and the SP contribution from parametrically injected magnons starts to grow. For example, at a pumping power of 100 W the SP contribution to the total ISHE voltage at the end of the pumping pulse is as large as the contribution from SSE.

Already in the original unprocessed data one can see that, after pumping is switched off, at high pumping powers the detected voltage experiences a significant jump (for an example, see solid line in Fig. 2a). The time scales and the sign of this jump reveals the SP origin of this voltage. To extract the pure SP contribution to the total ISHE voltage additional data processing is required. At the beginning of the pumping pulse the dynamics of the SSE and its interplay with the SP signal is complicated and is beyond the frame of this Report. Here we focus only on the ISHE voltage evo-

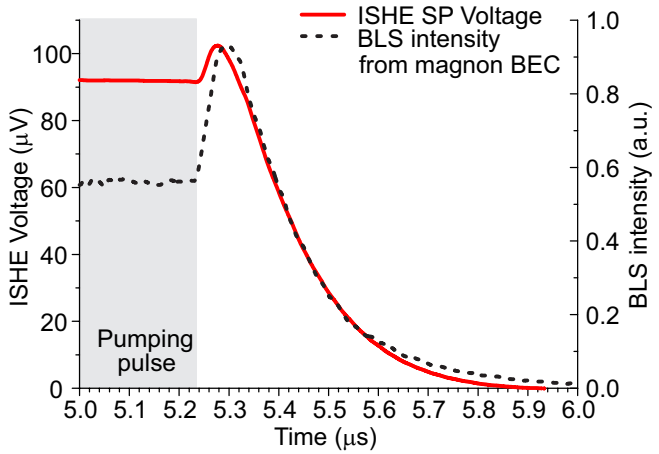

Fig. 3: The time profile of the extracted SP voltage pulse (solid line) and corresponding BLS intensity profile at the bottom of spin-wave spectrum (dashed line)

lution after equilibrium is reached. At this point it needs to be taken to account that caloric effects develop on much longer characteristic time scales than the process of magnon relaxation. Also, we assume that up to the end of the pumping pulse the thermal equilibrium is already established, so the SSE contribution becomes constant. These approximations allow us to extract the voltage corresponding to SSE by fitting the total ISHE voltage after a few microseconds after pumping pulse termination (see thick dashed lines in Fig. 2b). By extrapolating this fit in time to the trailing edge of the pumping pulse and by subtracting it from the measured ISHE voltage we obtain the pure SP contribution (see thick solid line in Fig. 2b). It is clearly visible that the ISHE SP voltage pulse experiences an upward jump just after the pumping is switched off.

In order to understand the physical nature of this phenomenon let us compare the obtained ISHE SP voltage profile with the *in-situ* measured evolution of the BLS signal from the bottom of the spin-wave spectrum (see dashed line in Fig. 3). One can see that the intensity of the scattered light also experiences an upward jump, which corresponds to the formation of the magnon BEC [6]. It is easy to see that the SP ISHE voltage peak (thick solid line in Fig. 3) correlates with the BLS intensity peak (see dashed line in Fig. 3). Thus, the observed phenomenon can be attributed to a spontaneous creation of a macroscopic coherent magnon state – the Bose-Einstein magnon condensate [10]. The mechanism of the peak formation could be a magnetoresistive rectification of a microwave current induced by the magnon BEC in the Pt layer. Recently, the spin Hall magnetoresistance (SMR) effect in YIG|Pt bilayers was discovered [11–13]. It has been shown that this effect allows the rectification of a microwave current at the frequency of a uniform magnetization precession excited in the YIG film. However, how the necessary uniformity can arise in our system if the carrier wavelength of the magnon BEC is smaller than 1 μm?

It is known, that during the action of a strong pumping pulse the effective temperature of the magnon gas can be so high that no magnon BEC formation is allowed [6]. In such a case the magnon gas dynamics is dominated by short wavelengths thermalized magnons, which contributes to the conventional ISHE voltage only: The microwave current contributions induced by these non-coherent magnons are canceled out after averaging over the macroscopic sample size, and thus no rectification component is detected in the ISHE voltage. After the termination of the pumping pulse, the effective magnon temperature rapidly decreases due to the evaporative super-cooling process [6] and the thermalized magnons spontaneously condense in two energy degenerated spectral states with opposite wavevectors at the bottom of a spin-wave spectrum. As it was shown in Ref. [14], these two coherent magnon condensates form a characteristic standing wave with a periodic pattern along the direction of the bias magnetic field $\mathbf{H}_0$.

We assume that exactly this standing BEC wave is responsible for the observed voltage pulse: A longitudinal component $\mathbf{m}_z$ of it's dynamic magnetization *uniformly* oscillates along $\mathbf{H}_0$ at twice the precessional frequency of the magnon BEC. As a result, an ac voltage and corresponding microwave current are induced at this frequency in the Pt layer due to Faraday's law. Finally, the ac current is rectified by means of the SMR effect and, thus, contributes to the dc voltage peak. A similar rectification mechanism acting in a magnetic metal film is described in the Report 4.7.

In conclusion, we demonstrate that the formation of a magnon BEC leads to the upward jump of a dc electric signal in a non-magnetic metal layer placed on the surface of the magnetic sample. We attribute this jump to the simultaneous action of two different phenomena – the inverse spin Hall effect and the spin Hall magnetoresistance effect. The latter is responsible for the rectification of the ac current, which is induced in the metal layer by the uniform magnetization component of the standing magnon BEC. The obtained results clear demonstrate the coherent nature of the magnon Bose-Einstein condensate and can be considered as a new approach to the detection of macroscopic quantum phase transitions of a magnon gas.

Financial support by the DFG within the SFB/TR49 and Graduate School Materials Science in Mainz is gratefully acknowledged.

References

[1] Y. Tserkovnyak, A. Brataas, G.E.W. Bauer, *Enhanced Gilbert damping in thin ferromagnetic films*, Phys. Rev. Lett. **88**, 117601 (2002).
[2] J.E. Hirsch, *Spin Hall effect*, Phys. Rev. Lett. **83**, 1834 (1999).
[3] D. Wei, M. Obstbaum, M. Ribow, C.H. Back, G. Woltersdorf, *Spin Hall voltages from a.c. and d.c. spin currents*, Nat. Commun. **5**, 3758 (2014).
[4] H. Kurebayashi, O. Dzyapko, V.E. Demidov, D. Fang, A.J. Ferguson, S.O. Demokritov, *Controlled enhancement of spin-current emission by three-magnon splitting*, Nature Materials **10**, 660 (2011).
[5] Y. Tserkovnyak, A. Brataas, G.E.W. Bauer, *Enhanced Gilbert damping in thin ferromagnetic films* Phys. Rev. Lett. **88**, 117601 (2002).
[6] A.A. Serga, V.S. Tiberkevich, C.W. Sandweg, V.I. Vasyuchka, D.A. Bozhko, A.V. Chumak, T. Neumann, B. Obry, G.A. Melkov, A.N. Slavin, B. Hillebrands, *Bose-Einstein condensation in an ultra-hot gas of pumped magnons*, Nat. Commun. **5**, 3452 (2014).
[7] A.G. Gurevich, G.A. Melkov, *Magnetization oscillations and waves*, (CRC, New York, 1996).
[8] C.W. Sandweg, M.B. Jungfleisch, V.I. Vasyuchka, A.A. Serga, P. Clausen, H. Schultheiss, B. Hillebrands, A. Kreisel, P. Kopietz, *Wide-range wavevector selectivity of magnon gases in Brillouin light scattering spectroscopy*, Rev. Sci. Instr. **81**, 073902 (2010).
[9] K. Uchida, S. Takahashi, K. Harii, J. Ieda, W. Koshibae, K. Ando, S. Maekawa, E. Saitoh, *Observation of the spin Seebeck effect*, Nature (London) **455**, 778 (2008).
[10] S.O. Demokritov, V.E. Demidov, O. Dzyapko, G.A. Melkov, A.A. Serga, B. Hillebrands, A.N. Slavin, *Bose-Einstein condensation of quasi-equilibrium magnons at room temperature under pumping*, Nature **443**, 430 (2006).
[11] Y.-T. Chen, S. Takahashi, H. Nakayama, M. Althammer, S.T.B. Goennenwein, E. Saitoh, G.E.W. Bauer, *Theory of spin Hall magnetoresistance*, Phys. Rev. B **87**, 144411 (2013).
[12] R. Iguchi, K. Sato, D. Hirobe, S. Daimon, E. Saitoh, *Effect of spin Hall magnetoresistance on spin pumping measurements in insulating magnet/metal systems*, Applied Physics Express **7**, 013003 (2014).
[13] H. Nakayama, M. Althammer, Y.-T. Chen, K. Uchida, Y. Kajiwara, D. Kikuchi, T. Ohtani, S. Geprägs, M. Opel, S. Takahashi, R. Gross, G.E.W. Bauer, S.T.B. Goennenwein, E. Saitoh, *Spin Hall magnetoresistance induced by a nonequilibrium proximity effect*, Phys. Rev. Lett. **110**, 206601 (2013).
[14] P. Nowik-Boltyk, O. Dzyapko, V.E. Demidov, N.G. Berloff, S.O. Demokritov, *Spatially non-uniform ground state and quantized vortices in a two-component Bose-Einstein condensate of magnons*, Sci. Rep. **2**, 482 (2012).

4.3 Stimulated thermalization of a parametrically driven magnon gas and Bose-Einstein condensation of dipole-exchange magnons

P. Clausen, D.A. Bozhko, V.I. Vasyuchka, B. Hillebrands, and A.A. Serga

In collaboration with G.A. Melkov, Faculty of Radiophysics, Taras Shevchenko National University of Kyiv, 01601 Kyiv, Ukraine

The technique of parallel parametric pumping [1,2], where an alternating magnetic pumping field $\mathbf{h}(t)$ is applied parallel to the direction of a bias magnetic field $\mathbf{H}$, can effectively couple the spin system of a magnetic material with an external microwave energy source. Therefore, parametric pumping is widely used to excite [3,4], amplify [5–7], and restore [8,9] spin-wave signals in macro- and micro-sized magnetic structures. Likewise, this technique fruitfully serves for experimental studies of nonlinear dynamics in multi-mode wave systems. One of the great achievements in this area was the realization of a Bose-Einstein condensation of magnons [10]. In a magnon Bose-Einstein condensate (BEC) the parametrically pumped magnon gas undergoes a phase transition leading to the spontaneous formation of a coherent state at the bottom of a spin-wave spectrum. From the time of this discovery, the physics of the parametrically driven magnon gases is under active theoretical and experimental investigation. Particularly, the time dependent behavior of the magnon gas in phase-energy space [11–15], the temperature of the magnon gas [16,17], the role of different scattering mechanisms in the thermalization process, and the interaction of the injected magnons with the phonon bath [18] are in the focus of attention.

Here, we provide experimental insight into the evolution of a magnon gas affected by four-magnon scattering in the presence of the external pumping field. We show that the magnons pumped to the transversal branch of the spin-wave spectrum (magnon wavevector $\mathbf{q} \perp \mathbf{H}$) do not scatter to the lowest energy states located at the longitudinal branch ($\mathbf{q} \parallel \mathbf{H}$). Such a scattering, and thus the formation of a BEC is associated with the parametric excitation of the second group of short-wavelength magnons propagating at an angle $\angle(\mathbf{q},\mathbf{H}) < 90°$. Simultaneously, the initially excited transversal magnon group is suppressed by a mutual action of the second magnon group and the external pumping field.

The measurements were performed using a low-damping ferrimagnetic film of yttrium iron garnet (YIG, $Y_3Fe_5O_{12}$) by means of a combined microwave and Brillouin light scattering (BLS) setup shown in Fig. 1a. The YIG film of 7.1 µm thickness with saturation magnetization $4\pi M_s = 1750\,\mathrm{G}$ was grown in the (111) crystallographic plane by liquid phase epitaxy. An in-plane magnetized film sample with lateral dimensions of $1.5 \times 30\,\mathrm{mm}^2$ was placed on top of a 50 µm wide microstrip resonator, which was used to induce the pumping Oersted field $\mathbf{h}(t)$. Every 100 µs the resonator was excited by a microwave pumping pulse having the carrier frequency $\omega_p/2\pi = 13.7\,\mathrm{GHz}$, a peak power from $P_{p,min} = 1\,\mathrm{mW}$ to $P_{p,max} = 5\,\mathrm{W}$ and a duration $t_p = 10\,\mu\mathrm{s}$. The chosen pulse separation was sufficiently long both for the relaxation of the magnon system to the ground state after each pumping event and for the avoiding of microwave-heating effects.

In course of the parallel pumping process the photons of the microwave pumping field split into magnons pairs with opposite wavevectors at half of the pumping frequency as it is shown in Fig. 1b. The strength of the bias field $H = 1735\,\mathrm{Oe}$ was chosen to pump the magnon pairs slightly above the ferromagnetic resonance frequency (FMR). In this case, firstly, the parallel pumping achieves its highest efficiency because the magnons are pumped to the transversal spectral branch, which has the lowest threshold of the parametric instability [19]. Secondly, no kinetic instability process is

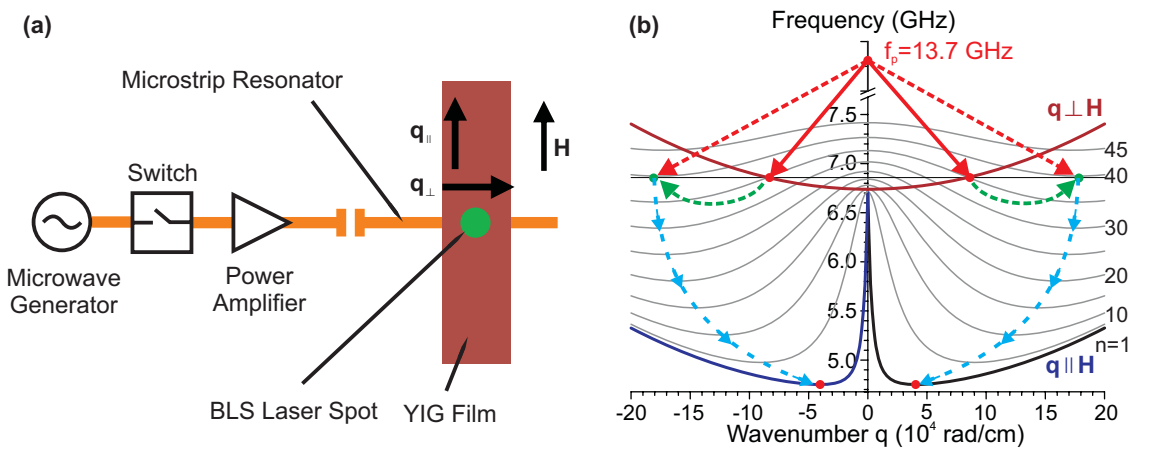

Fig. 1: a) Schematic illustration of the experimental setup. A microstrip resonator placed below the YIG film is driven by a circuit consisting of a microwave source, switch and amplifier. The green dot indicates the focus position of the BLS laser. The arrows indicate the directions of the bias magnetic field **H** and the in-plane wavevectors $\mathbf{q}_{\parallel}$ and $\mathbf{q}_{\perp}$ of the corresponding spin-wave branches. The magnon spectrum presented in b) is calculated in accordance with Ref. [22] for the first transverse ($\mathbf{q} \perp \mathbf{H}$) mode and several BVMSW thickness modes ($\mathbf{q} \parallel \mathbf{H}$). The solid red arrows illustrate the magnon injection by parametric pumping. The dashed red and green arrows outline the parametrically stimulated magnon scattering from the $\mathbf{q} \perp \mathbf{H}$ to the $\mathbf{q} \parallel \mathbf{H}$ branch of the dispersion relation. The dashed blue curves outline the thermalization by the four-magnon scattering process.

allowed by energy and momentum conservation [20]. The kinetic instability process corresponds to one-step scattering of the parametric magnons to the bottom of the spin-wave spectrum [21] and may disturb the magnon BEC.

The response of the magnon system was analyzed by means of time-resolved BLS spectroscopy [23] with a time resolution of 1 ns. A probing laser beam with a power of 5 mW and a wavelength of 532 nm was focused to a focal spot with a diameter of 50 µm in the middle of the microstrip. The optics to focus the BLS laser onto the YIG sample was also used to collect the scattered light, which was analyzed by a multipass tandem Fabry-Pérot interferometer.

In this experiment the BLS detection of magnons at the frequency $\omega_p/2$ and at the bottom of the spin-wave spectrum were performed simultaneously. The corresponding BLS signals were picked up in 150 MHz wide frequency bands. The necessary wavenumber sensitivity in the range from 1 rad/cm to $5 \cdot 10^4$ rad/cm was insured by using of a wide-aperture optics. The measurements were performed for different microwave pump powers from 1 mW to 5 W.

Figure 2a presents the dependencies of magnon densities in the chosen spectral areas on the input pumping power. The waveforms show the time evolution of the parametric (Fig. 2b–f) and the bottom magnons (Fig. 2g–i). One can see in Fig. 2b that the parametric magnons appear already at a small pumping power of 4.2 mW. The increase of the pumping power to 6.7 mW and to 9.6 mW results in the earlier appearance and in the faster saturation of the parametric magnons at higher density levels as shown in Fig. 2a. In accordance with the theory of the spin-wave parametric instability [24] this saturation is caused by nonlinear dephasing of the excited magnons relative to the microwave pumping field $\mathbf{h}(t)$.

Further increase of the pumping power leads to a consecutive *decrease* of the saturated magnon density. At the pumping power $P_p \simeq 1270$ mW, when the thermalized magnons start to be detected at the bottom of the spin-wave spectrum, the parametric magnons are already hardly visible (see waveforms in Fig. 2f and 2g). For all pumping powers P_p above 2770 mW the density of the low-

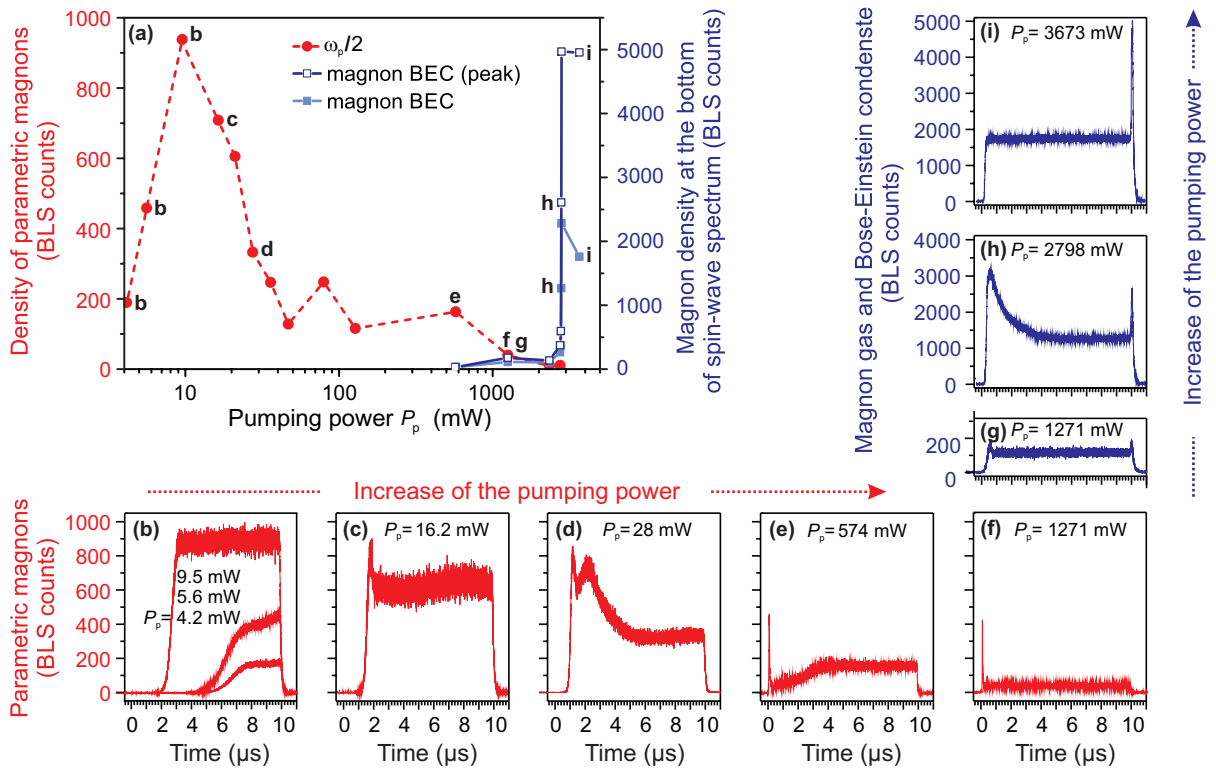

Fig. 2: The dependency of the magnon densities on the pumping power P_p is shown in a). The dots (dashed lines) represent the density of parametrically excited magnons at half of the pumping frequency $\omega_p/2$ and the squares (solid lines) the density of the magnons at the bottom of the spin-wave spectrum. The magnon densities are measured as the intensities of the corresponding BLS signals. The selected temporal profiles of these signals are presented in b–i. The pumping pulse of 10 μs duration is applied at zero moment of time. The data marked by the dots and by the filled squares were measured from the corresponding temporal profiles just before switching off the pump pulse. The open squares show the intensity of the peak of the magnon Bose-Einstein condensate, which is formed due to the evaporative supercooling [16] of the magnon gas after the pumping is shut down (see e.g. h–i). The letters near the data points relate them to the BLS temporal profiles. Three waveforms in b demonstrate the development of the conventional parametric instability.

energy magnons sharply jumps up due to the formation of the BEC, and - more significant - the parametric magnons are completely non-detectable.

Intriguingly, the result of our experiment clear demonstrates that the formation of the magnon BEC is preceded by the disappearance of the parametrically injected magnon group.

At first glance, the reason for such "disappearance" is trivial: the wavenumber of the parametric magnons increase above the detection limit of the experimental setup due to the downward frequency shift of the perpendicular magnon branch. This shift is caused by a decrease of the saturation magnetization $4\pi M_s$ with the growth of the total number of magnons [19, 25]. Indeed, it has been found that for $P_p = 8$ W the total magnetization precession angle can reach 5° [25]. This value corresponds to a 150 G decrease in $4\pi M_s$ and leads to a 180 MHz downward shift of the FMR frequency. At the same time, such a frequency shift can be easily compensated by a 50 Oe increase in the magnetizing field. However, no change of H helped us to restore the level of the BLS signal in the case of the high pumping powers.

The conventional four-magnon scattering processes can't be assumed as a reason for the disappearance of the parametrically pumped magnons. During the action of the external pumping this nonlinear mechanism can only limit but not reduce the number of the parametric magnons. The

decrease in their density will lead to the consequent decrease of the scattering efficiency and, thus, to the density saturation.

The phenomenon can be understood if one takes into account the role of the external pumping field in the four-magnon scattering process. When the pumping is switched on, the magnons, which have the lowest damping and the strongest coupling with the pumping field, are generated first [19]. The development of the process in the course of time t can be described by the following equation:

$$\frac{dc_q}{dt} = i\left(\omega_q c_q + V_q h e^{i\omega_p t} c^*_{-q} + \sum S_{qq'} c^*_{-q} c_{q'} c_{-q'}\right) \quad . \tag{1}$$

Here c_q is the amplitude of a spin wave having the wavevector $\mathbf{q}$ and the complex frequency $\omega_q = \omega'_q + i\Gamma_q$, where Γ_q is the spin-wave relaxation frequency. The nonlinear coefficient $S_{qq'}$ characterizes the interaction of spin-wave pairs (c_q, c_{-q}) and $(c_{q'}, c_{-q'})$. The interaction between the spin-wave pair (c_q, c_{-q}) and the pumping field h is represented by the coupling parameter V_q:

$$V_q = \frac{\gamma\omega_M}{4\omega_q} e^{i2\varphi_q} \sin^2\theta_q \quad , \tag{2}$$

where $\theta_q = \angle(\mathbf{q}, \mathbf{H})$ and $\varphi_q = \angle(\mathbf{q}, \mathbf{q}_\perp)$ are the polar and the azimuthal angles of the spin wave $c_q(\theta_q, \varphi_q)$, respectively. According to Eqs (1), (2) the magnons with $\theta_q = \pi/2 = \theta_1$ possess the minimal threshold value of the parametric generation:

$$h_{\text{th}1} = \Gamma_1 / V_1 \quad . \tag{3}$$

Above the threshold ($h > h_{\text{th}}$), the amplitude of the initially generated waves $c_1 = c_q(\frac{\pi}{2}, 0) = c_{-q}(\frac{\pi}{2}, \pi)$ is determined by the action of the pumping field h and by the self-action of these waves:

$$|c_1|^2 = \frac{N_1}{2} = \frac{(hV_1)^2 - \Gamma_1^2}{2S_{11}} \quad , \tag{4}$$

where S_{11} is the coefficient $S_{qq'}$ for the waves of the initially excited parametric group c_1.

Thus, the total pumping field in the sample consists of the external pumping field h and an internal pump field induced by the waves c_1. This pumping acts not only on the waves c_1 but on all other waves in the system. If its value exceeds the threshold of any wave $c_q(\theta_q \neq \frac{\pi}{2})$ the second wave group will be excited. The ratio of the external threshold fields of the second and the first spin-wave groups can be written as

$$\left(\frac{h_{\text{th}2}}{h_{\text{th}1}}\right)^2 = p = \frac{S_{11}^2}{\Gamma_1^2} \frac{\Gamma_\theta^2 - \Gamma_1^2 \sin^2\theta}{(S_{11}\sin^2\theta - S_{\theta 1})^2} + 1 \quad , \tag{5}$$

where Γ_θ is the relaxation frequency of the second wave group excited under the polar angle $\theta \neq \pi/2$, $S_{\theta 1}$ is the coefficient $S_{qq'}$ for $c_q(\frac{\pi}{2}, 0)$ and $c_{q'}(\theta, \varphi_{q'})$.

After the excitation of the second spin-wave group the total pumping will consist of three components: the action of the external pumping field and the reactions of the first and the second wave groups. The effects of this complex pumping are manifold. For example, the pumping can lead to the excitation of a third wave group. It can also lead to the *suppression* of the first group of the parametric magnons. The total pumping that drives the first group

$$|P_1|^2 = (hV_1)^2 + (S_{11}N_1 + S_{21}N_2)^2 - 2(S_{11}N_1 + S_{21}N_2)\left((hV_1)^2 - \Gamma_1^2\right)^{1/2} \quad , \tag{6}$$

where S_{21} describes the action of the second group on the first one and $N_2 = 2|c_2|^2$. The minus sign before the last term in Eq. (6) denotes the decrease of the pump acting on the first group. If $|P_1|^2 < |\Gamma_1|^2$ the first group will decay and only the second group will survive in course of time. This process can be understood as a stimulated scattering of the initially injected magnons to a new spectral area. In an isotropic case, when $S_{11} = S_{\theta 1}$ and $\Gamma_\theta = \Gamma_1$, the secondary wave group is excited under the angle $\theta_q = 0$. In the case of $S_{11} \neq S_{\theta 1}$ and an unbounded medium $\theta_q \simeq 50°$ [26].

It is worth noting that the exact spectral position of the parametrically excited magnons strongly depends on their damping. For a spatially localized pumping, when an excited wave can leak from the pumping area, its loss is significantly influenced by the direction and the value of its group velocity. In our experiment the first magnon group with $\theta_1 = \pi/2$ propagates along the microstrip resonator and, thus, does not suffer any radiation loss. All other groups with $\theta_q \neq \pi/2$ can easily leak out of the 50 µm width pumping area. As a result their excitation threshold jumps significantly up [27]. Therefore, the formation of the second (or higher) parametric wave group is only possible around the local minima of the magnon spectrum (see Fig. 1b), where the spin-wave group velocities are close to zero. For example, under the given experimental conditions the initial magnons preferably scatter to the energy minima of the 40th thickness mode, as it is shown in Fig. 1b by the dotted arrows.

Such a scattering has two important consequences. Firstly, because the secondary magnons possess wavenumbers of about $2 \cdot 10^5$ rad/cm they are not visible by means of BLS spectroscopy. Secondly, the stimulated scattering brakes the orthogonality between the initially injected magnon group ($\theta_q = 90°$) and the magnons from the bottom of the spin-wave spectrum ($\theta_q = 0$), and thus enables Bose-Einstein condensation. It is obvious that no magnon-magnon scattering process inside of the initial magnon group is able to turn the magnon wavevector from $\mathbf{q} \parallel \mathbf{H}$ to $\mathbf{q} \perp \mathbf{H}$ orientation. At the same time, such a conversion is naturally realized by the excitation of the secondary spin-wave group with a sufficiently large wavevector component along $\mathbf{H}$. The secondary magnons, collected in the energy minimum of the 40th longitudinal spin-wave mode, can scatter by conventional four-magnon scattering to the energy minima of the 41st and 39th modes while conserving energy and momentum. Our evaluation shows, that a step-by-step magnon transfer by four-magnon scattering from the energy minima of thickness mode n to $n-1$ is possible down to the first mode $n = 1$ where the BEC is formed in the global energy minimum near $4 \cdot 10^4$ rad/cm. However, the model, which assumes scattering between neighboring modes only, does not explain the fast formation of the magnon BEC observed in our experiment. The scattering between not-neighboring modes, which is also allowed by the momentum and energy conservation laws, increases the number of thermalization channels and results in faster thermalization. Nevertheless, this does not change the general principle of scattering from minimum to minimum, because magnons with a non-zero group velocity (> 0.1 µm/ns) will propagate out of the detection region and do not contribute to the formation of the magnon condensate.

In conclusion, our experimental findings suggest two distinctly different phases of the thermalization process of a parametrically driven magnon gas: the energy degenerated parametrically stimulated magnon scattering from the transverse branch of the spin-wave spectrum is followed by a multistage magnon transfer between the local energy minima of thickness spin-wave modes to the bottom of the magnon spectrum. The parametrically stimulated magnon thermalization is assumed to be the obligatory precondition for the formation of the magnon Bose-Einstein condensate.

Financial support from the the Deutsche Forschungsgemeinschaft within the SFB/TR 49 and from the Ukrainian Fund for Fundamental Research is gratefully acknowledged. D.B. was supported by a fellowship of the Graduate School Material Sciences in Mainz (MAINZ) through DFG funding of the Excellence Initiative (GSC-266).

References

[1] E. Schlömann, J.J. Green, U. Milano, *Recent developments in ferromagnetic resonance at high powerlevels*, J. Appl. Phys. **31**, 386S (1960).

[2] S.M. Rezende, F.M. de Aguiar, *Spin-wave instabilities, auto-oscillations, and chaos in yttrium-iron-garnet*, IEEE Proc. **78**, 6 (1990).

[3] S.O. Demokritov, A.A. Serga, V.E. Demidov, B. Hillebrands, M.P. Kostylev, B.A. Kalinikos, *Experimental observation of symmetry breaking nonlinear modes in an active ring*, Nature **426**, 159 (2003).

[4] T. Brächer, P. Pirro, B. Obry, B. Leven, A.A. Serga, B. Hillebrands, *Mode selective parametric excitation of spin waves in a $Ni_{81}Fe_{19}$ microstripe*, Appl. Phys. Lett. **99**, 162501 (2011).

[5] B.A. Kalinikos, M.P. Kostylev, *Parametric amplification of spin wave envelope solitons in ferromagnetic films by parallel pumping*, IEEE Trans. Magn. **33**, 3445 (1994).

[6] A.V. Bagada, G.A. Melkov, A.A. Serga, A.N. Slavin, *Parametric interaction of spin wave envelope solitons with localized electromagnetic pumping*, Phys. Rev. Lett. **79**, 2137 (1997).

[7] T. Brächer, P. Pirro, T. Meyer, F. Heussner, B. Lägel, A.A. Serga, B. Hillebrands, *Parallel parametric amplification of coherently excited propagating spin waves in a microscopic $Ni_{81}Fe_{19}$ waveguide*, Appl. Phys. Lett. **104**, 202408 (2014).

[8] G.A. Melkov, Yu.V. Kobljanskyj, A.A. Serga, A.N. Slavin, V.S. Tiberkevich, *Reversal of momentum relaxation*, Phys. Rev. Lett. **86**, 4918 (2001).

[9] A.V. Chumak, V.I. Vasyuchka, A.A. Serga, M.P. Kostylev, V.S. Tiberkevich, B. Hillebrands, *Storage-recovery phenomenon in magnonic crystal*, Phys. Rev. Lett. **108**, 257207 (2012).

[10] S.O. Demokritov, V.E. Demidov, O. Dzyapko, G.A. Melkov, A.A. Serga, B. Hillebrands, A.N. Slavin, *Bose-Einstein condensation of quasi-equilibrium magnons at room temperature under pumping*, Nature **443**, 430 (2006).

[11] V.E. Demidov, O. Dzyapko, S.O. Demokritov, G.A. Melkov, A.N. Slavin, *Thermalization of a parametrically driven magnon gas leading to Bose-Einstein condensation*, Phys. Rev. Lett. **99**, 037205 (2007).

[12] V.E. Demidov, O. Dzyapko, M. Buchmeier, T. Stockhoff, G. Schmitz, G.A. Melkov, S.O. Demokritov, *Magnon kinetics and Bose-Einstein condensation studied in phase space*, Phys. Rev. Lett. **101**, 257201 (2008).

[13] V. Demidov, O. Dzyapko, S. Demokritov, G. Melkov, A. Slavin, *Observation of spontaneous coherence in Bose-Einstein condensate of magnons*, Phys. Rev. Lett. **100**, 047205 (2008).

[14] A. Chumak, G. Melkov, V. Demidov, O. Dzyapko, V. Safonov, S. Demokritov, *Bose-Einstein condensation of magnons under incoherent pumping*, Phys. Rev. Lett. **102**, 187205 (2009).

[15] S.M. Rezende, *Theory of coherence in Bose-Einstein condensation phenomena in a microwave-driven interacting magnon gas*, Phys. Rev. B **79**, 174411 (2009).

[16] A.A. Serga, V.S. Tiberkevich, C.W. Sandweg, V.I. Vasyuchka, D.A. Bozhko, A.V. Chumak, T. Neumann, B. Obry, G.A. Melkov, A.N. Slavin, B. Hillebrands, *Bose-Einstein condensation in an ultra-hot gas of pumped magnons*, Nat. Commun. **5**, 4452 (2014).

[17] A.I. Bugrij, V.M. Loktev, *On the theory of Bose-Einstein condensation of quasiparticles: on the possibility of condensation of ferromagnons at high temperatures*, Low Temp. Phys. **33**, 37 (2007).

[18] J. Hick, T. Kloss, P. Kopietz, *Thermalization of magnons in yttrium-iron garnet: Nonequilibrium functional renormalization group approach*, Phys. Rev. B **86**, 184417 (2012).

[19] A.A. Serga, C.W. Sandweg, V.I. Vasyuchka, M.B. Jungfleisch, B. Hillebrands, A. Kreisel, P. Kopietz, M.P. Kostylev, *Brillouin light scattering spectroscopy of parametrically excited dipole-exchange magnons*, Phys. Rev. B **86**, 134403 (2012).

[20] G.A. Melkov, S.V Sholom, *Kinetic instability of spin waves in thin ferrite films*, Sov. Phys. JETP **72**, 341 (1991).

[21] G.A. Melkov, V.L. Safonov, A.Y. Taranenko, S.V. Sholom, *Kinetic instability and bose condensation of nonequilibrium magnons*, J. Magn. Magn. Mater. **132**, 180 (1994).

[22] B.A. Kalinikos, A.N. Slavin, *Theory of dipole-exchange spin wave spectrum for ferromagnetic films with mixed exchange boundary conditions*, J. Phys. C: Solid State Phys. **19**, 7013 (1986).

[23] O. Büttner, M. Bauer, S.O. Demokritov, B. Hillebrands, Yu.S. Kivshar, V. Grimalsky, Yu. Rapoport, A.N. Slavin, *Linear and nonlinear diffraction of dipolar spin waves in yttrium iron garnet films observed by space- and time-resolved Brillouin light scattering*, Phys. Rev. B **61**, 11576 (2000).

[24] A.G. Gurevich, G.A. Melkov, *Magnetization oscillations and waves* (CRC Press, New York, 1996).
[25] A.A. Serga, T. Schneider, B. Hillebrands, M.P. Kostylev, A.N. Slavin, *Shaping of microwave pulses using phase-sensitive spin-wave amplifier*, Appl. Phys. Lett. **90**, 022502 (2007).
[26] V.V. Zautkin, V.E. Zakharov, V.S. L'vov, S.L. Musher, S.S. Starobinets, *Parallel spin-wave pumping in Yttrium Garnet single crystals*, Sov. Phys. JETP **35**, 926 (1972).
[27] T. Neumann, A.A. Serga, V.I. Vasyuchka, B. Hillebrands, *Field-induced transition from parallel to perpendicular parametric pumping for a microstrip transducer*, Appl. Phys. Lett. **94**, 192502 (2009).

4.4 Anomalous dynamics of a Bose-Einstein magnon condensate in a thermal gradient

P. Clausen, D.A. Bozhko, V.I. Vasyuchka, A.V. Chumak, B. Hillebrands, and A.A. Serga

In collaboration with G.A. Melkov, Faculty of Radiophysics, Taras Shevchenko National University of Kyiv, 01601 Kyiv, Ukraine,
S. Eggert, Department of Physics and Research Center OPTIMAS, University of Kaiserslautern, 67663 Kaiserslautern, Germany,
and Y. Tserkovnyak, Department of Physics and Astronomy, University of California, Los Angeles, California 90095, USA

Bose-Einstein condensation [1] can be achieved either by decreasing the temperature of boson gases [2] or by increasing their density. The last method is especially applicable to gases of weakly interacting quasi-particles such as excitons [3], polaritons [4, 5], photons [6], and magnons [7, 8]. When a spin system is pumped, and when the injected magnons thermalize through scattering processes conserving both their number and the total energy, a Bose-Einstein condensate (BEC) can appear at the lowest energy state of the energy-momentum spectrum even at high temperature [8, 9]. As the condensed magnon phase is localized in the global energy minimum, its group velocity is exactly zero and no energy transport can be generally associated with the magnon BEC. The situation can change drastically in a potential gradient, when a magnon supercurrent driven by a gradient in the phase of the wavefunction of a magnon condensate can be excited. However, the dynamics of magnon condensates in a potential gradient is still *terra incognita*. Here we provide experimental insight into the evolution of a magnon BEC in a thermal gradient generated by local laser heating. We show that such heating influences both the steady state characteristics and the transitional behavior of the magnon BEC, which can be understood using the concept of the magnon supercurrents.

We study the temporal evolution of a magnon BEC in a single-crystal yttrium iron garnet (YIG) film by time-resolved Brillouin Light Scattering (BLS) spectroscopy [10]. In our experiment, a focused laser beam combines the role of the magnon probe with the role of the local sample heater.

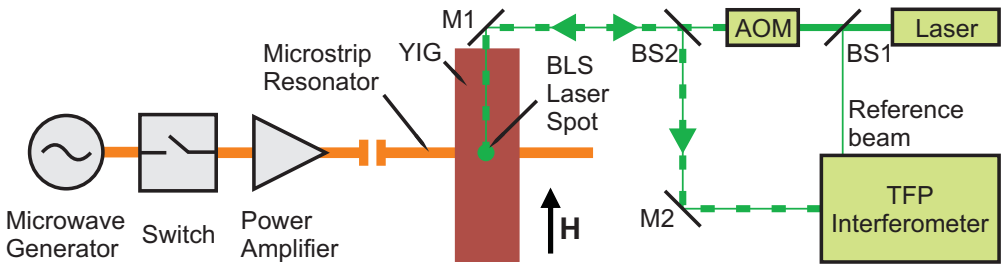

Fig. 1: Schematic illustration of the experimental setup. On the left hand side, the microwave circuit consisting of a microwave source, switch and amplifier is shown. This circuit drives a microstrip resonator, which is placed below a YIG film. The arrow indicates the directions of the applied external bias magnetic field **H**. The green dot illustrates the focus position of the BLS laser. On the right hand side, the BLS laser beam path is indicated. The light of a solid-state laser ($\lambda = 532\,\mathrm{nm}$) is split by a beam splitter (BS1). The sample beam is sent to an acousto-optic modulator and the reference beam to the interferometer. The modulated sample beam is guided through the second beam splitter (BS2) and the mirror (M1) to the YIG film where it scatters. The scattered light is reflected again at M1 and deflect by BS2 to the Tandem Fabry-Pérot interferometer.

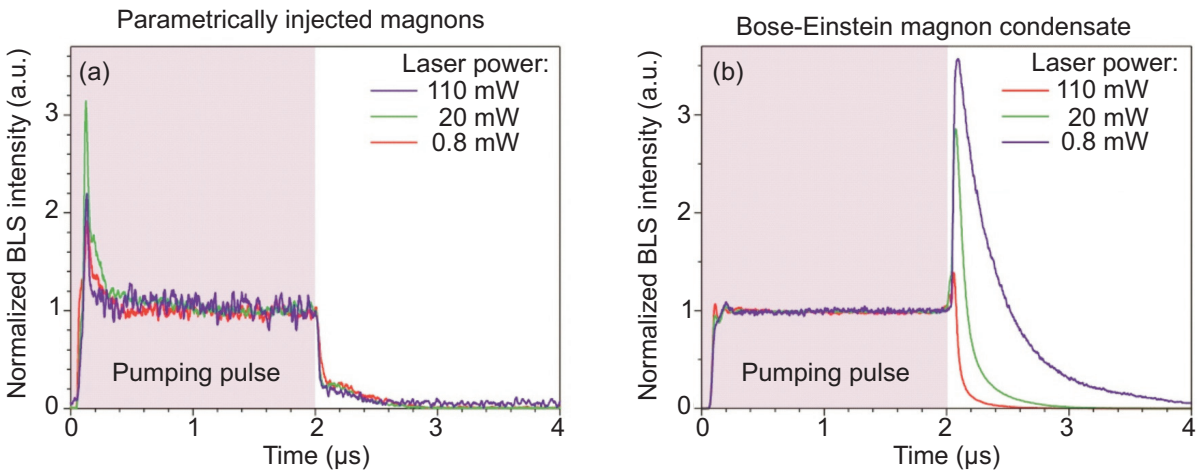

Fig. 2: Time-resolved Brillouin light scattering intensity for different cw laser powers. The dependencies are normalized to the steady-state magnon density of the pumping pulse. a) The evolution of magnons parametrically injected at the ferromagnetic resonance frequency. b) The evolution of the magnons condensed at the bottom of the spin-wave spectrum.

Furthermore, the heating time is adjusted using the amplitude modulation of a probing laser beam by an acousto-optic modulator (AOM). The experimental setup, which consists of a YIG film sample, microwave circuit, and BLS laser system, is shown in Fig. 1. The in-plane magnetized YIG sample is 6.7 µm thick, 10 mm long and 2 mm wide. The direction of a bias magnetic field **H** is indicated by the black arrow. The microwave circuit comprising a microwave source, switch and amplifier is shown on the left hand side. This circuit drives a microstrip resonator, which is tuned to the pumping frequency of $f_\mathrm{p} = 13.550\,\mathrm{GHz}$ and is placed below the YIG film. During the action of a pumping Oersted field, which is induced around the microstrip resonator by microwave pumping pulses, magnons are injected into the YIG sample at frequency $f_\mathrm{p}/2$ by means of a parallel parametric pumping mechanism [11, 12]. The BLS laser beam path mainly consists of a laser, laser modulator and Tandem Fabry-Perot (TFP) interferometer. The light of a solid-state laser ($\lambda = 532\,\mathrm{nm}$) is split by a beam splitter (BS1). The sample beam is sent to the acousto-optic modulator and the reference beam to the interferometer. The modulated sample beam is guided through a second beam splitter (BS2) and a mirror (M1) to the YIG film where it has a power of 260 mW and scatters on magnons. The scattered light is reflected again at M1 and deflected by BS2 to the interferometer. The on-time of the laser is varied between 4 µs to 106 µs with a repetition time of 1 ms. The microwave pulses, AOM and a time-resolved BLS setup are synchronized by a multi-channel pulse generator.

First of all, we investigated the effects of continuous laser heating on the magnon BEC. The time-resolved Brillouin light scattering intensities for different cw laser powers are shown in Fig. 2. The intensity curves are normalized to the steady-state magnon density of the pumping pulse. Figure 2a shows the evolution of the parametrically injected magnons at the ferromagnetic resonance frequency. No dependence of the laser power on the decay of the BLS intensity is visible. This implies, that the dynamics of the parametric magnons is not affected by the local laser heating.

The evolution of the condensed magnons at the bottom of the spin-wave spectrum is shown in Fig. 2b. It drastically differs from the evolution of the parametric magnons: Just after the pumping pulse is switched off, the gaseous magnons fall to the global energy minima and the density of the condensed magnons dramatically jumps up. At the same time, the density of parametrically injected magnons decays monotonically (see Fig. 2a). This characteristic BEC behavior occurs due

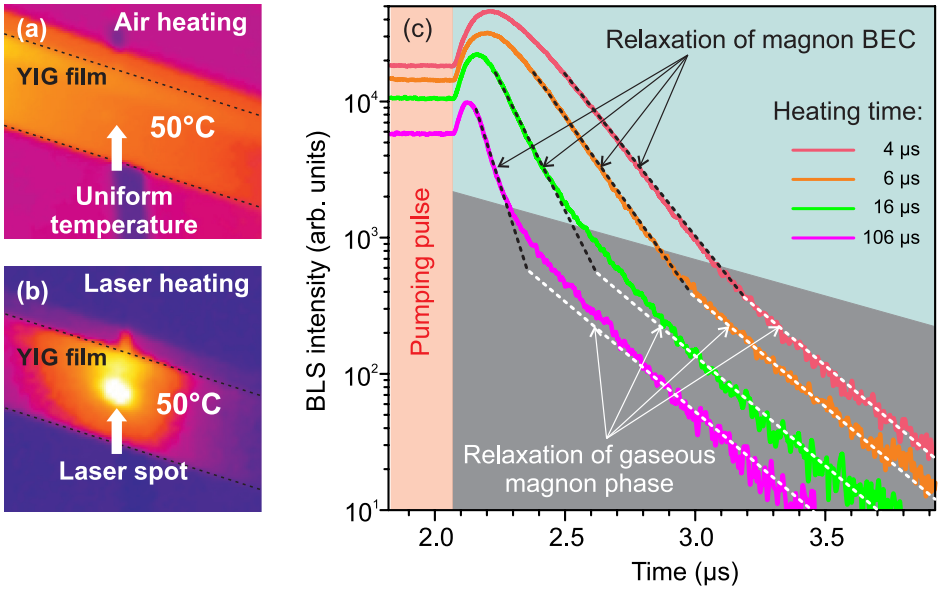

Fig. 3: False color images of the heated YIG film by uniform air heating a) and local laser heating b). The temporal dynamics of the Bose-Einstein magnon condensate under local laser heating is shown in c). The increase of the laser pulse duration, and thus the heating time, leads to a decrease of the BEC density and to a faster relaxation of the BEC phase. This faster relaxation is indicated by the black dotted lines. The relaxation time of the residual gaseous magnons after destruction of the magnon BEC is independent of the heating. This is shown by the dotted white lines.

to the fact that thermalization processes, which underpin the formation of the magnon condensate, develop over a very narrow region of the lowest energy states where the magnon gas is strongly overheated ($T > 30,000\,\mathrm{K}$) by the external pumping [9]. Because of nonlinear magnon-magnon scattering, some gaseous magnons may gain an additional energy and leave the thermalized region, thus reducing the average energy of the remaining magnons. This mechanism is similar to the well known process of evaporative cooling in real atomic gases. After the pumping is switched off this cooling mechanism reduces the temperature of the magnon gas, and thus significantly improves the process of magnon condensation [9].

One can observe a pronounced dependence of this magnon dynamics on the laser power. At a power of 0.8 mW, the sharp peak caused by the formation of the magnon condensate is clearly visible. The increase of the probing laser power to 20 mW leads to the partial suppression of the BEC peak. At 110 mW the peak in the magnon density is barely visible. Upon closer examination, not only the BEC's amplitude is reduced but also the BEC's lifetime is significantly decreased at high laser powers.

To investigate effects from an increase of temperature, we changed the experiment to use only low laser powers and uniform air heating of the YIG film. Figure 3a shows an infrared picture of the temperature distribution of the YIG film. The temperature was increased from 2 K to 30 K above the room temperature. No influence on the BEC's lifetime nor on the amplitude was observed in the uniform air heating experiment. In comparison, the distribution for the laser light induced local heating is shown in Fig. 3b.

The BEC could be affected by the local temperature gradient induced from the intense laser beam. Alternatively the intense photon field might lead to a nonlinear scattering of laser photons with magnons. To discriminate between these two effects, we need to decrease the effect of heating while keeping a strong photon field present. This is realized by modulating the probing laser beam.

The length of the laser pulse was varied from 4 µs to 106 µs. The influence of this heating effect on the temporal dynamics of the magnon BEC is shown in Fig. 3c. As in the previous experiment, the magnon density rises sharply and the magnon BEC is created after the microwave pumping pulse is switched off. Two different phases of the decay of the BEC are clearly visible. In the first phase, the relaxation of the BEC is highly increased with increase of heating duration. The black dotted lines serve as a guide to the eye. The correlation between heating time and faster relaxation is clearly visible. Longer laser pulse duration, and thus more heating, leads to a decrease of the BEC density and to faster relaxation of the BEC phase. In the second phase, where the density of the condensed magnon significantly decreases, the decay time starts to be independent of the heating. This is clearly shown by the dotted white lines. The relaxation time of the residual gaseous magnons after destruction of the magnon BEC is independent of the heating.

Thus, we found that a temperature gradient generated in a focus of the probing laser beam in our BLS experiments decreases both the lifetime and the density of a magnon Bose-Einstein condensate. The fact that no such kind of influence on the parametrically injected magnons as well as on the magnon gaseous phase is detected allows us to attribute this fascinating dynamics to the magnon BEC as a specific feature of this macroscopic quantum state. The possible scenario is as follows. The laser heating locally changes the saturation magnetization and, thus, induces a phase gradient in the magnon condensate. As a result, a phase-induced magnon current or, in other words, a magnon supercurrent flows out of the hot area of the focal point. This outflow decreases the density of the magnon BEC in a steady state pump regime and increases the decay of the freely evolving magnon condensate after the termination of the pumping pulse. After some time, the decrease in the magnon density results in the disappearance of the condensate and thus of the supercurrent, and consequently this leads to the restoration of the conventional relaxation dynamics.

Financial support from the Deutsche Forschungsgemeinschaft within the SFB/TR 49 and from the Ukrainian Fund for Fundamental Research is gratefully acknowledged. D.B. was supported by a fellowship of the Graduate School Material Sciences in Mainz (MAINZ) through DFG funding of the Excellence Initiative (GSC-266).

References

[1] A. Einstein, *Quantentheorie des einatomigen idealen Gases*, Sitz. Ber. Preuss. Akad. Wiss. **22**, 261 (1924).

[2] M.H. Anderson, J.R. Ensher, M.R. Matthews, C.E. Wieman, E.A. Cornell, *Observation of Bose-Einstein condensation in a dilute atomic vapor*, Science **269**, 198 (1995).

[3] L.V. Butov, A.L. Ivanov, A. Imamoglu, P.B. Littlewood, A.A. Shashkin, V.T. Dolgopolov, K.L. Campman, A.C. Gossard *Stimulated scattering of indirect excitons in coupled quantum wells: Signature of a degenerate Bose-gas of excitons*, Phys. Rev. Lett. **86**, 5608 (2001).

[4] J. Kasprzak, M. Richard, S. Kundermann, A. Baas, P. Jeambrun, J.M.J. Keeling, F.M. Marchetti, M.H. Szyman Acuteska, R. André, J.L. Staehli, V. Savona, P.B. Littlewood, B. Deveaud, Le Si Dang, *Bose-Einstein condensation of exciton polaritons*, Nature **443**, 409 (2006).

[5] R. Balili, V. Hartwell, D. Snoke, L. Pfeiffer, K. West, *Bose-Einstein condensation of microcavity polaritons in a trap*, Science **316**, 1007 (2007).

[6] J. Klaers, J. Schmitt, F. Vewinger, M. Weitz, *Bose-Einstein condensation of photons in an optical microcavity*, Nature **468**, 545 (2010).

[7] Yu.D. Kalafati, V.L. Safonov, *Thermodynamic approach in the theory of paramagnetic resonance of magnons*, Sov. Phys. JETP **68**, 1162 (1989).

[8] S.O. Demokritov, V.E. Demidov, O. Dzyapko, G.A. Melkov, A.A. Serga, B. Hillebrands, A.N. Slavin, *Bose-Einstein condensation of quasi-equilibrium magnons at room temperature under pumping*, Nature **443**, 430 (2006).

[9] A.A. Serga, V.S. Tiberkevich, C.W. Sandweg, V.I. Vasyuchka, D.A. Bozhko, A.V. Chumak, T. Neumann, B. Obry, G.A. Melkov, A.N. Slavin, B. Hillebrands, *Bose-Einstein condensation in an ultra-hot gas of pumped magnons*, Nat. Commun. **5**, 3452 (2014).

[10] O. Büttner, M. Bauer, S. Demokritov, B. Hillebrands, Y. Kivshar, V. Grimalsky, Y. Rapoport, A. Slavin, *Linear and nonlinear diffraction of dipolar spin waves in yttrium iron garnet films observed by space- and time-resolved Brillouin light scattering*, Phys. Rev. B **61**, 576 (2000).

[11] E. Schlömann, J.J. Green, U. Milano, *Recent developments in ferromagnetic resonance at high power levels*, J. Appl. Phys. **31**, 386 (1960).

[12] S.M. Rezende, F.M. de Aguiar, *Spin-wave instabilities, auto-oscillations, and chaos in yttrium-iron-garnet*, IEEE Proc. **78**, 6 (1990).

4.5 Parallel parametric amplification of coherently excited propagating spin waves in a microscopic $Ni_{81}Fe_{19}$ waveguide

T. Brächer, P. Pirro, T. Meyer, F. Heussner, A.A. Serga, and B. Hillebrands

In collaboration with B. Lägel, Nanostructuring Center (NSC), TU Kaiserslautern, 67663 Kaiserslautern

In recent years, there has been an increased interest in the fields of magnonics and magnon spintronics [1–3]. This is mainly motivated by the potentially huge benefits to be expected from the utilization of spin-currents carried by magnons, the spin-wave quanta, for data transfer and processing. Besides the fact that these spin currents can propagate in electric insulators [4], magnons feature large decay lengths in comparison to the spin-diffusion length of electrons in metallic ferromagnets [5]. Moreover, the wave nature of spin waves offers interesting aspects for the creation of wave-based logic devices [6, 7]. However, for any device, efficient amplification sources are needed in order to recover a signal. Recently, a compensation of the spin-wave damping by the Spin Transfer Torque effect (STT) has been proposed. While a damping compensation could be achieved in a confined geometry [8, 9], only a small reduction of the spin-wave damping in a non-local geometry has been reported [10]. A major drawback of these approaches using STT is that STT couples to all existing spin-wave modes at arbitrary frequencies, meaning that the energy inserted into the spin-wave system is distributed to all these modes. In this context, the technique of parallel parametric amplification [11] is superior, since it primarily interacts with spin waves at a discrete frequency. In general, parallel parametric amplification describes the conversion of microwave photons in magnon pairs. It is based on the interaction of a dynamic microwave field with the longitudinal component of the dynamic magnetization. In thin films, the latter arises from the shape anisotropy and the resulting ellipticity of precession of dipolar spin waves [12, 13]. Due to this interaction, energy is inserted into the spin-wave system, and, if this energy exceeds the damping losses, the parametric instability occurs and spin-wave amplification as well as generation can be observed [12, 14, 15]. Here, parametric *amplification* refers to the interaction of the pumping field with externally excited signal spin waves, while *generation* means the amplification of thermal spin waves. As has been recently demonstrated [16], the preferably generated and, thus, amplified spin-wave mode in a magnonic waveguide is the lowest available transverse spin-wave mode, which is the most interesting mode for many applications since it features the largest group velocity and the largest net dynamic magnetic moment.

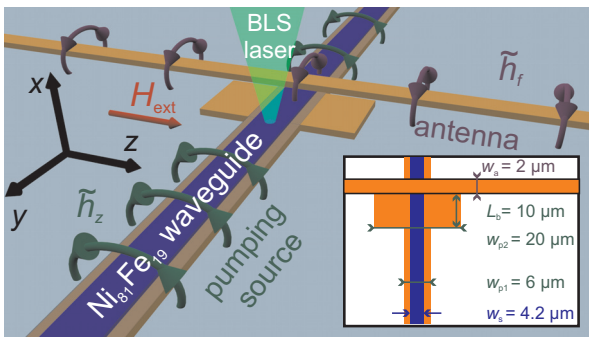

Fig. 1: Schematic view of the investigated sample: A $Ni_{81}Fe_{19}$ waveguide has been patterned on top of a Cu stripline. The used coordinate system is shown. Across the waveguide, a microstrip antenna has been fabricated. In front of the antenna, the stripline features a widened region. The inset shows the relevant dimensions.

This work has been recently published in Applied Physics Letters [31].

Here, we report on the parallel parametric amplification of coherently excited spin waves in a transversely magnetized, microstructured magnonic $Ni_{81}Fe_{19}$ waveguide. Coherent excitation is achieved locally by a microstrip antenna (see Fig. 1) patterned across the waveguide [5]. An additional micro-stripline acting as source for the pumping field has been structured underneath the magnonic waveguide [16]. By employing microfocussed Brillouin Light Scattering (BLS) spectroscopy [17], we show that a direct amplification of the excited spin waves is possible, as well as an amplification of spin waves which have already partially decayed during the course of their propagation. Furthermore, we study the dependencies of the amplified spin-wave signal on the spin-wave excitation power as well as on the power and the duration of the pumping pulse, thereby identifying a regime of efficient amplification.

The investigated sample, as sketched in Fig. 1, consists of a $Ni_{81}Fe_{19}$ waveguide (length $L_s = 50\,\mu m$, width $w_s = 4.2\,\mu m$, thickness $d_s = 40\,nm$) which has been structured on top of a Cu micro-stripline and capped with a $d_c = 5\,nm$ thick MgO layer. The Cu and the $Ni_{81}Fe_{19}$ layers are separated by a $d_i \approx 250\,nm$ thick Hydrosilesquioxane insulation layer. The stripline is $d_a = 200\,nm$ thick and has a base width of $w_{p1} = 6\,\mu m$. An external bias field $\mu_0 H_{ext} = 35\,mT$ is applied to magnetize the waveguide along its short axis. A microstrip antenna has been patterned across the $Ni_{81}Fe_{19}$ waveguide ($w_a = 2\,\mu m$, $d_a = 500\,nm$). The microwave current sent through this antenna creates an Oersted field which provides a localized spin-wave excitation in this geometry [5, 18]. In front of this antenna, the stripline features a widened region with a length $L_b = 10\,\mu m$ and a width $w_{p2} = 20\,\mu m$.

In order to excite and amplify spin waves in the waveguide, microwave currents from separate, non phase-locked microwave sources are sent through the stripline and the antenna. Both microwave currents are applied via pulses in the ns regime with MHz repetition rates to avoid sample heating and nonlinear effects. For the direct spin-wave excitation by the antenna, the pulses have a carrier frequency of $f_{SW} = 5\,GHz$. For the external field of $\mu_0 H_{ext} = 35\,mT$ applied in this study, $f_{SW} = 5\,GHz$ can be associated with a spin-wave wavelength of $\lambda \approx 17\,\mu m$ from the spin-wave dispersion relation of a transversely in-plane magnetized waveguide [19–21]. The pulses send through the stripline have a carrier frequency of $f_p = 2 f_{SW} = 10\,GHz$, and the dynamic Oersted field created by this current is aligned parallel to the external bias field. Therefore, it can be used for parametric amplification [11, 16] by means of parallel pumping of spin waves in the $Ni_{81}Fe_{19}$ waveguide. Hence, in the following, the stripline is referred to as *pumping source*.

As shown in Fig. 1, the pumping source features a widened region in front of the antenna. As has been shown in Ref. [22], such a geometric variation can be used to modulate the pumping field in space. The Oersted field component $\tilde{h}_z$ arising from the microwave current flowing through the pumping source has been calculated using the COMSOL radiofrequency module for an applied microwave frequency of $f = 10\,GHz$ in the continuous wave regime at a distance of $\delta x = 250\,nm$ above the stripline. In the center of the widened region ($y = 5\,\mu m$), $\tilde{h}_z$ is lowered to 75% of its original value (see dotted line in Figs 2a and b). Therefore, in the widened region the applied power needed to exceed the threshold of the parametric instability, i.e., to overcompensate the damping, is up to $\Delta P \approx 2.5\,dB$ larger. Thus, it is possible to overcome the threshold of the parametric instability outside this region while the field inside stays below the threshold. This results in a decay of the spin waves inside the widened region which allows, on the one hand, for the visualization of the initial amplification of spin waves at the point of their excitation and, on the other hand, for the amplification of the partially decayed spin waves beyond this region.

As mentioned above, the pumping can interact with the externally excited signal magnons and with thermal magnons. In macroscopic systems [15, 23, 24], the externally excited and the dominantly

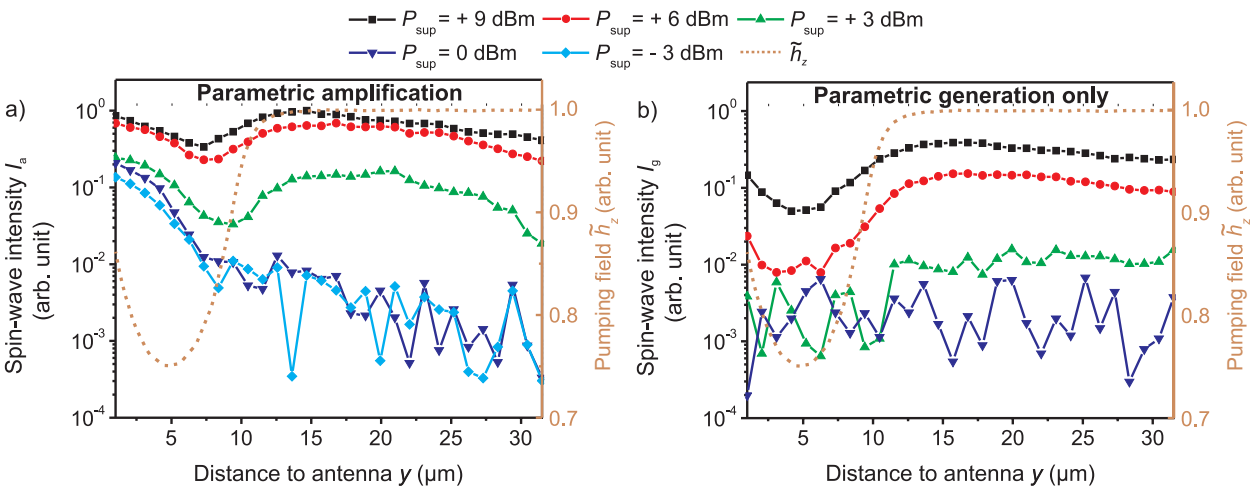

Fig. 2: Logarithmic spin-wave intensity in the center of the waveguide measured along the y-direction for different supercritical powers P_{sup} for: (a) Spin waves being excited by the antenna and (b) No spin-wave excitation by the antenna. In both cases, the dotted line represents the spatial distribution of the pumping field.

generated spin-wave mode are different and, in general, the parametric instability threshold of one of the thermal spin-wave modes is the lowest. However, in a microstructured magnonic waveguide this situation is changed due to quantization [16]. Since the first waveguide mode features the lowest parametric instability threshold and is predominantly excited by the antenna, parallel parametric amplification and generation feature the same instability threshold and can, thus, take place simultaneously. In this situation, the main differences between amplification and generation are the starting amplitude and the degree of coherency of the spin waves interacting with the pumping field. While the spin waves excited by the antenna are coherent, the thermal spin waves possess a random phase. The phase of the spin waves interacting with the pumping field is conserved [25]. However, in this experiment only the spin-wave intensity is studied and no information on the phase is extracted. This is due to the fact, that parallel pumping creates overlapping magnon pairs with $\pm k_y$ and, thus, a phase determination, which could potentially be performed by optical methods for single spin waves [26], turns out to be impossible in the given experimental conditions. The remaining difference between the amplified and generated waves is their starting amplitude.

Figure 2 shows the spin-wave intensity recorded along the center of the waveguide as a function of the distance from the antenna. In Fig. 2a, spin waves are excited at the microstrip antenna and the pumping is switched on while Fig. 2b shows the spin-wave intensity if only the pumping is switched on. Both microwave currents are applied in $\tau_f = \tau_{2f} = 25\,\text{ns}$ long pulses every 63 ns and arrive at the sample at the same time $t_0 \pm 1\,\text{ns}$. Due to the high group velocity $v_g = 6.1\,\mu\text{m/ns}$ of the spin waves [19], all applied pumping pulses ($\tau_{2f} > 20\,\text{ns}$) are long enough to amplify the spin waves during their whole propagation along the probed area, which takes about 5 ns. This ensures the maximum possible amplification. The spin-wave excitation power at the antenna is fixed to $P_f = 0\,\text{dBm}$ while the microwave power applied to the pumping source is varied from $P_{2f} = 18\,\text{dBm}$ to 30 dBm. The parametric instability threshold has been determined in an additional measurement (not shown) to $P_{\text{th}} = 21\,\text{dBm}$ for $\tau_{2\text{f}} = 1\,\mu\text{s}$ long pulses [27]. In the following, we will express P_{2f} in terms of the supercritical power $P_{\text{sup}} = P_{2f} - P_{\text{th}}$. In both, Figs 2a and b, the spin-wave intensities have been normalized to the maximum spin-wave intensity measured for the largest pumping power $P_{\text{sup}} = +9\,\text{dBm}$ and $P_f = 0\,\text{dBm}$ (squares in Fig. 2a). The diamonds in Fig. 2a show the spin-wave intensity for spin waves being excited by the antenna and $P_{2\text{f}}$ below the instability threshold ($P_{\text{sup}} = -3\,\text{dBm}$). Obviously, the spin waves decay in the course of their propagation

along the waveguide. The spin-wave intensity decay length in this case is determined to $\delta = (3.2 \pm 0.3)\,\mu\text{m}$, which is in excellent agreement with the theoretical prediction [28] of $\delta = 3.3\,\mu\text{m}$ for these waveguide dimensions, spin-wave frequency, external bias field and with $\alpha = 0.01$. At a distance of $y \approx 8\,\mu\text{m}$, the spin-wave intensity has decreased to the thermal noise level and, for larger distances, the signal is dominated by noise fluctuations. If a microwave power equal to the parametric instability threshold power is applied ($P_{\text{sup}} = 0\,\text{dBm}$, downward triangles in Figs 2a and b) the spin-wave intensity in front of the antenna increases, as here the spin-wave damping is reduced by the pumping field. However, the spin waves decay when they enter the widened region, where the pumping field falls below the instability threshold. Again, no influence of the spin-wave excitation by the antenna can be seen for distances larger than $y \approx 10\,\mu\text{m}$. Figure 2b shows the spin-wave intensity for $P_{\text{sup}} = 0\,\text{dBm}$ and no spin-wave excitation at the antenna. No influence of parametric generation can be observed in this case, since for a power at or just above the instability threshold, a real amplification or generation can only be observed for infinitely long pulses.

The situation changes for an applied microwave power of $P_{\text{sup}} = +3\,\text{dBm}$ (upward triangles in Figs 2a and b). In this case, the spin-wave intensity does not decay as strongly as for lower pumping powers and, thus, spin waves propagate beyond the widened region. This is due to the parametric amplification, which takes place strongly in front of the widened region and weakly inside of it, since inside the applied power is just above the instability threshold. Past this region, the spin waves again interact with the stronger pumping field. Thus, the spin waves are amplified during the course of their propagation and the spin-wave intensity is amplified almost up to its initial value at the antenna. As can be seen in Fig. 2b, for this applied P_{sup} a small increase in the spin-wave intensity above the thermal noise level by parametric generation can be observed as well.

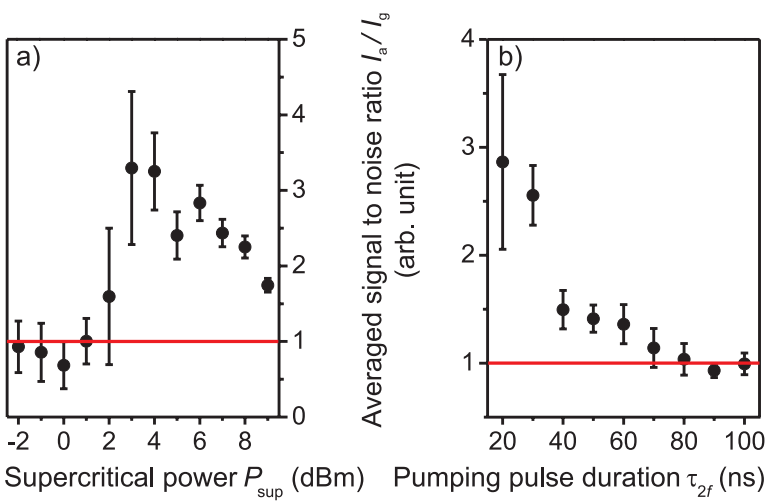

Fig. 3: Spatially averaged (from $y = 16\,\mu\text{m}$ to $y = 26\,\mu\text{m}$) signal to noise ratio I_a/I_g: (a) As a function of the applied pumping power P_{sup} ($P_f = 0\,\text{dBm}$, $\tau_f = \tau_{2f} = 25\,\text{ns}$). (b) As a function of the duration of the pumping pulse τ_{2f} ($P_{\text{sup}} = +3\,\text{dBm}$, $P_f = 0\,\text{dBm}$, $\tau_f = 100\,\text{ns}$).

If the power applied to the pumping source is increased further, even larger spin-wave intensities are observed in front and behind the widened region (squares and dots in Figs 2a and b). However, as can be seen in Fig. 2b, also a pronounced parametric generation takes place for such large powers. As discussed above, the parametrically generated spin waves constitute an unwanted background noise in this experiment. Therefore, as a figure of merit we define the signal to noise ratio, i.e., the ratio of the spin-wave intensity I_a for spin waves being emitted from the antenna and, consequently, amplified, over the spin-wave intensity I_g for the case that only parametric generation takes place inside the waveguide. Figure 3a shows this ratio spatially averaged from $y = 16\,\mu\text{m}$ to

$y = 26\,\mu\text{m}$. At a power of $P_{\text{sup}} = +2\,\text{dBm}$, the signal to noise ratio starts to increase, as for this applied microwave power a small amount of spin waves passes the widened region and is amplified thereafter. The signal to noise ratio exhibits a maximum at $P_{\text{sup}} = +3\,\text{dBm}$ and decreases for higher applied powers. This is mainly caused by the increased amount of parametrically generated spin waves. The error bar represents the standard deviation of the signal to noise ratio in the region where the averaging is performed. Since for an applied power of $P_{\text{sup}} = +3\,\text{dBm}$ a rather large spin-wave intensity is present while practically no parametrically generated spin waves are visible, this constitutes the optimum working point in this configuration. For these parameters, one can clearly distinguish whether or not spin waves are excited at the antenna at distances $y > 25\,\mu\text{m}$, which are large in comparison to the spin-wave decay length of $\delta = 3.2\,\mu\text{m}$.

As can be seen from Fig. 2a, the spin-wave intensity exhibits a maximum at distances beyond the widened region. The maximum shifts to smaller distances y as the pumping power is increased because the spin waves are amplified during the course of their propagation with different amplification rates, depending on the applied supercritical power. This is mediated by the fact that the supercritical spin-wave intensity itself is a rather complicated function of the applied power, as nonlinear damping and dephasing mechanisms limit the intensity to a certain level [14, 15, 29]. Moreover, for large distances or large supercritical powers, respectively, the traveling spin waves enter an area where already a large number of parametrically generated magnons are present and the interaction with these waves limits the amplification further.

In the measurements presented above, pulses with a rather short duration of $\tau_f = \tau_{2f} = 25\,\text{ns}$ have been applied. Figure 3b shows the spatially averaged signal to noise ratio as a function of the pumping pulse duration τ_{2f} for a fixed duration $\tau_f = 100\,\text{ns}$ of the excitation pulses for fixed $P_f = 0\,\text{dBm}$ and $P_{\text{sup}} = +3\,\text{dBm}$. It is obvious that an increase in the pumping pulse duration leads to a monotonous decrease of the signal to noise ratio. This is mainly due to the fact that the spin-wave intensity saturates for long pumping pulses [14]. As discussed above, since the same spin-wave mode is parametrically amplified and generated, the saturation level of the spin-wave intensity is the same for both processes and mainly determined by P_{sup}. Therefore, at longer times, i.e., when the intensity reaches the saturation level, it is not possible to distinguish between the parametrically generated and amplified spin waves anymore. Hence, the utilization of short pumping pulses ensures that mainly parametrically *amplified* spin waves are detected and results in a high signal to noise ratio.

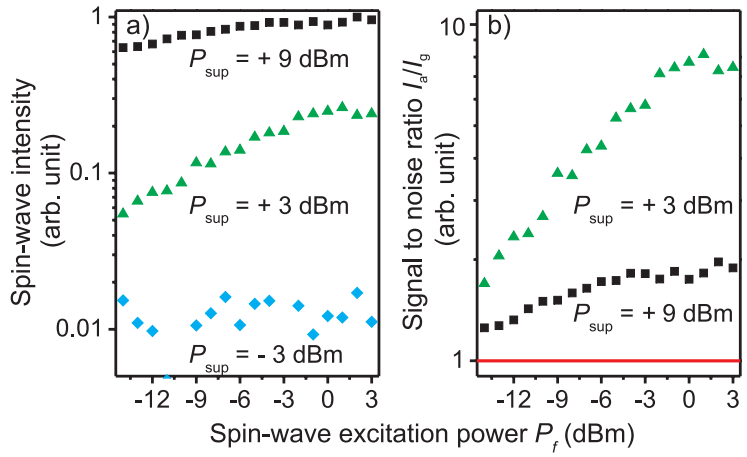

Fig. 4: (a) Spin-wave intensity and (b) signal to noise ratio as a function of the applied spin-wave excitation power P_f for $P_{\text{sup}} = -3\,\text{dBm}$ (diamonds), $P_{\text{sup}} = +3\,\text{dBm}$ (upward triangles) and $P_{\text{sup}} = +9\,\text{dBm}$ (squares) ($\tau_f = \tau_{2f} = 25\,\text{ns}$, $y = 21\,\mu\text{m}$).

Finally, we want to address the influence of the initial spin-wave excitation power applied to the

antenna. Figure 4a shows the spin-wave intensity as a function of the applied spin-wave excitation power P_f for $P_{\text{sup}} = -3\,\text{dBm}$ (diamonds), $P_{\text{sup}} = +3\,\text{dBm}$ (upward triangles) and $P_{\text{sup}} = +9\,\text{dBm}$ (squares). The measurement is performed at a distance $y = 21\,\mu\text{m}$ from the antenna with $\tau_f = \tau_{2f} = 25\,\text{ns}$. No influence of the spin waves excited at the antenna is visible for $P_{\text{sup}} = -3\,\text{dBm}$ and the measured BLS intensity is only caused by thermal noise. However, if the pumping power is increased to $P_{\text{sup}} = +3\,\text{dBm}$, a clear influence of the direct excitation is visible. Moreover, for low excitation powers, a monotonous increase in the spin-wave intensity with the applied power is observed. For larger powers, the spin-wave intensity saturates, as the maximal achievable spin-wave intensity is again limited by P_{sup}. For $P_{\text{sup}} = +9\,\text{dBm}$, a similar behavior is observed. In this case, much larger spin-wave intensities are observed, even for small applied P_f due to the stronger amplification. However, the relative increase in the spin-wave intensity with P_f is smaller than for $P_{\text{sup}} = +3\,\text{dBm}$ and saturation is reached for smaller P_f. For a better understanding, Fig. 4b shows the signal to noise ratio for $P_{\text{sup}} = +3\,\text{dBm}$ and $P_{\text{sup}} = +9\,\text{dBm}$ [30]. In both cases, the dependency of the signal to noise ratio on P_f generally reflects the observations in Fig. 4a. Since for $P_{\text{sup}} = +9\,\text{dBm}$ a large amount of spin waves is parametrically generated, the overall signal to noise ratio is lower.

To conclude, we have demonstrated parallel parametric amplification of propagating spin waves in a microstructured magnonic $Ni_{81}Fe_{19}$ waveguide. We have shown that an influence of the spin waves excited at the antenna can be detected at distances of about $30\,\mu\text{m}$ which corresponds to almost 10 times the non-amplified spin-wave decay length under the investigated conditions. To achieve an efficient and noise free amplification, short pulses with pumping powers close to the threshold power of parametric generation should be used. This is due to the fact that an increase in the pumping pulse duration and power not only increases the amount of amplified spin waves, it also leads to a large amount of parametrically generated spin waves. Furthermore, for small spin-wave excitation powers, the amplified spin-wave intensity at large distances is proportional to the excitation power and, thus, information on the initial excitation can be extracted. For larger excitation powers, the spin-wave excitation power does not influence the amplified spin-wave intensity. The potential to amplify a small spin-wave signal in a microstructured magnonic waveguide is a crucial step for the field of magnonics. The presented results show the feasibility of parallel pumping in order to achieve this milestone. This paves the way for the realization of a network of pure spin-wave logic devices.

The authors thank the *Nanostructuring Center* of the TU Kaiserslautern as well as T. Fischer, M. Geilen and B. Heinz for their assistance in sample preparation. T. Brächer is supported by a fellowship of the Graduate School Materials Science in Mainz (MAINZ) through DFG-funding of the Excellence Initiative (GSC 266). Financial support by the DFG (TRR49) is gratefully acknowledged.

References

[1] B. Lenk, H. Ulrichs, F. Garbs, M. Münzenberg, *The building blocks of magnonics*, Physics Reports **507**, 107 (2011).
[2] A.A. Serga, A.V. Chumak, B. Hillebrands, *YIG magnonics*, J. Phys. D: Appl. Phys. **43**, 264002 (2010).
[3] S. Neusser, D. Grundler, *Magnonics: Spin waves on the nanoscale*, Adv. Mater. **21**, 2927 (2009).
[4] A.V. Chumak, A.A. Serga, M.B. Jungfleisch, R. Neb, D.A. Bozhko, V.S. Tiberkevich, B. Hillebrands, *Direct detection of magnon spin transport by the inverse spin Hall effect*, Appl. Phys. Lett. **100**, 082405 (2012).
[5] P. Pirro, T. Brächer, K. Vogt, B. Obry, H. Schultheiss, B. Leven, B. Hillebrands, *Interference of coherent spin waves in micron-sized ferromagnetic waveguides*, Phys. Status Solidi B **248**, 2404 (2011).
[6] A. Khitun, M. Bao, K.L. Wang, *Magnonic logic circuits*, J. Phys. D: Appl. Phys. **43** 264005 (2010).

[7] T. Schneider, A.A. Serga, B. Leven, R.L. Stamps, M.P. Kostylev, B. Hillebrands, *Realization of spin-wave logic gates*, Appl. Phys. Lett. **92**, 022505 (2008).

[8] M. Madami, S. Bonetti, G. Consolo, S. Tacchi, G. Carlotti, G. Gubbiotti, F.B. Mancoff, M.A. Yar, J. Akerman, *Direct observation of a propagating spin wave induced by spin-transfer torque*, Nat. Nanotechnology **6**, 635 (2011).

[9] V.E. Demidov, S. Urazhdin, H. Ulrichs, V. Tiberkevich, A.N. Slavin, D. Baither, G. Schmitz, S.O. Demokritov, *Magnetic nano-oscillator driven by pure spin curren*, Nature Materials **11**, 1028 (2012).

[10] Z. Wang, Y. Sun, M. Wu, V. Tiberkevich, A.N. Slavin, *Control of spin waves in a thin film ferromagnetic insulator through interfacial spin scattering*, Phys. Rev. Lett. **107**, 146602 (2011).

[11] E. Schlömann, J.J. Green, U. Milano, *Recent developments in ferromagnetic resonance at high power levels*, J. Appl. Phys. **31**, 386S (1960).

[12] A.G. Gurevich and G.A. Melkov, *Magnetization oscillations and waves*, (CRC, New York, 1996).

[13] A.A. Serga, C.W. Sandweg, V.I. Vasyuchka, M.B. Jungfleisch, B. Hillebrands, A. Kreisel, P. Kopietz, M.P. Kostylev, *Brillouin light scattering spectroscopy of parametrically excited dipole-exchange magnons*, Phys. Rev. B **86**, 134403 (2012).

[14] V.E. Zakharov, V.S. L'vov, S.S. Starobinets, *Stationary nonlinear theory of parametric excitation of waves*, Sov. Phys. JETP **32**, 656 (1971).

[15] S. Schäfer, A.V. Chumak, A.A. Serga, G.A. Melkov, B. Hillebrands, *Microwave spectral analysis by means of nonresonant parametric recovery of spin-wave signals in a thin magnetic film*, Appl. Phys. Lett. **92**, 162514 (2008).

[16] T. Brächer, P. Pirro, B. Obry, B. Leven, A.A. Serga, B. Hillebrands, *Mode selective parametric excitation of spin waves in a $Ni_{81}Fe_{19}$ microstripe*, Appl. Phys. Lett. **99**, 162501 (2011).

[17] V.E. Demidov, S.O. Demokritov, B. Hillebrands, M. Laufenberg, P.P. Freitas, *Radiation of spin waves by a single micrometer-sized magnetic element*, Appl. Phys. Lett. **85**, 2866 (2004).

[18] V.E. Demidov, M.P. Kostylev, K. Rott, P. Krzysteczko, G. Reiss, S.O. Demokritov, *Excitation of microwaveguide modes by a stripe antenna*, Appl. Phys. Lett. **95**, 112509 (2009).

[19] This field is in the vicinity of the field of the most efficient generation for the mode $n = 1$ with $k_y \approx 0\,\mathrm{rad/\mu m}$ at $\mu_0 H_{\mathrm{ext}} = 36\,\mathrm{mT}$. For a saturation magnetization of $M_s = 800\,\mathrm{kA/m}$ and an exchange constant of $A = 16\,\mathrm{pJ/m}$, the wavelength $\lambda = 17\,\mu\mathrm{m}$ as well as a group velocity $v_{\mathrm{g}} = 6.1\,\mu\mathrm{m/ns}$ follow from the dispersion relation for spin waves in thin films for an effective field of $\mu_0 H_{\mathrm{eff}} = 29\,\mathrm{mT}$ and an effective waveguide width of $w_{\mathrm{eff}} = 3\,\mu\mathrm{m}$.

[20] B.A. Kalinikos and A.N. Slavin, *Theory of dipole-exchange spin wave spectrum for ferromagnetic films with mixed exchange boundary conditions*, J. Phys. C: Solid State **19**, 7013 (1986).

[21] K.Yu. Guslienko, S.O. Demokritov, B. Hillebrands, A.N. Slavin, *Effective dipolar boundary conditions for dynamic magnetization in thin magnetic stripes*, Phys. Rev. B **66**, 132402 (2002).

[22] T. Brächer, P. Pirro, F. Heussner, A.A. Serga, B. Hillebrands, *Localized parallel parametric generation of spin waves in a $N_{81}Fe_{19}$ waveguide by spatial variation of the pumping field*, Appl. Phys. Lett. **104**, 092418 (2014).

[23] C.W. Sandweg, Y. Kajiwara, A.V. Chumak, A.A. Serga, V.I. Vasyuchka, M.B. Jungfleisch, E. Saitoh, B. Hillebrands, *Spin pumping by parametrically excited exchange magnons* Phys. Rev. Lett. **106**, 216601 (2011).

[24] A.V. Chumak, V.I. Vasyuchka, A.A. Serga, M.P. Kostylev, V.S. Tiberkevich, B. Hillebrands, *Storage-recovery phenomenon in magnonic crystal*, Phys. Rev. Lett. **108**, 257207 (2012).

[25] A.A. Serga, S.O. Demokritov, B. Hillebrands, S.-G. Min, A.N. Slavin, *Phase control of non-adiabatic parametric amplification of spin wave packets*, J. Appl. Phys. **93**, 8585 (2003).

[26] K. Vogt, H. Schultheiss, S.J. Hermsdoerfer, P. Pirro, A.A. Serga, B. Hillebrands, *All-optical detection of phase fronts of propagating spin waves in a $Ni_{81}Fe_{19}$ microstripe*, Appl. Phys. Lett. **95**, 182508 (2009).

[27] It should be noted that the parametric instability threshold is defined for infinitely long pumping pulses. In $Ni_{81}Fe_{19}$, pulses of $\tau = 1\,\mu\mathrm{s}$ are sufficiently long to be close to this limit. However, if the pulse duration is shortened, higher powers are needed to amplify the thermal spin waves to a level that can be detected with BLS within the duration of the pumping pulse.

[28] D.D. Stancil, A. Prabhakar, *Spin waves - theory and applications* (Springer, New York, Berlin, Heidelberg, 2009).

[29] G.A. Melkov, A.A. Serga, A.N. Slavin, V.S. Tiberkevich, A.N. Oleinik, A.V. Bagada, *Parametric interaction of magnetostatic waves with a nonstationary local pump*, JETP **89**, 1189 (1999).

[30] The parametrically generated spin-wave intensity at $y = 21\,\mu\mathrm{m}$ in the absence of a direct excitation has been recorded in an additional measurement which is not presented here.

[31] T. Brächer, P. Pirro, T. Meyer, F. Heussner, B. Lägel, A.A. Serga, B. Hillebrands, *Parallel parametric amplification of coherently excited propagating spin waves in a microscopic $Ni_{81}Fe_{19}$ waveguide*, Appl. Phys. Lett. **104**, 202408 (2014).

4.6 A localized spin-wave amplifier on the micrometer scale realized by parallel pumping

T. Brächer, F. Heussner, P. Pirro, T. Fischer, M. Geilen, B. Heinz, A.A. Serga, and B. Hillebrands

In collaboration with B. Lägel, Nanostructuring Center (NSC), TU Kaiserslautern, 67663 Kaiserslautern

The field of magnonics [1, 2] deals with the processing of information through the utilization of spin waves and their quanta, magnons. The prospect to transmit spin currents through electrical insulators in the form of spin waves [3] and the creation of a wave-based logic [4, 5] where the information is encoded into their amplitude and phase [6, 7] have led to an increased research effort in this field. Although first experiments using materials which feature a small spin-wave damping have already shown promising results [8, 9], one of the main challenges for the field of magnonics is still the limited lifetime of spin waves. Parallel parametric amplification, or in short, parallel pumping, is one possible way to overcome this issue [2]. Parallel pumping describes the splitting of microwave photons into pairs of magnons at half the photon frequency [10]. Recently, it was demonstrated that this technique can be used to amplify externally excited spin waves in a microstructured $Ni_{81}Fe_{19}$ magnonic waveguide [11]. This allows for a significant increase in their effective lifetime and, thus, propagation distance. Still, parallel pumping also amplifies thermal spin waves, leading to parametric generation. If the pumping is applied along the whole waveguide, the coexistence of the parametric amplification of the externally excited spin waves with the parametric generation reduces the efficiency of the amplification and makes an experimental separation of these two processes challenging.

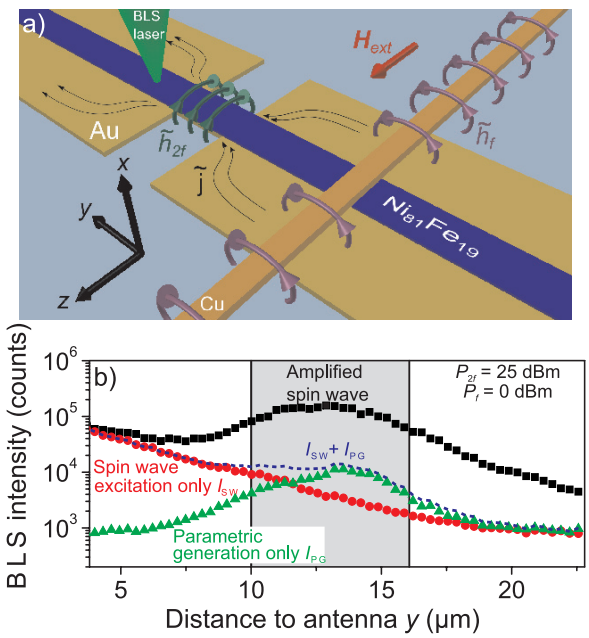

Fig. 1: (a) Sample schematic: A $Ni_{81}Fe_{19}$ waveguide lies on top of a microstrip transmission line. The dynamic Oersted field $\tilde{h}_f$ created by a microstrip antenna across the waveguide provides an external spin-wave excitation in the transversely in-plane magnetized waveguide. At a distance of 10 μm from this antenna, the transmission line features a narrowed region where the microwave current density $\tilde{j}$ and, consequently, the dynamic Oersted field $\tilde{h}_{2f}$ are enhanced, acting as the amplifier. (b) Logarithmic BLS intensity vs. distance from the antenna (integrated over the waveguide width) for different configurations. Dots: only spin-wave excitation by the antenna (I_{SW}). Triangles: only parametric generation (I_{PG}). Squares: spin-wave amplification. Dashed line: I_{SW} + I_{PG} for comparison. The shaded area marks the geometric extents of the amplifier.

Here, we report on the localized parallel parametric amplification of externally excited spin waves in a transversely in-plane magnetized $Ni_{81}Fe_{19}$ magnonic waveguide. In particular, we demonstrate how the parametrically generated magnons limit the efficiency of the amplification. We show that

there are two possible regimes to use the parametric amplifier: In the high-power regime, the externally excited spin waves are only amplified if the pumping is switched on after the spin waves have entered the amplifier region while, in the low-power regime, the spin-wave packet can enter at an arbitrary time within the pumping pulse and its amplification is always observed.

The investigated sample is sketched in Fig. 1a and consists of a $Ni_{81}Fe_{19}$ magnonic waveguide (length $L_s = 75\,\mu m$, width $w_s = 4\,\mu m$, thickness $d_s = 40\,nm$) which has been patterned on top of a $d = 250\,nm$ thick Au microstrip transmission line. The Au and the Py are separated by a $d_{HSQ} = 250\,nm$ thick insulation layer made from Hydrosilesquioxane. In an additional step, a Cu microstrip antenna ($w_a = 2\,\mu m$, $d_a = 500\,nm$) has been patterned across the magnonic waveguide. The waveguide is magnetized transversely in-plane by an applied magnetic bias field of $\mu_0 H_{ext} = 47\,mT$. As a result, the dynamic Oersted field $\tilde{h}_f$ created by the microstrip antenna is perpendicular to H_{ext} and, thus, acts as an effective spin-wave excitation source [12]. The regular width of the transmission line is $w_1 = 20\,\mu m$. At a distance of $l_1 = 10\,\mu m$ from the microstrip antenna, the transmission line features a $l_2 = 6\,\mu m$ long narrowed region with a width of $w_2 = 4\,\mu m$. In this narrowed region, the current density is larger than in the wider parts of the transmission line and, thus, the local dynamic Oersted field is enhanced. As it has been demonstrated in Ref. [19], the combination of this local enhancement with the strong dependency of the parametric amplification on the microwave field can be used to create a local parallel parametric amplifier [10] for spin waves in a transversely in-plane magnetized magnonic waveguide. In the following, this region is, therefore, addressed as the *amplifier*.

As mentioned above, parallel pumping describes the creation of magnon pairs at frequency f out of microwave photons with frequency $2f$ and relies on the coupling of the microwave field to the longitudinal component of the dynamic magnetization. The latter arises from the ellipticity of precession [13]. The magnon creation opposes the magnon damping and, if the number of magnons injected per unit time exceeds the losses, the parametric instability threshold is reached and the number of magnons exponentially grows over time [14]. In general, parallel pumping can interact with externally excited, coherent magnons and can be used to amplify these spin waves [11,15]. On the other hand, it can also interact with thermal magnons present in the magnonic waveguide and, if the instability threshold of these spin waves is reached, one refers to parametric generation [16].

Figure 1b shows the functionality of the localized spin-wave amplifier: Spin waves are excited at the antenna by a $\tau_f = 15\,ns$ long microwave pulse with a carrier frequency of $f = 6\,GHz$ and an excitation power of $P_f = 0\,dBm$ and propagate towards the amplifier. Just after the spin-wave packet has entered the amplifier, a $\tau_{2f} = 25\,ns$ long microwave pulse with a carrier frequency of $2f = 12\,GHz$ and a power of $P_{2f} = 25\,dBm$ is applied to the pumping transmission line. Since the microwaves are applied by two different, not phase-locked microwave generators the phase between the excitation and the amplification is random and not fixed in time. This corresponds to the real operation conditions of the majority of amplifiers, where the phase of the input waves is unknown. The applied pumping power P_{2f} is larger than the power needed to overcome the parametric instability threshold in the center of the amplifier, which has been determined to be $P_{2f,th} = 20\,dBm$ in an additional measurement with longer microwave pulses (not shown), by 5 dB. Utilizing microfocussed Brillouin Light Scattering spectroscopy (BLS) [17] the total spin-wave intensity (integrated across the width of the waveguide) at $f = 6\,GHz$ is studied as a function of the distance to the microstrip antenna. The scenario described above (i.e. spin waves being emitted and interacting with the pumping field) is shown by the squares in Fig. 1b. As can be seen from the figure, the spin waves decay initially and are amplified once they enter the effective amplifier region. The geometric confinement of the amplifier is indicated by the shaded area in Fig. 1b.

However, the effective size of the amplifier region, as has been demonstrated in Ref. [19], is larger due to the redistribution of the current in the wider part of the transmission line. After the spin waves have passed the center of the amplifier, where the amplification is strongest, the spin-wave intensity decreases. Once the spin waves leave the effective amplifier region they decay without amplification. For comparison, the dots show the BLS intensity I_{SW} if spin waves are excited at the antenna and no pumping is present during the spin-wave propagation. The triangles show the BLS intensity I_{PG} arising from parametric generation only, i.e., if the pumping pulse is applied and no spin waves are excited at the antenna. For reference, the dashed curve shows the sum of the two individual signals $I_{\mathrm{SW}} + I_{\mathrm{PG}}$ which would arise if the spin-wave packet and the pumping are not interacting with each other. Comparing the squares and the dashed curve, it is obvious that a strong amplification takes place and, as a consequence, the spin waves travel significantly farther than without amplification while the small number of parametrically generated spin waves is negligible at distances larger than 20 µm from the antenna. The latter is a general benefit of the localized amplification in comparison to the non-local amplification studied in Ref. [11].

The generated spin waves as well as the majority of the spin waves excited by the antenna have been identified with the first waveguide mode $n = 1$ from the BLS measurements of the spin-wave mode profiles (not shown) [6, 16, 18]. In addition, a fraction of the spin waves excited by the antenna consists of higher transverse spin-wave modes. However, these waves feature a smaller group velocity and, thus, decay strongly before they enter the amplifier. Therefore, the influence of higher width modes on the amplification can be neglected in the following. The spin-wave wavelength of the mode $n = 1$ is determined to $\lambda = 13.6\,\mu\mathrm{m}$, which is large in comparison to the extents of the amplifier [20–22]. Nevertheless, it should be noted that interference effects arising from the fact that the wavelength exceeds the length of the amplifier [23,24] play no significant role in this experiment, since the phase between the spin-wave excitation and the pumping is random.

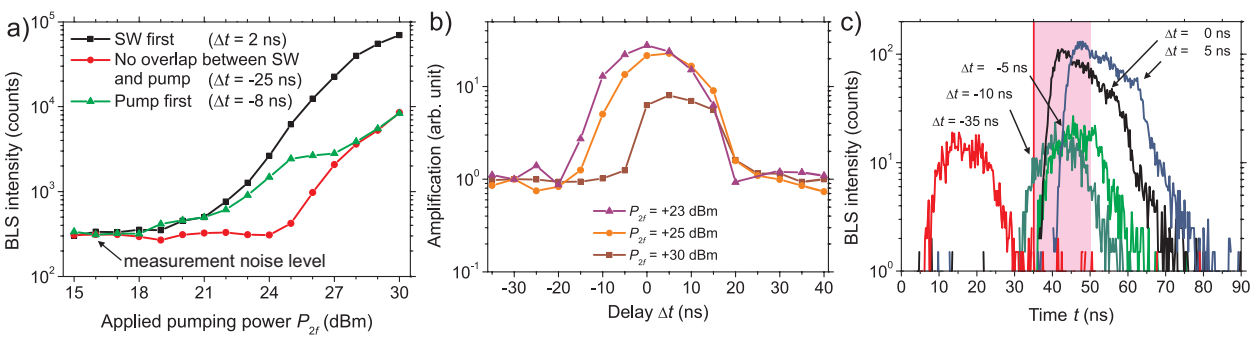

Fig. 2: (a) Influence of the applied pumping power on the measured BLS intensity 9 µm behind the amplifier (25 µm from the antenna) for different pulse configurations. Squares: Spin wave arrives first ($\Delta t > 0$). Dots: Spin-wave packet and pumping pulse have no temporal overlap. Triangles: Pumping pulse arrives first ($\Delta t < 0$). (b) Influence of delay Δt for different P_{2f}. (c) Time-resolved BLS intensity for different delays Δt for $P_{2f} = 30\,\mathrm{dBm}$. The shaded area indicates the extents of the externally excited spin-wave packet in time.

To study the efficiency of the amplifier, the amount of amplified as well as generated spin waves at a distance of about 25 µm from the antenna is analyzed as a function of the applied pumping power P_{2f} and the delay $\Delta t = \mathrm{t}_{0,2\mathrm{f}} - \mathrm{t}_{0,\mathrm{f}}$, where t_0 denotes the starting time of the respective pulses. The P_{2f} dependency for three different delays is shown in Fig. 2a: Squares: The spin-wave packet enters the amplifier shortly before the pumping is applied. Dots: The spin-wave and the pumping pulse are completely displaced in time, i.e. there is no temporal overlap and, thus, no amplification. Triangles: The spin-wave packet enters the amplifier after the pumping pulse is applied. If there is

no temporal overlap between the excitation and the amplification (dots in Fig. 2a), the spin waves excited at the antenna decay without amplification.

From Fig. 1b it can be extrapolated that the spin waves have decayed to about 10% of the noise level at the measurement point of Fig. 2a. Thus, the remaining BLS intensity at $P_{2f} < 25\,\mathrm{dBm}$ in this scenario is mainly caused by the measurement noise. As mentioned above, the power needed to overcome the instability threshold has been determined to $P_{2f,\mathrm{th}} = 20\,\mathrm{dBm}$. However, for applied powers in the vicinity of the threshold power $P_{2f,\mathrm{th}}$ the number of parametrically generated magnons during the short pumping pulse is not sufficient to be detected at the measurement point. Consequently, parametrically generated spin waves are only detected if the parametric instability threshold power is overcome by several dB ($P_{2f} > 24\,\mathrm{dBm}$). In contrast, if the excitation and the amplification overlap in time, the BLS intensity already starts to increase for powers larger than $P_{2f} = 18\,\mathrm{dBm}$, i.e., below the instability threshold. This is due to the fact that even below this threshold the signal spin waves exhibit a reduced damping within the amplifier area. In the vicinity of the threshold, this enables a sufficient amount of spin waves to reach the measurement point.

Comparing the dependencies marked by the squares and the triangles, it is obvious that for rather low P_{2f}, the increase in the BLS intensity with P_{2f} is almost independent of the shift between the pulses and it does not really matter whether the spin-wave packet or the pumping pulse arrives first. However, for large $P_{2f} > 24\,\mathrm{dBm}$ the detected intensities in these two cases deviate drastically from each other: If the pumping pulse arrives prior to the traveling spin waves, the BLS intensity does not increase further with P_{2f} and, finally, coincides with the intensity created from parametric generation only, while it continuously increases with P_{2f} if the spin waves arrive first. Since at large powers, there is a large number of parametrically generated spin waves within the amplifier before the spin-wave packet arrives, this is a strong hint that the presence of these waves suppresses the amplification.

To further analyze the influence of the arrival time of the signal spin-wave packet at the amplifier relative to the beginning of the pumping pulse, the influence of the delay Δt is studied more systematically. In Fig. 2b the amplification is shown as a function of Δt for different powers P_{2f} recorded at the same measurement point as in Fig. 2a. To estimate the amplification, the measurement noise is extrapolated from Fig. 1b and subtracted from the BLS intensity. Subsequently, the amplification is calculated relative to the intensity measured for a delay of $\Delta t = -30\,\mathrm{ns}$, where no temporal overlap between the pulses exists. Therefore, the measured intensity corresponds to the sum of the intensities of two individual, independent spin-wave packets: One packet excited at the antenna and one generated in the amplifier. Two striking differences between rather large and rather small powers P_{2f} above the threshold are visible: 1) For powers $P_{2f} > 23\,\mathrm{dBm}$, the amplification decreases with increasing power P_{2f}. Still, the net amount of spin waves reaching the measurement point increases (cf. Fig. 2a). 2) While for small powers the amplification is symmetric with respect to $\Delta t = 0\,\mathrm{ns}$, it becomes increasingly asymmetric with increasing P_{2f} and for $P_{2f} = 30\,\mathrm{dBm}$ a notable amplification is only obtained if the spin-wave packet arrives first at the amplifier ($\Delta t > 0$).

In order to understand these dynamics, Fig. 2c shows the time-resolved BLS intensity recorded at the same measurement position for an applied power of $P_{2f} = 30\,\mathrm{dBm}$ for different delays Δt. The extent of the externally excited spin-wave packet in time is indicated by the shaded area. For $\Delta t = -35\,\mathrm{ns}$, the spin-wave packet created by parametric generation occurs at early times t while the spin-wave packet created by the antenna is not visible. This does not change up to a delay of $\Delta t = -5\,\mathrm{ns}$, even though in this case there is quite a substantial overlap between the spin-wave and the pumping pulse. It should be noted that the pumping pulse starts about 5 ns before the

generated spin waves are detected with BLS, since, initially, a sufficient amount of spin waves needs to be generated in order to be detectable. In contrast, if the spin-wave packet arrives prior to the pumping, the profile of the measured pulse changes and a net amplification of the spin-wave packet can be observed. In this case, i.e., for $\Delta t = 0\,\text{ns}$, the BLS intensity rises to an one order of magnitude higher level in comparison to the parametrically generated packet. This intensity level slowly decreases in time due to nonlinear magnon-magnon interactions. It should be noted that the observed effects are in agreement with the observations made in Ref. [11], where especially for large powers a decreased range for an efficient amplification was observed.

The strong dependence of the amplification on the arrival time of the spin-wave packet relative to the pumping pulse for large pumping powers can be understood as follows: If the spin-wave packet arrives after the pumping has started, parametric generation rapidly increases the number of thermal spin waves within the amplifier. Thus, at the time the spin-wave packet arrives, there is already a substantial amount of parametrically generated magnons present. The interaction of the externally excited spin waves and the pumping field with these generated magnons suppresses the amplification and limits the output of the amplifier.

Therefore, the parametric amplifier can be operated in two different regimes. In the large power regime, the pumping leads to very high spin-wave intensities with a decent amplification if applied with proper timing (the amplification in the case of $P_{2f} = 30\,\text{dBm}$ in Fig. 2b still measures about 10 dB). However, if the spin waves arrive too late, the amplification is suppressed. Thus, in this working regime, the amplifier can be used to filter spin waves in time. On the other hand, if the pumping power is just above the instability threshold, it is possible to operate the amplifier in a quasi CW mode and the spin-wave packet can enter the amplifier at practically any time during the pumping pulse. This case corresponds to the measurements with low powers P_{2f} presented in Fig. 2b, where the amplification is symmetric with respect to the arrival time of the spin-wave packet in the amplifier. To demonstrate this important working point, Fig. 3 shows the time-resolved BLS intensity obtained if a spin-wave packet with $\tau_f = 15\,\text{ns}$ is shifted in time throughout a $\tau_{2f} = 148\,\text{ns}$ long pumping pulse, whose temporal position is indicated by the shaded area. The measurement has been performed within the amplifier for an applied pumping power $P_{2f} = 22\,\text{dBm}$. While no parametric generation can be observed, the spin-wave packet is amplified as long as it has a temporal overlap with the pumping pulse. Hereby, the efficiency of the amplification is almost independent of the arrival time, since even for long delays only a very small number of parametrically generated magnons is present in the amplifier when the spin-wave packet arrives.

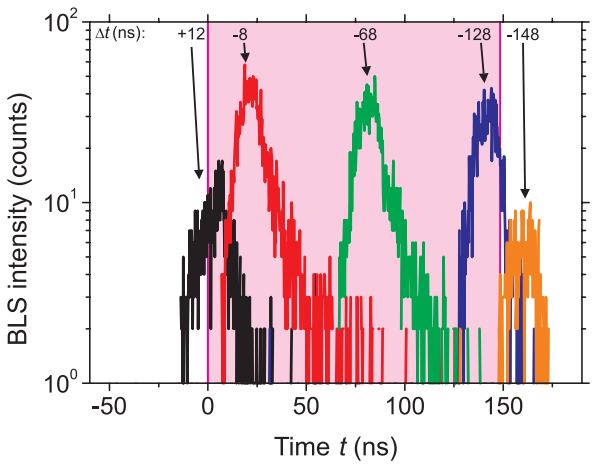

Fig. 3: Time-resolved BLS intensity for different delays Δt for a short spin-wave packet shifted throughout a long pumping pulse with $P_{2f} = 22\,\text{dBm}$ The shaded area marks the position of the pumping pulse in time.

To conclude, we have demonstrated the realization of a localized spin-wave amplifier based on the parallel parametric amplification of spin waves in a transversely in-plane magnetized $Ni_{81}Fe_{19}$ waveguide. Due to the localization it was possible to study the influence of the parametrically generated magnons on the amplification process. We have shown that the device always works as an efficient amplifier as long as the pumping is timed properly with respect to the arrival time of the spin-wave packet. In the case of a strong pumping, this timing is crucial and the spin waves have to arrive prior to the pumping pulse. This allows for a filtering of spin waves in the time domain. On the other hand, if the applied pumping is rather weak, the timing becomes less important and a higher gain can be achieved. We demonstrated that, in this regime, it is possible to amplify a short spin-wave packet within a long pumping pulse, practically independent of the arrival time of the spin-wave packet within the pumping pulse. This allows for an efficient, frequency selective amplification of spin waves in microstructures for subsequent data processing with a high flexibility for the arrival time.

The authors thank the Nano Structuring Center of the Technische Universität Kaiserslautern for their assistance in sample preparation. T. Brächer was supported by a fellowship of the Graduate School Materials Science in Mainz (MAINZ) through DFG-funding of the Excellence Initiative (GSC 266). Financial support by the DFG (TRR49) is gratefully acknowledged.

References

[1] B. Lenk, H. Ulrichs, F. Garbs, M. Münzenberg, *The building blocks of magnonics*, Physics Reports **507**, 107 (2011).
[2] A.A. Serga, A.V. Chumak, B. Hillebrands, *YIG Magnonics*, J. Phys. D: Appl. Phys. **43**, 264002 (2010).
[3] R.L. Stamps, S. Breitkreutz, J. Åkerman, A.V. Chumak, Y. Otani, G.E.W. Bauer, J.-U. Thiele, M. Bowen, S.A. Majetich, M. Kläui, I.L. Prejbeanu, B. Dieny, N.M. Dempsey, B. Hillebrands, *The 2014 Magnetism Roadmap*, J. Phys. D: Appl. Phys. **47**, 333001 (2014).
[4] T. Schneider, A.A. Serga, B. Leven, R.L. Stamps, M.P. Kostylev, B. Hillebrands, *Realization of spin-wave logic gates*, Appl. Phys. Lett. **92**, 022505 (2008).
[5] A.V. Chumak, A.A. Serga, B. Hillebrands, *Magnon transistor for all-magnon data processing*, Nat. Commun. **5**, 4700 (2014).
[6] P. Pirro, T. Brächer, K. Vogt, B. Obry, H. Schultheiss, B. Leven, B. Hillebrands, *Interference of coherent spin waves in micron-sized ferromagnetic waveguides*, Phys. Status Solidi B **248**, 2404 (2011).
[7] K.-S. Lee, S.-K. Kim, *Conceptual design of spin wave logic gates based on a Mach-Zehnder-type spin wave interferometer for universal logic functions*, J. Appl. Phys. **104**, 053909 (2008).
[8] T. Sebastian, Y. Ohdaira, T. Kubota, P. Pirro, T. Brächer, K. Vogt, A.A. Serga, H. Naganuma, M. Oogane, Y. Ando, B. Hillebrands, *Low-damping spin-wave propagation in a micro-structured $Co_2Mn_{0.6}Fe_{0.4}Si$ Heusler waveguide*, Appl. Phys. Lett. **100**, 112402 (2012).
[9] P. Pirro, T. Brächer, A.V. Chumak, B. Lägel, C. Dubs, O. Surzhenko, P. Görnert, B. Leven B. Hillebrands, *Spin-wave excitation and propagation in microstructured waveguides of yttrium iron garnet/Pt bilayers*, Appl. Phys. Lett. **104**, 012402 (2014).
[10] E. Schlömann, J.J. Green, U. Milano, *Recent developments in ferromagnetic resonance at high power levels*, J. Appl. Phys. **31**, 386S (1960).
[11] T. Brächer, P. Pirro, T. Meyer, F. Heussner, B. Lägel, A.A. Serga, B. Hillebrands, *Parallel parametric amplification of coherently excited propagating spin waves in a microscopic $Ni_{81}Fe_{19}$ waveguide*, Appl. Phys. Lett. **104**, 202408 (2014).
[12] V.E. Demidov, M.P. Kostylev, K. Rott, P. Krzysteczko, G. Reiss, S.O. Demokritov, *Excitation of microwaveguide modes by a stripe antenna*, Appl. Phys. Lett. **95**, 112509 (2009).
[13] A.G. Gurevich, G.A. Melkov, *Magnetization oscillations and waves* (CRC, New York, 1996).
[14] V.S. L'vov, *Wave turbulence under parametric excitation* (Springer-Verlag, Berlin-Heidelberg, 1994).
[15] K.R. Smith, V.I. Vasyuchka, M. Wu, G.A. Melkov, C.E. Patton, *Cloning and trapping of magnetostatic spin-wave pulses by parametric pumping*, Phys. Rev. B **76**, 054412 (2007).
[16] T. Brächer, P. Pirro, B. Obry, B. Leven, A.A. Serga, B. Hillebrands, *Mode selective parametric excitation of spin waves in a $Ni_{81}Fe_{19}$ microstripe*, Appl. Phys. Lett. **99**, 162501 (2011).

[17] V.E. Demidov, S.O. Demokritov, B. Hillebrands, M. Laufenberg, P. P. Freitas, *Radiation of spin waves by a single micrometer-sized magnetic element*, Appl. Phys. Lett. **85**, 2866 (2004).
[18] D.D. Stancil, A. Prabhakar, *Spin waves - theory and applications* (Springer, New York, Berlin, Heidelberg, 2009).
[19] T. Brächer, P. Pirro, F. Heussner, A.A. Serga, B. Hillebrands, *Localized parallel parametric generation of spin waves in a $Ni_{81}Fe_{19}$ waveguide by spatial variation of the pumping field*, Appl. Phys. Lett. **104**, 092418 (2014).
[20] The spin-wave wavelength $\lambda = 13.6\,\mu\text{m}$ is derived from the spin-wave dispersion relation for thin films inserting an effective magnetization of $M_s = 800\,\text{kA/m}$, an effective field of $\mu_0 H_{\text{eff}} = 40.5\,\text{mT}$ and an effective waveguide width $w_{\text{eff}} = 3.5\,\mu\text{m}$ [21, 22].
[21] B.A. Kalinikos, A.N. Slavin, *Theory of dipole-exchange spin wave spectrum for ferromagnetic films with mixed exchange boundary conditions*, J. Phys. C: Solid State **19**, 7013 (1986).
[22] K.Yu. Guslienko, S.O. Demokritov, B. Hillebrands, A.N. Slavin, *Effective dipolar boundary conditions for dynamic magnetization in thin magnetic stripes*, Phys. Rev. B **66**, 132402 (2002).
[23] G.A. Melkov, A.A. Serga, V.S. Tiberkevich, Yu.V. Kobljanskij, A.N. Slavin, *Nonadiabatic interaction of a propagating wave packet with localized parametric pumping*, Phys. Rev. E **63**, 066607 (2001).
[24] A.A. Serga, S.O. Demokritov, B. Hillebrands, S.-G. Min, A.N. Slavin, *Phase control of nonadiabatic parametric amplification of spin wave packets*, J. Appl. Phys. **93**, 8585 (2003).

4.7 Planar Hall effect induced dc voltage generation by short-wavelength microwave magnons

A.A. Serga and B. Hillebrands

In collaboration with Yu.V. Kobljanskyj and G.A. Melkov, Faculty of Radiophysics, Taras Shevchenko National University of Kyiv, 01601 Kyiv, Ukraine;
A.N. Slavin, Department of Physics, Oakland University, Rochester, Michigan 48309, USA.

The study of phenomena caused by the mutual influence of a dynamic magnetization and an electric field attracts a lot of attention in the modern magnonics. One of the reasons for such influence is a spin-orbital (SO) interaction. Recently, it has been discovered that in in-plane magnetized [magnetic insulator]/[non-magnetic metal] bilayers this interaction leads to a new type of magnetoresistance caused by interplay of the direct and inverse spin-Hall effects [1, 2].

In the case of an in-plane magnetized conductive magnetic film the SO interaction is responsible for the conventional anisotropic magnetoresistance [3, 4]. The dependence of the electrical resistance R of magnetic conductors and semiconductors as well as artificial nanostructures on the angle Θ between the magnetization $\mathbf{M}$ and an electric current $\mathbf{I}$ is given by $R(\Theta) = R + \triangle R(\Theta)$. The maximal variation of the resistance $\triangle R = R(0^\circ) - R(90^\circ)$ characterizes the magnitude of the effect. For Permalloy (Py, $Fe_{0.2}Ni_{0.8}$) the ratio $\triangle R/R$ is about 4% [4, 5]. In the case of a nanoscale magnetic tunnel junction the effect is larger by one order of magnitude [6]. If an external magnetic field of frequency ω enforces the precession of the magnetization vector $\mathbf{M}$ the angle Θ is a function of time: $\Theta = \Theta(t)$. In this case, both the resistance $R(\Theta)$ and the current flowing through it are functions of time: $R(\Theta) \sim \cos(\omega t + \varphi_R)$, $I \sim \cos(\omega t + \varphi_I)$. As a result, the voltage drop $V = IR(\Theta) \sim \cos(\omega t + \varphi_R)\cos(\omega t + \varphi_I)$ at $R(\Theta)$ contains a dc component V_{dc}. It means that the incident microwave radiation is rectified at a magnetic conductor, semiconductor, or nanoscale magnetic tunnel junction [4, 6]. The effect reaches a maximum if $\varphi_R = \varphi_I$ and is absent if $\varphi_R = \varphi_I \pm \pi/2$.

Another effect, which is caused by the SO interaction in the in-plane magnetized magnetic film, is the planar Hall effect (PHE) [4, 7]. Here, similarly to the conventional Hall effect the flow of conduction electrons is deflected from straight-line propagation; however, this deflection is not caused by the Lorentz force. It occurs based on the interaction of electrons with the lattice due to the SO coupling. As a result, the electric current I flowing in the plane of a film sample creates the voltage V between the lateral faces of the sample [7]:

$$V = I\triangle R(\Theta) = I\triangle R \sin\Theta\cos\Theta \quad , \tag{1}$$

where, as previously, Θ is an angle between the current $\mathbf{I}$ and the bias magnetic field $\mathbf{H}$. It is worth noting that, as opposed to the conventional Hall effect, the field $\mathbf{H}$ lies in the film plane. The relative value of this effect $\triangle R/R$ has the same order of magnitude as in the case of the anisotropic magnetoresistance.

In this Report, we predict theoretically and demonstrate experimentally the ability to rectify microwave signals using the planar Hall effect. Moreover, such rectification can be realized not only for the case of a uniform or quasi-uniform magnetization precession (as it was already shown using the anisotropic magnetoresistance), but also for the case of short-wavelength spin waves.

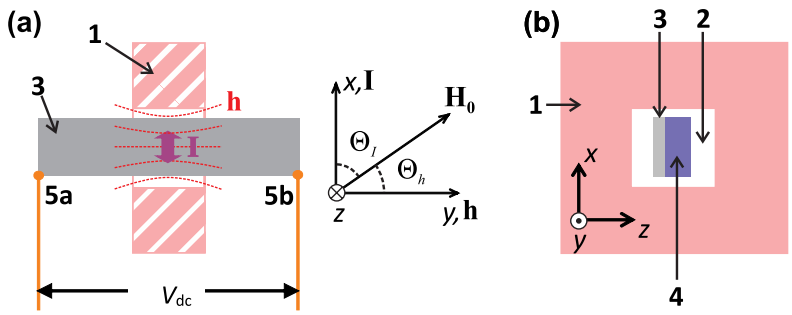

Fig. 1: Schematic view of the experimental setup for the detection of a microwave induced PHE voltage V_{dc}. Panels (a) and (b) show the top and side view of the experimental setup, respectively. 1 – open dielectric resonator with an axial rectangular hole 2; 3 – Permalloy film sputtered on a Si substrate 4; 5a-b – ohmic contacts to measure V_{dc}. The red dashed curves indicate field lines of the microwave magnetic field **h** of the dielectric resonator. The double-sided bold arrow shows the direction of an inductive current **I**. The inset presents the orientation of **h** and **I** relative to the bias magnetic field $\mathbf{H}_0$.

First of all, let us derive the equation for the voltage V_{dc} caused by the planar Hall effect. In the case of the ferromagnetic resonance induced by an external alternating magnetic field $\mathbf{h} = \mathbf{h}_0 \cos \omega t$

$$\Theta = \Theta(t) = \Theta_I + \Theta_c \cos(\omega t - \varphi_R) \quad , \tag{2}$$

where Θ_I is an angle between **I** and an external magnetic field $\mathbf{H}_0$ in the absence of the external microwave magnetic field h_0. If $h_0 \neq 0$ the magnetic moment precesses around $\mathbf{H}_0$ with frequency ω. This situation is taken into account by the second term of Eq. (2). In fact, Θ_c is the amplitude of the uniform precession that, at $\Theta_c \ll 1$, is equal to the ratio of the uniform dynamic magnetization to the saturation magnetization M_0 of the magnetic material. At resonance, when $\omega = \gamma\sqrt{H_0(H_0 + 4\pi M_0)}$ [8],

$$\Theta_c^{\text{res}} = \frac{\gamma H_0 + 4\pi\gamma M_0}{\gamma H_0 + 2\pi\gamma M_0} \frac{h_0}{\triangle H} \sin\Theta_h, \tag{3a}$$

$$\varphi_R = \pi/2. \tag{3b}$$

Here $\triangle H$ is the ferromagnetic resonance line width and Θ_h is the angle between **h** and $\mathbf{H}_0$.

In order to find the constant voltage V_{dc} using Eqs (1)-(3) one needs to know the relation between the alternating magnetic field h and the current I. This relation essentially depends on the experimental conditions. For resonator based measurements, as used in this work, when the sample is placed at the maximum of the field h and consequently at the minimum of the electric field [8], the current is practically exclusively induced by the magnetic field $h = h_0 \cos \omega t$. Moreover, this field excites the magnetization precession.

$$I = A h_0 \cos(\omega t - \varphi_I), \varphi_I = \pi/2 = \varphi_R \quad , \tag{4}$$

where A is a constant, which depends on the boundary conditions at the film's surfaces, the film thickness d and the skin-layer depths δ. For films of thickness of $d \geq \delta$ the constant A is about δ. With a decrease in the film thickness the constant A decreases below δ to the value about 1 µm. As the eddy current **I** is directed perpendicularly to **h** (**I** $\perp$ **h**) $\Theta_h + \Theta_I = \pi/2$.

Substituting Eqs (2)-(4) into Eq. (1) and assuming, as previously $\Theta_c^{\text{res}} \ll 1$, one obtains

$$V_{dc} = \frac{1}{2} A \triangle R \frac{\gamma H_0 + 4\pi\gamma M_0}{\gamma H_0 + 2\pi\gamma M_0} \frac{h_0^2}{\triangle H} \sin\Theta_h \cos 2\Theta_h \quad . \tag{5}$$

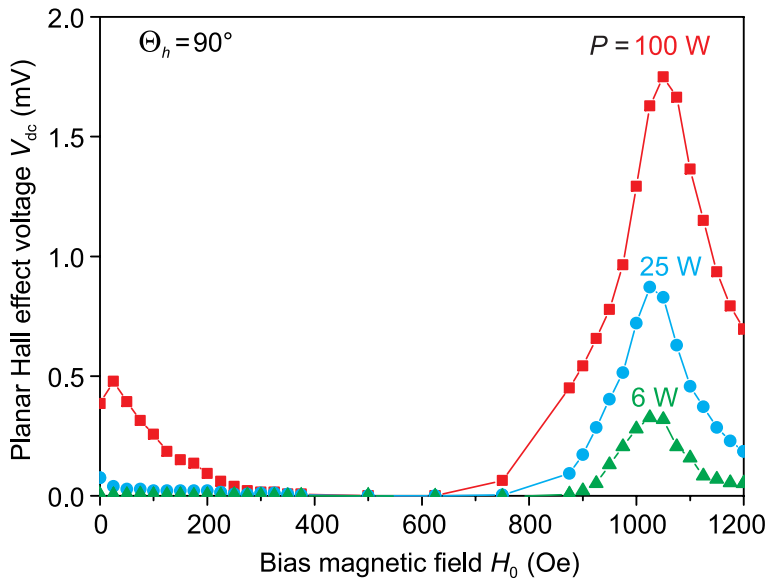

Fig. 2: (Color online) Dependencies of the PHE voltage V_{dc} on the magnitude of the bias magnetic field H_0 for three different input microwave powers: $P = 6, 25$, and 100 W. $\Theta_h = 90°(\mathbf{H}_0 \perp \mathbf{h})$.

Equation (5) shows the cardinal difference between the rectification effects caused by the PHE and by the anisotropic magnetoresistance: the PHE induced voltage reaches its maximum in the case of perpendicular magnetization ($\mathbf{H}_0 \perp \mathbf{h}, \Theta_h = 90°$). In contrary, in such case the voltage caused by the anisotropic magnetoresistance equals zero [4]. Equation (5) can be simplified using the amplitude of the uniform precession Θ_c

$$V_{dc} = \frac{h_0}{2} A \triangle R \Theta_c \cos 2\Theta_h \quad . \tag{6}$$

For the experimental investigation of the PHE related rectification phenomenon we used the resonator-based technique. The Py film sample was placed into the axial hole made in the center of an open dielectric resonator (ODR) (see Fig. 1), where the strength of the microwave magnetic field of the $H_{11\delta}$ mode [9] of such a resonator is maximal. The resonator is produced from a thermostable ceramic with a dielectric permeability $\varepsilon \simeq 80$ and has a rectangular shape of size $3.5 \times 3.5 \times 2\,\mathrm{mm}^3$. The hole has a size of $1.7 \times 0.7 \times 2\,\mathrm{mm}^3$. The resonance frequency of the resonator with the inserted sample is 9350 MHz. All our measurements have been made at this frequency. In order to excite the resonator mode $H_{11\delta}$ the resonator was placed into the antinodal point of the microwave magnetic field of the waveguide mode H_{01} near the closed end of a conventional rectangular waveguide. The maximum microwave power at the waveguide input reached 100 W and was controlled by a precise attenuator. In order to avoid sample heating the experiment was performed in a pulsed regime: microwave pulses of 5 µs duration were applied with a repetition time of 20 ms.

A $Fe_{19}Ni_{81}$ film of a size of 25 mm × 1.5 mm × 25 nm was sputtered on a high-resistance Si substrate of 0.2 mm thickness. The film resistance is 100 ± 2 Ohm. Two ohmic contacts deposited to the opposite sides of the film (see Fig. 1a) are used to connect the sample to an oscilloscope for the measurement of the V_{dc} voltage.

The application of the microwave power P to the waveguide leads to the appearance of on alternating magnetic field $\mathbf{h}$ in the resonator's hole. The field lines are marked in Fig. 1a by red dotted curves. The preferred orientation of this field in the Py film area is along the y axis (see the inset in Fig. 1a) and, consequently, the eddy current $\mathbf{I}$ is directed along the x axis. Due to the PHE, the corresponding electron flow deflects from $\mathbf{x}$ towards the $\mathbf{y}$ direction. This leads to the creation of

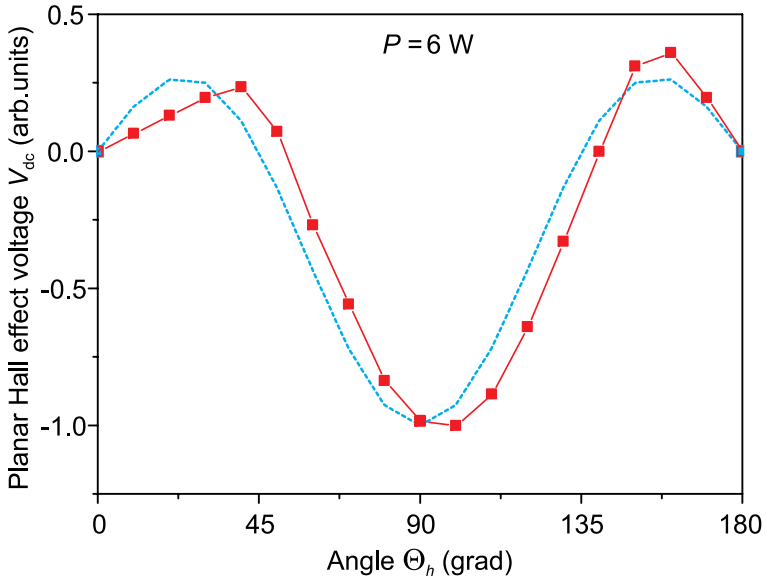

Fig. 3: Angular dependence of the PHE voltage V_{dc} measured for 6 W microwave power in the case of excitation at the ferromagnetic resonance ($H_0 = 1020$ Oe). Filled red squares – experiment. Dashed line $\sim \sin\Theta_h \cos 2\Theta_h$ is a theoretical curve calculated in accordance with Eq. (6).

the rectified voltage V_{dc} between the contacts 6a and 6b in Fig. 1a. The orientation of the constant magnetic field $\mathbf{H}_0$ is shown by the inset in Fig. 1a. In accordance with Eq. (5) and (6) the voltage V_{dc} must reach a maximum when $\mathbf{H}_0 \perp \mathbf{h}$ ($\Theta_h = 90°, \Theta_I = 0$).

It is worth noting that the inverse spin Hall effect or the anomalous Hall effect, which could potentially disturb the experimental results, in reality do not contribute to the measured voltage V_{dc} since, under the given experimental conditions (when the electric current, spins of the conducting electrons, and the induced electric field lie in the same plane), their efficiency is negligible.

According to Eq. (6), the voltage V_{dc} is proportional to the amplitude of the uniform precession Θ_c and, thus, reaches its maximum at the FMR frequency $\omega = \gamma\sqrt{H_0(H_0 + 4\pi M_0)}$. Indeed, from Fig. 2, which shows the experimental dependence of V_{dc} on the bias magnetic field H_0, one can see the resonance increase of the amplitude of the output rectified voltage V_{dc} near the ferromagnetic resonance field $H_0 = H_{res} = 1020$ Oe. It is remarkable that in the case where the input microwave power P exceeds 8 W an additional output signal is observed in the region of small magnetic fields $H_0 < H_{res}$. The nature of this signal will be discussed later.

The dependence of the amplitude of the rectified signal V_{dc} on the angle Θ_h between the constant bias magnetic field $\mathbf{H}_0$ and the alternating magnetic field $\mathbf{h}$ in the case of the FMR is shown in Fig. 3. The experimental curve corresponds well to the angular part of Eq. (5), which is proportional to $\sim \sin\Theta_h \cos 2\Theta_h$.

The absolute value of the FMR induced PHE output voltage V_{dc} measured for $\Theta_h = 90°$ ($\mathbf{H}_0 \perp \mathbf{h}$, the amplitude of the uniform precession Θ_c^{res} is maximal, and thus the value of V_{dc} is maximal) is presented in Fig. 4 (curve 1) as a function of the input microwave power P. At low powers P one can see the linear dependence $V_{dc} = V_{dc}(P)$. This result directly follows from Eq. (5). The slope of this linear area of the curve is $2 \cdot 10^{-4}$ V/W. It is worth noting that this value is by one order of magnitude larger than the previously reported value of a rectified signal obtained by using the anisotropic magnetoresistance [10]. For good agreement with the experiment the constant A in Eq. (5) should be chosen to be 0.4 µm.

With an increase in the microwave power P above 10 W the rectified voltage saturates. This saturation can be understood as a result of the well known saturation of the precessional amplitude Θ_c due to the parametric excitation of short-wavelength spin waves at the frequency of the microwave

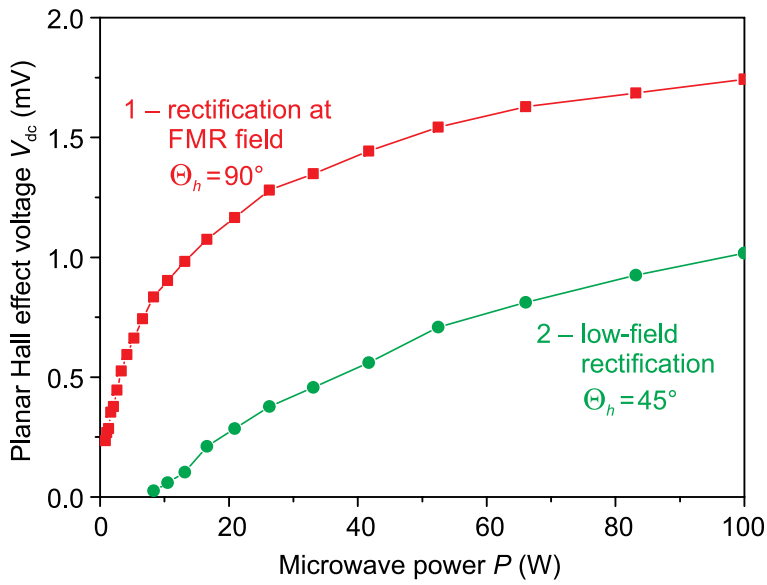

Fig. 4: Dependencies of the PHE voltage V_{dc} on the input microwave power P in the case of excitation at the ferromagnetic resonance (curve 1, $H_0 = 1020\,\mathrm{Oe}$) and in the low-field region (curve 2, $H_0 = 125\,\mathrm{Oe}$), respectively.

signal ω (so-called Suhl's instability of the second order [11]).

Figure 2 shows that at low microwave powers the rectified PHE signal can be observed only around the resonance field $H_{\mathrm{res}} = 1020\,\mathrm{Oe}$. There are two reasons for this dependence. Firstly, the uniform precession angle Θ_c decreases when H_0 is shifted from its resonance value H_{res}. Far from the resonance

$$\Theta_c^{\mathrm{n\,res}} \simeq \frac{\omega_M}{\omega}\frac{h_0}{\omega/\gamma}\sin\Theta_h \ll \Theta_c^{\mathrm{res}} \quad . \tag{7}$$

Secondly, the shift of the phase of the dynamic magnetization φ_R to π neglects the rectification effect.

At the same time, from Fig. 2 one sees that along with the increase in the input microwave power P a second low-field rectification area appears in the region of small bias magnetic fields $H_0 < 250\,\mathrm{Oe}$. Moreover, the angular dependencies of the rectified voltage in this area are significantly different from the FMR case shown in Fig. 3. Two of such dependencies measured at the maximum microwave power $P = 100\,\mathrm{W}$ are presented in Fig. 5 for $H_0 = 125\,\mathrm{Oe}$ and $250\,\mathrm{Oe}$, respectively. The maximum of the rectified voltage is observed in Fig. 5 at $\Theta_h = 45°$. At the same time, no pronounced voltage maximum can be observed for the case where the constant and the alternating magnetic fields are perpendicular to each other ($\mathbf{H}_0 \perp \mathbf{h}$, $\Theta_h = 90°$): here, both the magnitude and the polarity of the rectified signal depend on the value of the bias magnetic field. Figure 6 demonstrates the magnetic field dependence of V_{dc} in the low-field area measured at different microwave powers at the optimal angle $\Theta_h = 45°$. It is clear that the rectified signal appears in a threshold manner and its region of existence increases with increasing microwave power. The threshold character of the rectified voltage is also clearly visible from the second curve in Fig. 4, which shows the behavior of the V_{dc} voltage measured in the low-field area at optimal conditions ($\Theta_h = 45°$ $H_0 = 125\,\mathrm{Oe}$). For microwave powers $P < 8\,\mathrm{W}$ there is no signal. Above this threshold power the function $V_{\mathrm{dc}}(P)$ increases almost linearly with the slope of $1.5 \cdot 10^{-5}\,\mathrm{V/W}$. This value is approximately one order of magnitude smaller than in the case of FMR.

The threshold character of the appearance of the low-field rectification area can be associated with the parametric excitation of spin waves at half of the microwave frequency or, in other words, with the Suhl's instability of the first order [8]. This kind of instability is possible when half of the input microwave frequency lies in the spin-wave frequency band. In the case of an in-plane magnetized

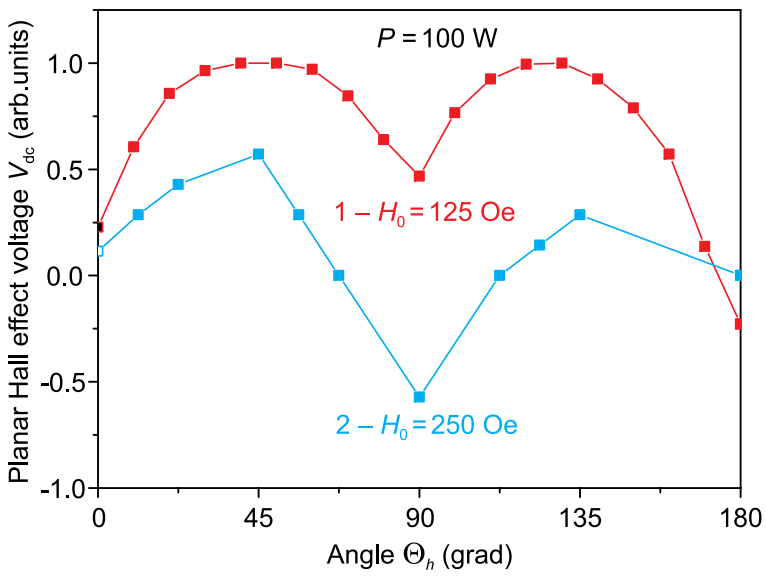

Fig. 5: Angular dependencies of the PHE voltage V_{dc} in the low-field region at $H_0 = 125\,\mathrm{Oe}$ (curve 1) and at $H_0 = 250\,\mathrm{Oe}$ (curve 2). Microwave power $P = 100\,\mathrm{W}$.

film this condition is satisfied for $H_0 < H_c$, where

$$H_c = -2\pi M_0 + \left[(2\pi M_0)^2 + (\frac{\omega}{2\gamma})\right]^{1/2} \quad . \tag{8}$$

The calculation shows that under our experimental conditions $H_c \simeq 300\,\mathrm{Oe}$ this value corresponds perfectly with the observed value of the threshold bias field (see Fig. 6). It is also known that the area of parametric instability broadens to the region of small bias magnetic fields with an increase in the microwave pumping power. This feature is also clearly visible in Fig. 6.

The microwave threshold field of the first order parametric instability can be written [8] as

$$h_{\mathrm{thr}} \simeq \triangle H \frac{\omega_{\mathrm{p}}}{\omega_M} \frac{1}{\sin 2\Theta_k} \quad , \tag{9}$$

where Θ_k is a polar angle $\angle \mathbf{k}\mathbf{H}_0$ of a spin wave, which is parametrically excited at half of the microwave pumping frequency ω_{p} with a wavevector $\mathbf{k}$. Under our experimental conditions the calculated threshold power of the spin-wave instability P_{thr} is about 10 W in the optimal situation when $\sin 2\Theta_k = 1$. This value is close to the experimentally measured threshold power, which is about 8 W.

Thus, we can conclude that in the low-field area the rectified PHE voltage V_{dc} is determined by the parametric excitation of spin waves of frequency $\omega_k = \omega_p/2$ and wavenumber $k \geq 10^4\,\mathrm{cm}^{-1}$ lying in the film plane [8]. This conclusion is completely non-trivial because previously it was assumed that the reason for the appearance of the PHE and anisotropic magnetoresistance based rectification effects is the uniform in the film plane (not necessarily along the film thickness [12]) magnetization precession ($k = 0$) excited at the frequency of the external pumping field ω_p. In the case of the parametrically excited short spin-waves both these prerequisites are violated. As a result, the direct interaction of the uniform current I with the dynamic non-uniform magnetization of short-wavelength spin waves becomes impossible because their interaction integral tends towards zero if the integration is made over a macroscopic sample with a size $\gg 2\pi/k$. Moreover, no constant voltage can result from such interaction due to the fact that the frequency ω_p of the current I differs from the frequency of the dynamic magnetization of the parametrically excited spin waves.

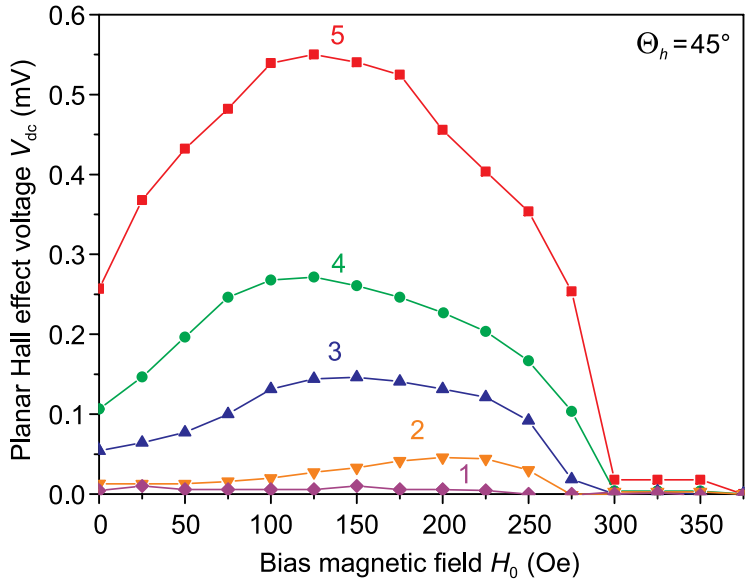

Fig. 6: Magnetic field dependencies of the PHE voltage V_{dc} on the microwave power P in the low-field region: 1 – 6 W; 2 – 11 W; 3 – 25 W; 4 – 50 W; 5 – 100 W. $\Theta_h = 45°$

However, it is well known [13] that two parametric spin waves produce an additional dynamic magnetization, which is determined by the product $a_k a_{-k}$ of the amplitudes of two spin waves with wavevectors $\mathbf{k}$ and $-\mathbf{k}$. This magnetization satisfies all rectification conditions: it is uniformly distributed in space and oscillates exactly at the frequency ω_p. The product $a_k a_{-k}$, which is known as an anomalous correlator, can significantly exceed the intensity of the uniform precession $\Theta_c^2 \equiv a_0^2$ [13]:

$$|a_k a_{-k}| = |a_k|^2 \simeq |a_0|^2 (h_0/h_{\text{thr}}) \quad . \tag{10}$$

Moreover, at the moment when the threshold value of h is reached, the phase of the anomalous correlator (and consequently φ_R) becomes equal to $\pi/2$. As a result, the spin-wave rectification effect appears under the optimal phase condition. Further increase of the microwave power leads to a shift in the phase of the anomalous correlator from this optimal value [13], and thus results in a saturation of the V_{dc} voltage (see curve 2 in Fig. 5).

Finally, let us discuss the angular dependencies of V_{dc} in the low-field area shown in Fig. 5. In fact, the change of the angle Θ_h leads to a transition from the parallel ($\Theta_h = 0$) to the perpendicular ($\Theta_h = 90°$) pumping regime [14]. In the case of parallel pumping the alternating magnetization created by the anomalous correlator $a_k a_{-k}$ is directed along the bias field H_0 [13]. In this case $\triangle R = 0$ [3, 4] and $V_{dc} = 0$ which is observed in the experiment (see, please, Fig. 5 at $\Theta_h = 0°$ and 180°). Under perpendicular pumping the product $a_k a_{-k}$ has a component of the alternating magnetization that is perpendicular to H_0 and, thus, is able to contribute to the rectification process. The value of this component is proportional to $\sin 2\Theta_k$ [11], where Θ_k is the polar angle of the parametrically excited spin waves. This angle strongly depends on the magnitude of the bias magnetic field H_0 and can be responsible for the field dependent variations of V_{dc}, which are visible in Fig. 5 at $\Theta_h = 90°$.

In conclusion, the generation of the dc-voltage V_{dc} caused by the rectification of a microwave signal due to the planar Hall effect was experimentally observed and measured in a thin ferromagnetic film using a specially developed resonator based technique. It is found that the dependence $V_{dc}(H_0)$ has a resonance character with its maximum close to the ferromagnetic resonance (FMR). At the FMR the detected voltage V_{dc} depends on the angle Θ_h between a microwave magnetic field $\mathbf{h}$ and a bias magnetic field $\mathbf{H}_0$ as a function $\sin(\Theta_h)\cos(2\Theta_h)$. An increase in the input microwave

power above 10 W results in the saturation of V_{dc} due to the second order Suhl's instability.

At the same time, at high input powers the rectified voltage appears at bias fields that are significantly smaller than the FMR field. In this case the dc-voltage generation is related to the short-wavelength parametrically excited magnons propagating in a film plane with wavenumbers $k \geq 10^4\,\mathrm{cm}^{-1}$. It is remarkable that this phenomenon is associated not with single magnons but rather with magnon pairs a_k and a_{-k} having a non-zero anomalous correlator $a_k a_{-k}$. In the low field region, the angular dependencies of V_{dc} can be understood if both the orientation of the dynamic magnetization of the anomalous correlator and the angular excitation efficiency of the parametric magnons are taken into account. For example, in the event of parallel pumping ($\mathbf{H}_0 || \mathbf{h}$) this magnetization is directed along the bias magnetic field. As a result, $V_{dc} = 0$. In the event of perpendicular pumping ($\mathbf{H}_0 \perp \mathbf{h}$, the Suhl's process of the first order) the voltage value depends on the polar angle $\angle \mathbf{k}\mathbf{H}_0$ of the parametrically excited waves.

Support by the Deutsche Forschungsgemeinschaft within the SFB/TR 49 is gratefully acknowledged.

References

[1] R. Iguchi, K. Sato, D. Hirobe, S. Daimon, E. Saitoh, *Effect of spin Hall magnetoresistance on spin pumping measurements in insulating magnet/metal systems*, Appl. Phys. Express **7**, 013003 (2014).

[2] Y.-T. Chen, S. Takahashi, H. Nakayama, M. Althammer, S.T.B. Goennenwein, E. Saitoh, G.E.W. Bauer, *Theory of spin Hall magnetoresistance*, Phys. Rev. B **87**, 144411 (2013).

[3] Kimin Hong, N. Giordano, *Approach to mesoscopic magnetic measurements*, Phys. Rev. B **51**, 9855 (1955).

[4] D. Fang, *Current induced torque driven ferromagnetic resonance in magnetic microstructures* (PhD dissertation. Department of Physics, University of Cambrige, Downing College, 2010).

[5] T.R. McGuire, R.I. Potter, *Anisotropic magnetoresistance in ferromagnetic 3D alloys*, IEEE Trans. Magn. **11**, 1018 (1975).

[6] J. Zhu, J.A. Katine, G.E. Rowlands, Y.J. Chen, Z. Duan, J.G. Alzate, P. Upadhyaya, J. Langer, P.K. Amiri, K.L. Wang, I.N. Krivorotov, *Voltage-induced ferromagnetic resonance in magnetic tunnel junctions*, Phys. Rev. Lett. **108**, 197203 (2012).

[7] K.M. Koch, *Zum Problem der galvanomagnetischen Effekte in Ferromagneticis*, Z. Naturforsch. **10a**, 496 (1955).

[8] A.G. Gurevich, G.A. Melkov, *Magnetization oscillations and waves* (CRC, New York, 1996).

[9] A. Okaya, L.F. Barash, *The dielectric microwave resonator*, Proc. IRE **50**, 2081 (1962).

[10] O. Mozendz, V. Vlaminck, J.E. Pearson, F.Y. Fradin, G.E.W. Bauer, S.D. Bader, A. Hoffmann, *Detection and quantification of inverse spin Hall effect from spin pumping in permalloy/normal metal bilayers*, Phys. Rev. B **82**, 214403 (2010).

[11] H. Suhl, *The theory of ferromagnetic resonance at high signal powers*, J. Phys. Chem. Solids **1**, 209 (1957).

[12] Y.S. Gui, L.H Bai, C.M. Hu, *The physics of spin rectification and its application*, Sci. China–Phys. Mech. Astron. **56** 124 (2013).

[13] V.S. L'vov, *Wave Turbulence under parametric excitations. Applications to magnetics* (Springer-Verlag, 1994).

[14] T. Neumann, A.A. Serga, V.I. Vasyuchka, B. Hillebrands, *Field-induced transition from parallel to perpendicular parametric pumping for a microstrip transducer*, Appl. Phys. Lett. **94**, 192502 (2009).

B. Magnon Spintronics

Spintronics is the field of spin-based data storage and processing. In conventional spintronics the electron is used as a carrier of spin. In particular, the manipulation of spin currents in nanostructures has potential applications in computing devices and magnetic memory. For the successful utilization of spin information, difficulties like the short distance over which an electron retains memory of its spin direction, the so-called spin diffusion length, have to be overcome. Here, a promising approach is the combination of standard spintronics with spin-wave dynamics resulting in *magnon spintronics*. A magnon, i.e. the quantum of a spin wave, carries an angular momentum or spin as well and can be used for storage, processing and transport of spin information, building on its outstanding properties such as long lifetime and potential for dissipationless transport. The field of magnon spintronics is currently emerging, and the main objects of studies are magnon to charge current converters and magnon-based data processing devices.

The first three Reports of the chapter (Reports 4.8, 4.9, and 4.10) address the conversion of a magnon current into a charge current. An effective method for detecting magnonic spin currents is the combination of spin pumping and the inverse spin Hall effect (ISHE). Spin pumping refers to the generation of spin-polarized electron currents in a normal metal from the magnetization precession in an attached magnetic material. These spin-polarized electron currents are transformed into conventional charge currents by the ISHE, which allows for a convenient electric detection of spin-wave spin currents. Report 4.8 deals with yttrium iron garnet (YIG)/ Platinum (Pt) bi-layers and addresses the question of the dependence of spin-pumping on the frequency of the magnetization precession. The theoretical predictions show that the ISHE voltage should decrease monotonically with increase in frequency (for frequencies above the 3-magnon splitting region). However, our experiments demonstrate a maximum of the ISHE signal at a frequency of about 11 GHz. This behavior might be associated with the ellipticity of the magnetization precession or with field-dependent spin pinning conditions. In the second Report 4.9 we concentrate on the question of the sign of the ISHE voltage and compare it to the sign of the spin Seebeck voltage. Although many experimental results were published by different groups, not sufficient attention has been paid to the sign of these voltages. Thus, it was not possible to define if all the results are in agreement or not. Therefore, in collaboration with colleagues from several other labs, we performed systematic studies regarding this question. In the third Report 4.10 we examine the influence of crystal growth and Pt thickness on the spin-pumping induced inverse spin Hall effect in Fe/Pt bi-layers.

The next three reports (Reports 4.11, 4.12, and 4.13) are devoted to magnon-based data processing. In Report 4.11 we present the first realization of a magnon transistor - a device in which information is carried and processed using magnons and is fully decoupled from free electrons. In this three-terminal device the density of magnons flowing from the transistor's source to its drain can be decreased three orders of magnitude by the injection of magnons into the transistor's gate. The operational principle of the transistor is based on a nonlinear four-magnon scattering process strongly enhanced by a magnonic crystal ensuring high magnon densities at the gate. The transistor has potential to be a key component of future single-chip magnonic circuits. In Report 4.12 we study another all-magnon device for computing - the majority gate. Although the idea of the spin-wave majority gate has been proposed some time ago, no realization was reported so far. One of the challenges facing the design of such a device is the coexistence of different spin-wave modes that makes data read-out impossible. Using numerical simulations, we propose a solution for the spin-wave mode selection and demonstrate that the device can perform a majority operation as well as that it can be used as AND, OR, NAND, and NOR logic gate. Finally, in Report 4.13 we present

a novel type of a dynamic magnonic crystal - an artificial magnetic material with periodically-varied properties that can be changed on a very fast time scale. The proposed crystal is based on a width-modulated spin-wave waveguide and is suitable for miniaturization and for decrease in power consumption of such type of devices. An AND logic gate without Mach-Zehnder interferometer geometry was realized on the basis of a dynamic magnonic crystal.

B. Magnon-Spintronik

Die Spintronik umfasst das Gebiet der Spin-basierten Informationsspeicherung und Verarbeitung. In der konventionellen Spintronik wird das Elektron als Träger des Spins verwendet. Ein besonderes Augenmerk im Hinblick auf potentielle Anwendungen in Computern oder magnetischen Speichern liegt auf der Manipulation von Spinströmen in Nanostrukturen. Für eine erfolgreiche Nutzung der Spininformationsübertragung ist es allerdings notwendig, Schwierigkeiten wie die vergleichbar kurze Länge der Erhaltung der Spinausrichtung in Materialien, der sogenannten Spindiffusionslänge, zu überwinden. Ein sehr erfolgreicher Ansatz ist hier die Kombination der Spintronik mit der Spinwellendynamik, die “Magnon-Spintronik”. Ein Magnon, das Quant einer Spinwelle, trägt ebenfalls einen Drehimpuls oder Spin und kann analog zur konventionellen Spintronik für den Spin-basierten Datentransfer und die Datenverarbeitung genutzt werden, bietet aber zusätzlich herausragende Möglichkeiten wie z. B. lange Lebensdauern und das Potential eines verlustfreien Transports. Das Feld der Magnon-Spintronik befindet sich derzeit in einer sich rasant bewegenden Entwicklungsphase. Dabei liegt der hauptsächliche Augenmerk der hier vorgestellten Studien auf der Konversion von Magnonenströme in Elektronenströme sowie auf der Entwicklung von Elementen zur Datenverarbeitung auf Basis von Magnonen.

Die ersten drei Berichte des Kapitels (Bericht 4.8, 4.9 und 4.10) sind der Konversion von Magnonenflüssen in Ladungsströme gewidmet. Eine effiziente Methode zur Detektion von Magnonenströmen ist die Kombination des Spinpumpens mit dem inversen Spin Hall Effekt (ISHE). Dabei bezeichnet das Spinpumpen die Generation eines spinpolarisierten Elektronenstroms in einem nicht-magnetischen Metall durch die Spinpräzession im angrenzenden magnetischen Material. Dieser spinpolarisierte Elektronenstrom wird durch den ISHE in einen konventionellen Ladungsträgerstrom umgewandelt, was eine herkömmliche elektrische Detektion von Spinströmen auf Spinwellenbasis ermöglicht. Der Bericht 4.8 behandelt Doppelschichten bestehend aus Yttrium-Eisen-Granat (YIG) und Platin (Pt) und untersucht dabei die Abhängigkeit des Spinpumpens von der Frequenz der Präzession der Magnetisierung. Theoretische Vorhersagen zeigen, dass die Spannung durch den ISHE monoton mit steigender Frequenz abfallen sollte (für Frequenzen oberhalb der Drei-Magnonen-Streuung). Allerdings zeigen unsere Experimente, dass ein Maximum der ISHE-Spannung bei einer Frequenz von ungefähr 11 GHz auftritt. Dieses Verhalten könnte durch die Änderung der Elliptizität der Präzession oder durch ein feldabhängiges Pinning der Spins hervorgerufen werden. Im zweiten Bericht 4.9 wird die Frage des Vorzeichens des ISHE behandelt und dieses Vorzeichen mit dem des Spin Seebeck Effektes verglichen. Obwohl viele Veröffentlichungen experimenteller Resultate dieser Effekte vorliegen, wurde die Frage des Vorzeichens bisher nicht ausreichend beachtet. Deshalb war es bisher nicht möglich festzustellen, ob alle Resultate bezüglich dieses Aspekts übereinstimmen. Um hier Abhilfe zu schaffen wurde in Zusammenarbeit mit mehreren anderen Forschungsgruppen eine systematische Studie zu dieser Frage durchgeführt. Im dritten Bericht 4.10 wurde der Einfluss der Kristallwachstums und der Schichtdicke von Pt auf den durch Spinpumpen hervorgerufenen ISHE in Fe/Pt Doppelschichten untersucht.

Die nächsten drei Berichte (Bericht 4.11, 4.12 und 4.13) sind der Magnonen-basierten Datenverarbeitung gewidmet. Im ersten Bericht 4.11 präsentieren wir die erste Realisierung eines Magnonen-Transistors, also eines Bauelements, in welchem Informationen durch Magnonen transportiert und verarbeitet werden und welches komplett von beweglichen Elektronen entkoppelt ist. In diesem Element mit drei Anschlüssen kann die Dichte der Magnonen, welche vom Emitter zum Kollektor fließen, durch die Injektion von Magnonen an der Transistorbasis um drei Größenordnungen verringert werden. Das Operationsprinzip dieses Transistors beruht auf einem nichtlinearen Vier-Magnonen-Streuprozess, welcher durch einen magnonischen Kristall verstärkt wird, wodurch eine hohe Magnonendichte im Bereich der Basis des Transistors erreicht wird. Dieser Transistor hat das Potential, eine Schlüsselrolle in zukünftigen, rein magnonischen Logikgattern zu spielen. Im nächsten Bericht 4.12 wird ein weiteres Bauteil einer reinen Magnonenlogik behandelt - das Majoritätsgatter. Obwohl ein Spinwellenmajoritätsgatters bereits vor einiger Zeit prinzipiell vorgeschlagen wurde, wurde bis jetzt keine entsprechende Realisierung demonstriert. Eine der Herausforderungen beim Bau eines solchen Elements ist die Koexistenz von verschiedenen Spinwellenmoden, welche das Auslesen von Daten unmöglich machen kann. Mit Hilfe numerischer Simulationen demonstrieren wir eine Möglichkeit zur Modenselektion und zeigen, dass das vorgeschlagene Logikelement sowohl die Majoritätsoperation, als auch UND- sowie ODER-Operationen und deren Negationen ausführen kann. Im letzten Bericht 4.13 präsentieren wir einen neuartigen dynamischen Kristall - ein künstliches magnetisches Material, dessen räumlich periodisch variierte Eigenschaften zusätzlich auch auf sehr kurzen Zeitskalen moduliert werden können. Der vorgeschlagene Kristall basiert auf einem Spinwellenleiter mit modulierter Breite, welcher für eine Miniaturisierung geeignet ist und einen geringen Leistungsbedarf aufweist. Mit diesem dynamischen magnonischen Kristall wurde ein UND-Gatter ohne den Einsatz einer Mach-Zehnder-Interferometer-Geometrie demonstriert.

4.8 Spin pumping by magnetization precession in a wide frequency range

V. Lauer, T. Brächer, B. Hillebrands, and A.V. Chumak

Spin pumping refers to the spin-current generation caused by magnetization precession [1]. In particular, it allows for the injection of a spin current by magnetization precession in an insulating magnetic film like $Y_3Fe_5O_{12}$ (YIG) into an adjacent non-magnetic metal film. This spin current, in turn, can be converted into a charge current via the inverse spin Hall effect (ISHE) [2]. For this purpose a metal with a large spin-orbit interaction, such as Pt, needs to be used. The combination of spin pumping and the ISHE attracted much attention in the last decade with regard to possible applications in the field of spintronics [3–8].

It is indispensable to study the influence of various parameters on spin-pumping and spin Hall experiments, in order to prove theory and to understand the physical principles behind. This Report particularly addresses the frequency dependence of spin pumping. Kurebayashi *et al.* [9] reported on a strong increase of the spin-pumping induced ISHE voltage at frequencies below $f \approx 3.2\,\mathrm{GHz}$ (5.1 µm thick YIG film) and explained the observation by three-magnon splitting. After that, Castel *et al.* [10] observed an increased spin-pumping induced signal below $f \approx 3.4\,\mathrm{GHz}$ on a 200 nm thick YIG film system, where three-magnon splitting is prohibited and the results are assumed to account for secondary spin-wave modes.

To the best of our knowledge, no experimental analysis of the frequency range above the three-magnon splitting region has been reported so far. Using a phenomenological model [4, 11–13] the ISHE voltage V_{ISHE} induced by the uniform mode precession of frequency f is predicted to follow

$$V_{\mathrm{ISHE}} \propto j_{\mathrm{s}} = (\mu_0 h_{\mathrm{ac}} \gamma)^2 \cdot \frac{\hbar g_{\mathrm{eff}}^{\uparrow\downarrow}}{8\pi\alpha_{\mathrm{eff}}^2} \cdot \frac{\mu_0 M_{\mathrm{s}} \gamma + \sqrt{(\mu_0 M_{\mathrm{s}} \gamma)^2 + 16(\pi f)^2}}{(\mu_0 M_{\mathrm{s}} \gamma)^2 + 16(\pi f)^2}. \tag{1}$$

Here, j_{s} is the induced spin current density, h_{ac} is the excitation field, μ_0 is the vacuum permeability, γ is the gyromagnetic ratio, $g_{\mathrm{eff}}^{\uparrow\downarrow}$ is the real part of the effective spin mixing conductance, α_{eff} is the effective Gilbert damping, and M_{s} is the saturation magnetization. According to Eq. (1) the voltage V_{ISHE} is a monotonically decreasing function in f. In this Report, we present our preliminary results of a spin pumping experiment in the range of $f = 1 - 45\,\mathrm{GHz}$. The detected V_{ISHE} signal turns out to be a more complex function of frequency and exhibits a pronounced maximum at around $f \approx 11\,\mathrm{GHz}$.

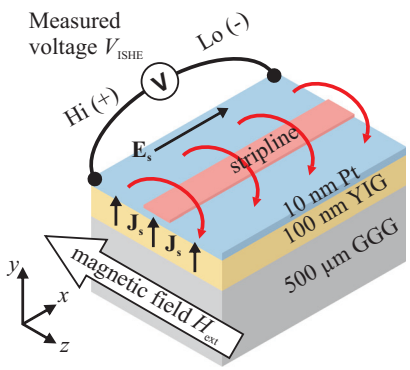

Fig. 1: Used measurement geometry and sample structure. The YIG film is magnetized in-plane by H_{ext} and its magnetization precession is excited by the stripline. In order to measure the FMR peaks of V_{ISHE}, the microwave frequency is fixed and H_{ext} is swept. $\mathbf{J}_{\mathrm{s}}$ denotes the spin current generated by spin pumping, and $\mathbf{E}_{\mathrm{s}}$ is the induced electrostatic field due to the ISHE. The stripline and the Pt film are separated electrically by an insulating layer (not shown).

The investigated sample consists of a YIG|Pt bilayer with dimensions 2 mm×4 mm. The 100 nm thick YIG film was grown by liquid phase epitaxy on gadolinium gallium garnet (GGG) [14] and the 10 nm thick Pt film was subsequently sputtered on top of the YIG film. The measurement geometry is illustrated in Fig. 1. An external magnetic field H_{ext} magnetizes the YIG film in-plane and the magnetization precession is excited by means of a stripline. The spin current $\mathbf{J}_{\mathrm{s}}$ generated by spin pumping is transformed into a charge current via the ISHE in the Pt film, leading to the voltage V_{SIHE} as

$$V_{\mathrm{ISHE}} = -\mathbf{l}\cdot\mathbf{E}_{\mathbf{s}} \propto -\mathbf{l}\cdot\frac{\rho}{A}\theta_{\mathrm{SH}}(\mathbf{J}_{\mathbf{s}}\times\hat{\mathbf{m}}) \quad . \tag{2}$$

Here, $\mathbf{l}$ is the length vector from contact "Lo (-)" to contact "Hi (+)" in Fig. 1. The parameters ρ, A, θ_{SH} and $\hat{\mathbf{m}}$ denote the resistivity of the Pt film, the YIG|Pt interface area, the spin Hall angle and the spin-polarization unit vector, respectively. The signs of H_{ext}, $\mathbf{J}_{\mathbf{s}}$, $\mathbf{E}_{\mathbf{s}}$ and V_{ISHE} correspond to the conventions in Report 4.9 and [15].

Ferromagnetic resonance (FMR) peaks of the V_{ISHE} signal are measured by sweeping the external field for each fixed microwave frequency. In our setup field values of more than $\mu_0 H_{\mathrm{ext}} = 1.5\,\mathrm{T}$ can be realized. Figure 2 presents typical V_{ISHE} data for four selected excitation frequencies $f =$ 5 GHz, 11 GHz, 23 GHz and 45 GHz. The sensitivity of the V_{ISHE} measurements is enhanced by a lock-in technique. For this purpose, the applied microwave signal is amplitude modulated by $f_{\mathrm{mod}} = 500\,\mathrm{Hz}$. In our experiment, a microwave signal of a power peak level $P \approx 3\,\mathrm{mW}$ was used, generated by an Agilent E8257D signal source.

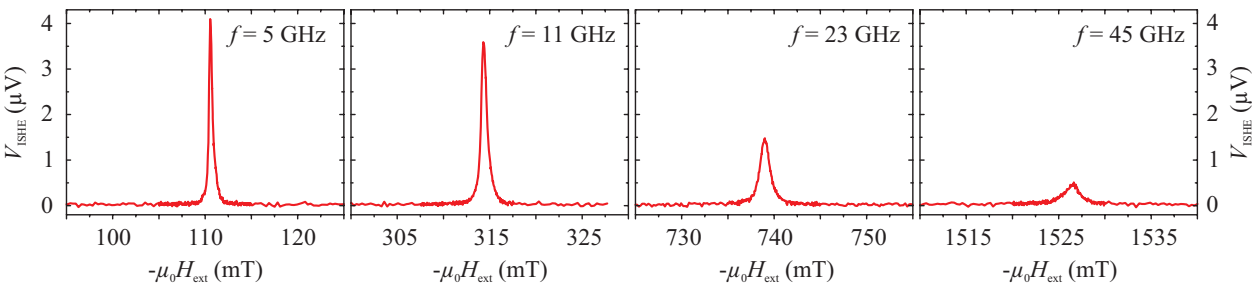

Fig. 2: V_{ISHE} data for the excitation frequencies $f = 5\,\mathrm{GHz}$, 11 GHz, 23 GHz and 45 GHz. For each frequency a Lorentzian shaped peak arises when the FMR condition is met. The field direction is negative ($-y$-direction).

Each of the V_{ISHE} signals (see Fig. 2) exhibits one pronounced peak at a corresponding resonant field. From Lorentzian fits to the V_{ISHE} data one can extract the resonant field values $H_{\mathrm{ext,FMR}}$, the linewidths ΔH_{ext} (full width at half maximum) and the signal maxima $V_{\mathrm{ISHE}}^{\mathrm{max}}$.

The $H_{\mathrm{ext,FMR}}$ values are shown in Fig. 3a, and a fit to the Kittel equation [16] (solid line in Fig. 3a)

$$f = \frac{\mu_0\gamma}{2\pi}\sqrt{H_{\mathrm{ext,FMR}}(H_{\mathrm{ext,FMR}} + M_{\mathrm{s}})} \quad , \tag{3}$$

yields the saturation magnetization $M_{\mathrm{s}} = (138 \pm 1)\,\mathrm{kA/m}$, which is in agreement with values reported for thin YIG films [17].

The ΔH values are shown in Fig. 3b. According to [13, 18] ΔH relates to the effective Gilbert damping α_{eff} as

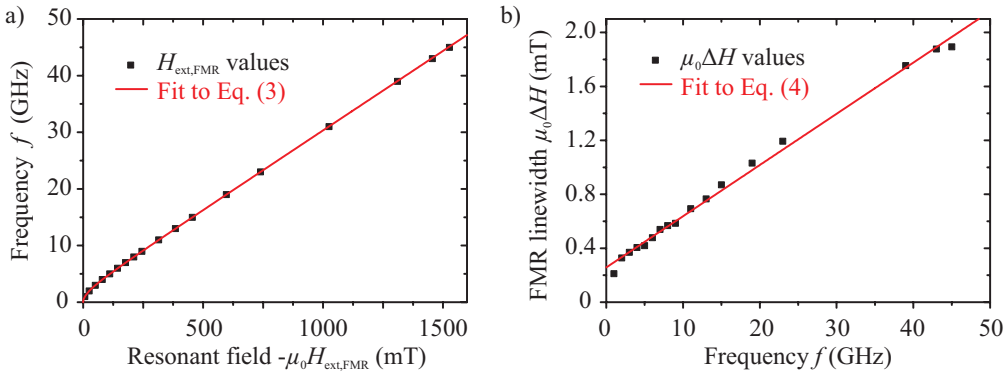

Fig. 3: Extracted values from Lorentzian fits to V_{ISHE} data. a) Squares denote the resonant field values $H_{\mathrm{ext,FMR}}$, the solid line is a fit to Eq. (3). b) Squares denote the linewidth values ΔH, the solid line is a fit to Eq. (4).

$$\mu_0 \Delta H = 4\pi f \alpha_{\mathrm{eff}}/\gamma + \mu_0 \Delta H(0) \quad . \tag{4}$$

By fitting Eq. (4) to our data (solid line in Fig. 3b) the effective Gilbert damping value of $\alpha_{\mathrm{eff}} = (5.3 \pm 0.1) \times 10^{-4}$ and a zero frequency offset $\Delta H(0) = (0.26 \pm 0.01)\,\mathrm{mT}$, caused by long-range magnetic inhomogeneities, are obtained. By using the relation $\alpha_{\mathrm{eff}} = \alpha_0 + \frac{g\mu_{\mathrm{B}}}{4\pi M_{\mathrm{s}} d_{\mathrm{YIG}}} g_{\mathrm{eff}}^{\uparrow\downarrow}$ [13], the effective spin mixing conductance $g_{\mathrm{eff}}^{\uparrow\downarrow} = (3.74 \pm 0.21) \times 10^{18}\,\mathrm{m}^{-2}$ is calculated. For this has been used the g-factor g, the Bohr magneton μ_{B}, the YIG film thickness $d_{\mathrm{YIG}} = 100\,\mathrm{nm}$ and the original Gilbert damping $\alpha_0 = (1.3 \pm 0.1) \times 10^{-4}$, which was obtained by standard FMR measurements on a bare YIG film of the same wafer, using a vector network analyzer.

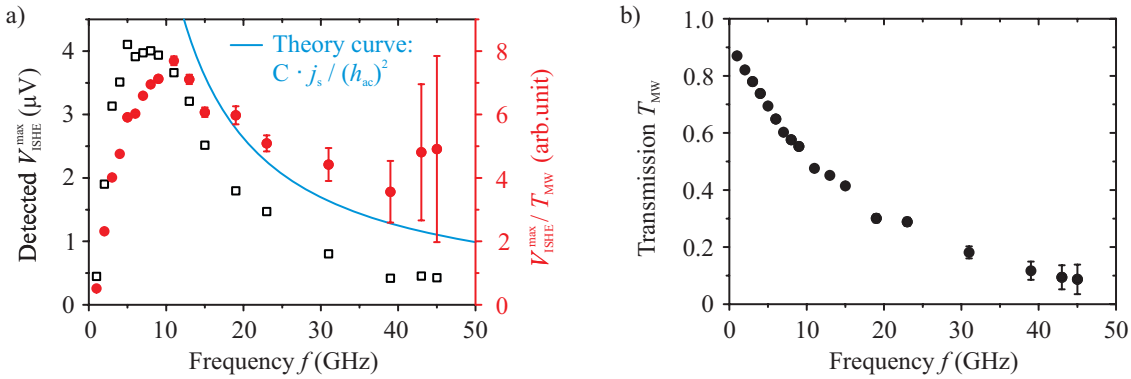

Fig. 4: a) The empty squares present the original $V_{\mathrm{ISHE}}^{\mathrm{max}}$ values (left scale). The filled circles present recalculated $V_{\mathrm{ISHE}}^{\mathrm{max}}/T_{\mathrm{MW}}$ values (right scale), taking into account the frequency dependent excitation field h_{ac}. The solid line is a theory curve to $C \cdot j_{\mathrm{s}}/h_{\mathrm{ac}}^2$, using C as a frequency independent scaling factor. b) Microwave transmission T_{MW} of cables and stripline. It is assumed $T_{\mathrm{MW}} \propto h_{\mathrm{ac}}^2$.

Finally, the frequency dependency of the voltage maxima $V_{\mathrm{ISHE}}^{\mathrm{max}}$ is demonstrated by the empty squares in Fig. 4a. It increases with f for frequencies below 5 GHz and decreases for frequencies higher than 9 GHz. Since Eq. (1) is a monotonically decreasing function of f, it cannot explain the increase of $V_{\mathrm{ISHE}}^{\mathrm{max}}$ for frequencies $f < 9\,\mathrm{GHz}$. Still, it could describe the trend for higher frequencies. In order to fit Eq. (1) to our data, the frequency dependence of the excitation field h_{ac} needs to be taken into account. We assume $(h_{\mathrm{ac}})^2$ to be proportional to the microwave transmission T_{MW} of the used cables and the stripline (Fig. 4b), and thus calculate $V_{\mathrm{ISHE}}^{\mathrm{max}}/T_{\mathrm{MW}} \propto j_{\mathrm{s}}/h_{\mathrm{ac}}^2$ (filled circles in Fig. 4a). This recalculated values show a pronounced maximum at around $f = 11\,\mathrm{GHz}$. The solid

line in Fig. 4a is a theory curve to $C \cdot j_s/h_{ac}^2$, using a frequency independent scaling factor C as the only unknown parameter. The values for $g_{eff}^{\uparrow\downarrow}$, α_{eff} and M_s are taken from our previous calculations.

The theory curve in Fig. 4a related to Eq. (1) basically reproduces the trend of the recalculated values V_{ISHE}/T_{MW} in the frequency range $f = 11 - 39\,\text{GHz}$. The reason for the deviation in the range $f < 11\,\text{GHz}$ may be a frequency dependent excitation efficiency due to the precession ellipticity [11], that is not taken into account here. Furthermore, the possible change of pinning conditions with the external field is not included in the used model. It also should be noted that the accuracy of V_{ISHE}/T_{MW} decreases with f (error bars in Fig. 4a) due to the estimated T_{MW} values in Fig. 4b.

In summary, an unexpected maximum of the V_{ISHE} signal was observed at around $f \approx 11\,\text{GHz}$. Further investigations are required in order to clarify this behavior, which might be associated with magnetization dynamics or with field-dependent pinning conditions. The analysis of the frequency dependence of V_{ISHE} is of great importance for a deeper understanding of the spin-pumping phenomena as well as for applications that aim for high values of spin-pumping induced ISHE voltages.

Financial support by the Deutsche Forschungsgemeinschaft (CH 1037/1-1) is gratefully acknowledged.

References

[1] Y. Tserkovnyak, A. Brataas, G.E.W. Bauer, *Enhanced Gilbert damping in thin ferromagnetic films*, Phys. Rev. Lett. **88**, 117601 (2002).

[2] J.E. Hirsch, *Spin Hall effect*, Phys. Rev. Lett. **83**, 1834 (1999).

[3] E. Saitoh, M. Ueda, H. Miyajima, G. Tatara, *Conversion of spin current into charge current at room temperature: Inverse spin-Hall effect*, Appl. Phys. Lett. **88**, 182509 (2006).

[4] K. Ando, Y. Kajiwara, S. Takahashi, S. Maekawa, K. Takemoto, M. Takatsu, E. Saitoh, *Angular dependence of inverse spin-Hall effect induced by spin pumping investigated in a $Ni_{81}Fe_{19}/Pt$ thin film*, Phys. Rev. B **78**, 014413 (2008).

[5] Y. Kajiwara, K. Harii, S. Takahashi, J. Ohe, K. Uchida, M. Mizuguchi, H. Umezawa, H. Kawai, K. Ando, K. Takanashi, S. Maekawa, E. Saitoh, *Transmission of electrical signals by spin-wave interconversion in a magnetic insulator*, Nature **464**, 262-266 (2010).

[6] C.W. Sandweg, Y. Kajiwara, K. Ando, E. Saitoh, B. Hillebrands, *Enhancement of the spin pumping efficiency by spin wave mode selection*, Appl. Phys. Lett. **97**, 252504 (2010).

[7] A.V. Chumak, A.A. Serga, M.B. Jungfleisch, R. Neb, D.A. Bozhko, V.S. Tiberkevich, B. Hillebrands, *Direct detection of magnon spin transport by the inverse spin Hall effect*, Appl. Phys. Lett. **100**, 082405 (2012).

[8] M.B. Jungfleisch, V. Lauer, R. Neb, A.V. Chumak, B. Hillebrands, *Improvement of the yttrium iron garnet/platinum interface for spin pumping-based applications*, Appl. Phys. Lett. **103**, 022411 (2013).

[9] H. Kurebayashi, O. Dzyapko, V.E. Demidov, D. Fang, A.J. Ferguson, S.O. Demokritov, *Controlled enhancement of spin-current emission by three-magnon splitting*, Nature Materials **10** 660-664, (2011).

[10] V. Castel, N. Vlietstra, B.J. van Wees, J. Ben Youssef, *Frequency and power dependence of spin-current emission by spin pumping in a thin-film YIG/Pt system*, Phys. Rev. B **86**, 134419 (2012).

[11] K. Ando, T. Yoshino, E. Saitoh, *Optimum condition for spin-current generation from magnetization precession in thin film systems*, Appl. Phys. Lett. **94**, 152509 (2009).

[12] K. Ando, S. Takahashi, J. Ieda, Y. Kajiwara, H. Nakayama, T. Yoshino, K. Harii, Y. Fujikawa, M. Matsuo, S. Maekawa, E. Saitoh *Inverse spin-Hall effect induced by spin pumping in metallic system*, J. Appl. Phys. **109**, 103913 (2011).

[13] H. Nakayama, K. Ando, K. Harii, T. Yoshino, R. Takahashi, Y. Kajiwara, K. Uchida, Y. Fujikawa, *Geometry dependence on inverse spin Hall effect induced by spin pumping in* $Ni_{81}Fe_{19}/Pt$ *films*, Phys. Rev. B **85**, 144408 (2012).

[14] P. Pirro, T. Brächer, A.V. Chumak, B. Lägel, C. Dubs, O. Surzhenko, P. Görnert, B. Leven, B. Hillebrands, *Spin-wave excitation and propagation in microstructured waveguides of yttrium iron garnet/Pt bilayers*, Appl. Phys. Lett. **104**, 012402 (2014).

[15] M. Schreier, G.E.W. Bauer, V. Vasyuchka, J. Flipse, K. Uchida, J. Lotze, V. Lauer, A.V. Chumak, A.A. Serga, S. Daimon, T. Kikkawa, E. Saitoh, B.J. van Wees, B. Hillebrands, R. Gross, S.T.B. Goennenwein, *Sign of inverse spin Hall voltages generated by ferromagnetic resonance and temperature gradients in yttrium iron garnet\platinum bilayers*, arXiv:1404.3490 (2014).
[16] C. Kittel, *On the theory of ferromagnetic absorption*, Phys. Rev. **73**, 155 (1948).
[17] N. Kumar, D.S. Misra, N. Venkataramani, S. Prasad, R. Krishnan, *Magnetic properties of pulsed laser ablated YIG thin films on different substrates*, J. Magn. Magn. Mater. **272**, 899 (2004).
[18] C. Burrowes, B. Heinrich, B. Kardasz, E.A. Montoya, E. Girt, Y. Sun, Y.-Y. Song, M. Wu, *Enhanced spin pumping at yttrium iron garnet/Au interfaces*, Appl. Phys. Lett. **100**, 092403 (2012).

4.9 Sign of inverse spin Hall voltages generated by ferromagnetic resonance and temperature gradients in yttrium iron garnet | platinum bilayers

V. Lauer, V.I. Vasyuchka, A.V. Chumak, A.A. Serga, and B. Hillebrands

In collaboration with:
M. Schreier, J. Lotze, Walther-Meißner-Institut, Bayerische Akademie der Wissenschaften and Physik-Department, Technische Universität München, 85748 Garching, Germany;
G.E.W. Bauer, Institute for Materials Research and WPI Advanced Institute for Materials Research, Tohoku University, Sendai 980-8577, Japan, and Kavli Institute of NanoScience, Delft University of Technology, 2628 CJ Delft, The Netherlands;
J. Flipse, B.J. van Wees, Physics of Nanodevices, Zernike Institute for Advanced Materials, University of Groningen, 9747 AG Groningen, The Netherlands;
K. Uchida, Institute for Materials Reasearch, Tohoku University, Sendai 980-8577, Japan, and PRESTO, Japan Science and Technology Agency, Saitama 332-0012, Japan;
S. Daimon, T. Kikkawa, Institute for Materials Research, Tohoku University, Sendai 980-8577, Japan;
E. Saitoh, Institute for Materials Research and WPI Advanced Institute for Materials Research, Tohoku University, Sendai 980-8577, Japan, and Advanced Science Research Center, Japan Atomic Energy Agency, Tokai 319-1195, Japan, and CREST, Japan Science and Technology Agency, Tokyo 102-0076, Japan;
R. Gross, Walther-Meißner-Institut, Bayerische Akademie der Wissenschaften, 85748 Garching, Germany, and Nanosystems Initiative Munich, 80799 Munich, Germany, and Physik-Department, Technische Universität München, 85748 Garching, Germany;
S.T.B. Goennenwein, Walther-Meißner-Institut, Bayerische Akademie der Wissenschaften, 85748 Garching, Germany, and Nanosystems Initiative Munich, 80799 Munich, Germany.

This Report addresses the (inverse) spin Hall effect and related phenomena [1–5]. In studies of these effects often only the sign differences between related quantities like magnetic fields and generated spin and charge currents are determined. Our group jointly with four partner groups addressed the issue of the absolute sign of the inverse spin Hall effect voltage generated by spin currents injected into a normal metal: (1) the Institute for Materials Research, Tohoku University, (2) the Zernike Institute for Advanced Materials, the University of Groningen, (3) the Walther-Meißner-Institut in Garching, and (4) the Technische Universität Kaiserslautern. The results of all works are presented in a joint manuscript [6]. The focus lies on bilayers of the ferrimagnetic insulator $Y_3Fe_5O_{12}$ (yttrium iron garnet, YIG) and platinum at room temperature. Spin currents $\mathbf{J_s}$ are generated by microwave radiation and temperature gradients and transformed via the inverse spin Hall effect (ISHE) into charge currents [2], that can be measured electrically. Measurement data of all institutes are compared and found to be consistent. The observations agree with the standard theories for spin Seebeck effect (SSE) [7, 9] and spin pumping driven by ferromagnetic resonance (FMR) [8]. By carefully accounting for all experimental parameters and definitions, it is possible to determine the absolute and relative signs of generated spin and charge currents.

In this Report exclusively the experiment performed at Technische Universität Kaiserslautern is presented. It gives detailed information regarding the sample, the measurement technique and shows the experimental results, which are not entirely included in [6] due to space limits. The absolute signs of all parameters and definitions used here are in accordance with [6].

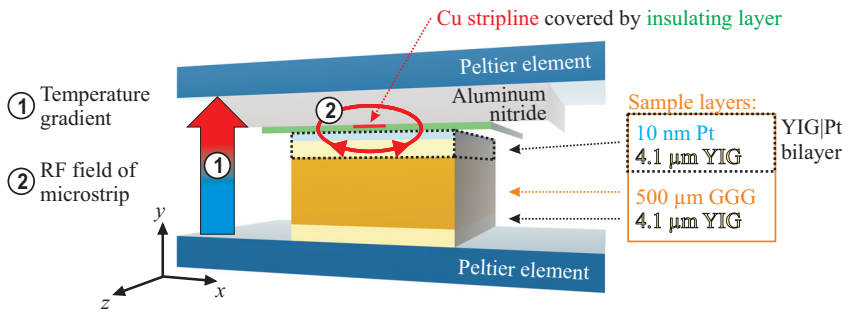

Fig. 1: The layer stack of the experimental setup is shown. In the first part of the experiment, Peltier elements are used to apply a thermal gradient perpendicular to the YIG|Pt interface. In the second part, the magnetization of the YIG film is resonantly excited by a microwave field originating from the Cu stripline.

The investigated sample has lateral sizes of 3 mm×4 mm. It consists of a 500 µm thick $Gd_3Ga_5O_{12}$ (GGG) substrate, both sided covered by 4.1 µm thick YIG films by means of liquid phase epitaxy. Subsequently, on one side of the sample a 10 nm Pt film is grown by molecular beam epitaxy, creating a YIG|Pt bilayer. For our further discussion only this bilayer is of interest. The layer stack order of the sample is depicted in Fig. 1.

During the measurements, the YIG|Pt bilayer is located close to a 600 µm wide Cu stripline, which is structured on an aluminum nitride substrate. By applying a microwave signal to the stripline, one can resonantly excite magnetization precession of the YIG film. Furthermore, a Peltier element is placed under the substrate and a second one on top of the sample, in order to generate a thermal gradient perpendicular to the YIG|Pt interface. An insulating layer prevents shortcuts between Pt and the Cu stripline, and the aluminum nitride substrate eliminates in-plane thermal gradients due to its high thermal conductivity. The sketch in Fig. 1 illustrates the setup geometry. During the measurements, this sandwich-like structure is placed inside of a brass box, and an external magnetic field H_{ext} is applied in $\pm z$-direction.

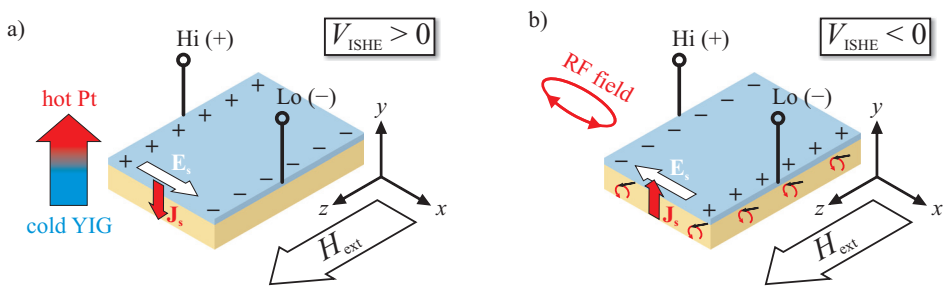

Fig. 2: Sketch of the YIG|Pt bilayer. a) A thermal gradient is applied in $+y$-direction (Pt hotter than YIG) and H_{ext} is oriented in $+z$-direction. The arising spin current $\mathbf{J}_s$ from Pt to YIG due to SSE is opposite to the thermal gradient, and the electrostatic field $\mathbf{E}_s$ is generated by the ISHE. b) The magnetization precession of the YIG film is excited at FMR by the RF field of the stripline. $\mathbf{J}_s$ is injected from YIG into Pt due to spin pumping and $\mathbf{E}_s$ generated due to the ISHE.

Generally, the accomplishment of the experiment can be divided into two parts, both realized in the described setup. In the first part, a thermal gradient is applied in $\pm y$-direction, using the two Peltier elements. A spin current $\mathbf{J_s}$ occurs antiparallel to the thermal gradient due to the SSE [7]. The case of thermal gradient in $+y$-direction is illustrated in Fig. 2a. Consequently, $\mathbf{J_s}$ is transformed via the ISHE into a charge current, leading to charge accumulation and an electrostatic field $\mathbf{E_s}$ in x-direction under open circuit conditions:

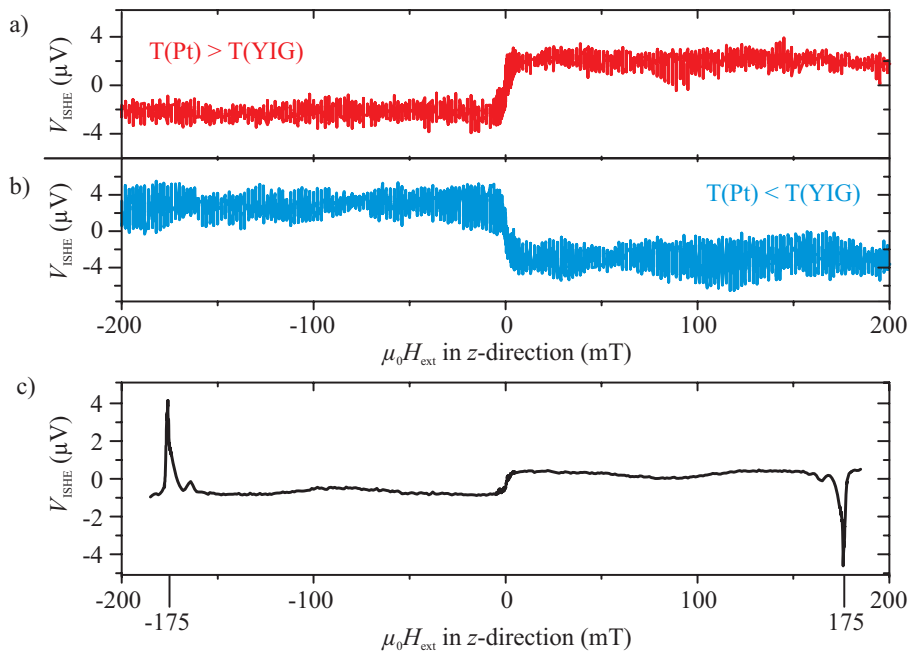

Fig. 3: a) SSE induced ISHE voltage V_{ISHE} measured as function of the external magnetic field H_{ext}, when the thermal gradient is applied in $+y$-direction (Pt hotter than YIG). b) V_{ISHE} measured for a reversed thermal gradient (Pt colder than YIG). c) V_{ISHE} signal in presence of a RF field, leading to spin pumping induced signal peaks at resonant field values $\mu_0 H_{ext} \cong \pm 175\,\mathrm{mT}$.

$$\mathbf{E_s} = \frac{-e\rho}{A}\theta_{SH}(\mathbf{J_s} \times \hat{\mathbf{m}}) \tag{1}$$

Here, $-e$, ρ, A and θ_{SH} ($\theta_{SH} > 0$ for Pt) denote the electron charge, the resistivity of the Pt film, the YIG|Pt interface area and the spin Hall angle respectively. The unit vector $\hat{\mathbf{m}}$ of the equilibrium magnetization is determined by the external field. The corresponding ISHE voltage $V_{ISHE} = -\mathbf{E_s} \cdot \mathbf{l}$ is measured via gold wire contacts at the edges of the sample, using a simple voltmeter. $\mathbf{l}$ is the length vector from contact "Lo (-)" to contact "Hi (+)" (see Fig. 2a), it has a length of 3 mm in our case. Figure 3a presents the V_{ISHE} signal as a function of the external magnetic field, when a thermal gradient is applied in $+y$-direction (Pt hotter than YIG). The V_{ISHE} signal measured for positive H_{ext} values corresponds to the situation depicted in Fig. 2a. Applying an opposite thermal gradient (Pt colder than YIG) leads to the V_{ISHE} signal shown in Fig. 3b.

In the second part of the experiment, an Agilent Signal Generator E8257D is used to apply a microwave signal of a fixed frequency of $f = 7\,\mathrm{GHz}$ and a power of $P \cong 50\,\mathrm{mW}$ to the Cu stripline. When the FMR condition is fulfilled, the magnetization precession of the YIG film is excited by the RF field of the stripline and a spin current $\mathbf{J_s}$ is injected from YIG into Pt by spin pumping [8]. This case is illustrated in Fig. 2b. The detected V_{ISHE} signal as a function of the external field exhibits two opposite resonance peaks at the field values $\mu_0 H_{ext} \cong \pm 175\,\mathrm{mT}$ (see Fig. 3c). The negative voltage peak at $\mu_0 H_{ext} \cong +175\,\mathrm{mT}$ corresponds to the situation of Fig. 2b. It should be mentioned that the applied microwave signal is amplitude modulated by $f_{mod} = 500\,\mathrm{Hz}$. Therefore, also the V_{ISHE} signal is modulated and can be detected by a lock-in technique. This is the reason for the high signal to noise ratio in Fig. 3c. In contrast, Peltier element based SSE measurements can hardly be combined with a lock-in technique.

If one compares Fig. 3a and Fig. 3c at non-resonant field values, it becomes apparent that the V_{ISHE} signals show the same trend. From this we can conclude that the RF field heats up the Pt film to a higher temperature than the YIG film, adding a SSE contribution to the detected signal in Fig. 3c. The injected spin currents by the SSE and by spin pumping at FMR are obviously oppositely oriented.

In summary, in frame of our joint research the absolute and relative signs of spin currents generated

by SSE and spin pumping, as well as the correspondingly measured ISHE voltages are determined. Our results are in agreement with results obtained by the other groups under various experimental conditions and on various YIG|Pt bilayers. The relative signs of SSE and spin pumping are consistent with theoretical predictions.

The presented experiment was financially supported by the DFG via project SE 1771/4-1 (SPP 1538 "Spin Caloric Transport") and project CH 1037/1-1.

References

[1] M.I. D'yakonov, V.I. Perel', *Possibility of orienting electron spins with current*, JEPT Lett. **13**, 457 (1971).
[2] J.E. Hirsch, *Spin Hall effect*, Phys. Rev. Lett. **83**, 1834 (1999).
[3] S. Zhang, *Spin Hall effect in the presence of spin diffusion*, Phys. Rev. Lett. **85**, 393 (2000).
[4] E. Saitoh, M. Ueda, H. Miyajima, G. Tatara, *Conversion of spin current into charge current at room temperature: Inverse spin-Hall effect*, Appl. Phys. Lett. **88**, 182509 (2006).
[5] A. Hoffmann, *Spin Hall effects in metals*, IEEE Trans. Magn. **49**, 5172 (2013).
[6] M. Schreier, G.E.W. Bauer, V. Vasyuchka, J. Flipse, K. Uchida, J. Lotze, V. Lauer, A.V. Chumak, A.A. Serga, S. Daimon, T. Kikkawa, E. Saitoh, B.J. van Wees, B. Hillebrands, R. Gross, S.T.B. Goennenwein, *Sign of inverse spin Hall voltages generated by ferromagnetic resonance and temperature gradients in yttrium iron garnet|platinum bilayers*, arXiv:1404.3490 (2014).
[7] Y. Tserkovnyak, A. Brataas, G.E.W. Bauer, *Enhanced Gilbert damping in thin ferromagnetic films*, Phys. Rev. Lett. **88**, 117601 (2002).
[8] J. Xiao, G.E.W. Bauer, K. Uchida, E. Saitoh, S. Maekawa, *Theory of magnon-driven spin Seebeck effect*, Phys. Rev. B **82**, 099904 (2010).
[9] H. Adachi, J. Ohe, S. Takahashi, S. Maekawa, *Linear-response theory of spin Seebeck effect in ferromagnetic insulators*, Phys. Rev. B **83**, 094410 (2011).

4.10 Platinum thickness dependence on the spin pumping in Fe | Pt bilayers

S. Keller, L. Mihalceanu, A. Conca, V. Lauer, B. Hillebrands, and E.Th. Papaioannou

In collaboration with Jörg Lösch, Institut für Oberflächen- und Schichtanalytik (IFOS) and Landesforschungszentrum OPTIMAS, Trippstadter Str. 120, 67663 Kaiserslautern, Germany

The spin pumping effect allows for the injection of a spin current from a ferromagnetic (FM) layer into an attached non-magnetic metal (NM) layer [1]. This spin current is subsequently transformed into a charge current by the inverse spin Hall effect (ISHE). Although many aspects of magnetization dynamics in FM | NM bilayers have been investigated by means of spin pumping and the inverse spin Hall effect (ISHE) in different materials [2,3], no systematic work on epitaxial samples has been performed. Epitaxial films have the advantage of high quality interfaces and they offer additionally the possibility to study spin current effects in different crystallographic directions.

In this work, we study the spin pumping effect in epitaxially grown Fe | Pt interfaces. We address the influence of the Pt thickness on the spin pumping efficiency, and therefore, on the ISHE signal strength.

In a previous work [4] we have shown that by modifying the structural and interfacial quality of Fe | Pt bilayers we managed to optimize the spin pumping efficiency. Here, we choose the growth temperature (300 °C) for which the best spin pumping efficiency is achieved, we keep the magnetic layer thickness constant and we alter the thickness of the Pt layer.

Fe (12 nm) | Pt (2, 4 and 10 nm) bilayers were grown on MgO (100) substrates at 300 °C substrate temperature by electron-beam evaporation in an ultrahigh vacuum (UHV) chamber with a base pressure of below 1.0×10^{-11} mbar. A Fe (12 nm) | Al (2.5 nm) reference film was also fabricated at the same experimental conditions as the Fe | Pt samples. The Al layer was deposited as a capping layer in order to form naturally an Al_2O_3 oxide protective layer.

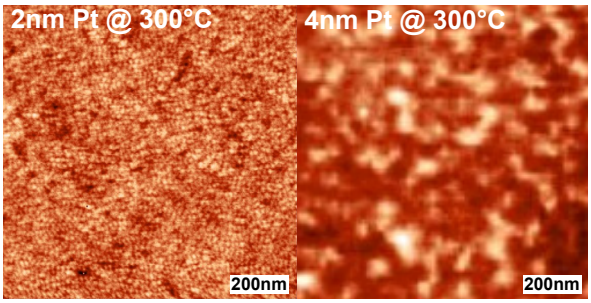

Fig. 1: AFM images of Pt surfaces on top of Fe surface grown on MgO substrate at 300 °C. Left: the sample with 2 nm Pt. Right: 4 nm Pt. The 4 nm sample exhibits a higher R_{rms} value.

In Fig. 1 we present AFM images for two samples grown at 300 °C having different Pt thicknesses: 2 nm and 4 nm. The growth of 2 nm Pt results in smaller values of roughness $R_{rms}^{2nm} = 0.174$ nm, while $R_{rms}^{4nm} = 0.287$ nm. The sample with 10 nm obtains an intermediate value $R_{rms}^{10nm} = 0.235$ nm.

In Fig. 2, X-ray diffraction pattern (XRD) figures for the three Fe | Pt samples are presented. The XRD patterns together with pole figures (not shown here) confirm for all samples the 45° in plane epitaxial relation (Fe[100] || MgO[110], Fe[110] || MgO[010]) between the substrate and Fe for all samples. Well defined Pt (200) diffraction peaks are observed for the sample with 10 and 4 nm Pt while no Pt peak is observed for the Pt 2 nm thickness due to the very small thickness. The

epitaxial growth of the fcc Pt layer on bcc Fe along the [100] plane direction can be correlated to the Bain epitaxial orientation [5] in which the Pt cell is 45° rotated with respect to the Fe lattice.

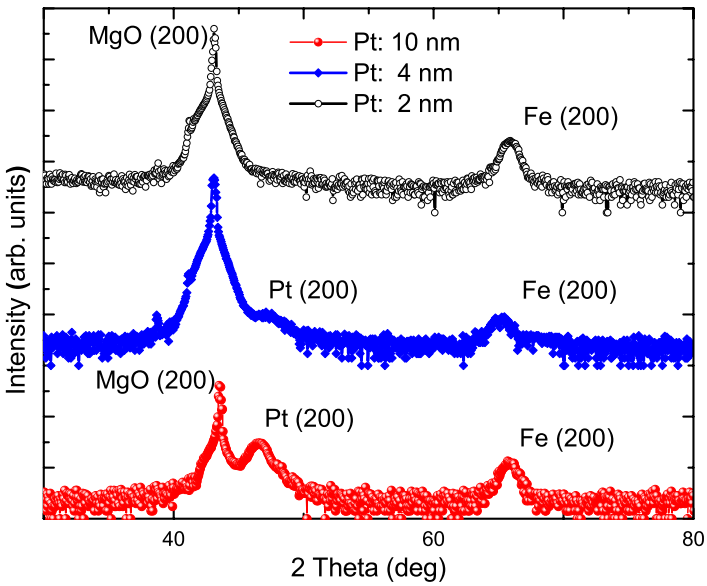

Fig. 2: XRD graphs for three Fe/Pt samples grown at 300 °C: (top) Pt = 2 nm, (middle) Pt= 4 nm, and bottom Pt= 10 nm. Diffraction peaks of Pt (220) on Fe are observed for Pt= 4 nm and 10 nm. The curves have been vertically shifted for clarity.

In the following we discuss the spin pumping measurements in the epitaxial Fe | Pt bilayers with different Pt thicknesses. The magnetization dynamics are excited by a microwave magnetic field generated by a 600 µm Cu microstrip antenna, while an external magnetic field is swept. We measure the spin pumping induced ISHE-voltage [4,6] that appears across the edges of the Pt layer perpendicular to the external magnetic field. In Fig. 3a the measured voltage (V_{meas}) as a function of the external magnetic field applied in the [110] direction is presented, measured at 7.0 GHz. With the field reversal a sign reversal in V_{meas} signal is observed at the same absolute field values. The field values where the V_{meas} peaks are measured correspond with the FMR resonance positions at the measured frequency. The reason for the presence of two FMR peaks is the splitting of the dispersion curve of the FMR in two branches due to the pronounced cubic and uniaxial anisotropy terms along the hard axis [4].

In Fig. 3b the magnitude of V_{meas} with respect to the Pt thickness is presented. V_{meas} is increasing with decreasing Pt thickness in accordance with previous results [7,8]. The maximum of V_{meas} due to spin pumping is expected to occur for Pt thickness $\approx \lambda_{SD}$, where λ_{SD} is the spin diffusion length in Pt.

As it has been previously discussed [9], V_{meas} is the sum of three contributions: the spin pumping effect at the FMR frequency, the anisotropic magnetoresistance (AMR) effect at microwave fields, and the anomalous Hall effect (AHE). We have evaluated the data based on the different contributions of symmetric and antisymmetric components on V_{meas} [4]. The ISHE voltage (V_{ISHE}) at the FMR frequency obeys a Lorentz shape curve that can be decomposed into a symmetric and an antisymmetric part. The physical origin of the symmetric part is the ISHE itself together with contributions from AMR and AHE, while the antisymmetric part has only contributions from AMR and AHE.

In order to separate the symmetric ISHE contribution from the overlapping symmetric AMR and AHE signals, reference Fe/Al_2O_3 samples were fabricated. By measuring these reference samples, where no V_{ISHE} is present, we could calculate the symmetric and antisymmetric contributions of

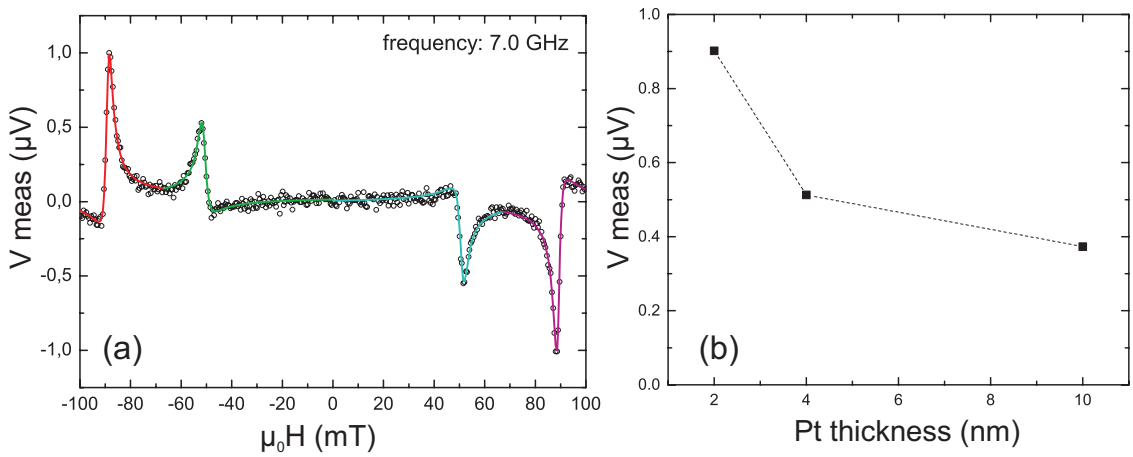

Fig. 3: (a) Measured voltage at 7.0 GHz along the [110] direction (hard axis) for the sample with 2 nm Pt thickness. The overlapping lines are fittings with symmetric and antisymmetric functions. (b) thickness dependence of the measured voltage.

the reference samples. Assuming that these contributions are the same in the Fe | Pt samples (grown at the same time under the same experimental conditions) we could extract the symmetric part (V_{ISHE}) by fitting the curve in Fig. 3a with symmetric and antisymmetric functions [4].

The ISHE current (I_{ISHE}), is then calculated from $I_{ISHE} = V_{ISHE}/R$. Furthermore, V_{ISHE} depends also on the absorbed microwave power at FMR frequency. To be able to compare the capability of different Pt thicknesses to convert an amount of absorbed energy via spin pumping into a DC current, we define the inverse spin Hall efficiency as: $\varepsilon = I_{ISHE}/P_{Abs}$, where P_{Abs} is the measured absorbed microwave power via the FMR mechanism. Fig. 4 shows that the efficiency significantly rises by decreasing the Pt thickness.

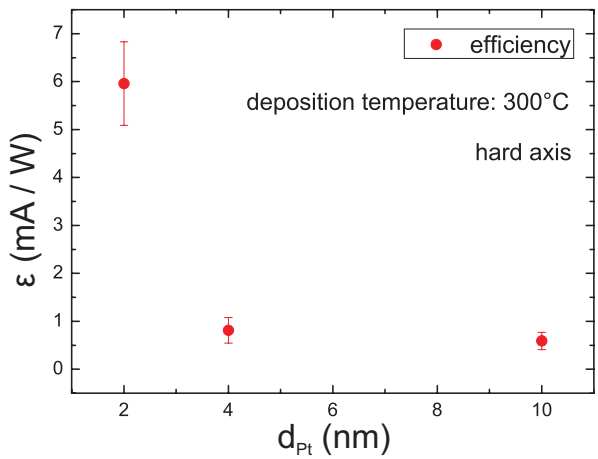

Fig. 4: ISHE efficiency with respect to the thickness of the Pt layer. The data were taken for an applied microwave power of 250 mW and refer to the V_{ISHE} peak that corresponds to the saturated state along the hard direction.

To elucidate further our results we performed FMR measurements in order to measure the effective Gilbert damping parameter α of the samples. The damping was calculated from the slope of the field resonance line width versus frequency. α can be considered as a sum of two terms: the contribution of the pure magnetic film α_{film} and a term due to the additional damping due to the spin pumping α_{SP}. Although the thickness of the magnetic layer is constant, α is decreasing with the Pt thickness from $\alpha = (8.4 \pm 1) \times 10^{-3}$ for the 10 nm to $\alpha = (6.0 \pm 0.7) \times 10^{-3}$ for 4 nm and to $(3.9 \pm 0.1) \times 10^{-3}$ for the 2 nm Pt. This behaviour can be understood if we consider the magnetic

proximity effects at the Fe | Pt interface. It is known that Fe induces a finite magnetic polarisation in Pt with its magnetic moment aligned parallel to the Fe moment [10]. The induced Pt moment is basically located close to the Fe | Pt interface and decreases rapidly for the inner Pt layers. On the other side, the FMR technique measures an effective Gilbert damping of the entire sample. As mentioned, due to the hybridization effects at the interface, Pt acquires a magnetic moment. This would increase the effective FM layer thickness and decrease the Gilbert damping. On the other side, the increase of ε in Fig. 4 reveals that the contribution of the spin pumping to the damping α_{SP} is enhanced.

In summary, we presented the thickness dependence of the spin pumping driven ISHE voltage in Fe | Pt bilayers. By choosing the growth temperature we have achieved epitaxy of Pt on Fe. To interpret our data correctly we have accounted for effects that are superimposed on the spin pumping signal. The presence of polarised Pt leads to a decrease of α with the Pt thickness. However, this decrease is not associated with a decrease on the spin pumping efficiency. On the contrary the presence of 2 nm Pt overlayer leads to a significant increase of the ISHE current and the ISHE efficiency. We show that in spite of Pt polarisation effects thinner Pt layers are preferable as spin current detectors.

Financial support by Carl Zeiss Stiftung is gratefully acknowledged.

References

[1] Y. Tserkovnyak, A. Brataas, G.E.W. Bauer, *Spin pumping and magnetization dynamics in metallic multilayers*, Phys. Rev. B **66**, 224403 (2002).

[2] A. Hoffmann, *Spin Hall effects in metals*, IEEE Transactions on Magnetics **49**, 5172 (2013).

[3] D. Czeschka, L. Dreher, M.S. Brandt, M. Weiler, M. Althammer, I.M. Imort, G. Reiss, A. Thomas, W. Schoch, W. Limmer, H. Huebl, R. Gross, S.T.B. Goennenwein, *Scaling behavior of the spin pumping effect in ferromagnet-platinum bilayers*, Phys. Rev. Lett. **107**, 046601 (2011).

[4] E.Th. Papaioannou, P. Fuhrmann, M.B. Jungfleisch, T. Brächer, P. Pirro, V. Lauer, J. Lösch, B. Hillebrands, *Optimizing the spin-pumping induced inverse spin Hall voltage by crystal growth in Fe/Pt bilayers*, Appl. Phys. Lett. **103**, 162401 (2013).

[5] B. Daniels, W. Nix, B. Clemens, *Enhanced mechanical hardness in compositionally modulated Fe(001)Pt(001) and Fe(001)Cr(001) epitaxial thin films*, Thin Solid Films **253**, 218(1994).

[6] M.B. Jungfleisch, V. Lauer, R. Neb, A.V. Chumak, B. Hillebrands, *Improvement of the yttrium iron garnet/platinum interface for spin pumping-based applications*, Appl. Phys. Lett. **103**, 022411 (2013).

[7] L.H. Vilela, G.L. da Silva, C. Salvador, S.M. Rezende, A. Azevedo, *Direct current voltage generated in metallic layers by spin pumping*, Appl. Phys. Lett. **109**, 07C910 (2011).

[8] H. Nakayama, K. Ando, K. Harii, T. Yoshino, R. Takahashi, Y. Kajiwara, K. Uchida, Y. Fujikawa, E. Saitoh, *Geometry dependence on inverse spin Hall effect induced by spin pumping in $Ni_{81}Fe_{19}$/Pt films*, Phys. Rev. B **85**, 144408 (2012).

[9] O. Mosendz, V. Vlaminck, J.E. Pearson, F.Y. Fradin, G.E.W. Bauer, S.D. Bader, A. Hoffmann, *Detection and quantification of inverse spin Hall effect from spin pumping in permalloy/normal metal bilayers*, Phys. Rev. B **82**, 214403 (2010).

[10] F. Wilhelm, P. Poulopoulos, G. Ceballos, H. Wende, K. Baberschke, P. Srivastava, D. Benea, H. Ebert, M. Angelakeris, N.K. Flevaris, D. Niarchos, A. Rogalev, N.B. Brookes, *Layer-resolved magnetic moments in Ni/Pt multilayers*, Phys. Rev. Lett. **85**, 413 (2000).

4.11 Magnon transistor: One magnon current controls another

A.V. Chumak, A.A. Serga, and B. Hillebrands

An attractive direction in next-generation information processing is the development of systems employing particles or quasi-particles other than electrons – ideally with low dissipation – as information carriers. One such candidate is the magnon: the quasi-particle associated with the eigen-excitations of magnetic materials known as spin waves. Magnonics, the field of science dealing with magnon-based data operations, encompasses a full spectrum of phenomena used in general wave-based signal processing [1]. The data can be coded into magnon phase or density and processed using wave effects such as interference. This approach has already been realised in spin-wave logic gates performing XNOR and NAND operations [2–4]. The main drawback of these gates is that the input data was coded in a form of DC electric pulses manipulating magnon phases, while the output signal was carried by the magnons themselves. Obviously, that made it impossible to combine two logic gates without additional magnon-to-voltage converters. Moreover, the processing of large amounts of data has to be made on the same magnetic chip exclusively within the magnonic system. This fact stimulated a search for a way to control one magnon by another magnon and for the development of the all-magnon device.

In this Report we present an insulator-based magnon transistor. The information is carried and processed in this three-terminal device using magnons and is fully decoupled from free electrons. The device demonstrated here has the potential to be scaled down to the sub-ten nanometer scale using exchange magnons. Regarding frequency, there is large potential for ultra-fast data processing since magnon frequencies can reach up into the THz range. The detailed analysis of the perspectives for a miniaturization, an increase in the operating frequency, and a decrease in the

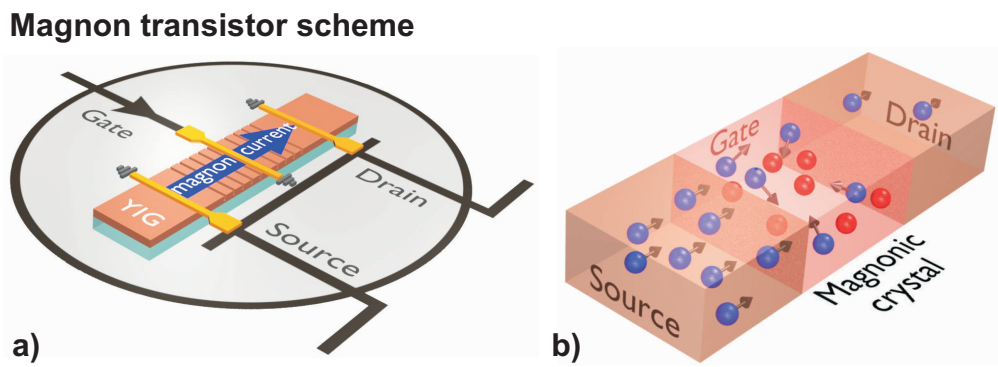

Fig. 1: (Color online) Schematic of the magnon transistor and the transistor's operational principle. a) The transistor is based on a magnonic crystal designed in the form of a yttrium iron garnet (YIG) film with an array of parallel grooves at its surface. The magnons are injected into the transistor's source and are detected at its drain using microstrip antennas. The magnons that control the source-to-drain magnon current, are injected directly into the magnonic crystal (transistor's gate) using an identical antenna. c) A magnon transistor allows for the suppression of the source-to-drain magnon current (shown by blue spheres) via the injection of the gate magnons (red spheres) into the gate region. A nonlinear four-magnon scattering mechanism is responsible for the transistor's operational principle. The high degree of gate magnon localization inside the crystal serves as an enhancer of the nonlinear effects.

This work has been recently published in Nature Communications [5].

energy consumption of the device are done in Ref. [5].

The magnon transistor is shown schematically in Fig. 1a. Its main element is an artificial magnetic material - a magnonic crystal [6–9] designed in the form of a yttrium iron garnet (YIG) strip with periodic modulation of its thickness [10]: In our demonstrator an array of 20 parallel grooves was etched into the surface of the strip. The flow of magnons propagating through the crystal is partially reflected from each groove and the influence of the grooves is negligible for most of the magnons. Nevertheless, the magnons which have wavelengths satisfying the Bragg condition $k_a = m\pi/a$ (where m is an integer and $a = 300\,\mu\text{m}$ is the crystal lattice constant) will be resonantly scattered back resulting in the generation of rejection bands (band gaps) in a spin-wave spectrum over which magnon propagation is fully prohibited. The measured magnonic-crystal transmission spectrum shows pronounced band gaps and is displayed in the inset of Fig. 2b.

The YIG magnonic crystal is magnetized along its long axis, and thus along the magnon propagation direction, by an applied biasing magnetic field $B = 177\,\text{mT}$. This provides the conditions for the excitation and propagation of backward volume magnetostatic waves [11]. In order to inject the magnons into and to collect them from the transistor, as well as to control them by the gate magnons, three identical microstrip antennas are placed at equal distances 4 mm apart - see Fig. 1a. The antenna that injects magnons into the transistor's gate is placed at the middle of the magnonic crystal area while the source and the drain antennas are placed outside in the non-structured YIG film areas. It has to be emphasized that all antennas are only used as an instrument for magnon injection and detection, and thus they are not part of the transistor. In forthcoming all-magnon circuits (see Fig. 3) the antennas will be absent and the magnons will be injected into or collected from another magnon data processing unit via magnon conduits.

The operational principle of the transistor is shown in Fig. 1b. The idea is as follows: Magnons are injected into the transistor's source (S-magnons shown in blue in the scheme in Fig. 1b) at a frequency corresponding to the magnon transmission band, i.e. $f_S = 7.025\,\text{GHz}$, see the inset in Fig. 2b. In the case of absence of magnons in the transistor's gate the S-magnons propagate towards the drain practically without distortion. Therefore, the density of the magnons at the drain (D-magnons) n_D is given by the density of the S-magnons n_S with additional consideration being given to magnetic losses due to weak magnon-phonon scattering. In order to manipulate the magnon current flowing from the transistor's source to the drain, magnons are injected into the gate region (G-magnons, shown in red in Fig. 1b). The frequency of the G-magnons $f_G = 7\,\text{GHz}$ is chosen to be in the center of the magnonic crystal band gap what prohibits the flow of the G-magnons out of the magnonic crystal area. This confinement allows for a large increase of the G-magnon concentration and, consequently, for an increase in the related efficiency of nonlinear phenomena. The spatial localization of the G-magnons in the central part of the gate was proved using the technique of Brillouin Light Scattering [5]. Further, the S-magnons injected into the source region, while propagating through the transistor's gate populated with G-magnons, are scattered and, therefore, are able to reach the transistor's drain only partially (Fig. 1b).

To demonstrate this principle experimentally we applied a pulsed microwave signal of 50 ns duration at time $t = 0$ to the source antenna. The injected S-magnon packets propagate a distance of 8 millimetres to the transistor's drain in approximately 300 ns inducing the output microwave signal at the drain antenna (this value corresponds well with the calculated propagation time of 286 ns). The applied rectangular input pulse as well as, the transmitted magnon signal, which is slightly distorted from the rectangular shape due to a dispersion spreading, are shown in Fig. 2a. The detected D-magnon density is maximal in the absence of gate magnons, i.e. $n_G = 0\,\text{mW}$, and its maximum density is denoted as n_{D0}. (Please note that for simplicity we measure the magnon den-

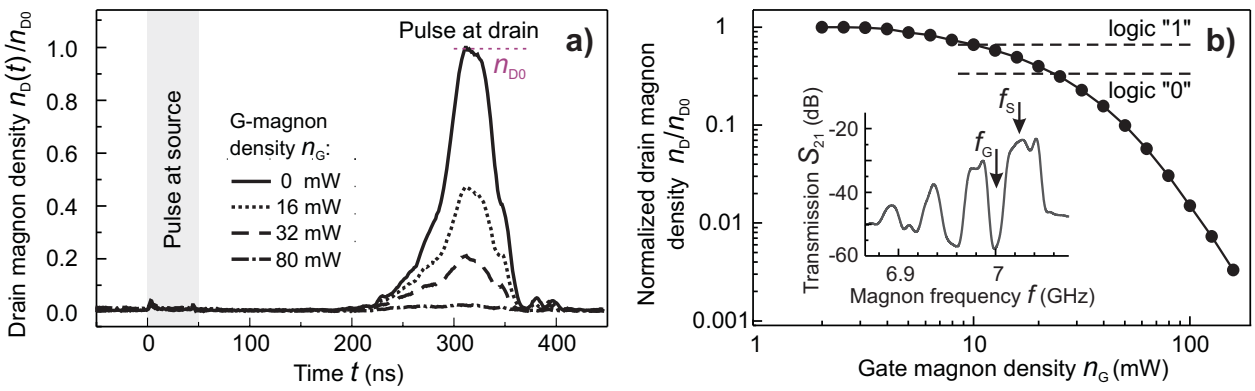

Fig. 2: Suppression of the source-to-drain magnon current by gate magnons. The inset in panel b) shows the magnon transmission characteristics through the magnonic crystal as a function of the magnon frequency. a) The time evolution of the signal at the transistor's drain carried by 50 ns-long magnon packets injected into the transistor's source at the time $t = 0$ ns. A magnon packet requires about 300 ns to travel the 8 mm distance to the drain. The injection of magnons into the gate region ($n_G > 0$) results in the suppression of the travelling magnon packet density while preserving the packet shape. b) To show the degree of the suppression, the drain magnon density n_D normalized to the original value n_{D0} is presented as a function of the gate magnon density n_G. A suppression of about three orders of magnitude is achieved. The horizontal dashed lines splits the density n_D to the signals corresponding to a logic "1" and to a logic "0".

sities in Watts corresponding directly to the power of the microwave signals applied to or measured at the antennas.) The application of a continuous-wave signal to the gate antenna and the injection of the G-magnons result in the suppression of the transmitted signal as shown in the figure. The profile of the transmitted signal subject to suppression remains undisturbed thus ensuring information preservation. For relatively large magnon densities of $n_G \geq 80$ mW almost no magnons are able to propagate through the gate region and the peak density of the D-magnons (marked as n_D) approaches zero. The four-magnon scattering [11–13] is the nonlinear physical mechanism underlying the efficient control of one magnon flow by another: Please see Ref. [5] for details. The dependence of the D-magnon density n_D normalized to the original density n_{D0} is shown in Fig. 2b as a function of the G-magnon density. It can be seen that the suppression increases monotonically with an increase in the G-magnon density and spans almost three orders of magnitude. We would like to emphaseize, that such very high efficiency of the magnon current suppression is of high importance for future magnonic circuits composing of a large number of magnon transistors. For the purpose of digital data processing we use the approach used in CMOS assuming that logic "0" corresponds to the amplitude of the signal smaller than 1/3 of the signal maximum ($n_D/n_{D0} < 1/3$) and logic "1" corresponds to signals larger than 2/3 ($n_D/n_{D0} > 2/3$). Figure 2b shows that it is sufficient to inject G-magnons having a density of only 25 mW in order to switch the binary signal from "1" to "0".

Semiconductor transistors are widely used not only for logical operations but also for the amplification of electronic signals. Such amplification is based on the control of a large signal applied to the transistor's source by a weak one at the gate. To demonstrate the possibility of this kind of amplification using our device we have performed a set of $n_D(n_G)$ measurements for different densities of S-magnons at the signal source [5]. It was demonstrated that a high density of S-magnons can be manipulated by a small density of G-magnons, i.e. $n_G < n_S$. The lowest n_G/n_S ratio at which the transistor's source-to-drain magnon current is influenced by G-magnons is near 0.01 in our experiments. In semiconductor electronics, a transistor can be embedded into an electronic circuit in such a way that the output signal at the drain is an amplified copy of the input signal at

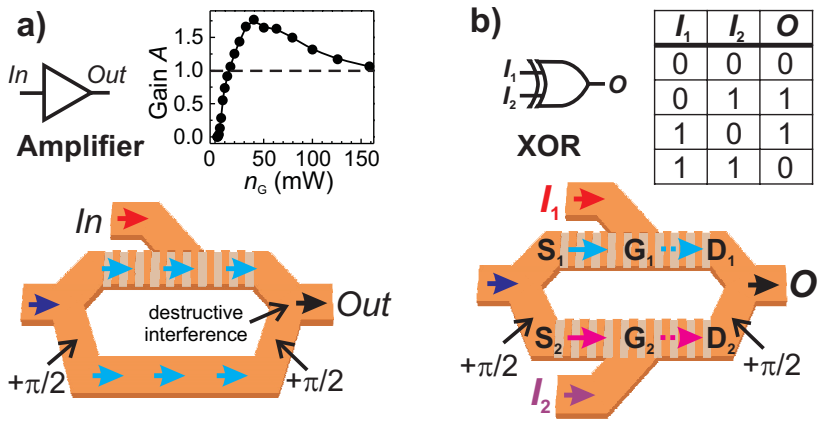

I_1	I_2	O
0	0	0
0	1	1
1	0	1
1	1	0

Fig. 3: (Color online) Amplification of magnon-carried signals and logic operations. a) A magnonic amplifier based on a Mach-Zehnder interferometer with the magnon transistor embedded in one of its two arms. b) The operational principle of a XOR logic gate based on the magnon transistor.

the gate. It is also possible for similar results to be obtained in the case of magnon transistor by using, for example, the magnonic circuit shown schematically in Fig. 3a. It is based on a Mach-Zehnder interferometer with the magnon transistor embedded in one of its two arms. One arm of the interferometer is chosen to be slightly longer in order to induce a π phase shift of the spin wave (see the two $\pi/2$ phase shifts in Fig. 3a) relative to the other arm. As a result, in the case of an input signal equal to zero $n_I = n_G = 0$ (no G-magnon are injected into the gate), the transistor is open and the destructive interference between the spin waves from both arms leads to an output signal of zero, $n_O = 0$. The injection of the G-magnons results in the reduction of the magnonic signal in one of the arms, in the consequent suppression of the destructive interference, and, finally, in the increase of the output signal n_O. Thus, the temporal evolution of the density of the magnons at the output of the interferometer n_O will reproduce the temporal evolution of the input (gate) density n_I (with a short time delay determined by the propagation time of the magnon from the gate to the drain). Important is, that the magnitude of the output magnon signal n_O, in this case, is determined by the density of the source magnons n_S rather than by the gate magnon density n_G. Thus, if the condition $n_S > n_G$ is fulfilled [5], amplification of the magnonic current can be realized. The gain factor A given by the ratio $A = n_O/n_I$ was estimated for our concrete realization of the transistor for the S-magnon density n_S of 200 mW and is shown in the inset of Fig. 3a as a function of the G-magnon density n_G. The gain initially increases with an increase in n_G but after reaching some maximum value, it slowly decreases. The maximum gain factor A achievable in our case is 1.8 but it can be considerably improved by an increase in concentrations of G-magnons during the course of further miniaturization / optimization of the transistor.

Hovewer, the main motivation behind the development of the magnon transistor is the possibility to perform all-magnon processing of digital data. As was shown in the original papers on spin-wave logic gates [2–4], the usage of a Mach-Zehnder interferometer allows for the realization of different types of logic gates. Here as an outline we also propose the use of a similar concept, but with two magnon transistors embedded into the arms of the interferometer. The operational principle of such a logic gate is given with the example of a XOR gate and is shown in Fig. 3b. Firstly, the feeding magnon current, which is sent to the interferometer (the left arrow in the Figure), is divided into two identical currents. These currents n_{S1} and n_{S2} are directly applied to the transistors' sources S_1 and S_2 and are independently controlled by the input magnon signals $I_1 = n_{G1}$ and $I_2 = n_{G2}$ injected into the gates G_1 and G_2. The input signal $I =$ "1" corresponds to the critical gate magnon

density n_{Gcrit} large enough to decrease the magnon density at the drain to the value $n_{\mathrm{D}} < n_{\mathrm{D0}}/3$; the input $I =$ "0" means the absence of the gate magnons (the transistor is open). In the case when both input signals are zero $I_1 = I_2 =$ "0" the output signal O after the combiner has zero value "0" due to the destructive interference (see permanent $\pi/2$ phase shift which appears twice in Fig. 3b). The application of a signal to only one of the transistors switches off one of the magnon currents and therefore switches off the destructive interference resulting in $O =$ "1". Finally, switching off both currents results in the absence of magnons at the devices output $O =$ "0" – see the truth table in the Fig. 3b. The great advantage of this kind of wave-based logic gate is that the simple change of the induced phase shifts due to the increased length of the waveguide in the bottom interferometer arm from $\pi/2$ to 0 results in the construction of a universal NAND rather than an XOR gate: $I_1 = I_2 =$ "1" results in $O =$ "1" due to the constructive interference, the rest is as in the case of the XOR gate. Moreover, the presented single-chip magnon XOR gate comprises two transistors only, while the CMOS XOR logic gate consists of 8 field-effect transistors. Finally, the key advantage of the logic gates based on magnon transistors, that makes it different from any other realization of spin-wave logic, is that the output signal from the gate can be directly sent as an input signal to the next logic gate allowing, in such a way, for the design of all-magnon circuits similar to the integrated circuits in CMOS.

In conclusion, we have realized a magnon transistor in which the source-to-drain magnon current is controlled by the injection of magnons into the transistor's gate. The operational principle of the transistor is based on a nonlinear four-magnon scattering process enhanced by the magnonic crystal ensuring high magnon densities at the gate. We have shown that the transistor can be used for the designing of logic gates in all-magnon circuits and enables the amplification of signals coded into the magnon density. The presented device is a key element for a future particle-less technology, in which information will be carried and processed by magnons rather than by electrons.

Financial support from the Deutsche Forschungsgemeinschaft (Grant no. SE 1771/1-2) and from by EU-FET (Grant InSpin 612759) is acknowledged.

References

[1] V.V. Kruglyak, S.O. Demokritov, D. Grundler, *Magnonics*, J. Phys. D: Appl. Phys. **43**, 264001 (2010).
[2] M.P. Kostylev, A.A. Serga, T. Schneider, B. Leven, B. Hillebrands, *Spin-wave logical gates*, Appl. Phys. Lett. **87**, 153501 (2005).
[3] T. Schneider, et al. *Realization of spin-wave logic gates*, Appl. Phys. Lett. **92**, 022505 (2008).
[4] A. Khitun, M. Bao, K. L. Wang, *Magnonic logic circuits*, J. Phys. D: Appl. Phys. **43**, 264005 (2010).
[5] A.V. Chumak, A.A. Serga, B. Hillebrands, *Magnon transistor for all-magnon data processing*, Nat. Commun. **5**, 4700 (2014).
[6] A.A. Serga, A.V. Chumak, B. Hillebrands, *YIG magnonics*, J. Phys. D: Appl. Phys. **43**, 264002 (2010).
[7] G. Gubbiotti, et al. *Brillouin light scattering studies of planar metallic magnonic crystals*, J. Phys. D: Appl. Phys. **43**, 264003 (2010).
[8] B. Lenk, H. Ulrichs, M. MÃijnzenberg, *The building blocks of magnonics*, Phys. Rep. **507**, 107 (2011).
[9] M. Krawczyk, D. Grundler, *Review and prospects of magnonic crystals and devices with reprogrammable band structure*, J. Phys.: Cond. Matter **26**, 123202 (2014).
[10] A.V. Chumak, A.A. Serga, B. Hillebrands, M.P. Kostylev, *Scattering of backward spin waves in a one-dimensional magnonic crystal*, Appl. Phys. Lett. **93**, 022508 (2008).
[11] A.G. Gurevich, G.A. Melkov, *Magnetization oscillations and waves*, CRC, New York, (1996).
[12] V.S. L'vov, *Wave turbulence under parametric excitation*, Springer, Berlin, (1994).
[13] G.T. Kazakov, A.V. Kozhevnikov, Yu.A. Filimonov, *The effect of parametrically excited spin waves on the dispersion and damping of magnetostatic surface waves in ferrite films*, J. Exp. Theor. Phys. **99**, 174 (1999).

4.12 Numerical simulations of a spin-wave majority gate employing mode selection

S. Klingler, P. Pirro, T. Brächer, B. Leven, B. Hillebrands, and A.V. Chumak

An important step towards the application of spin-wave devices in modern information technology is the realization of spin-wave logic gates by encoding information in the spin-wave's phase and exploitating the interference between spin waves for data processing [2–5]. In this context, the majority gate is of special interest since it allows for the evaluation of the majority of an odd number of logic input signals, as given in Tab. 1. Furthermore, not only can majority operations be performed with this gate but also AND- or OR-operations, if one input (see input 3 in Tab. 1) is used as a control input. Hence, the advantage of the majority gate is its configurability and functionality [6]. In a spin-wave majority gate the phase ϕ of the waves is used as an information carrier (ϕ_0 corresponds to logic "0", logic "1" is represented by $\phi_0 + \pi$). Although the idea of such a majority gate was presented earlier [6], no practical realization suitable for the integration into magnonic circuits has thus far been proposed.

One of the main problems of a realistic spin-wave majority gate is the coexistence of different spin-wave modes with different wavelengths at a fixed frequency in the structure [7] due to the multimode character of the spin-wave waveguides. As a result, the output signal is given by overlaying modes of various phases and, thus, the majority function is lost. As a solution, a design which guarantees for a single-mode operation has to be used. Here, we present the design of an all-magnon majority gate and prove its functionality using numerical simulations. The width of the output waveguide has been chosen in a way such as to obtain single-mode operation. The operational characteristics of the majority gate have been studied for different phases. AND-, OR-, NAND- and NOR-operations have been demonstrated using the same majority gate device.

For the simulations, the material parameters of 100 nm-thick Yttrium-Iron-Garnet (YIG) are used: a saturation magnetization [8] of $M_s = 140\,\mathrm{kA/m}$, an exchange constant [9] of $A = 3.5\,\mathrm{pJ/m}$ and a Gilbert damping [10] of $\alpha = 5 \cdot 10^{-4}$ which are realistic values for YIG films of nanometer thickness. The use of YIG is motivated by its large intrinsic spin-wave propagation distance which is larger than the size of the microstructures [8, 10], allowing for the construction of complex magnonic networks [4].

The design of the investigated majority gate is shown in Fig. 1. It can be divided into three areas: The first area (I) consists of three input waveguides where spin waves can be excited with different phases. The second area (II) is the spin-wave combiner where the outer waveguides are merged into the central waveguide at an angle of 45°. The area (III) is defined by the output waveguide

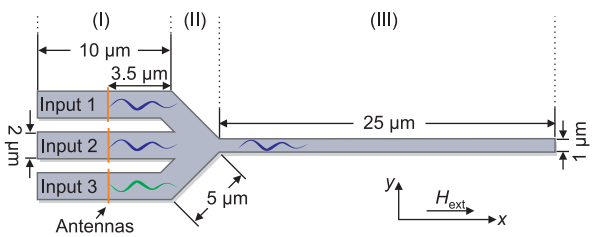

Fig. 1: Geometry of the majority gate. Spin waves are excited by the antennas (I), interfere in the combiner (II) and are emitted in the output waveguide (III). The phase of the spin wave in the output is determined by the phase of the incoming spin waves.

This work has been recently published in Applied Physics Letters [1].

Input 1 Signal	Input 2 Signal	Input 3 Control	Output	
0	0	0	0	AND
1	0	0	0	
0	1	0	0	
1	1	0	1	
0	0	1	0	OR
1	0	1	1	
0	1	1	1	
1	1	1	1	

Table 1: Truth table of the majority operation. The majority of the input signals passes through the gate. In addition, input 3 can be seen as a control gate which switches the function of the gate between AND (Input 3 = 0) and OR (Input 3 = 1) operation. NAND- and NOR-operations can be performed through shifting the phase of the output signal by π.

where spin waves propagate with the same phase as the majority of the incoming spin waves. To ensure the possibility of a practical experimental realization of the gate, all dimensions are chosen to be in the micrometer range [4, 10].

The input waveguides (I) have a width of $w = 2\,\mu\text{m}$ and a length of $10\,\mu\text{m}$. In this area, the spin-wave excitation by micropstrip antennas crossing the waveguides orthogonally is modeled. The magnetization and the wavevector point in the direction parallel to the long axes of the waveguide. For this configuration the dispersion relations [12] of different width modes n, where n refers to the number of anti-nodes across the width of the waveguide, are shown in Fig. 2a. For low values of k, where the spin waves are known as backward-volume magnetostatic waves, the frequency decreases with increasing wave vector due to dipolar interactions. Thus, spin waves with low k are in the dipolar spin wave regime. For large values of k the frequency increases with increasing wave vector due to exchange interaction, and the spin waves are in the exchange regime. The excitation efficiency of the microstrip antenna decreases with increasing wave vector [13]. This allows for the excitation of the dipolar spin waves at a frequency of 2 GHz with sufficient efficiency while the excitation of the exchange waves can be neglected (marked with filled and unfilled dots, respectively). The even numbered width modes cannot be excited with a homogeneous antenna field. Thus, only the first width mode was employed in the transmitting and processing of information in the investigated majority gate. In the spin-wave combiner (part II), the length of the bends was chosen to be a multiple of the spin-wave wavelength, in order that changes in the phase due to the propagation through the bend were prevented. However, scattering into higher width modes can occur in the combiner since in the bend the transitional symmetry is broken [14]. To avoid these

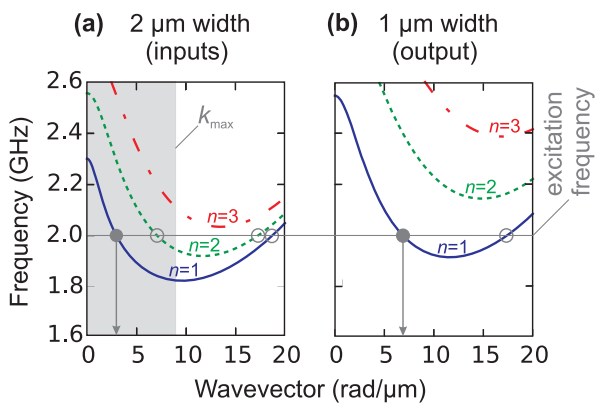

Fig. 2: Dispersion characteristics of a 2 µm and a 1 µm wide waveguide in backward-volume geometry and an external magnetic field of 24 mT. Dynamic strayfields due to the finite size of the microstructures were considered using an effective stripe width [11]. (a) The first and the second width mode can exist in the waveguide. The regime with an efficient spin-wave excitation is shaded in grey. (b) At a frequency of 2 GHz only the first width mode can exist in the waveguide.

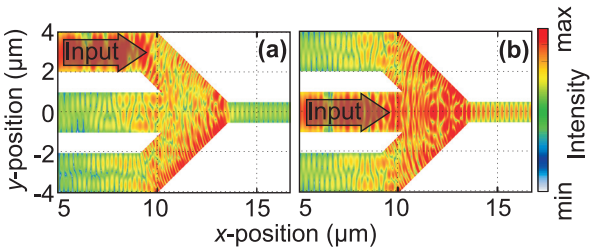

Fig. 3: (Color online) Time averaged intensity distribution for a single arm excitation. The color code is in a logarithmic scale. (a) The upper arm of the majority gate is excited, and a strong intensity flow into the lower arm is observed. The spin wave intensity is only partially emitted into the output arm. (b) The central input arm is excited. The emission of intensity is symmetric into the other input arms. The intensity distribution in the output arm is much higher in comparison to the upper arm excitation.

higher-order width modes in the output waveguide (III), its width is chosen to be 1 µm. As can be seen in Fig. 2b, the minima of the dispersion relations are shifted to higher frequency values for the 1 µm wide stripe due to the smaller quantization width. This can be used to shift the dispersion relation of higher order modes beyond the excitation frequency of 2 GHz. Thus, for this frequency, higher width modes are prohibited in the output waveguide. Additionally, the wavevector of the spin wave is increased in the 1 µm-wide stripe to $k = 6.3\,\mathrm{rad}/\mu\mathrm{m}$ (cf. gray vertical arrows in Fig. 2).

To investigate the spin-wave dynamics in the proposed structure (shown in Fig. 1), numerical simulations using MuMax2, an approach of parallel computation in micromagnetic simulations using graphics cards (GPUs) [15], were performed. This allows for the simulation of the spin-dynamics in a micron-sized area with a resolution of a few nanometers [7]. A static field of 24 mT is applied in x-direction, and the spin waves propagate parallel to the magnetization. The spin-wave excitation is modeled by an alternating magnetic field ($f = 2\,\mathrm{GHz}$) which is produced by a microstrip antenna with a width of 700 nm and a height of 400 nm. Thus, the simulated excitation field is not restricted to the antenna region and models realistic experimental conditions. [5] The magnetization configuration was saved with a time resolution of 4 ps. Please see [1] for more details.

At first, the spin-wave dynamics in the combiner were investigated if only one arm is excited. By this, information about the intensity and the mode distribution in the structure can be obtained. In Fig. 3a, the time averaged intensity is shown when only the upper arm is excited. The spin waves in the bend have a wavevector component in y-direction, which is perpendicular to the static magnetization. The group velocity component in the y-direction is larger than that of the component parallel to the magnetization. Thus, the intensity flow into the lower arm is preferred in comparison to the output waveguide. Furthermore, the second width mode is excited in the other input arms due to the scattering processes in the combiner. In Fig. 3b, the intensity distribution is shown if the spin wave is excited in the central arm. The intensity flow into the output waveguide is increased in comparison to the situation in Fig. 3a, since the spin waves do not have to bend around a corner to reach the output waveguide. Thus, the amplitude of the spin-wave excitation in the central arm will be attenuated by a factor of 0.2 in the following in order to equalize the amplitudes of the output signals. In both cases, higher modes are excited in the combiner due to its large quantization width. However, it has to be emphasized that only the first width modes (dipolar and exchange) exist in the output waveguide, which determine the shape of the interference patterns visible in the output waveguide.

The previous section explored the spin-wave intensity contributions in the combiner. Now, the operational characteristics of the majority gate are discussed for the cases where all inputs are excited and the excitation of the spin wave in the center waveguide is attenuated by a factor of 0.2. For this, the phase information of the combined spin waves in the output waveguide is extracted

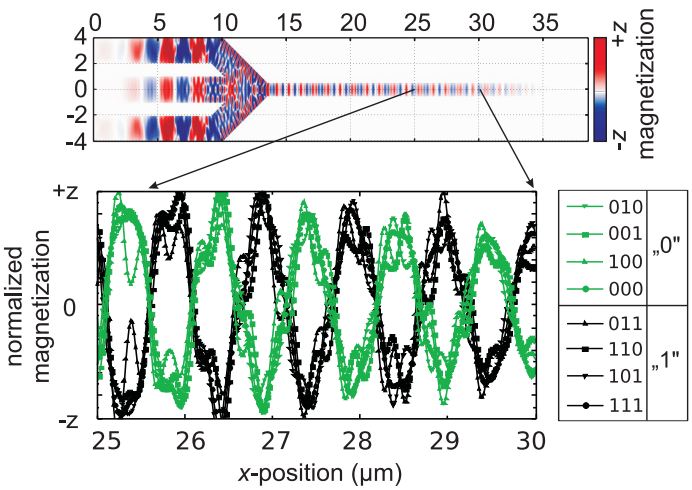

Fig. 4: Top: z-magnetization at the last time step of the 0-0-0-simulation (the spin waves in all inputs are excited without additional phase shift). The color code in the upper graph displays the deviations in the magnetization distribution. Bottom: Extracted m_z in area (III) shows a mode interference between the dipolar and the exchange spin wave in the output waveguide.

from the z-magntization at a fixed timestep for every input combination. A snapshot of m_z from the 0-0-0-simulation (i.e., in the first, second and third input spin waves are excited without additional phase shift) is shown in the upper graph in Fig. 4. In the lower graph, m_z at the center of the output waveguide is extracted for all input combinations. It can be seen that the observed signals are a superposition of two waves with different wavelength. The large wavelength ($\lambda \approx 1\,\mu\text{m}$ and $k \approx 6.3\,\text{rad}/\mu\text{m}$) can be identified with the dipolar wave, the small wavelength can be attributed to the exchange wave in the dispersion relation in Fig. 2b. It is clearly visible that all excitation combinations with a majority phase of 0 (blue) are in phase, and simultaneously in anti-phase to all combinations with a majority phase of π (green). With this, the majority operation from Tab. 1 is reproduced and it is shown that the phase of the spin wave in the output is always defined by the phase of the majority of the input waves.

In addition, it has to be highlighted that the investigated all-magnon majority gate also allows for a full set of spin-wave logic operations (AND, OR, NAND and NOR). For this purpose, input 3 has exemplarily been chosen as a control input (see Tab. 1). For a fixed readout position, e.g., $x = 29\,\mu\text{m}$, AND-operations are performed when the spin waves at input 3 are excited without an additional phaseshift, i.e., the logic value of input 3 is "0". By switching the phase in input 3 to π, i.e., the logic value of input 3 becomes "1", OR-operations are performed at the fixed readout position. By shifting the readout position by a half of the wavelength of the dipolar wave, e.g., from $x = 29\,\mu\text{m}$ to $x = 29.5\,\mu\text{m}$, the phase of the readout signal is shifted by π and all logic output values are negated. Thus, NAND- and NOR-operations are simultaneously performed dependent on the control input. This is a general benefit of coding data into the spin-wave phase [6].

In summary, a fully operational spin-wave majority gate has been presented, where data transmission and processing are realized with spin waves. By choosing the proper width of the output waveguide, it is possible to select the first width mode from the combiner, since the dispersion relations of the higher modes can be shifted above the excitation frequency with decreasing waveguide width. Logic AND- and OR-operations can be performed by choosing a fixed readout positions in the output waveguide, whereas NAND- and NOR-operations can be performed by shifting the readout position by a half of the spin-wave wavelength. It has to be emphasized, that the data processing in the proposed majority gate occurs fully in the magnonic system. With this, the output signal can be directly used in combination with an all-magnon transistor [4] and various spin-wave devices [5, 17].

This research has been supported by the EU-FET grant InSpin 612759.

References

[1] S. Klingler, P. Pirro, T. Brächer, B. Leven, B. Hillebrands, A.V. Chumak, *Design of a spin-wave majority gate employing mode selection*, Appl. Phys. Lett. **105**, 152410 (2014).

[2] T. Schneider, A.A. Serga, B. Leven, B. Hillebrands, R.L. Stamps, M.P. Kostylev, *Realization of spin-wave logic gates*, Appl. Phys. Lett. **92**, 022505 (2008).

[3] A. Khitun, M. Bao, K.L. Wang, *Magnonic logic circuits*, J. Phys. D: Appl. Phys. **43**, 264005 (2010).

[4] A.V. Chumak, A.A. Serga, B. Hillebrands, *Magnon transistor for all-magnon data processing*, Nat. Commun. **5** , 4700 (2014).

[5] T. Brächer, P. Pirro, J. Westermann, T. Sebastian, B. Lägel, B. Van de Wiele, A. Vansteenkiste, B. Hillebrands, *Generation of propagating backward volume spin waves by phase-sensitive mode conversion in two-dimensional microstructures*, Appl. Phys. Lett. **102**, 132411 (2013).

[6] A. Khitun K.L. Wang, *Spin Wave Magnetic NanoFabric: A New Approach to Spin-Based Logic Circuitry*, IEEE Trans. Magn. **44**, 2141 (2008).

[7] P. Pirro, T. Brächer, K. Vogt, B. Obry, H. Schultheiss, B. Leven, B. Hillebrands, *Interference of coherent spin waves in micron-sized ferromagnetic waveguides*, Phys. Status Solidi **248**, 2404 (2011).

[8] A.A. Serga, A.V. Chumak, B. Hillebrands, *YIG magnonics*, J. Phys. D: Appl. Phys., **43**, 264002 (2010).

[9] E.E. Anderson, *Molecular field model and the magnetization of YIG*, Phys. Rev. **134**, A1581 (1964).

[10] P. Pirro, T. Brächer, A. V. Chumak, B. Lägel, C. Dubs, O. Surzhenko, P. Görnert, B. Leven, B. Hillebrands, *Spin-wave excitation and propagation in microstructured waveguides of yttrium iron garnet/Pt bilayers*, Appl. Phys. Lett. **104**, 012402 (2014).

[11] K. Guslienko, S. Demokritov, B. Hillebrands, A.N. Slavin, *Effective dipolar boundary conditions for dynamic magnetization in thin magnetic stripes*, Phys. Rev. B **66**, 132402 (2002).

[12] B. Kalinikos A.N. Slavin, *Theory of dipole-exchange spin wave spectrum for ferromagnetic films with mixed exchange boundary conditions*, J. Phys. C: Solid State Phys. **19**, 7013 (1986).

[13] V.E. Demidov, M.P. Kostylev, K. Rott, P. Krzysteczko, G. Reiss, S.O. Demokritov, *Excitation of microwaveguide modes by a stripe antenna*, Appl. Phys. Lett. **95**, 112509 (2009).

[14] P. Clausen, K. Vogt, H. Schultheiss, S. Schäfer, B. Obry, G. Wolf, P. Pirro, B. Leven, B. Hillebrands, *Mode conversion by symmetry breaking of propagating spin waves*, Appl. Phys. Lett. **99**, 162505 (2011).

[15] A. Vansteenkiste B. Van de Wiele, *MuMax: a new high-performance micromagnetic simulation tool*, J. Magn. Magn. Mater. **323**, 2585 (2011).

[16] G. Abo, Y. Hong, J. Park, J. Lee, W. Lee, B. Choi, *Definition of magnetic exchange length*, IEEE Trans. Magn. **49**, 4937 (2013).

[17] K. Vogt, F.Y. Fradin, J.E. Pearson, T. Sebastian, S.D. Bader, B. Hillebrands, A. Hoffmann, H. Schultheiss, *Realization of a spin-wave multiplexer*, Nat. Commun. **5**, 3727 (2014).

4.13 Novel dynamic magnonic crystal for spin-wave logic gates

A.V. Chumak, A.A. Serga, V.I. Vasyuchka, and B. Hillebrands

In collaboration with A.A. Nikitin, A.B. Ustinov, A.A. Semenov, B.A. Kalinikos, Department of Physical Electronics and Technology, St. Petersburg Electrotechnical University, St. Petersburg, 197376 Russia;
E. Lähderanta, Department of Mathematics and Physics, Lappeenranta University of Technology, Lappeenranta, 53850 Finland

Wave-based computing in which waves rather than particles such as electron are used to transfer and process information is a technology with the potential to overcome the drawbacks of modern CMOS technology. Spin waves and their quanta magnons in that respect are a good choice of wave system due to the wide range of wavelengths available, that is, down to the nanometer regime and up to frequencies in the THz range. [1]. This allows for the design of ultra-fast post-CMOS processors with nanometer sizes. Logic gates, that are key components of such processors, operating with spin waves have been proposed recently [2–4]. All of them are based on a Mach-Zehnder interferometer in which either the phase or the amplitude of the spin waves is controlled by external electric currents representing the logical inputs. The output of the devices is then determined by the amplitude or phase of a spin-wave pulse after interference. Majority gates [4, 5] and magnon transistors [1], in which data are processed purely by magnons without electric current, represent an additional interest.

Magnonic crystals [6–9], which are artificial magnetic materials with periodically-varying properties, are of particular interest for potential applications although they have already been used for magnon-based computing application such as for magnon waveguides [8, 9], microwave signal processing [6, 7], power limiting [10], magnetic field sensoring [11], short-time data storage [12] and even as a key component of a magnon transistor [1]. Dynamic magnonic crystals, which have properties that can be varied on a very fast time scale, open an additional dimensionality in the wave-based information processing [13]. E.g., all-linear frequency converters and time reversers have been demonstrated [14]. However, the full potential of the dynamic magnonic crystals as well as of dynamic artificial materials in general, is not realized so far.

In this Report we present a completely new type of dynamic magnonic crystal and apply it to the realization of a logic AND gate. The usage of the magnonic crystal allows for the exclusion of Mach-Zehnder interferometer from the design of a logic gate making it drastically simpler. Moreover, the high sensitivity of the magnonic crystal to the magnetic field [11] is intended for further studies for a decrease in the power consumption of these devices.

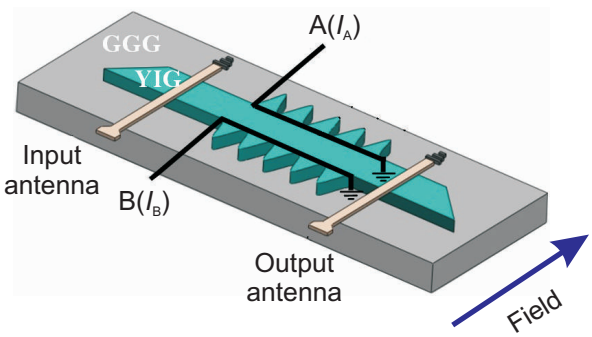

Fig. 1: A sketch of the width-modulated dynamic magnonic crystal. The DC electric currents I_A and I_B sent through the ports A and B are used for the local modulation of the biasing magnetic field and represent logical inputs.

A schematic of the logic gate comprising a dynamic magnonic crystal is shown in Fig. 1. The magnonic crystal is represented as a spin-wave waveguide of variable width made from a 8.5 µm-thick yttrium-iron-garnet (YIG) film. The periodic sinusoidal width modulation of a YIG waveguide in the range from 1.5 mm to 1.9 mm has been created by chemical etching using hot orthophosphoric acid. The period of the modulation (lattice constant) is 400 µm and the magnonic crystal comprises 10 periods. The biasing magnetic field of 160 mT is applied across the YIG strip in order to ensure conditions for the excitation and propagation of surface magnetostatic spin waves [6]. Two microwave stripline antennas, which are placed at equal distances from the modulated area and 10 mm apart, are used for spin-wave excitation and detection. In order to achieve dynamic properties and to realize logic gate functionality, two 50 µm-thick gold wires are placed on the YIG film surface along the modulated edges as shown in Fig. 1. The DC currents sent through these wires change the bias magnetic fields at the geometrically shaped crystal edges, and thus modify the spin-wave transmission properties of the device.

The geometric shape of the magnonic crystal is shown in the top panels of Fig. 2 by a black solid line. The applied magnetic field is shown by means of a colour intensity map in the same panels. The operational principle of the dynamic magnonic crystal is as follows: In the absence of a DC current through the wires, the magnonic crystal is located in the uniform magnetic field – see Fig. 2a. As a results, it exhibits a pronounced band gap (region of frequencies in which spin-wave propagation is forbidden) as is the case with any static width-modulated magnonic crystal [16–18] – see the measured spin-wave transmission characteristics in the inner panels of Fig. 2. Furthermore, the application of an electric current to one of the wires leads to the decrease the

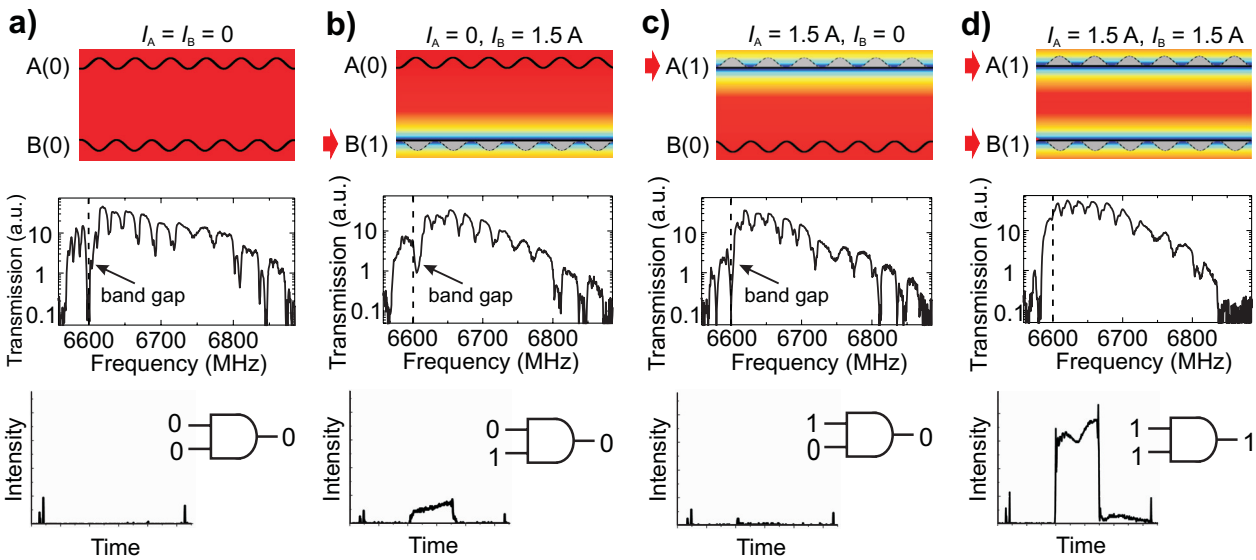

Fig. 2: (Color online) Distributions of the bias magnetic field (top panels), spin-wave transmission (middle panels) and waveforms of the transmitted spin-wave intensity (bottom panels). The geometrical shape of the YIG waveguide is shown by a solid black line in the top panels. The biasing magnetic field with and without DC current applied to ports *A* and *B* are shown by a colour map (linear scale, blue corresponds to 157 mT, red corresponds to 160 mT). The transmitted spin-wave intensity between two antennas is shown in the inner panels. Deeps in the transmission correspond to the standing thickness spin-wave modes [15]. The band gap due to the periodic modulation of the waveguide width is marked. In order to demonstrate operational principle of the logic gate, a 1.5 µs-long pulse at a carrier frequency of 6.6 GHz is sent through the dynamic crystal – see waveforms in the bottom panels. Application of the input DC-current signals to the ports *A* and *B* allows for the realization of the AND gate as it is shown in the panels. The logic output is given by the intensity of the spin-wave pulse.

Oersted magnetic field at one side of the waveguide (the direction of the DC current was chosen in a way to decrease the biasing field). The small values of the magnetic field, by turn, prohibits the existence of spin waves in this region at a given frequency. As a result, the localized field "cuts off" the modulated edge of the crystal realizing an effective plane edge of the waveguide, see Fig. 2b and 2c. Nevertheless, the width of the waveguide is still periodically modulated due to the opposite edge and the crystal exhibits practically the same band gap. Finally, the application of a DC currents simultaneously to both wires converts the magnonic crystal into a conventional straight waveguide resulting in the absence of the band gap (Fig. 2d).

In our experiments, the dynamic magnonic crystal was switched on and off on a time scale of 5 ns which is small when compared to the spin-wave propagation time through the crystal of about 200 ns. This ensures the realization of a real dynamic magnonic crystal in which the properties of the media are changed faster relative to the spin-wave characteristic times [14]. The advantage of this type of a dynamic magnonic crystal compared to the previously reported realization, where a current conducting meander structure was attached to the surface of the regular spin-wave waveguide [13], is that there is no energy consumption required for the crystal to stay in the "on" state. Moreover, the design of the dynamic crystal proposed here is suitable for down-scaling since the surface magnetostatic spin waves preserve their high group velocities in thin magnetic micro-structures [19] as opposed to backward volume waves used in previous device.

To perform logic operations using a dynamic magnonic crystal, we performed an additional experiment in which a 1.5 µs-long spin-wave pulse was sent through the dynamic crystal. The frequency of the spin wave was chosen to be $f_0 = 6.6$ GHz and corresponds to the band gap of the crystal. The output of the logic gate is given by the spin-wave intensity at this frequency. The logic inputs are given by DC-current signals applied to ports A and B (see Fig. 1). The spin-wave pulses received at the output antenna are shown in the bottom panels of Fig. 2. The absence of the spin-wave transmission, which corresponds to the logic output "0", is seen in all cases when the magnonic crystal is "on" (see Fig. 2a-c). Please note that the small transmission observed in Fig. 2b is related to a slight asymmetry between the positions of two current conducting wires. However, it does not disturb the processing of data if one defines the logic "0" as a spin-wave intensity below 1/3 of the original value and logic "1" is above 2/3 [1]. As opposed to the previous cases, application of the signals $A =$ "1" and $B =$ "1" to the logic gate suppresses the magnon band gap and, thus, results in a pronounced spin-wave transmission through the crystal and the output signal "1". All these data processing operations correspond to the truth table of an AND logic gate which is shown schematically in the bottom panels of Fig. 2.

In conclusion, a new dynamic magnonic crystal suitable for miniaturization and for a decreasing the power consumption was developed and studied. This crystal was used to realize an AND logic gate without using a Mach-Zehnder interferometer geometry. The presented results indicate a significant step towards new data processing technology in which data is communicated and processed by spin waves rather than by electrons.

Financial support from the Deutsche Forschungsgemeinschaft is gratefully acknowledged.

References

[1] A.V. Chumak, A.A. Serga, B. Hillebrands, *Magnon transistor for all-magnon data processing*, Nat. Commun. **5**, 4700 (2014).

[2] M.P. Kostylev, A.A. Serga, T. Schneider, B. Leven, B. Hillebrands, *Spin-wave logical gates*, Appl. Phys. Lett. **87**, 153501 (2005).

[3] T. Schneider, A.A. Serga, B. Leven, B. Hillebrands, R.L. Stamps, M.P. Kostylev *Realization of spin-wave logic gates*, Appl. Phys. Lett. **92**, 022505 (2008).
[4] A. Khitun, M. Bao, K.L. Wang, *Magnonic logic circuits*, J. Phys. D: Appl. Phys. **43**, 264005 (2010).
[5] S. Klingler, P. Pirro, T. Brächer, B. Leven, B. Hillebrands, A.V. Chumak, *Design of a spin-wave majority gate employing mode selection*, Appl. Phys. Lett. **105**, 152410 (2014).
[6] A.A. Serga, A.V. Chumak, B. Hillebrands, *YIG magnonics*, J. Phys. D: Appl. Phys. **43**, 264002 (2010).
[7] G. Gubbiotti, S. Tacchi, M. Madami, G. Carlotti, A.O. Adeyeye, M.P. Kostylev *Brillouin light scattering studies of planar metallic magnonic crystals*, J. Phys. D: Appl. Phys. **43**, 264003 (2010).
[8] B. Lenk, H. Ulrichs, M. Münzenberg, *The building blocks of magnonics*, Phys. Rep. **507**, 107 (2011).
[9] M. Krawczyk, D. Grundler, *Review and prospects of magnonic crystals and devices with reprogrammable band structure*, J. Phys.: Cond. Matter **26**, 123202 (2014).
[10] A.B. Ustinov, A.V. Drozdovskii, B.A. Kalinikos, *Multifunctional nonlinear magnonic devices for microwave signal processing*, Appl. Phys. Lett. **96**, 142513 (2010).
[11] M. Inoue, A. Baryshev, H. Takagi, P.B. Lim, K. Hatafuku, J. Noda, K. Togo, *Investigating the use of magnonic crystals as extremely sensitive magnetic field sensors at room temperature*, Appl. Phys. Lett. **98**, 132511 (2011).
[12] A.V. Chumak, V.I. Vasyuchka, A.A. Serga, M.P. Kostylev, V.S. Tiberkevich, B. Hillebrands, *Storage-recovery phenomenon in magnonic crystal*, Phys. Rev. Lett. **108**, 257207 (2012).
[13] A.V. Chumak, T. Neumann, A.A. Serga, B. Hillebrands, M.P. Kostylev, *A current-controlled, dynamic magnonic crystal*, J. Phys. D: Appl. Phys. **42**, 205005 (2009).
[14] A.V. Chumak, V.S. Tiberkevich, A.D. Karenowska, A.A. Serga, J.F. Gregg, A.N. Slavin, B. Hillebrands, *All-linear time reversal by a dynamic artificial crystal*, Nat. Commun. **1**, 141 (2010).
[15] B.A. Kalinikos, A.N. Slavin, *Theory of dipole-exchange spin wave spectrum for ferromagnetic films with mixed exchange boundary conditions*, J. Phys. C , **19**, 7013 (1986).
[16] K.S. Lee, D.S. Han, S.K. Kim, *Physical origin and generic control of magnonic band gaps of dipole-exchange spin waves in width-modulated nanostrip waveguides*, Phys. Rev. Lett. **102**, 127202 (2009).
[17] A.V. Chumak, P. Pirro, A.A. Serga, M.P. Kostylev, R.L. Stamps, H. Schultheiss, K. Vogt, S.J. Hermsdoerfer, B. Laegel, P.A. Beck, B. Hillebrands, *Spin-wave propagation in a microstructured magnonic crystal*, Appl. Phys. Lett. **95**, 262508 (2009).
[18] F. Ciubotaru, A.V. Chumak, N.Yu. Grigoryeva, A.A. Serga, B. Hillebrands, *Magnonic band gap design by the edge modulation of micro-sized waveguides*, J. Phys. D: Appl. Phys. **45**, 255002 (2012)
[19] T. Brächer, P. Pirro, J. Westermann, T. Sebastian, B. Lägel, B. van de Wiele, A. Vansteenkiste, B. Hillebrands,*Generation of propagating backward volume spin waves by phase-sensitive mode conversion in two-dimensional microstructures*, Appl. Phys. Lett. **102**, 132411 (2013).

C. Spin Caloric Transport

Spin Caloric Transport is a dynamically growing field of research, which investigates the interplay between spin- and heat-based transport phenomena. The observation of the spin Seebeck effect (SSE) in a magnetic insulator demonstrates the crucial role of collective magnetization excitations, i.e. spin waves and their quanta, magnons, in spin caloric transport processes, and illustrates the conceptual distinction between this phenomenon and conventional thermoelectric generation. Most interesting and important is the conversion of a heat gradient into a magnon current and vice versa in a magnetic insulator. On a long time scale this may lead to the utilization of heat currents to support the transfer and processing of spin information.

In Report 4.14 we present a concept of the employment of optically-induced thermal landscapes for manipulation of spin waves, which allows for the realization of almost any two-dimensional pattern in the saturation magnetization of a magnetic material. This enables for the efficient control of spin-wave properties as demonstrated on examples of one- and two-dimensional magnonic crystals. Our proposed technique allows for a full control of spin waves, required for future dynamic spin-wave logic devices operating with multi-purpose computing units.

In Report 4.15 we demonstrate the influence of a thermal gradient on the spin-wave propagation through a static magnonic crystal. Besides the Bragg scattering of spin waves and formation of band gaps, a simultaneous spatial transformation of the spin-wave wavevector takes place that makes the magnonic crystal in a thermal gradient effectively asymmetric. We have found that a positive thermal gradient (propagation of spin waves into a hotter region of the magnonic crystal) leads to an effective frequency shift of the band gaps towards lower frequencies. In contrast, a negative thermal gradient results in a frequency shift towards higher frequencies. The effective broadening of band gaps is observed for both gradients.

Report 4.16 presents microwaves as a perspective heating technique to generate a thermal gradient in ferromagnetic insulator|normal metal systems to study the longitudinal spin Seebeck effect. The measurements provide crucial information about the relative direction of the spin current flow in the spin pumping and longitudinal SSE processes. Within a single experiment we demonstrate that in the process of longitudinal SSE, a spin current flows from the normal metal (hot) to the ferromagnet (cold) while in the case of spin pumping, the spin current flow is inverted.

C. Spin-kalorischer Transport

Der spin-kalorische Transport ist ein rasant wachsendes Forschungsfeld, welches das Zusammenspiel zwischen spin- und wärmebasierten Transportphänomenen untersucht. Die Untersuchungen des Spin-Seebeck-Effekts (SSE) in magnetischen Isolatoren zeigen dabei die wichtige Rolle auf, welche die kollektiven Anregungen des magnetischen Systems - also Spinwellen - in spin-kalorischen Transportprozessen spielen. Weiterhin verdeutlichen diese Beobachtungen die konzeptuelle Unterscheidung zwischen diesen Phänomenen auf der einen sowie den konventionellen thermoelektrischen Effekten auf der anderen Seite. Von größtem Interesse und von größter Wichtigkeit in diesem Forschungsgebiet ist die Untersuchung der Umwandlung von Temperaturgradienten in reine Spinströme in Isolatoren. Perspektivisch kann das Verständnis dieser Prozesse zur Nutzung von Wärmeströmen für den Transport sowie die Verarbeitung von Spin-Information beitragen.

In Bericht 4.14 stellen wir ein Konzept vor, Spinwellen mit Hilfe optisch induzierter thermischer Landschaften zu beeinflussen, mit dem sich nahezu jede zweidimensionale Verteilung der Sättigungsmagnetisierung eines magnetischen Materials realisieren lässt. Es erlaubt eine effiziente Kontrolle der Spinwelleneigenschaften, wie an Beispielen ein- und zweidimensionaler magnonischer Kristalle gezeigt wird. Unsere vorgestellte Technik erlaubt eine vollständige Kontrolle von Spinwellen, wie sie für zukünftige dynamische Spinwellenlogikelemente, die mit multifunktionalen Recheneinheiten betrieben werden, benötigt wird.

In Bericht 4.15 zeigen wir den Einfluss eines thermischen Gradienten auf die Spinwellenpropagation durch einen statischen magnonischen Kristall. Neben der Braggstreuung von Spinwellen und der Ausbildung von Bandlücken findet eine gleichzeitige Transformation des Spinwellen-Wellenvektors im Raum statt, der den magnonischen Kristall im thermischen Gradienten praktisch asymmetrisch werden lässt. Wir haben entdeckt, dass ein positiver thermischer Gradient (Propagation von Spinwellen in den wärmeren Bereich des magnonischen Kristalls) zu einer effektiven Frequenzverschiebung der Bandlücken hin zu niedrigeren Frequenzen führt. Im Gegensatz dazu führt ein negativer thermischer Gradient zu höheren Frequenzen. Eine effektive Verbreiterung der Bandlücken wird für beide Gradienten beobachtet.

Bericht 4.16 präsentiert den Einsatz von Mikrowellen als eine verheißungsvolle Heiztechnik um einen thermischen Gradienten in Bilagen aus einem ferromagnetischen Isolator und einem normalen Metall zu erzeugen und somit den longitudinalen Spin-Seebeck-Effekt zu studieren. Die Messungen liefern wesentliche Informationen über die relative Richtung der Spinstromflüsse in Spinpump- und longitudinalen SSE-Vorgängen. Mithilfe eines einzigen Experimentes zeigen wir dass beim longitudinalen SSE ein Spinstrom vom normalen Metall (warm) zum Ferromagneten (kalt) fließt, wohingegen im Falle des Spinpumpens der Fluß umgekehrt ist.

4.14 Control of spin-waves by optically induced thermal landscapes

M. Vogel†, A.V. Chumak, E.H. Waller†, T. Langner, V.I. Vasyuchka, B. Hillebrands, and G. von Freymann†

† Arbeitsgruppe "Optische Technologien und Photonik", Fachbereich Physik and Landesforschungszentrum OPTIMAS, Technische Universität Kaiserslautern, 67663 Kaiserslautern, Germany
G. von Freymann is also affiliated with Fraunhofer-Institute for Physical Measurement Techniques (IPM), 67663 Kaiserslautern, Germany

In order to make use of spin waves in data processing it is necessary to control and influence their propagation characteristics in manifold ways [1–7]. Currently, all available methods to control the spin-wave propagation are spatially constant and do not allow for modifications of the spintronic device's properties after a rather time-consuming fabrication [8, 9]. In this Report an alternative method for use in the manipulation of spin waves is shown, that is, by fully-tuneable light patterns (computer-generated holograms): Optically induced thermal patterns/landscapes modify the spin-wave dispersion relation and, hence, the propagation. Thus, the functionality of the magnetic element can be chosen and quickly changed on demand; the same element can be used for example as a conduit, a logic gate or a data buffering element.

The setup used for the realization of the light patterns consists of a 532 nm continuous-wave laser as light source, an acousto-optical modulator for temporal, and a spatial light modulator for spatial intensity control (see Fig. 1a). We study the influence of the thermal gradient induced by the intensity patterns on the spin-wave propagation on a ferrimagnetic 5 µm thick Yttrium Iron Garnet (YIG) waveguide grown on a 500 µm Gadolinium Gallium Garnet (GGG) substrate (see Fig. 1b). GGG is almost transparent, while YIG absorbs about 40% of the green light used in the experiment. In order to increase the efficiency of the heating we use a black absorber painted on top of the YIG layer. Moreover, the absorber increases the contrast of the thermal landscape in YIG due to its approximately one order of magnitude smaller thermal conductivity [11] compared to YIG [12,13].

The heat landscape spatially modulates the saturation magnetization M_s, which is one of the key parameters defining the spin-wave properties. In order to determine the dependence of M_s on the temperature T, the Néel model formalism is used [14]. The saturation magnetization decreases with increasing T and vanishes at the Curie temperature (559 K for YIG). However, in the range from 298 K to 398 K, it is practically linear and following approach can be used ($M_{S,\,298\,K} \approx 140\,\mathrm{kA/m}$ is the saturation magnetization at 298 K):

$$M_S(T) \approx M_{S,\,298\,K} - 313\frac{\mathrm{A}}{\mathrm{K\,m}} \cdot (T - 298\,\mathrm{K}) \tag{1}$$

We now demonstrate the viability of our approach by realizing several one-dimensional magnonic crystals on a single sample: An array of parallel stripes oriented perpendicular to the spin-wave propagation direction is projected onto the sample. The lattice constant $a = 740\,\mu\mathrm{m}$ is shown schematically in Fig. 1b. An infrared camera synchronized to the pulsed laser illumination measures the resulting temperature distribution from the absorber side. The left panel in Fig. 1c shows the thermal profiles after 5 ms of heating and a repetition time of 100 ms with the laser impinging onto the GGG side. Besides a pronounced temperature background a small local temperature increase by the stripes is seen. However, this temperature profile is different from the one inside the

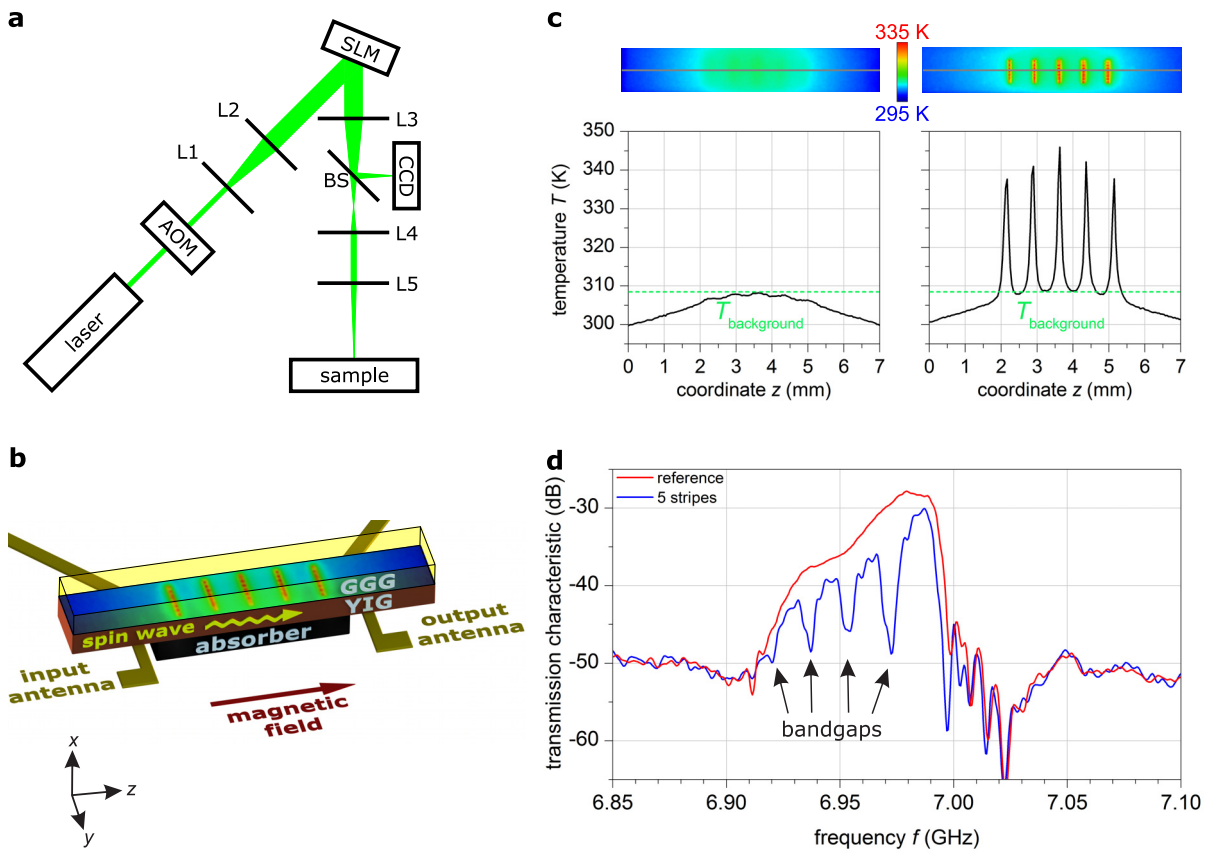

Fig. 1: a) Scheme of the setup for realization of thermal landscapes: The intensity of a continuous wave laser (wavelength 532 nm) is controlled by an acousto-optical modulator (AOM). A spatial light modulator (SLM) generates the light pattern/hologram by modifying the phase fronts of the incoming laser beam to achieve the desired intensity distribution in the focal plane of lens L5 on the magnetic sample. Holograms are calculated with a variation of the Gerchberg-Saxton algorithm [15, 16], resulting in arbitrary patterns covering an area of $8 \times 1.5\,\mathrm{mm}^2$ with approximately 500 mW maximal integral power on the sample. A CCD camera after a beam sampler (BS) is used to observe the intensity distribution [17]. b) Schematic of the sample structure consisting of a GGG/YIG/absorber multilayer system. The optical properties of our sample are as follows: The GGG is almost transparent, YIG absorbs about 40% of the used light, and 30% is transmitted through GGG/YIG and finally absorbed by the absorber layer. Spin-waves are excited and detected by microstrip antennas. A typical thermal landscape is shown on the waveguide. c) Thermal profile of the absorber taken with infrared camera (top panels) after illuminating the sample for 5 ms from GGG side (left panel) and absorber side (right panel). The grey lines in the IR picture mark the positions of cross sections of the thermal landscapes (bottom panels). Determination of the background temperature is done via averaging the minimal values of the heat profile cross section between the sharp peaks. d) Measured spin-wave transmission characteristic (solid blue line) in the thermal landscape schematically shown in c (magnonic crystal with 5 periods, lattice constant 740 µm) and reference data (red) without projected pattern. Four bandgaps for the magnonic crystal are clearly observed in the transmission characteristic.

YIG, because the infrared camera measures the temperature from both the thin YIG and the thick GGG layers. In order to obtain the relevant temperature distribution inside the YIG, we perform another experiment with the laser impinging from the absorber rather than the GGG side (Fig. 1c, right panel): Distinct peaks are visible in the temperature profile. Since the 50 µm-thick absorber is in direct contact to the YIG and has low thermal conductivity, the measured thermal landscape describes qualitatively well the one in YIG.

In the created one-dimensional thermal landscape, we expect the following spin-wave dynamics: First, spin waves are excited at the input antenna, where the YIG temperature is 301 K. Then,

they propagate to the region of the magnonic crystal (with a background temperature of 309 K). During propagation, a smooth wavelength-transformation takes place due to conservation of the spin wave's frequency [18]. Thus, practically no reflection occurs in this region. In contrast, the sharp temperature peaks inside the magnonic crystal region cause strong reflections due to the large mismatch of the spin-wave wave impedance [19]. Finally, after the spin waves have passed the magnonic crystal's area, wavelengths are smoothly transformed back to the original values (at 301 K where the output antenna is located). A vector network analyzer is used to measure the transmitted spin-wave power as a function of frequency f. Both, the reference transmission only in the presence of the background temperature profile and the transmission through five thermal barriers are shown in Fig. 1d. The appearance of four bandgaps is clearly visible as dips in the transmission characteristic.

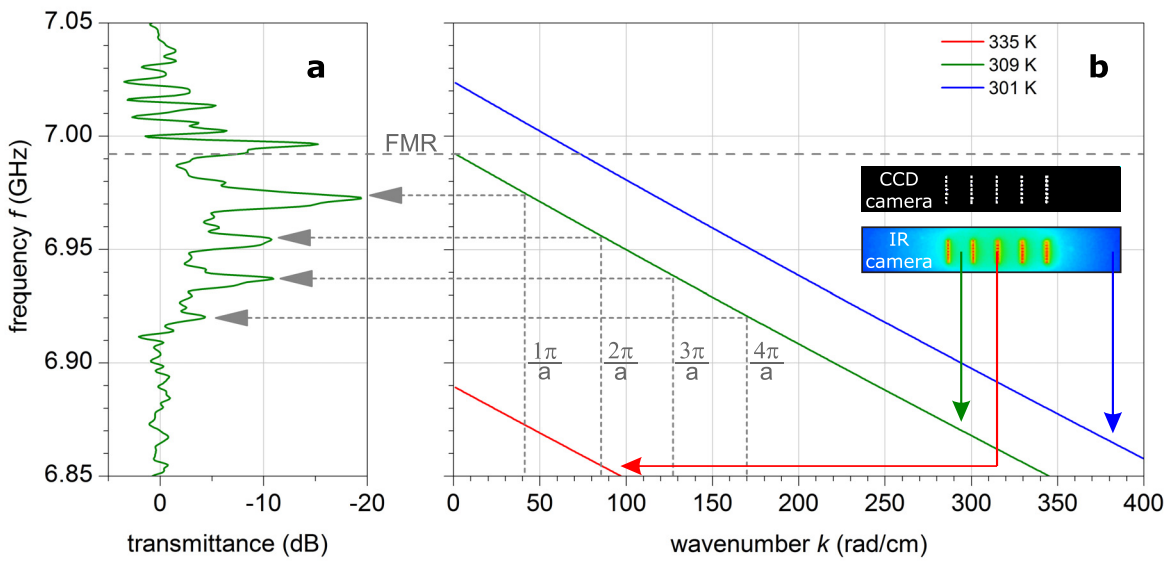

Fig. 2: a) Transmittance through a 1D magnonic crystal with five layers extracted via subtraction of the reference measurement from transmission characteristics in Fig. 1d. Maximal suppression of transmittance is observed for the fundamental bandgap and reaches almost 20 dB. The full width at half maximum of the bandgaps is around $6-8$ MHz. b) Dispersion relation of the backward volume magnetostatic spin waves for different temperatures according to Fig. 1c. The green curve, corresponding to the background temperature, is used to define the frequency bandgaps. The inset shows the hologram intensity distribution (CCD camera) and the thermal profile on the sample (IR camera), respectively. The ferromagnetic resonance (FMR) is around 6.99 GHz. The drop in transmittance near this frequency (see Fig. 2a) is due to the not perfectly fitting falling edge of the transmission characteristics for reference and magnonic crystal measurement in Fig. 1d.

To understand this transmission characteristic, a closer look at the spin-wave dispersion relation - the dependence of the spin-wave angular frequency $\omega = 2\pi f$ on its wavenumber k - is necessary. The dispersion relations calculated for different temperatures are shown in Fig. 2b. No spin-wave propagation occurs at the point $k = 0\,\mathrm{rad/m}$ (known as ferromagnetic resonance - FMR). Increasing T decreases $M_s(T)$ and thus $f(k)$ shifts to lower frequencies.

In order to analyze the influence of the thermal landscape on the spin-wave properties, the transmittance measurement is shown in Fig. 2a. Four bandgaps in the frequency range from 6.91 to 6.99 GHz are observed. For defining the frequencies of the bandgaps, we use a background temperature of 309 K, rather than the temperature at the positions of the antennas. As expected, the frequencies of the bandgaps correspond to wavenumbers $k_n = na$, where n is the number of the bandgap.

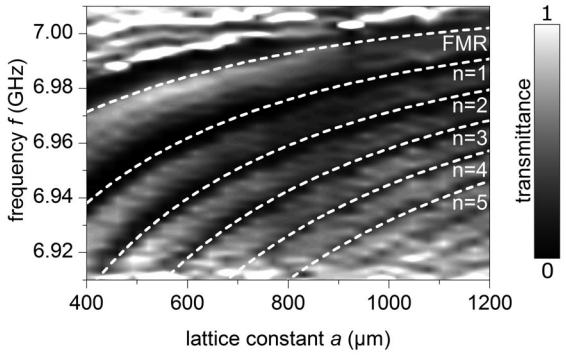

Fig. 3: Measured spin-wave transmittance for different lattice constants of the magnonic crystal. For all lattice constants the bandgaps are well pronounced. Measurements are compared to theoretically expected frequencies for bandgaps with number n (white dashed lines). The ferromagnetic resonance (FMR) corresponds to $n = 0$.

To demonstrate the flexibility of the proposed approach, the transmittance of magnonic crystals with different lattice constants is depicted in Fig. 3. As different magnonic crystals can simply be programmed into the laser hologram, only a single YIG sample is used - in contrast to all existing static methods. In this two-dimensional map, 27 different lattice constants between 400 µm and 1200 µm are investigated and the transmittance is plotted as a function of frequency f and lattice constant a. It is worth noting, that, with changing a the density of the laser stripes varies resulting in a modification in the background temperature. A very good agreement between theory and experiment is observed.

Finally, we demonstrate the potential of the proposed technique by realizing different two-dimensional magnonic crystals. In Fig. 4a, the hologram intensity distributions (CCD camera panel), temperature patterns, and the crystal's transmission characteristics are shown and compared with the case of the one-dimensional magnonic crystal. In these structures, an additional lattice constant appears for the wave propagating along the shifted stripes ($a/4$ for middle panel and $a/2$ for the bottom panel), forming a waveguide. As a result, specific bandgaps disappear for the two-dimensional crystals as compared with the one-dimensional-crystal: for the pattern in the center we observe the disappearance of the second bandgap, while the first and third bandgaps vanish for the bottommost structure. To explain this behaviour qualitatively, we perform a fast Fourier transformation (see Fig. 4c) of the effective hologram intensity shown in Fig. 4b (only the axis oriented along the spin-wave propagation direction is analyzed). The Fourier transformation of the distribution of M_s in coordinate space gives the spin-wave spectrum in wavenumber-space (and consequently in frequency-space), in Fig. 4c the existence/absence of corresponding wavenumbers for each band gap is clearly visible.

To conclude, the presented concept of optically-induced thermal landscapes is a powerful tool, which allows for the realization of almost any two-dimensional pattern in saturation magnetization of a magnetic material. This enables for the efficient control of spin-wave properties as demonstrated on examples of one- and two-dimensional magnonic crystals. Our proposed technique allows for a full control of spin-waves, required for future dynamic spin-wave logic devices operating with multi-purposed computing units.

The authors wish to thank the Nano Structuring Center (NSC) of the TU Kaiserslautern for support with the sample preparation. Financial support by DFG priority program SPP 1538 "Spin Caloric Transport" (project VA 735/1-2) is gratefully acknowledged.

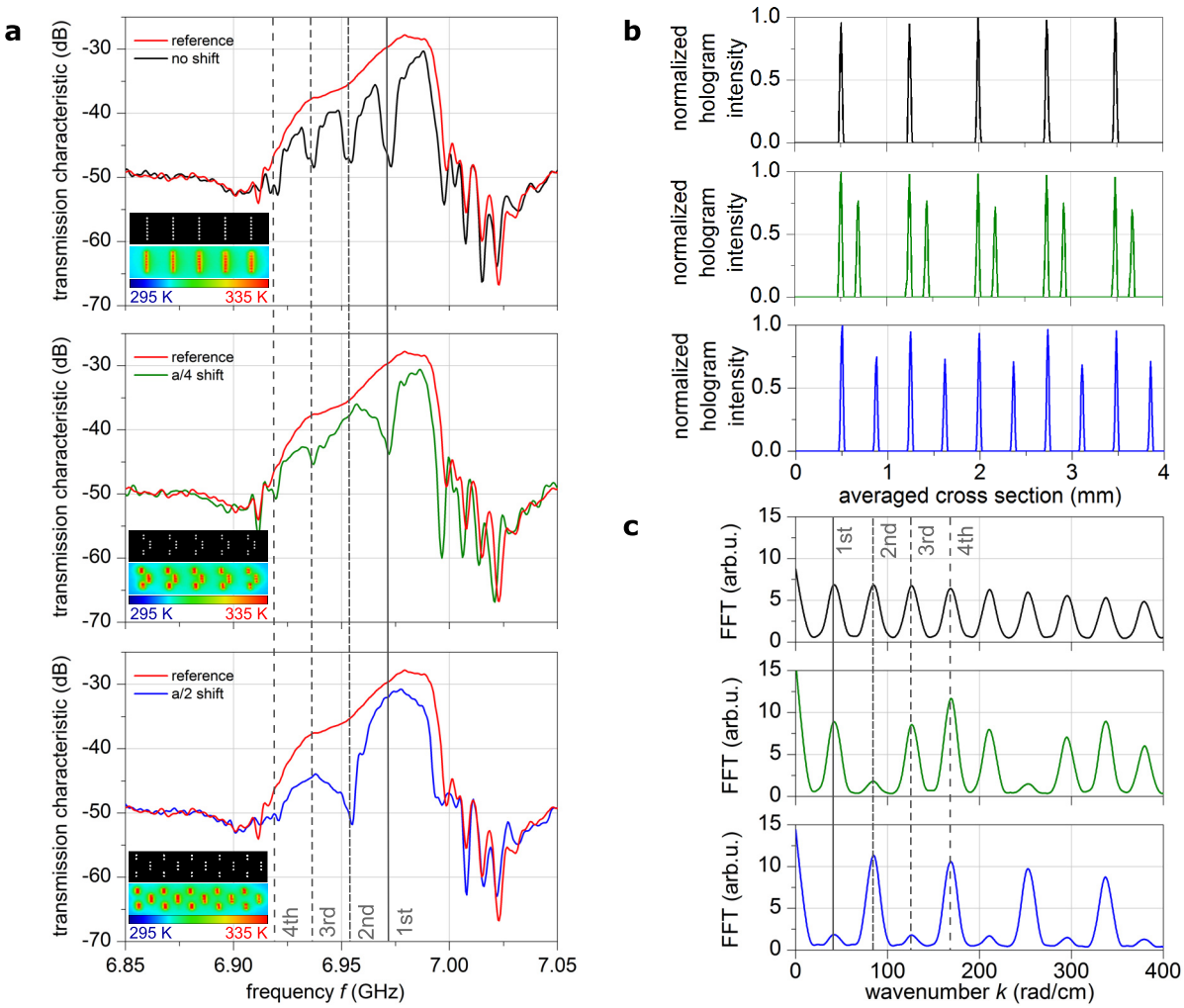

Fig. 4: a) Measured spin-wave transmission characteristics for different lattice shifts. The center of the stripes is moved in z-direction (for the coordinate system see Fig. 1b). The inset shows the hologram intensity and the temperature distribution, respectively. b) These two-dimensional magnonic crystals can be described by an effective one-dimensional thermal landscape or intensity profile I_{eff} of the hologram. The mean value of I_{eff} in y-direction of the hologram intensity distribution (normalized to maximum) as a function of the z coordinate. c) The Fast Fourier transformation of I_{eff} assigns the spacing between the stripes to wavenumbers and, thus, to the number of the corresponding bandgap (pronounced peaks in the plot). Again, theory and experiment are in good qualitative agreement. Indeed, both the experiment and the calculations show vanishing bandgaps due to interference of reflected spin waves for specified lattice shifts.

References

[1] B. Lenk, H. Ulrichs, F. Garbs, M. Münzenberg, *The building blocks of magnonics*, Physics Reports **507**, 107 (2011).

[2] M. Krawczyk, D. Grundler, *Review and prospects of magnonic crystals and devices with reprogrammable band structure*, J. Phys.: Condens. Matter **26**, 123202 (2014).

[3] A.A. Serga, A.V. Chumak, B. Hillebrands, *YIG magnonics*, J. Phys. D: Appl.Phys. **43** 264002 (2010).

[4] A.V. Chumak, A.A. Serga, B. Hillebrands, *Magnon transistor for all-magnon data processing*, Nat. Commun. **5**, 4700 (2014).

[5] A.V. Chumak, V.I. Vasyuchka, A.A. Serga, M.P. Kostylev, V.S. Tiberkevich, B. Hillebrands, *Storage-recovery phenomenon in magnonic crystal*, Phys. Rev. Lett. **108**, 257207 (2012).

[6] J. Topp, D. Heitmann, M.P. Kostylev, D. Grundler, *Making a reconfigurable artificial crystal by ordering bistable magnetic nanowires*, Phys. Rev. Lett. **104**, 207205 (2010).

[7] A.V. Chumak, V.S. Tiberkevich, A.D. Karenowska, A.A. Serga, J.F. Gregg, A.N. Slavin, B. Hillebrands, *All-linear time reversal by a dynamic artificial crystal*, Nat. Commun. **1**, 141 (2010).

[8] G. Gubbiotti, S. Tacchi, M. Madami, G. Carlotti, A.O. Adeyeye, M. Kostylev, *Brillouin light scattering studies of planar metallic magnonic crystals*, J. Phys. D: Appl. Phys. **43**, 264003 (2010).

[9] T. Schwarze, D. Grundler, *Magnonic crystal wave guide with large spin-wave propagation velocity in CoFeB*, Appl. Phys. Lett. **102**, 222412 (2013).

[10] B. Obry, T. Meyer, P. Pirro, T. Brächer, B. Lägel, J. Osten, T. Strache, J. Fassbender, B. Hillebrands, *Microscopic magnetic structuring of a spin-wave waveguide by ion implantation in a $Ni_{81}Fe_{19}$ layer*, Appl. Phys. Lett. **102**, 022409 (2013).

[11] H. Ebadi-Dehaghani, M. Nazempour, *Thermal conductivity of nanoparticles filled polymers*, in A. Hashim (Ed.), Smart nanoparticles technology (InTech 2012).

[12] M. Schreier, A. Kamra, M. Weiler, J. Xiao, G.E.W. Bauer, R. Gross, S.T.B. Goennenwein, *Magnon, phonon, and electron temperature profiles and the spin Seebeck effect in magnetic insulator/normal metal hybrid structures*, Phys. Rev. B **88**, 094410 (2013).

[13] S.M. Rezende, R.L. Rodríguez-Suárez, J.C. Lopez-Ortiz, A. Azevedo, *Thermal properties of magnons and the spin Seebeck effect in yttrium iron garnet/normal metal hybrid structures*, Phys. Rev. B **89**, 134406 (2014).

[14] D.D. Stancil, A. Prabhakar, *Spin waves: theory and applications*, Springer, Berlin (2009).

[15] R.W. Gerchberg, W.O. Saxton, *A practical algorithm for the determination of the phase from image and diffraction plane pictures*, Optik **35**, 237 (1972).

[16] O. Ripoll, V. Kettunen, H.P. Herzig, *Review of iterative Fourier-transform algorithms for beam shaping applications*, Opt. Eng. **43**, 25492555 (2004).

[17] E.H. Waller, G. von Freymann, *Multi foci with diffraction limited resolution*, Optics Express **21**, 21708 (2013).

[18] B. Obry, V.I. Vasyuchka, A.V. Chumak, A.A. Serga, B. Hillebrands, *Spin-wave propagation and transformation in a thermal gradient*, Appl. Phys. Lett. **101**, 192406 (2012).

[19] S. Neusser, D. Grundler, *Magnonics: Spin waves on the nanoscale*, Adv. Mater. **21**, 2927 (2009).

4.15 Spin-wave propagation through a magnonic crystal in a thermal gradient

T. Langner, A.A. Serga, A.V. Chumak, B. Hillebrands, and V.I. Vasyuchka

Magnonic crystals, spin-wave waveguides with periodic variations of their magnetic properties, provide a high potential for applications in data processing using magnons [1–6]. To use this potential the stability of the magnonic crystal functionality is of high importance. One possible way to influence this stability and the crystal parameters is heating and the creation of thermal gradients along the waveguide structure due to waste heat generation [7] in logic devices using magnonic crystal elements. The influence of these temperature effects on their functionality has not been explored so far. Furthermore this new knowledge might also provide additional possibilities to control spin waves by using heat.

In this Report we present studies of a static magnonic crystal [8–13] that is affected by a temperature gradient along the spin-wave propagation direction. On one hand spin waves are scattered at the magnonic crystal structure under Bragg conditions, on the other hand a spatial transformation of the spin-wave wavevector takes place [14] that makes the magnonic crystal effectively asymmetric.

The magnonic crystal investigated here consists of a one-dimensional array of 20 grooves of 500 nm depth and 30 µm width. The lattice constant is $a = 300\,\mu\text{m}$. The grooves are chemically etched onto a 5.9 µm thick spin-wave waveguide of the material yttrium iron garnet (YIG). The YIG layer is grown on a 500 µm thick gallium gadolinium garnet (GGG) substrate by liquid phase epitaxy. More details about the used sample can be found in [9]. A scheme of the experimental setup is shown in Fig. 1. The measurements are performed using a network analyzer. A range of microwave frequencies is applied on a 50 µm wide input microstrip antenna. The microwave currents create alternating Oersted fields around the input antenna that excite coherent spin waves into the waveguide. The spin waves then propagate through the magnonic crystal structure and are detected using an output microstrip antenna. The transmission loss with respect to the microwave frequency is recorded. The distance between the excitation and the detection antenna is 10 mm. An external magnetic field of 175 mT is applied along the long axis of the waveguide, so that we excite spin waves in the backward volume geometry [15]. To apply a temperature gradient both ends of the waveguide are mounted on a Peltier element each. The local temperatures are monitored using an infrared camera. Thus it can also be confirmed that the gradient is linear along the waveguide.

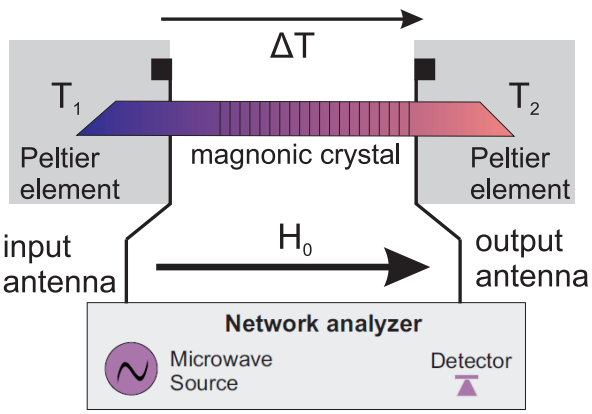

Fig. 1: Sketch of the experimental setup. The magnonic crystal is mounted on two Peltier elements that create the thermal gradient $\Delta T = T_2 - T_1$. An infrared camera was used to monitor the temperature distribution and to control the stability of the gradient. Using a network analyzer the transmission loss of microwaves between an input and an output antenna in a defined frequency range was measured. The position of the magnonic crystal is asymmetric with respect to the antennas for a better excitation of traveling spin waves.

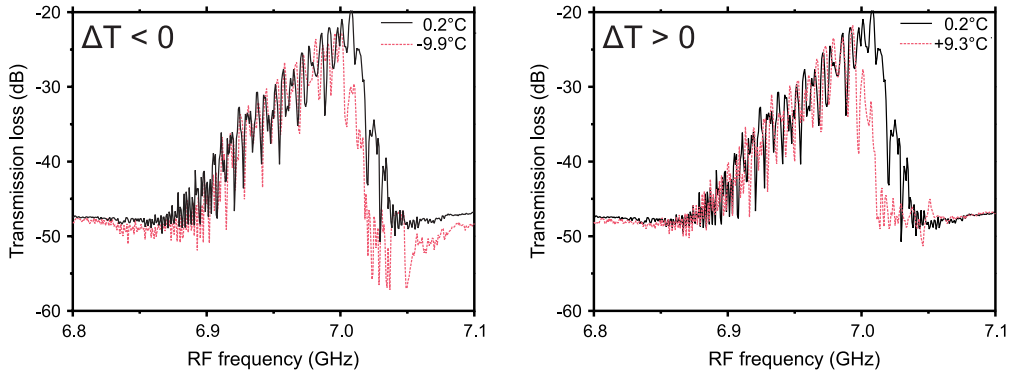

Fig. 2: a) Reference spectra measured on a plane film for negative temperature gradients $\Delta T < 0$, b) for positive temperature gradients $\Delta T > 0$. The temperature in the center between the antennas is set constant to 22 °C. It can be seen that there is no strong influence of the temperature gradient on the reference spectrum. Only a shift in the upper frequency bound for positive gradients can be found due to the forbidden propagation of long spin-wave wavelengths in the gradient (see explanation in the text).

First reference measurements on an unstructured waveguide with same dimensions are performed. The temperature in the center between the antennas is 22 °C. The gradient is applied around this middle temperature. It can be seen in Fig. 2 that there is no strong effect of applying a temperature gradient on the transmission spectrum, which is the dependence of the transmission losses of spin waves on the frequency. Only a shift in the upper bound frequency can be observed in the case of positive gradients (see Fig. 2a), that means a higher temperature at the output antenna compared to the excitation antenna. This takes place because higher frequencies applied at the excitation antenna create long-wavelength spin waves that are only able to travel up to the point where no spin-wave propagation is allowed. It happens due to a shift of the dispersion relation according to the decrease in the saturation magnetization. The dispersion relation changes since the saturation magnetization, which depends on the temperature [14], is directly included there.

We now analyze results of the measurements performed on the magnonic crystal structure described above. In the measurement results shown in Fig. 3 we have kept the temperature at the excitation antenna constant (22 °C) for all measurements. Thus the initially created spin-wave spectrum is the same for all measurements. The measurement with constant temperature along the structure shows the typical influence of the magnonic crystal on the spin-wave propagation (see Fig. 3, upper panels). We see pronounced band gaps as a result of the impedance mismatch for spin waves whose wavelength, or its higher orders, corresponds to the lattice constant. By applying temperature gradients along the waveguide (Fig. 3, middle and lower panels) the bandgaps become broader and the general losses become higher. The gradient leads to a continuous conversion of the wavevector and thus the wavelength "fits" only for one part of the crystal, and not for the whole structure any more. Since a broad spectrum is applied there are more generated spin-wave wavevectors that can find their Bragg resonance condition inside the crystal what makes the band gaps effectively broader. The decrease of the general transmission is understood as a decrease in the detection efficiency. Spin waves that are excited with a certain efficiency with respect to the wavevector are detected with the same efficiency in the case of identical antennas for both processes. Since there is a shift of the wavevector for each applied microwave frequency due to the temperature gradient between the two antennas the detected resulting efficiency becomes smaller.

To obtain a better understanding of the measurement results additional numerical calculations are performed. Here we use a T-matrix formalism [9–11] in which the saturation magnetization M_s is

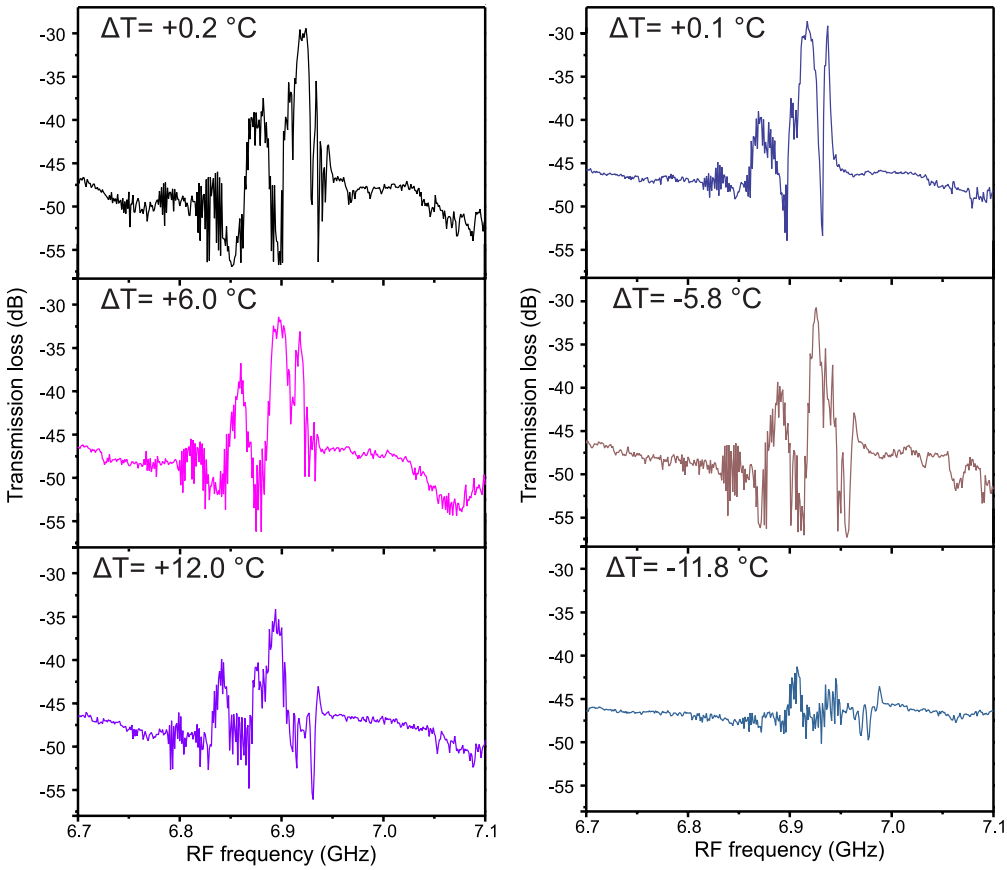

Fig. 3: Measured transmission spectra of the magnonic crystal for positive and negative temperature gradients. A shift in the transmission spectra is seen together with a decrease of the intensity and broadening of the bandgaps. The reference spectra in the upper panels are slightly different due to a repositioning of the sample between the two measurement series.

changed in a step-like manner for every single groove:

$$M_S(\Delta T, n) = M_S(0) + \frac{a}{L} \cdot \Delta T \cdot \frac{dM_S}{dT} \cdot (n-1) + M_{\text{offset}} \quad , \tag{1}$$

where ΔT is the temperature gradient, n the groove number, $M_S(0)$ the saturation magnetization for $T = 0\,°\text{C}$, L the total distance between the antennas (10 mm) and a the lattice constant of the magnonic crystal. The offset M_{offset} is the saturation magnetization initially changed by the propagation from the excitation antenna to the first groove. To get a link between the temperature and the change in the saturation magnetization ($\frac{dM_S}{dT}$) the result from [14] is used. The T-matrix for the crystal can then be written as:

$$T^{mc} = \prod_{n=1}^{N} [T_n^{(1)} \cdot T^{(2)} \cdot T_n^{(3)} \cdot T^{(4)}] \quad . \tag{2}$$

The T-matrix for the whole magnonic crystal T^{mc} is a matrix product of the T-matrices for every single groove. $T_l^{(1)}$ and $T_l^{(3)}$ describe the groove number dependent propagations of spin waves between the grooves and inside the grooves, where the YIG thickness is reduced. $T^{(2)}$ and $T^{(4)}$

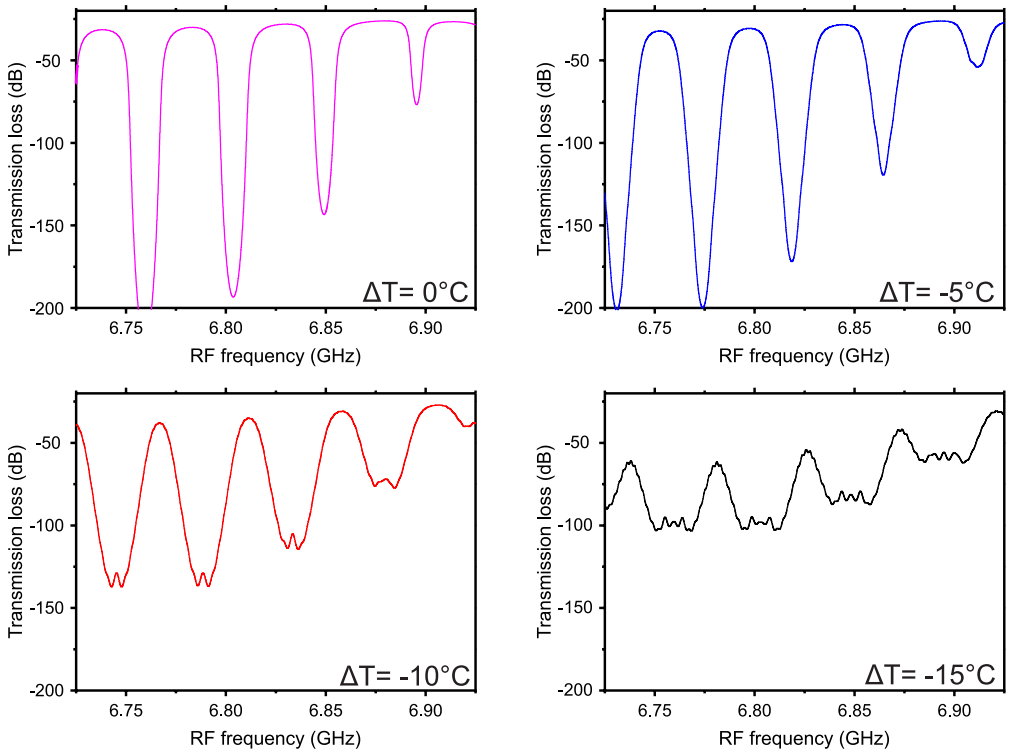

Fig. 4: Results of the numerical calculations using the modified T-matrix formalism. The results show a negative temperature gradient with steps of 5 °C. It can be seen that the bandgaps become broader, but the maximal transmission loss decreases. Furthermore the maximum level decreases. The modulation inside the bandgaps is due to a limited number of grooves inside the crystal.

imply the behavior at the junctions and are the same for all grooves. The relative transmitted power is then written as the inverse square of the absolute value of the diagonal elements:

$$P_{tr} = \frac{1}{|T_{11}^{mc}|^2} = \frac{1}{|T_{22}^{mc}|^2} \quad . \tag{3}$$

The initial dispersion relation (BVMSW) can be found for the case without temperature gradient using the approximated formula [15, 16]:

$$f = \gamma \sqrt{H_0 (H_0 + 4\pi M_S \frac{1 - \exp(-\sqrt{(\pi d/w)^2 + (kd)^2})}{\sqrt{(\pi d/w)^2 + (kd)^2}})} \quad , \tag{4}$$

where H_0 is the externally applied magnetic field, M_S the saturation magnetization, d is the thickness of the waveguide and w its width.

Compared to the experimental data we can see very deep bandgaps of down to a level of $-200\,\mathrm{dB}$ for the case of $\Delta T = 0\,^\circ\mathrm{C}$ (see Fig. 4). The minimum level in the experiment is around $-60\,\mathrm{dB}$ due to a direct electromagnetic leakage between the two antennas that is neglected in the calculations. By applying a temperature gradient the bandgaps become less deep, but broader. Furthermore a modulation inside the bandgaps can be seen. This modulation is due to the limited number of grooves in the magnonic crystal structure. As already mentioned above the increased number of wavevectors that can find their Bragg resonance condition inside the crystal with applied thermal gradient makes the bandgaps broader. On the other hand the bandgaps do not reach anymore that

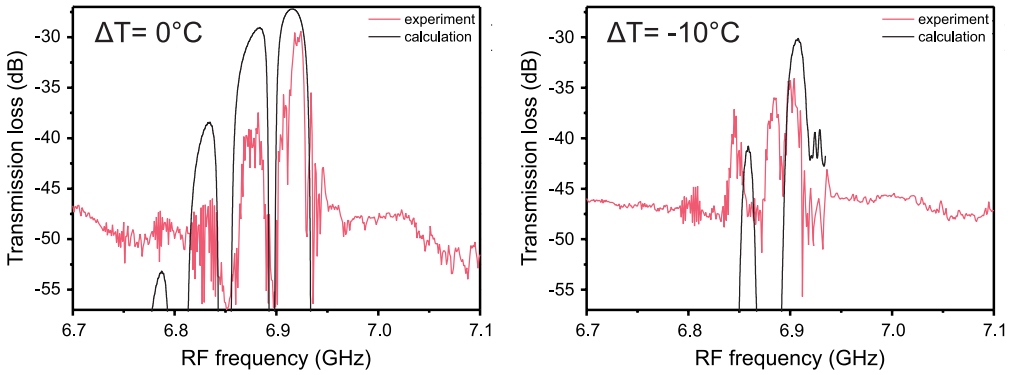

Fig. 5: Comparison between measured and calculated spin-wave spectra of the magnonic crystal with (right panel) and without (left panel) thermal gradients.

high maximal transmission loss since there is no single wavevector that is reflected in the whole crystal structure anymore at once.

The calculated transmission spectra can be refined by implying the excitation- and detection efficiency of the microstrip antennas. This leads to a correspondence with the measured results as it is shown in Fig. 5. It can be seen that there is a good match with the experimental results only if there is no temperature gradient applied. For an applied gradient there is a mismatch, where the second bandgap is not at the same position as in the experiment. The results show that the continuous transformation of spin waves must be taken into account. Finally the general behavior of the calculations corresponds to the experimental data.

In conclusion, the results show that a magnonic crystal does not immediately lose its properties in a thermal gradient, but there is a continuous change with increasing gradients. For a magnonic crystal used as a logic device one must take into account that the properties of the system will change if heat generation appears. A global temperature change lets the bandgaps shift in their position and an applied temperature gradient leads to a change in the functionality. Further investigations of spin waves in such a system contain BLS measurements to obtain more information about the spatial behavior, especially in terms of reflection processes.

We gratefully acknowledge financial support by Deutsche Forschungsgemeinschaft (DFG) within priority program 1538 “Spin Caloric Transport” (project VA 735/1-2).

References

[1] M. Krawczyk, D. Grundler, *Review and prospects of magnonic crystals and devices with reprogrammable band structure*, J. Phys.: Condens. Matter **26**, 123202 (2014).

[2] A.V. Chumak, T. Neumann, A.A. Serga, B. Hillebrands, M.P. Kostylev, *A current-controlled, dynamic magnonic crystal*, J. Phys. D: Appl. Phys. **42**, 205005 (2009).

[3] A.V. Chumak, V.S. Tiberkevich, A.D. Karenowska, A.A. Serga, J.F. Gregg, A.N. Slavin, B. Hillebrands, *All-linear time reversal by a dynamic artificial crystal*, Nat. Commun. **1**, 141 (2010).

[4] A.V. Chumak, V.I. Vasyuchka, A.A. Serga, M.P. Kostylev, V.S. Tiberkevich, B. Hillebrands, *Storage-recovery phenomenon in magnonic crystal*, Phys. Rev. Lett. **108**, 257207 (2012).

[5] A.V. Chumak, A.A. Serga, B. Hillebrands, *Magnon transistor for all-magnon data processing*, Nat. Commun. **5**, 4700 (2014).

[6] J. Topp, D. Heitmann, M.P. Kostylev, D. Grundler, *Making a reconfigurable artificial crystal by ordering bistable magnetic nanowires*, Phys. Rev. Lett. **104**, 207205 (2010).

[7] A. Kirihara, K. Uchida, Y. Kajiwara, M. Ishida, Y. Nakamura, T. Manako, E. Saitoh, S. Yorozu, *Spin-current-driven thermoelectric coating*, Nat. Mater. **11**, 686-689 (2012).

[8] S.A. Nikitov, Ph. Tailhades, C.S. Tsai, *Spin waves in periodic magnetic structures - magnonic crystals*, J. Magn. Magn. Mater. **236**, 320-330 (2001).
[9] A.V. Chumak, A.A. Serga, B. Hillebrands, M.P. Kostylev, *Scattering of backward spin waves in a one-dimensional magnonic crystal*, Appl. Phys. Lett. **93**, 022508 (2008).
[10] A.V. Chumak, A.A. Serga, S. Wolff, B. Hillebrands, M.P. Kostylev, *Design and optimization of one-dimensional ferrite-film based magnonic crystals*, J. Appl. Phys. **105**, 083906 (2009).
[11] A.V. Chumak, P. Pirro, A.A. Serga, M.P. Kostylev, R.L. Stamps, H. Schultheiss, K. Vogt, S.J. Hermsdoerfer, B. Laegel, P.A. Beck, B. Hillebrands, *Spin-wave propagation in a microstructured magnonic crystal*, Appl. Phys. Lett. **95**, 262508 (2009).
[12] G. Gubbiotti, S. Tacchi, M. Madami, G. Carlotti, A.O. Adeyeye, M. Kostylev, *Brillouin light scattering studies of planar metallic magnonic crystals*, J. Phys. D: Appl. Phys. **43**, 264003 (2010).
[13] B. Obry, P. Pirro, T. Brächer, A.V. Chumak, J. Osten, F. Ciubotaru, A.A. Serga, J. Fassbender, B. Hillebrands, *A micro-structured ion-implanted magnonic crystal*, Appl. Phys. Lett. **102**, 202403 (2013).
[14] B. Obry, V.I. Vasyuchka, A.V. Chumak, A.A. Serga, B. Hillebrands, *Spin-wave propagation and transformation in a thermal gradient*, Appl. Phys. Lett. **101**, 192406 (2012).
[15] D.D. Stancil, A. Prabhakar, *Spin waves: theory and applications*, Springer, Berlin (2009).
[16] A.A. Serga, A.V. Chumak, B. Hillebrands, *YIG magnonics*, J. Phys. D: Appl. Phys. **43**, 264002 (2010).

4.16 Microwave-induced spin currents in ferromagnetic-insulator | normal-metal bilayer system

M. Agrawal, A.A. Serga, V. Lauer, E.Th. Papaioannou, B. Hillebrands, and V.I. Vasyuchka

The generation of a pure spin current in ferromagnet | normal metal (FM | NM) systems has attracted a great attention recently [2–5]. The spin Seebeck effect [6] is one route to generate spin current by applying a heat current to ferromagnets. In particular, the longitudinal spin Seebeck effect (LSSE) [7] is of much importance due to its technologically promising applications in energy harvesting [8] and position sensing [9]. Keeping the future application in focus, a comparative study of the spin current direction (flow) for different spin-current-generation processes like spin pumping (SP) and spin Seebeck effect (SSE) is very crucial. In previous studies, the direction of the spin current in these processes has been determined by combining the FMR technique with additional dc/ac or Peltier based heating techniques [4]. Here, we demonstrate microwaves as a simple-and-controlled tool to study these processes simultaneously in a single experiment. Our results show that in a FM|NM system, the spin current flows from the FM to the NM in the case of SP process, while the flow reverses for the LSSE provided that the NM is hotter than the FM. Moreover, the strength of spin current generated by spin pumping process depends on the intensity of spin waves excited in the FM.

The experiment was conducted using a bilayer of a magnetic insulator, Yttrium Iron Garnet (YIG), and a normal metal, Platinum (Pt). The sample structure consists of a 6.7 µm-thick YIG film of dimensions 14 mm×3 mm. The film was grown by liquid phase epitaxy on a 500 µm-thick Gallium Gadolinium Garnet (GGG) substrate. A 10 nm-thick Pt strip (dimensions 3 mm×100 µm) was deposited on top of the chemically-cleaned YIG-film-surface by molecular beam epitaxy at a growth rate of 0.05 nm/s. A 0.6 mm-wide and 17 µm-thick copper (Cu) microstrip antenna was fabricated on a dieletric substrate to apply microwaves to the YIG|Pt sample. To achieve a maximum microwave heating efficiency by eddy currents in the thin metal-film (Pt), the Pt-covered surface of the sample was placed closest to the micro-stripline. To avoid any galvanic contact, an insulation layer was inserted in between the sample and the micro-stripline. Gold wires were used to connect Pt with the external circuit.

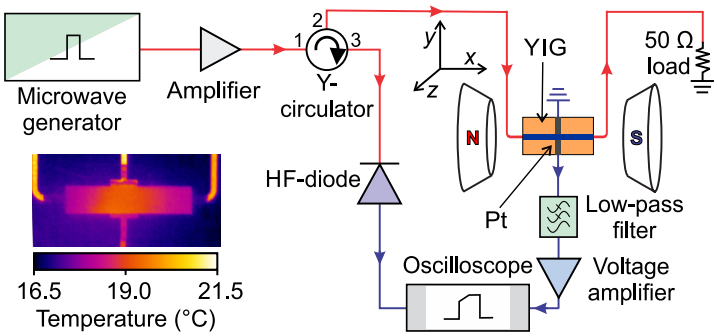

Fig. 1: A schematic diagram of the experimental setup. Microwaves were employed to heat the 10 nm-thick Pt strip grown over a 6.7 µm-thick YIG film mounted on top of the micro-stripline antenna. The reflected microwaves were examined on an oscilloscope. The inverse spin Hall voltage generated in the Pt strip was measured by the oscilloscope. The inset shows an infrared thermal image of the sample obtained by heating of the Pt strip using continuous microwaves.

This work has been recently published in Applied Physics Letters [1].

A schematic sketch of the experimental setup is depicted in Fig. 1. Microwaves from a generator were amplified (+30 dB) and guided to the sample structure. The microwaves are absorbed by the Pt metal strip and start to heat it up. As a result of this, a thermal gradient along the $+z$-direction was established in the sample. The reflected microwaves from the micro-stripline were collected by connecting a Y-circulator to the microwave circuit-line. The reflected microwaves were rectified by a high-frequency (HF) diode and monitored on an oscilloscope of bandwidth 350 MHz. The YIG film was magnetized in plane by an applied magnetic field $\mu_0 H$ along the x-axis.

The perpendicular thermal gradient in the YIG|Pt bilayer generates a spin current along the thermal gradient (z-axis) in the system due to the LSSE. In the normal metal Pt, which has high spin-orbital interaction, the spin current converts into a charge current by the inverse spin Hall effect (ISHE) [10] given as $\mathbf{J}_{\mathrm{ISHE}} \propto \mathbf{J}_{\mathrm{s}} \times \sigma$, where $\mathbf{J}_{\mathrm{s}}$ is the spin current, and σ the spin polarization. The generated charge current along the y-axis establishes a potential difference in the Pt strip which is amplified by a low-noise amplifier with bandwidth 200 MHz and observed on the oscilloscope.

In our experiment, continuous microwave measurements were carried out at a fixed frequency of 6.8 GHz by varying the magnetic field. In Fig. 2, the inverse spin Hall voltage V_{ISHE} in Pt is plotted versus the applied magnetic field $\mu_0 H$. Clearly, three features can be noticed here: (i) two peaks with opposite polarities at the applied magnetic fields of + 168.6 mT and - 168.6 mT, (ii) their unequal amplitude, and (iii) an offset for all non-resonant magnetic fields having an opposite polarity to the peaks. The first feature can be understood as the spin pumping process by spin waves excited close to ferromagnetic resonance (FMR) in the YIG film [11–13]. Here, the FMR conditions were achieved for both positive and negative magnetic field values. Respective to these fields, a spin current is injected into the Pt strip by the spin pumping process. The inverse spin Hall voltage generated in the Pt metal is given by $V_{\mathrm{ISHE}} \propto \theta_{\mathrm{SHE}} (\mathbf{J}_{\mathrm{s}} \times \sigma) \cdot \mathbf{l}$, where θ_{SHE} denotes the spin Hall angle and $\mathbf{l}$ is a vector along the length of the Pt strip. The direction of spin polarization, σ depends on the direction of the magnetic field. Therefore, on inverting the direction of magnetic field, the polarity of V_{ISHE} reverses.

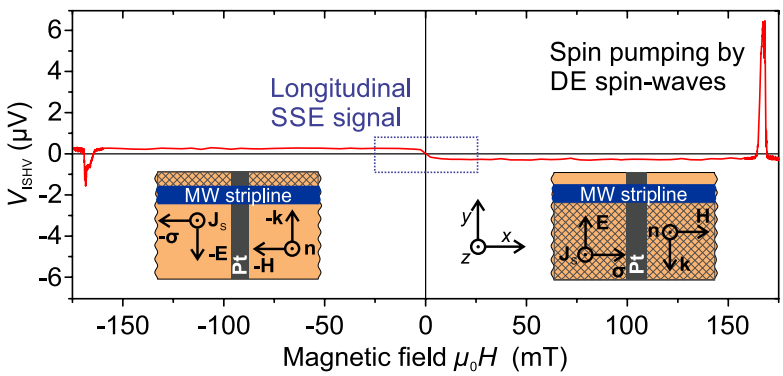

Fig. 2: The inverse spin Hall voltage (V_{ISHE}) generated in the Pt strip is plotted as a function of the applied magnetic field $\mu_0 H$. The asymmetry in the amplitude of V_{ISHE} at FMR-magnetic fields arises due to an unequal efficiency of Damon-Eshbach spin-waves excitation (shaded area) for the two opposite directions of the applied magnetic field as shown in the insets.

In order to interpret the second feature of the spectrum, i.e., the unequal amplitude of the signals, it is important to discuss the spin-wave mode excited in the YIG film for the given experimental geometry. As it is clear from the sample orientation, shown in Fig. 1 and inset to Fig. 2, the spin waves excited by the Oersted field of the micro-stripline propagate along the y-axis, perpendicular to the applied magnetic field along the x-axis. These spin waves with wave vector $\mathbf{k} \perp \mathbf{H}$ are known as magnetostatic surface spin waves (MSSW) or Damon-Eshbach (DE) spin waves [14]. The DE spin waves are nonreciprocal spin waves. They travel along a direction given by $\hat{\mathbf{k}} = \hat{\mathbf{H}} \times \hat{\mathbf{n}}$, where $\mathbf{n}$ represents the normal to the film surface. Therefore, the propagation of these spin waves on any

surface of a film can be reversed by inverting the magnetic field direction.

In the described experiment, when a magnetic field is applied along the $+x$-direction, the DE-spin waves, in the magnetic film surface close to the micro-stripline, are effectively excited along the $-y$-direction ($\hat{\mathbf{k}} = \mathbf{x} \times \mathbf{z}$) with respect to the micro-stripline as shown in the inset to Fig. 2. Contrarily, when the magnetic field is applied along the $-x$-direction, the spin waves propagate along the $+y$-axis. If the YIG film is not assembled symmetrically around the micro-stripline, as the case here, the effective YIG film area, where spin waves are excited, will be unequal for the two opposite magnetic fields as shown in the inset to Fig. 2. As the strength of the V_{ISHE} signal is proportional to the intensity of spin waves in the system [16], an unequal amplitude of V_{ISHE} is observed in the experiment. Alike measurements performed by displacing the YIG film reveal that the amplitude of the spin pumping signals can be altered by varying the relative position of the YIG film with respect to the micro-stripline. Therefore, it can be concluded that the unidirectional nature of the DE spin waves originates the asymmetry of the ISHE signal [15].

The third feature, i.e., an offset for non-resonant magnetic fields, is attributed to the longitudinal spin Seebeck effect. A similar kind of signal could also be produced by the anomalous Nernst effect in Pt due to the fact that Pt, in contact with a magnetic material, can be magnetized by the proximity effect. However, recent observations [17, 18] show that any such possibility in the YIG | Pt system will lead to a rather small contribution here. The polarity of the LSSE signal inverts with the direction of the magnetic field. However, note that for a same direction of the magnetic field, the LSSE signal has an opposite polarity than that of the signal at FMR. This evidence wipes out the possibility of non-resonant spin pumping in the system. When Pt is heated by microwave absorption, a thermal gradient (∇T_z) develops from YIG to Pt, normal to the interface. The thermal gradient generates a spin current that flows along the z-axis. Since Pt is hot, the spin current generated due to the longitudinal SSE ($\mathbf{J}_s \propto -\nabla T$) flows from Pt to YIG [19, 20], contrary to the spin pumping where the spin current flows from YIG to Pt [21]. This argument assists in understanding the opposite polarities of the resonant (spin pumping) and the non-resonant (longitudinal SSE) inverse-spin-Hall voltages (V_{ISHE}) as observed in Fig. 2. As discussed above, the non-resonant V_{ISHE} signal is attributed to the longitudinal SSE; henceforth, the non-resonant V_{ISHE} signal will be denoted as V_{LSSE}.

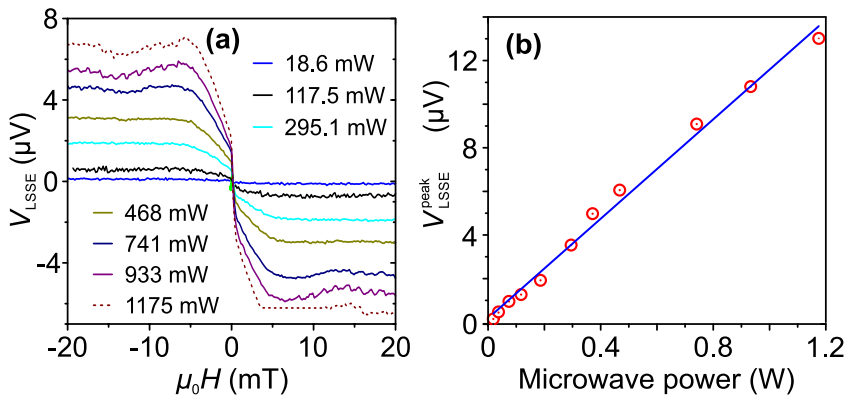

Fig. 3: (a) Plotted is V_{LSSE} versus the applied magnetic field for various applied microwave powers. (b) The peak-to-peak amplitude of V_{LSSE} is plotted as a function of the applied microwave power. The peak-to-peak amplitude scales linearly with the microwave power.

Magnetic-field-scans for various microwave input powers were carried out to study the impact of the thermal gradient. In Fig. 3, V_{LSSE} is plotted versus the magnetic field for various applied microwave powers. On increasing microwave power, the temperature in the Pt strip increases which enlarges the thermal gradient close to the YIG|Pt interface leading to injection of a larger spin current ($\mathbf{J}_s \propto -\nabla T$) into the YIG film [7, 19, 20]. A larger spin current generates a higher

V_{LSSE} signal highlighted in Fig. 3b. The peak-to-peak amplitude of V_{LSSE} scales linearly with the applied microwave power which verifies that the signal originates from the heating produced in Pt shown in the inset to Fig. 1.

In summary, microwaves are presented as a perspective heating technique to generate a thermal gradient in ferromagnetic insulator|normal metal systems to study the longitudinal spin Seebeck effect. The measurements provide crucial information about the relative direction of the spin current flow in the spin pumping and longitudinal SSE processes. The experiment exhibits that in the process of the longitudinal SSE, a spin current flows from the normal metal (hot) to the ferromagnet (cold) while in the case of spin pumping, the flow is opposite.

We acknowledge financial support by Deutsche Forschungsgemeinschaft (SE 1771/4) within Priority Program 1538 “Spin Caloric Transport”, and technical support from the Nano Structuring Center, TU Kaiserslautern.

References

[1] M. Agrawal, A.A. Serga, V. Lauer, E.Th. Papaioannou, B. Hillebrands, V.I. Vasyuchka, *Microwave-induced spin currents in ferromagnetic-insulator|normal-metal bilayer system*, Appl. Phys. Lett. **105**, 092404 (2014).

[2] R.L. Stamps, S. Breitkreutz, J. Åkerman, A.V. Chumak, Y. Otani, G.E.W. Bauer, J.U. Thiele, M. Bowen, S.A. Majetich, M. Kläui, I.L. Prejbeanu, B. Dieny, N.M. Dempsey, B. Hillebrands, *The 2014 Magnetism Roadmap*, J. Phys. D: Appl. Phys. **47**, 333001 (2014).

[3] G.E.W. Bauer, E. Saitoh, B.J. van Wees, *Spin caloritronics*, Nat. Mater. **11**, 391 (2012).

[4] M. Schreier, G.E.W. Bauer, V.I. Vasyuchka, J. Flipse, K. Uchida, J. Lotze, V. Lauer, A. Chumak, A. Serga, S. Daimon, T. Kikkawa, E. Saitoh, B.J. van Wees, B. Hillebrands, R. Gross, S.T.B. Goennenwein, *Sign of inverse spin Hall voltages generated by ferromagnetic resonance and temperature gradients in yttrium iron garnet|platinum bilayers*, *arXiv:1404.3490v1*.

[5] M. Agrawal, V.I. Vasyuchka, A.A. Serga, A. Kirihara, P. Pirro, T. Langner, M.B. Jungfleisch, A.V. Chumak, E.Th. Papaioannou, B. Hillebrands, *Role of bulk-magnon transport in the temporal evolution of the longitudinal spin-Seebeck effect*, Phys. Rev. B **89**, 224414 (2014).

[6] K. Uchida, S. Takahashi, K. Harii, J. Ieda, W. Koshibae, K. Ando, S. Maekawa, E. Saitoh, *Observation of the spin Seebeck effect*, Nature **455**, 778 (2008).

[7] K. Uchida, H. Adachi, T. Ota, H. Nakayama, S. Maekawa, E. Saitoh, *Observation of longitudinal spin-Seebeck effect in magnetic insulators* Appl. Phys. Lett. **97**,172505 (2010).

[8] A. Kirihara, K. Uchida, Y. Kajiwara, M. Ishida, Y. Nakamura, T. Manako, E. Saitoh, S. Yorozu, *Spin-current-driven thermoelectric coating*, Nat. Mater. **11**, 686 (2012).

[9] K. Uchida, A. Kirihara, M. Ishida, R. Takahashi, E. Saitoh, *Local spin-Seebeck effect enabling two-dimensional position sensing*, Jpn. J. Appl. Phys. **50**, 120211 (2011).

[10] E. Saitoh, M. Ueda, H. Miyajima, G. Tatara, *Conversion of spin current into charge current at room temperature: Inverse spin-Hall effect*, Appl. Phys. Lett. **88**,182509 (2006).

[11] Y. Kajiwara, K. Harii, S. Takahashi, J. Ohe, K. Uchida, M. Mizuguchi, H. Umezawa, H. Kawai, K. Ando, K. Takanashi, S. Maekawa, E. Saitoh, *Transmission of electrical signals by spin-wave interconversion in a magnetic insulator*, Nature **464**, 7286 (2010).

[12] M. Costache, M. Sladkov, S. Watts, C. van der Wal, B. van Wees, *Electrical detection of spin pumping due to the precessing magnetization of a single ferromagnet*, Phys. Rev. Lett. **97**, 216603 (2006).

[13] K. Ando, J. Ieda, K. Sasage, S. Takahashi, S. Maekawa, E. Saitoh, *Electric detection of spin wave resonance using inverse spin-Hall effect*, Appl. Phys. Lett. **94**, 262505 (2009).

[14] R.W. Damon, J.R. Eshbach, *Magnetostatic modes of a ferromagnet slab*, J. Phys. Chem. Solids **19**, 308 (1961).

[15] R. Iguchi, K. Ando, Z. Qiu, T. An, E. Saitoh, T. Sato, *Spin pumping by nonreciprocal spin waves under local excitation*. Appl. Phys. Lett. **102**, 022406 (2013).

[16] C. Sandweg, Y. Kajiwara, A.V. Chumak, A.A. Serga, V.I. Vasyuchka, M.B. Jungfleisch, E. Saitoh, B. Hillebrands, *Spin Pumping by parametrically excited exchange magnons*, Phys. Rev. Lett. **106**, 216601 (2011).

[17] S. Gepraegs, S. Meyer, S. Altmannshofer, M. Opel, F. Wilhelm, A. Rogalev, R. Gross, S.T.B. Goennenwein. *Investigation of induced Pt magnetic polarization in* $Pt/Y_3Fe_5O_{12}$ *bilayers*, Appl. Phys. Lett. **101**, 262407 (2012).

[18] T. Kikkawa, K. Uchida, Y. Shiomi, Z. Qiu, D. Hou, D. Tian, H. Nakayama, X.F. Jin, E. Saitoh, *Longitudinal spin Seebeck effect free from the proximity Nernst effect*, Phys. Rev. Lett. **110**, 067207 (2013).
[19] J. Xiao, G.E.W. Bauer, K. Uchida, E. Saitoh, S. Maekawa, *Theory of magnon-driven spin Seebeck effect*, Phys. Rev. B **81**, 214418 (2010).
[20] S.M. Rezende, R.L. Rodríguez-Suárez, R.O. Cunha, A.R. Rodrigues, F.L.A. Machado, G.A. Fonseca Guerra, J.C. Lopez Ortiz, A. Azevedo, *Magnon spin-current theory for the longitudinal spin-Seebeck effect*, Phys. Rev. B **89**, 014416 (2014).
[21] Y. Tserkovnyak, A. Brataas, G.E.W. Bauer, *Spin pumping and magnetization dynamics in metallic multilayers*, Phys. Rev. B **66**, 224403 (2002).

D. New Materials and Heusler Compounds

The material class of Heusler compounds contains several promising candidates regarding their utilization in the field of *spintronics* and in particular *magnon spintronics*. The major reasons for the interest in Heusler compounds are their high Curie temperature, their high spin polarization, and their low magnetic Gilbert damping.

Spintronics can be regarded as an extension of conventional electronics by using the electrons' spin as an additional degree of freedom for applications in data storage and sensing. Spintronic devices mainly rely on magneto-resistive effects such as the giant magneto resistance and tunneling magneto resistance. For the optimization of these effects, it is crucial to find materials with a high spin polarization such as the Heusler compounds. The field of magnon spintronics can mainly benefit from the low Gilbert damping in some of the Heusler compounds. The major motivation behind magnon spintronics is an energy-efficient information transport and processing that is purely based on magnons, which are the fundamental excitations in a magnetic material. A major challenge in magnon spintronics is the identification and development of suitable low-damping materials for the realization of magnon conduits on the microscale. This challenge can be addressed by the utilization of Heusler compounds.

Heusler compounds have the general composition X_2YZ or XYZ, where X and Y are transition metals, and Z is an element out of the main groups III-V. One of the most promising classes of Heusler materials is given by the cobalt-based compounds with the composition Co_2YZ. The reason for both, the high spin polarization as well as the low Gilbert damping, is the half-metallic character of Heusler compounds. Half metallicity describes the different features in the band structure of minority and majority electrons close to the Fermi energy. For the minority electrons, a band gap can be found at the Fermi energy. In contrast to this, the majority spin channel exhibits a finite density of states at the Fermi level and, thus, metallic character.

Our group is part of the joint Japanese-German research unit *Advanced Spintronic Materials and Transport Phenomena* (ASPIMATT), which addresses the development, the characterization, and the optimization of Heusler materials for the utilization in spintronics and magnon spintronics. The work package addressed by our group covers *nonlinear spin-wave dynamics and radiation properties of small Heusler devices* in the field of magnon spintronics.

Our recent experiments with ferromagnetic $Co_2Mn_{0.6}Fe_{0.4}Si$ revealed the great potential of this Heusler compound for future magnon spintronic applications. In Report 4.17 "All-optical characterization of the spintronic Heusler material $Co_2Mn_{0.6}Fe_{0.4}Si$", we present an extensive all-optical study of the material parameters, and in particular the Gilbert damping in individual microstructures, which is determined by time-resolved measurements of decaying spin-wave dynamics by means of Brillouin light scattering (BLS) microscopy.

Report 4.18 "Control of the effective damping in Heusler/Pt microstructures" presents our latest results on both decrease and increase of the spin-wave damping in a Co_2MnSi microdot by the spin-transfer-torque of a pure spin current created via the spin-Hall effect in the adjacent Pt layer. The variations in the effective damping are detected through BLS measurements of the intensity of spin waves excited by the parallel parametric pumping technique.

In Report 4.19 "Influence of a non-Gilbert damping mechanism on the nonlinear spin dynamics in a ferromagnetic Heusler compound", we analyze peculiarities of a four-magnon splitting phenomenon in thin $Co_2Mn_{0.6}Fe_{0.4}Si$ films and conclude about a strong non-Gilbert contribution to the total magnon relaxation rate caused by magnon-magnon scattering processes.

D. Neue Materialien und Heusler-Legierungen

In der Materialklasse der Heusler-Verbindungen finden sich zahlreiche vielversprechende Kandidaten hinsichtlich der Verwendung in den Feldern der *Spintronik* und der *Magnonspintronik*. Die Hauptgründe für das Interesse an den Heusler-Materialien sind ihre hohe Curie-Temperatur, ihre hohe Spinpolarisation und ihre niedrige magnetische Gilbert-Dämpfung.

Die Spintronik stellt eine Erweiterung konventioneller Elektronik dar, die durch die Nutzung des Elektronenspins als zusätzlichen Freiheitsgrad zur Datenspeicherung und in der Sensorik realisiert wird. Spintronische Bauelemente stützen sich hauptsächlich auf Effekte wie den Riesenmagnetowiderstand oder den Tunnelmagnetowiderstand. Die Optimierung dieser Effekte setzt Materialien mit einer hohen Spinpolarisation, wie die Heusler-Verbindungen, voraus. Das Feld der Magnonspintronik kann wiederum hauptsächlich von der niedrigen Gilbert-Dämpfung in Heusler-Materialien profitieren. Die Hauptmotivation hinter der Magnonspintronik ist eine energieeffiziente Datenverarbeitung auf Basis von Magnonen, welche die fundamentalen Anregungen in einem magnetischen Festkörper sind. Eine der großen Herausforderungen der Magnonspintronik ist die Identifizierung und die Entwicklung von geeigneten Materialen für die Realisierung von magnonischen Wellenleitern auf der Mikrometerskala. Diese Herausforderung kann durch die Verwendung von Heusler Materialien angegangen werden.

Heusler-Materialien zeigen eine generelle Zusammensetzung der Form X_2YZ oder XYZ. Hierbei sind X und Y Übergangsmetalle, während Z eine Element aus den Hauptgruppen III-V ist. Eine der interessantesten Untergruppen von möglichen Heusler-Verbindungen ist die Gruppe der Kobalt-basierten Materialien der Form Co_2YZ. Der Grund für die hohe Spinpolarisation sowie auch die geringe Gilbert-Dämpfung liegt in der halbmetallischen Natur der Heusler-Verbindungen. Dieser halbmetallische Charakter beschreibt die Unterschiede in der Bandstruktur der Majoritäts- und Minoritätsladungsträger insbesondere nahe der Fermi-Energie. Für die Minoritätselektronen lässt sich eine Bandlücke an der Fermi-Kante beobachten, während die Bandstruktur der Majoritätselektronen dort eine endliche Zustandsdichte, und damit metallischen Charakter, aufweist.

Unsere Gruppe ist Teil der japanisch-deutschen Forschergruppe *Advanced Spintronic Materials and Transport Phenomena* (ASPIMATT), welche die Entwicklung, Charakterisierung und Optimierung von Heusler-Materialien für die Verwendung in Spintronik und Magnonspintronik zum Ziel hat. Das Arbeitspaket, das in unserer Gruppe bearbeitet wird, trägt den Titel *Nonlinear spin-wave dynamics and radiation properties of small Heusler devices* und befasst sich mit dem Gebiet der Magnonspintronik.

Kürzlich durchgeführte Experimente zeigen das große Potential der Legierung $Co_{40}Fe_{20}B_{20}$ bezüglich zukünftiger Anwendungen in Spintronik oder Magnonspintronik. In Bericht 4.17 “All-optical characterization of the spintronic Heusler material $Co_2Mn_{0.6}Fe_{0.4}Si$”, präsentieren wir eine ausgedehnte Studie der Materialparameter und insbesondere der Gilbertdämpfung in speziell angefertigten Mikrostrukturen, die durch zeitaufgelöste Messungen der Dynamik einer zerfallenden Spinwellen mit Hilfe der Brillouin-Lichtstreuung (BLS) durchgeführt wird.

Bericht 4.18 “Control of the effective damping in Heusler/Pt microstructures” präsentiert unsere jüngsten Ergebnisse zur Verminderung der Spinwellendämpfung in einem Co_2MnSi Mikropunkt durch den Spin-Transfer-Torque eines reinen Spinstromes, der durch den Spin-Hall-Effekt in der aufgetragenen Pt-Schicht erzeugt wird.

In Bericht 4.19 “Influence of a non-Gilbert damping mechanism on the nonlinear spin dynamics in a ferromagnetic Heusler compound” analysieren wir Besonderheiten eines Viermagnonen-

Aufspaltungsphänomens in dünnen $Co_2Mn_{0.6}Fe_{0.4}Si$-Filmen und schließen daraus auf einen ausgeprägten, von der Gilbert-Dämpfung unabhängigen Beitrag zu der gesamten Magnonenrelaxation, der durch Magnon-Magnon-Streuprozesse verursacht wird.

4.17 All-optical characterization of the spintronic Heusler material $Co_2Mn_{0.6}Fe_{0.4}Si$

T. Sebastian, B. Obry†, T. Brächer, P. Pirro, D.A. Bozhko, A.A. Serga, and B. Hillebrands*

In collaboration with Y. Kawada, H. Naganuma, M. Oogane, and Y. Ando, Department of Applied Physics, Graduate School of Engineering, Tohoku University, Sendai 980-8579, Japan.

**Current affiliation: Institut für Ionenstrahlphysik und Materialforschung, Helmholtz-Zentrum Dresden-Rossendorf, 01328 Dresden, Germany*
†Current affiliation: Deutsche ACCUmotive GmbH & Co. KG, 73230 Kirchheim u. Teck, Germany

In the last years, the class of cobalt-based full Heusler compounds was subject to intensive research efforts related to the fields of spintronics and magnon spintronics [1–3]. Related studies range from basic research – including ab-initio calculations and the fabrication of novel materials – to application-oriented scenarios in the field of information technology utilizing the advantages given by this class of materials.

The huge interest in the cobalt-based Heusler compounds is mainly based on the half-metallic character of at least some of the possible compositions. This half-metallicity is a result of the different character of the minority- and majority-spin electrons. While the majority-spin electrons exhibit a metallic band structure with finite density of states at the Fermi level, the minority-spin electrons have a semi-conductor-like nature with a band gap at the Fermi level. As a result of this band structure, many cobalt-based Heusler compounds exhibit a remarkably high spin polarization compared to conventional 3d-ferromagnets and compounds. The high spin polarization and the high Curie temperature of the compounds make them promising candidates for spintronic applications in data storage or sensing devices. Another consequence of the half-metallicity is the low Gilbert damping of some of the compounds [4, 11, 19]. A low Gilbert damping opens the perspective for spin-torque driven spin dynamics [5–7] as well as for information processing using the concepts of magnon-spintronics, where information is transported via magnons, the quasi particles of spin waves [8, 9]. In particular, recent experiments indicate that the compound $Co_2Mn_{0.6}Fe_{0.4}Si$ (CMFS) is very suitable for spintronic and magnon spintronic applications [10–14].

For the design and optimization of advanced experimental studies as well as the technical applications, the knowledge of the material parameters is crucial. In this article, we demonstrate an all-optical evaluation of all material parameters that influence spin dynamics in the gigahertz regime via Brillouin light scattering (BLS) spectroscopy, which is the inelastic scattering of photons and magnons. These parameters are the gyromagnetic ratio, the saturation magnetisation, the anisotropy constant, and the exchange constant as well as the spin-wave damping. While the first four of these parameters were determined by wavevector-resolved BLS spectroscopy on a homogeneous thin film [15, 16], the damping parameter was determined via time-resolved BLS microscopy on an individual CMFS microstructure [17, 18]. Of particular interest in this study are the spin-wave damping in an individual microstructure as well as the exchange constant. These parameters are difficult to obtain via alternative standard techniques and have not been reported for CMFS.

For the evaluation of the material parameters, two sample structures A and B for the two exper-

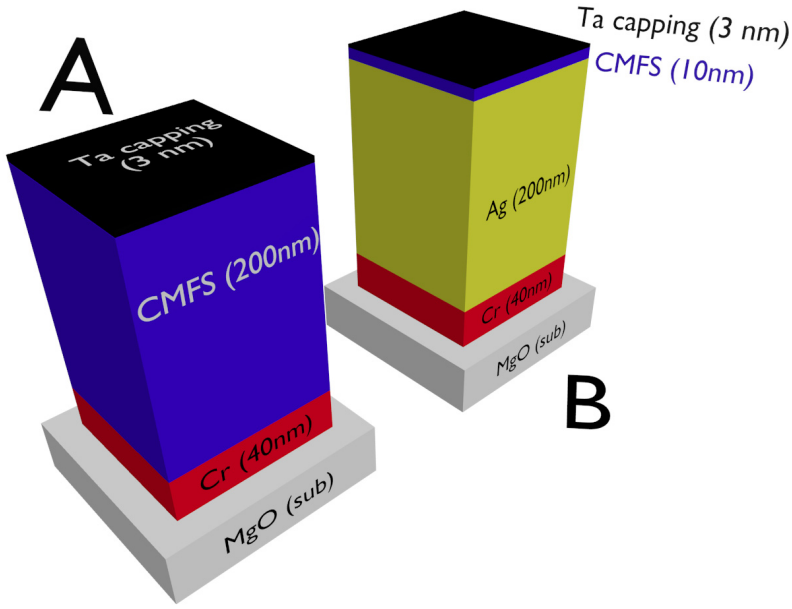

Fig. 1: Layer stacks for the wavevector-resolved (A) as well as for the time-resolved (B) BLS measurements. The thicknesses of the individual layers are indicated in the graph. While layer stack A was used for wavevector-resolved BLS measurements without further patterning, magnetic microstructures were patterned from layer stack B. The Ag in the stacking sequence was used to fabricate antennas for the external excitation of spin dynamics.

imental approaches were realized. The layer stacks A and B, that are presented in Fig. 1, were fabricated via magnetron sputtering on MgO substrates. In both cases, Cr served as a buffer layer to increase the surface flatness and Ta was used as a capping layer to prevent oxidation. The exact stacking sequences as well as the thicknesses of each of the layers is indicated in the corresponding sketches.

Post-deposition annealing was performed after the deposition of the Cr as well as of the CMFS layer for both layer stacks to ensure a high crystalline order of the system. This fabrication process leads to a dominating $L2_1$ order in the CMFS layers. This process is documented very well in previous studies. Therefore, more detailed descriptions of the fabrication and crystal structure of the resulting thin films can be found in previous reports as for example [10–12].

The thickness of layer stack A was chosen to meet the requirements of an investigation via wavevector-resolved BLS with respect to the evaluation of the corresponding material parameters. The rather large thickness of 200 nm allowed for the observation of several different thickness modes for fixed experimental parameters. In the measurements, the sample was used as it is without additional patterning. Via these investigations on the homogeneous CMFS films, the gyromagnetic ratio, the saturation magnetization, the anisotropy field, and the exchange constant were evaluated.

In contrast to these thin-film measurements, the evaluation of the damping was performed via time-resolved BLS microscopy on microstructures patterned from layer stack B. Patterning of the microstructures was achieved in a two-step process of electron-beam lithography and Ar ion milling. In the first step, both topmost layers, the Ta and the 30 nm thick CMFS, were patterned into elliptical microstructures on the remaining homogeneous Ag film. In the second step, an antenna structure was patterned from the 200 nm thick Ag film for the external excitation of spin dynamics in the CMFS microstructures. In the vicinity of the CMFS microstructures, the Ag antenna has a width of 8 µm. To allow for the connection to external microwave circuitry via picoprobe con-

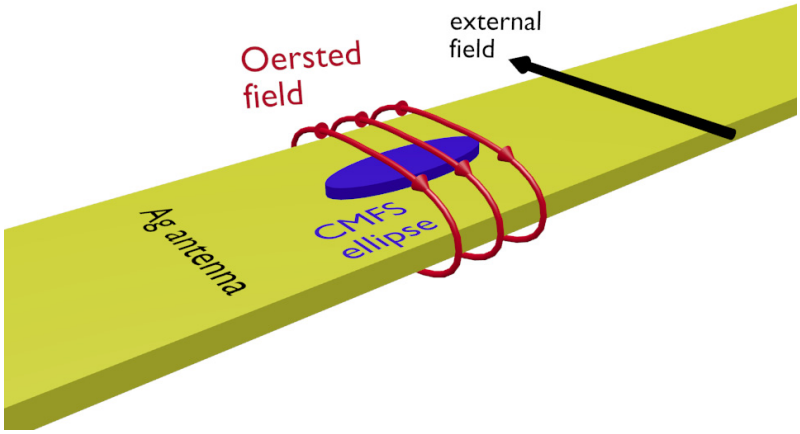

Fig. 2: Sample structure fabricated from layer stack B presented in Fig. 1. Patterning of the 8 µm wide Ag antenna for the external excitation as well as of the CMFS microstructures was performed in a two-step process of electron-beam lithography and Ar milling. The duration of the milling process was controlled via *in-situ* mass-spectrometry. The resulting CMFS structure had a thickness of 30 nm and major and minor axes of 3 µm and 2 µm, respectively.

nectors, this antenna structure broadens towards larger distances from the CMFS elements to form macroscopic contact pads. Both milling processes were controlled via *in-situ* mass-spectrometry of the sputtered material to avoid unintentional sputtering of subjacent materials.

A sketch of the final sample layout patterned from layer stack B can be found in Fig. 2. The details about the external excitation of spin dynamics will be discussed together with the results of the time-resolved BLS microscopy in section.

The excellent frequency resolution offered by electromagnetic microwave characterisation of magnetic materials allows for the determination of material parameters with high accuracy, for example in ferromagnetic resonance (FMR) measurements. Thus, FMR is one of the standard techniques for the evaluation of material parameters like the saturation magnetization, the gyromagnetic ratio, and the anisotropy constants. However, the possibility of wavevector-resolved measurements is strongly limited if using microwave methods. Therefore, the exchange constant - which dominates the spin-wave dispersion for small wavelengths - is hardly accessible.

In contrast, wavevector-resolved BLS is an excellent tool for a full analysis of the spin-wave dispersion relation [16]. In addition, the high sensitivity of BLS allows for the detection of thermally activated spin-wave modes. Thus, no external excitation of spin waves is needed in our study which could restrict the accessible wavevector range. Previous wavevector-resolved BLS studies of Co-based Heusler compounds can be found in references [15, 19].

In the following, we present the determination of the aforementioned CMFS material parameters including the exchange constant via wavevector-resolved BLS. As it was already mentioned, the sample used in this study was a 200 nm thick CMFS thin film. The rather large thickness of the film allows for the observation of several perpendicular standing spin-wave (PSSW) modes across the film thickness in a small frequency range. These PSSWs are - due to their rather small wavelength along the film thickness - good candidates for the evaluation of the exchange constant.

To evaluate the material parameters, spectra of thermally-activated spin waves were investigated for a varying external bias field $H_{\mathrm{ext}} = |\mathbf{H}_{\mathrm{ext}}|$ as well as for a varying incidence angle θ of the probing laser beam and, thus, for a varying in-plane spin-wave wavevector $k_{\mathrm{SW}}^{\parallel} = 4\pi/\lambda \sin\theta$ (with the

laser wavelength $\lambda = 532\,\mathrm{nm}$). The plane of the incidence of the laser light and the external magnetic field $\mathbf{H}_{\mathrm{ext}}$ were oriented perpendicular to each other in all measurements presented here. That fixes the angle between the in-plane component of the spin-wave wavevector and the magnetization at $\varphi = \angle(\mathbf{M}, \mathbf{k}^{\parallel}_{\mathbf{SW}}) = 90°$. This geometry allows for the detection both of the PSSWs modes and of the Damon-Eshbach (DE) surface mode [20, 21].

Approximate analytical expressions for DE spin waves as well as for PSSW modes illustrate the major dependencies of the spin-wave resonances on the material parameters of a magnetic film:

$$f_{\mathrm{DE}} = \mu_0\gamma\sqrt{H_{\mathrm{eff}}\cdot(H_{\mathrm{eff}}+M_{\mathrm{S}}) + \left(\frac{M_{\mathrm{S}}}{2}\right)^2\cdot\left(1-\exp(-2k^{\parallel}_{SW}d)\right)} \quad , \tag{1}$$

$$\begin{aligned} f_{\mathrm{PSSW}} &= \mu_0\gamma\Bigg(\left[H_{\mathrm{eff}} + \frac{2A}{M_{\mathrm{S}}}(k^{\parallel}_{SW})^2 + \frac{2A}{M_{\mathrm{S}}}\left(\frac{p\pi}{d}\right)^2\right] \\ &\times \left[H_{\mathrm{eff}} + M_{\mathrm{S}} + \left(\frac{2A}{M_{\mathrm{S}}} + H_{\mathrm{eff}}\left(\frac{M_{\mathrm{S}}}{H_{\mathrm{eff}}}\frac{d}{p\pi}\right)^2\right)(k^{\parallel}_{SW})^2 + \frac{2A}{M_{\mathrm{S}}}\left(\frac{p\pi}{d}\right)^2\right]\Bigg)^{1/2}, \end{aligned} \tag{2}$$

where d is the film thickness, γ is the gyromagnetic ratio, M_{S} is the saturation magnetization, A is the exchange constant, and H_{eff} represents the effective magnetic field, which consists of the external bias field H_{ext} and the anisotropy field H_{ani}. The out-of-plane components of the spin-wave wavevector are denoted by $p(\pi/d)$. In the case of DE surface waves, the out-of-plane component is purely imaginary. For PSSW modes it is purely real and can be described by the mode number p.

While the analytical solutions to the spin-wave dispersions allow for a qualitative description of the experimental observations, the quantitative analysis of the material parameters requires a more complex modeling. Therefore, we used the numerical models presented in Ref. [22] for the fitting of the experimental data, and, thus, for the estimation of the material parameters of the CMFS film. Figure 3 exemplary shows the spin-wave resonances experimentally observed at an incidence angle $\theta = 37.5°$ in comparison with the corresponding calculations. The numerical modeling is based on a gyromagnetic ratio of $\gamma = 28.7\,\mathrm{GHz/T}$, a saturation magnetization of $M_{\mathrm{S}} = 1000\,\mathrm{kA/m}$, an anisotropy field of $H_{\mathrm{ani}} = 3\,\mathrm{kA/m}$, and an exchange constant of $A = 18\,\mathrm{pJ/m}$. By comparison of Fig. 3a and Fig. 3b one can associate the high intensity BLS peak, which is observed close to $f = 26\,\mathrm{GHz}$, to the DE surface mode, while the other peaks can be attributed to PSSW modes. The higher intensity of the DE peaks is a result of the localization of the spin-wave intensity at the film surface, which is typical for DE surface waves. Since the intensity of the probing laser beam exponentially decreases for increasing penetration depth, the detection of DE surface waves is much more efficient than the detection of the PSSW modes. A second indicator for the nature of the DE mode is its nonreciprocal behaviour: Changing the polarity of the external bias field results in a reversal of the spin-wave propagation direction. Since the magnitude as well as the direction of the spin-wave wavevector is fixed by the geometry of the experiment, DE waves can only be detected for one field polarity. This behavior was observed for the high-intensity mode in the actual experiment.

The validity of our fit is additionally supported by Figure 3c, where the calculated dependencies of the spin-wave frequencies on the external magnetic field perfectly agree with the experimental BLS data.

Thus, we can conclude that the chosen material parameters allow for a self-consistent fit of the experimental data. Furthermore, these parameters are in reasonable agreement with previous stud-

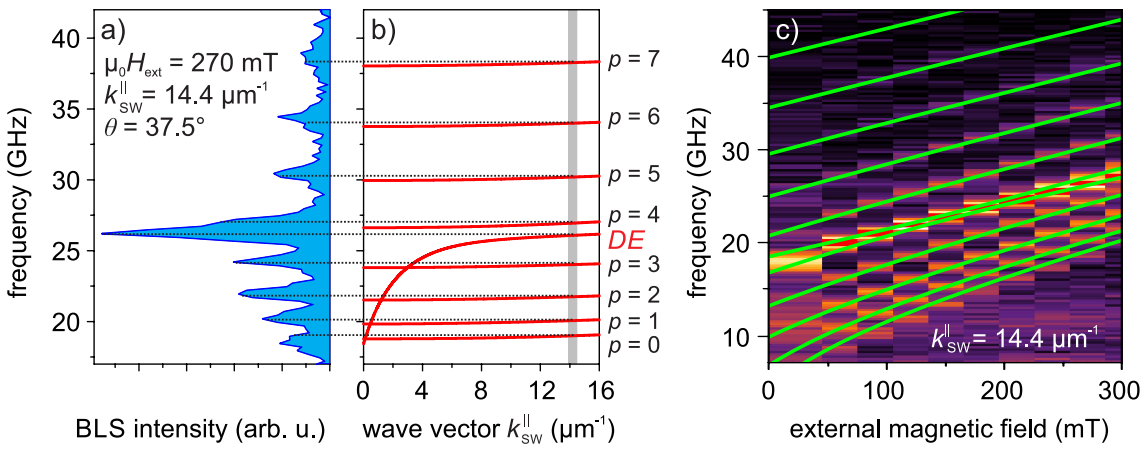

Fig. 3: Experimental data of the wavevector-resolved BLS probing as well as numerical modeling of these data. a) BLS spectra for an incidence angle $\theta = 37.5°$ and an external field of $\mu_0 H_{\text{ext}} = 270\,\text{mT}$. Extraction of the corresponding peak positions for varying angle of incidence θ as well as for different external fields allows for the numerical modeling of the spin-wave spectra by fitting of the material parameters of the CMFS sample: b) shows the dependence of the spin-wave frequency on the in-plane wavevector $k^{\parallel}_{SW}$, while c) illustrates both the experimental and theoretical field dependence of different spin-wave modes. The width of the gray vertical stripe in b) indicates the precision of the experimental determination of the spin-wave wavevector value in our experiment.

ies of CMFS as well as with data for other Co-based Heusler compounds with similar compositions [3, 13–15, 19].

The Gilbert damping in Heusler materials - among all other material parameters - strongly depends on the crystallographic order of the actual sample [23, 24]. The lowest Gilbert damping is usually reported for the highest order, the $L2_1$ state. While the analysis of the crystallographic order by x-ray diffraction and the evaluation of the Gilbert damping via ferromagnetic resonance (FMR) are standard techniques for thin films, the analysis turns out to be more complicated on the microscale [25]. At the same time, it is not self-evident that the crystallographic order and, therefore, the low Gilbert damping are preserved in the patterning process. Recent results on linear and nonlinear spin-wave propagation in CMFS microstructures indicate a still low Gilbert damping [13, 14]. However, a quantitative analysis has not been presented so far. Therefore, the question is, if the Gilbert damping of $\alpha_{\text{lit}} = 3 \times 10^{-3}$ reported in literature [19] for homogeneous CMFS thin films can still be observed on the microscale.

To evaluate the Gilbert damping parameter α via time-resolved BLS microscopy, the sample structure patterned from layer stack B was used (see Fig.1b for the stacking sequence and Fig. 2 for the final sample structure). The investigated element was an ellipse with a thickness of 30 nm and major and minor axes of 3 µm and 2 µm, respectively. For the external excitation of spin dynamics in the CMFS microstructure, microwave currents were applied to the Ag antenna below the magnetic element. As indicated in Fig. 1, the resulting oscillating Oersted field was parallel to the external bias field of $\mu_0 H_{\text{ext}} = 48.5\,\text{mT}$ and, therefore, parallel to the magnetization in the microstructure in all cases. Thus, in this geometry the Oersted field $\mathbf{h}$ cannot exert a torque on the magnetization $\mathbf{M}$ since $\mathbf{M} \parallel \mathbf{h}$. Instead, spin waves were amplified from the thermal level via parallel parametric excitation [26–28].

In this parametric process, microwave photons with frequency f_{MW} couple to the dynamic magnetization of magnons at half of their frequency, namely $f = f_{\text{MW}}/2$. Since parallel parametric amplification is a threshold process, amplification only occurs if the applied microwave power is

strong enough to compensate the damping in the system.

The temporal evolution of the spin-wave intensity in the process of parametric amplification is illustrated in Fig. 4 for two different powers above this threshold. The microwave frequency was fixed at $f_{\mathrm{MW}} = 15\,\mathrm{GHz}$ in both cases. Thus, the amplified and detected spin-wave modes had a frequency of $f = f_{\mathrm{MW}}/2 = 7.5\,\mathrm{GHz}$. Both graphs are subdivided into three different regions. In region I, no microwave power was applied to the antenna and the detected spin-wave intensity, therefore, corresponds to thermal activation.

The actual process of parametric excitation via the microwave power applied to the antenna can be seen in region II (shaded region in Fig. 4). Two different regimes can be distinguished: the rising slope, where the spin-wave intensity increases from the thermal level as well as the dynamic equilibrium with saturated intensity I_0. This observation is characterized by the competition between the applied power and the damping in the system.

At the beginning of the process of parametric excitation, the energy pumped into the system is distributed among all possible spin-wave modes at half of the pumping frequency. In particular, different modes are amplified with different efficiency and, thus, different time constants. The dynamic equilibrium and, thus, a saturation of the spin-wave intensity is determined by nonlinear magnon-magnon interactions as well as the de-phasing between spin dynamics and the dynamic Oersted field $\mathbf{h}$. A detailed discussion of the mechanisms behind the actual amplification as well as of the saturation can be found in additional literature like [29, 30].

However, it is important to note, that in the dynamic equilibrium the available microwave power is consumed by only one spin-wave mode, the dominant mode. Thus, only the intensity of the dominant mode, which is the mode with the lowest spin-wave damping, is above the thermal activation, while the intensity of the other modes dropped to the thermal level of region I.

Region III corresponds to a spin-wave system without external excitation. Therefore, and due to the spin-wave damping, the BLS intensity drops again from the saturation level I_0 of the dominant mode, that was reached in the parametric process in region II. The decay time τ, which can be extracted from the data via the following Eq. (3), will be used to quantify the damping parameter α:

$$I(t) = I_0 \exp\left(-2\frac{t}{\tau}\right) \quad . \tag{3}$$

Since the Gilbert damping refers to the spin-wave amplitude, while the BLS intensity is proportional to the spin-wave intensity, the exponent in Eq. (3) contains the pre-factor 2.

However, at this point it is crucial to consider the influence of our instrument on time-resolved measurements. Since BLS is a frequency-resolved technique, the possible time resolution is affected by the measurement process itself. The frequency resolution of BLS experiments is achieved via a tandem-Fabry-Pérot-interferometer [31]. This instrument consists of two individual Fabry-Pérot-interferometers (FPI), where each of them has to be passed three times by the probing laser beam.

Due to multiple reflections of the photons at the mirrors within each of the FPIs, photons need a certain time to pass the instrument. This time is not negligible with respect to the characteristic time scales of spin dynamics in metallic systems and has to be taken into account in the following evaluation of the experimental data. Therefore, a simple fitting of the decay time τ according to Eq. (3) is not sufficient to estimate the Gilbert damping.

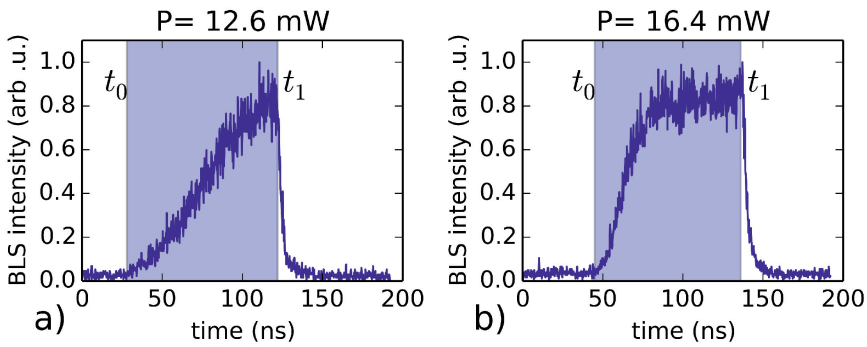

Fig. 4: Time-resolved BLS measurements of the parametric amplification of spin waves from the thermal level for different microwave powers. The microwave power was applied only in the time interval between t_0 and t_1 indicated by the shaded region in the graphs.

A single transmission of photons through one FPI as a function of time can be estimated via the total distance covered within the instrument divided by the speed of light. This total distance is given by the distance of the mirrors d times the number of reflections n until a photon is transmitted. The probability for transmission after n reflections is given by the reflectivity of the mirrors R: $(1-R)\cdot R^{2n}$, where mirror distance and reflectivity are known characteristics of the instrument. The transmission function of the FPI depending on time is

$$P(t) = (1-R)\cdot\sum_{n=0}^{\infty} R^{2n}\cdot\delta\left(t-\frac{2dn}{c}\right) \quad . \tag{4}$$

Thus, the observed time evolution in our experiment can be described via a convolution of the spin-wave intensity in Eq. (3) and the sixfold transmission through the FPIs described by function Eq. (4). The parameters used in the following evaluation are $d = 7.51\,\mathrm{mm}$ and $R = 0.95$.

Figure 5 shows exemplary experimental data together with modeling according to the considerations presented above for three different values of the decay time: $\tau_1 = 3.0\,\mathrm{ns}$, $\tau_2 = 4.0\,\mathrm{ns}$, and $\tau_3 = 5.0\,\mathrm{ns}$. As can be seen, best agreement of calculated and experimental data was found for a decay time of $\tau_2 = 4.0\,\mathrm{ns}$. This result extracted from the experimental data can finally be used together with the material parameters estimated in the previous section to determine the Gilbert damping according to [32]:

$$\alpha_{exp} = \frac{\tau_2}{\gamma\mu_0\left(H_{\mathrm{eff}}+M_{\mathrm{S}}/2\right)} = (2\pm1)\times10^{-3} \quad . \tag{5}$$

Our experimental value of $(2\pm1)\times10^{-3}$ is in good agreement with the literature value of $\alpha_{lit} = 3\times10^{-3}$ that can be found in [19]. In addition, this result supports previous observations of low-damping spin-wave propagation in CMFS microstructures [13, 14]. Thus, we conclude that patterning of micron sized CMFS elements does not increase the damping in the system.

In summary, we presented an all-optical study of the Heusler compound CMFS using wave-vector resolved BLS spectroscopy as well as time-resolved BLS microscopy. Via wave-vector resolved BLS we estimated a gyromagnetic ratio of $\gamma = 28.7\,\mathrm{GHz/T}$, a saturation magnetization of $M_{\mathrm{S}} = 1000\,\mathrm{kA/m}$, an anisotropy field of $H_{\mathrm{ani}} = 3\,\mathrm{kA/m}$, and an exchange constant of $A = 18\,\mathrm{pJ/m}$ by numerical modeling of the observed spin-wave spectra. Time-resolved BLS microscopy was used to estimate the Gilbert damping parameter of an individual CMFS microstructure via parallel

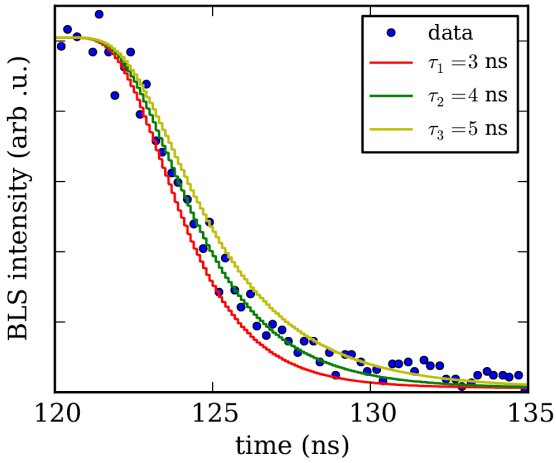

Fig. 5: Experimental data as well as convolution of Eqs. (3) and (4) to model the observed decay with different decay times $\tau_1 = 3.0\,\text{ns}$, $\tau_2 = 4.0\,\text{ns}$, and $\tau_3 = 5.0\,\text{ns}$. Best agreement of experimental and calculated values can be observed for $\tau_2 = 4.0\,\text{ns}$.

parametric amplification. The resulting value of $\alpha_{\text{exp}} = (2 \pm 1) \times 10^{-3}$ is in good agreement to values reported for homogeneous thin films via FMR. In particular, values for the exchange constant of CMFS as well as the Gilbert damping of an individual microstructure have not been reported in literature before.

We gratefully acknowledge financial support by the DFG Research Unit 1464 and the Strategic Japanese-German Joint Research Program from JST: ASPIMATT. T.B. and D.A.B are supported by a fellowship of the *Graduate School Materials Science in Mainz* (MAINZ) through DFG funding of the Excellence Initiative (GSC 266).

References

[1] C. Felser, B. Hillebrands, *New materials with high spin polarization: half-metallic Heusler compounds*, J. Phys. D: Appl. Phys. **40**, (2007).
[2] C. Felser, B. Hillebrands, *Cluster issue on Heusler compounds and devices*, J. Phys. D: Appl. Phys. **42**, 080301 (2009).
[3] S. Trudel, O. Gaier, J. Hamrle, B. Hillebrands, *Magnetic anisotropy, exchange and damping in cobalt-based full-Heusler compounds: an experimental review*, J. Phys. D: Appl. Phys. **43**, 193001 (2010).
[4] C. Liu, C.K.A. Mewes, M. Chshiev, T. Mewes, W.H. Butler, *Origin of low Gilbert damping in half metals*, Appl. Phys. Lett. **95**, 022509 (2009).
[5] H. Schultheiss, X. Janssens, M. van Kampen, F. Ciubotaru, S.J. Hermsdoerfer, B. Obry, A. Laraoui, A.A. Serga, L. Lagae, A.N. Slavin, B. Leven, B. Hillebrands, *Direct current control of three magnon scattering processes in spin-valve nanocontacts*, Phys. Rev. Lett. **103**, 157202 (2009).
[6] V.E. Demidov, S. Urazhdin, S.O. Demokritov, *Direct observation and mapping of spin waves emitted by spin-torque nano-oscillators*, Nat. Mater. **9**, 984 (2010).
[7] V.E. Demidov, S. Urazhdin, H. Ulrichs, V. Tiberkevich, A.N. Slavin, D. Baither, G. Schmitz, S.O. Demokritov, *Magnetic nano-oscillator driven by pure spin current*, Nat. Mater. **11**, 1 (2012).
[8] V.V. Kruglyak, S.O. Demokritov, D. Grundler, *Magnonics*, J. Phys. D: Appl. Phys. **43** 264001, (2010).
[9] B. Lenk, H. Ulrichs, F. Garbs, M. Münzenberg, *The building blocks of magnonics*, Phys. Rep. **507**, 107 (2011).
[10] T. Kubota, J. Hamrle, Y. Sakuraba, O. Gaier, M. Oogane, A. Sakuma, B. Hillebrands, K. Takanashi, Y. Ando, *Structure, exchange stiffness, and magnetic anisotropy of $Co_2MnAl_xSi_{1-x}$ Heusler compounds*, J. Appl. Phys. **106**, 113907 (2009).
[11] M. Oogane, T. Kubota, Y. Kota, S. Mizukami, H. Naganuma, A. Sakuma, Y. Ando, *Gilbert magnetic damping constant of epitaxially grown Co-based Heusler alloy thin films*, Appl. Phys. Lett. **96**, 252501 (2010).
[12] Y. Sakuraba, M. Ueda, Y. Miura, K. Sato, S. Bosu, K. Saito, M. Shirai, T.J. Konno, K. Takanashi, *Extensive study of giant magnetoresistance properties in half-metallic Co_2(Fe, Mn)Si-based devices*, Appl. Phys. Lett. **101**, 252408 (2012).
[13] T. Sebastian, Y. Ohdaira, T. Kubota, P. Pirro, T. Brächer, K. Vogt, A.A. Serga, H. Naganuma, M. Oogane, Y. Ando, B. Hillebrands, *Low-damping spin-wave propagation in a micro-structured $Co_2Mn_{0.6}Fe_{0.4}Si$ Heusler waveguide*, Appl. Phys. Lett. **100**, 112402 (2012).

[14] T. Sebastian, T. Brächer, P. Pirro, A. Serga, B. Hillebrands, T. Kubota, H. Naganuma, M. Oogane, Y. Ando, *Nonlinear emission of spin-wave caustics from an edge mode of a microstructured $Co_2Mn_{0.6}Fe_{0.4}Si$ waveguide*, Phys. Rev. Lett. **110** 067201 (2013).

[15] J. Hamrle, O. Gaier, S.-Gi. Min, B. Hillebrands, Y. Sakuraba, Y. Ando, *Determination of exchange constants of Heusler compounds by Brillouin light scattering spectroscopy: application to Co_2MnSi*, J. Phys. D: Appl. Phys. **42**, 084005, (2009).

[16] C.W. Sandweg, M.B. Jungfleisch, V.I. Vasyuchka, A.A. Serga, P. Clausen, H. Schultheiss, B. Hillebrands, A Kreisel, P. Kopietz, *Wide-range wavevector selectivity of magnon gases in Brillouin light scattering spectroscopy*, Rev. Sci. Instrum. 81(7):073902, (2010).

[17] V.E. Demidov, S.O. Demokritov, B. Hillebrands, M. Laufenberg, P.P. Freitas, *Radiation of spin waves by a single micrometer-sized magnetic element*, Appl. Phys. Lett. **85**, 2866 (2004).

[18] H. Schultheiss, C.W. Sandweg, B. Obry, S.J. Hermsdoerfer, S. Schäfer, B. Leven, B. Hillebrands, *Dissipation characteristics of quantized spin waves in nano-scaled magnetic ring structures*, J. Phys. D: Appl. Phys. **41** 164017 (2008).

[19] T. Kubota, S. Tsunegi, M. Oogane, S. Mizukami, T. Miyazaki, H. Naganuma, Y. Ando, *Half-metallicity and Gilbert damping constant in $Co_2Fe_xMn_{1-x}Si$ Heusler alloys depending on the film composition*, Appl. Phys. Lett. **94**, 122504 (2009).

[20] R.W. Damon, J.R. Eshbach, *Magnetostatic modes of a ferromagnetic slab*, J. Appl. Phys. **31**, (1960).

[21] R.W. Damon, J.R. Eshbach, *Magnetostatic modes of a ferromagnetic slab*, J. Phys. Chem. Solids **19**, 308 (1961).

[22] B.A. Kalinikos, A.N. Slavin, *Theory of dipole-exchange spin wave spectrum for ferromagnetic films with mixed exchange boundary conditions*, J. Phys. C: Solid State. **19**, 7013 (1986).

[23] Y. Miura, K. Nagao, M. Shirai, *Atomic disorder effects on half-metallicity of the full-Heusler alloys $Co_2Cr_{1-x}Fe_xAl$: A first-principles study*, Phys. Rev. B **69**, 144413 (2004).

[24] S. Picozzi, A.J.F.A. Continenza, A.J. Freeman, *Role of structural defects on the half-metallic character of Co_2MnGe and Co_2MnSi Heusler alloys*, Phys. Rev. B **69**, 094423 (2004).

[25] A. Banholzer, R. Narkowicz, C. Hassel, R. Meckenstock, S. Stienen, O. Posth, D. Suter, M. Farle, J. Lindner, *Visualization of spin dynamics in single nanosized magnetic elements*, Nanotechnology **22**, 295713 (2011).

[26] V.E. Zakharov, V.S. L'vov, S.S. Starobinets, *Stationary nonlinear theory of parametric excitation of waves*, Sov. Phys. JETP **32**, 656 (1971).

[27] T. Brächer, P. Pirro, B. Obry, B. Leven, A.A. Serga, B. Hillebrands, *Mode selective parametric excitation of spin waves in a $Ni_{81}Fe_{19}$ microstripe*, Appl. Phys. Lett. **99**, 162501 (2011).

[28] T. Brächer, P. Pirro, A. A. Serga, B. Hillebrands, *Localized parametric generation of spin waves in a longitudinally magnetized Ni_81Fe_19 waveguide*, Appl. Phys. Lett. **103**, 142415 (2013).

[29] V.E. Zakharov, V.S. L'vov, S.S. Starobinets, *Spin-wave turbulence beyond the parametric excitation threshold*, Sov. Phys. Uspekhi **17**, 896 (1975).

[30] S. Schäfer, V. Kegel, A.A. Serga, M.P. Kostylev, B. Hillebrands, *Variable damping and coherence in a high-density magnon gas*, Phys. Rev. B **83**, 184407 (2011).

[31] B. Hillebrands, *Progress in multipass tandem Fabry-Pérot interferometry: A fully automated, easy to use, self-aligning spectrometer with increased stability and flexibility*, Rev. Sci. Instrum. **70**, 1589 (1999).

[32] D.D. Stancil, *Phenomenological propagation loss theory for magnetostatic waves in thin ferrite films*, J. Appl. Phys. **59** 218 (1986).

4.18 Control of the effective damping in Heusler/Pt microstructures

T. Meyer, T. Brächer, T. Sebastian, P. Pirro, T. Fischer, A.A. Serga, and B. Hillebrands*

In collaboration with H. Naganuma, K. Mukaiyama, M. Oogane, and Y. Ando
Department of Applied Physics, Graduate School of Engineering, Tohoku University, Sendai 980-8579, Japan

**Current affiliation: Institut für Ionenstrahlphysik und Materialforschung, Helmholtz-Zentrum Dresden-Rossendorf, 01328 Dresden, Germany*

In the research field of magnonics, the Gilbert damping parameter is one of the most crucial parameters. It limits any possible application utilizing magnons, the quanta of spin waves, for information processing. To enable information transfer over sufficient distances, materials with a small Gilbert damping are substantially needed. Therefore, in the last years the development of new materials with a low Gilbert damping and a high spin polarization like the Cobalt-based Heusler compounds offered many new possibilities for future magnon spintronic devices and the observation of new phenomena [1,2]. In addition, investigations on parametric amplification of spin waves [3], and the manipulation of the magnon damping via the spin-transfer torque effect [4] gained a lot of interest. Utilizing the spin-Hall effect [5] to generate pure spin currents, the spin-transfer torque effect possesses the great potential to modify the effective magnon damping [6–10] and to decrease the damping in microstructures exhibiting novel properties [11]. This is very promising especially in low Gilbert damping Heusler materials as, here, the expected current densities are substantially lower.

In this Report, we present the control of the effective magnon damping in Heusler-Pt microstructures by the spin-transfer torque of a pure spin current created via the spin-Hall effect. Here, the used Heusler material is the low-damping Co_2MnSi (CMS) compound. Figure 1 shows the investigated sample. Using sputtering techniques, a 40 nm thick Cr layer, acting as a buffer layer, was grown on top of a MgO substrate. Subsequently, a 5 nm thick CMS layer was deposited. After annealing, a Pt layer with a thickness of 5 nm was grown on top of the CMS. The microstructuring into discs with a diameter of 4 µm was performed using e-beam lithography and ion milling. In order to apply currents, two triangular shaped and 250 nm thick copper contacts, spatially sep-

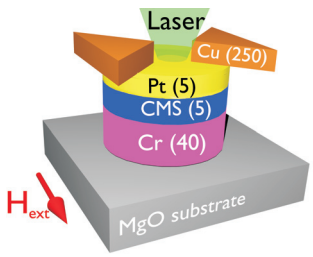

Fig. 1: Schematic sample setup with the corresponding layer thicknesses in nanometer in brackets and the direction of the externally applied magnetic field. The CMS layer was grown on a Cr buffer layer and after annealing, a Pt layer was grown on top of the stack. Subsequently, the patterning into discs with a diameter of 4 µm was performed. Finally, triangular shaped Cu contacts were structured on top of the discs. The contacts are separated by a gap of approximately 400 nm forcing an applied current to flow through the Pt layer. For all measurements the BLS laser was positioned approximately 700 nm away from the center between the triangels.

arated by approximately 400 nm from each other, are processed on top of the disc using lift-off techniques. Due to the gap in between the Cu contacts, an applied DC current is forced to flow through the disc, and especially through the Pt layer.

Via the spin-Hall effect, a DC charge current $\mathbf{J}_{cc}$ in the Pt layer generates a pure spin current $\mathbf{J}_{sc}$ flowing perpendicularly to $\mathbf{J}_{cc}$ and perpendicularly to the direction of the externally applied magnetic field $\mathbf{H}_{ext}$. In the given geometry, the direction of the spin current is normal to the film plane, thus, the spin current from the Pt injected into the CMS is given by [12]

$$\mathbf{J}_{sc}^{Pt} \propto \theta_{SH}^{Pt} \left(\hat{\mathbf{m}} \times \mathbf{J}_{cc}\right) \quad . \tag{1}$$

Here, $\hat{\mathbf{m}}$ is the unit vector along the direction of the spin polarization, and in general parallel or antiparallel to $\mathbf{H}_{ext}$. This pure spin current flowing into the CMS layer will then exert a torque on the magnetization via the spin-transfer torque effect. The direction of this torque can be parallel or antiparallel to the Gilbert-damping torque, referred to as a damping-like torque. Thus, depending on the sign of the injected pure spin current, the exerted torque can either increase or decrease the effective magnon damping in the CMS.

It is worth to note that the DC current will not only flow in the Pt layer but also in the CMS and Cr layers since all layers are metallic. This gives rise to an additional pure spin current from the Cr layer into the CMS layer, causing another torque on the magnetization in the CMS. Here, one has to consider that the sign of the spin-Hall angle of Pt is positive $\theta_{SH}^{Pt} > 0$ [13] and the spin-Hall angle of Cr is reported to be negative $\theta_{SH}^{Cr} < 0$ [14]. However, as the spin current from the Pt enters the CMS from the top, along the $-\hat{\mathbf{z}}$-direction, the spin current from the Cr reaches the CMS layer from the $+\hat{\mathbf{z}}$-direction. Taking this into account and given Eq. (1), both injected spin currents add up, resulting in a further increased torque in the CMS.

In the performed measurements, thermal spin waves are amplified using parallel parametric amplification [15]. The process of parametric amplification of spin waves utilizes the elliptic precession of magnetic moments in thin films, and, thus, a modulation of the magnetization component along the external field with twice the frequency of the precession. Due to this ellipticity, spin waves can be amplified by applying a dynamic magnetic field, e.g. the dynamic Oersted field of a RF current, with twice the frequency pointing parallel to the external field. This geometry is fulfilled if the RF current for the amplification is applied in addition to the DC current to the Cu contacts of the investigated structure as depicted in Fig. 1. Furthermore, the process of parametric amplification also allows for the investigation of the change in the effective magnon damping as the amplification process shows a threshold character [3]. Only if the applied dynamic magnetic field $\tilde{h}_{RF}$ is large

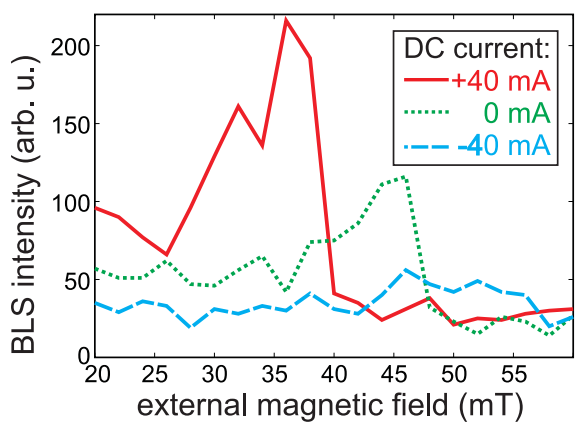

Fig. 2: Measured spin-wave intensity depending on the external applied magnetic field for different applied DC currents. Spin waves were amplified by means of parallel parametric amplification at a frequency of $f_{RF} = 14.2\,\text{GHz}$ and a power of $P_{RF} = 30\,\text{dBm}$

enough to compensate the damping, an amplification of spin waves can take place. In the experiments, $\tilde{h}_{RF}$ can be controlled by the applied RF power P_{RF} since $\tilde{h}_{RF} \propto \sqrt{P_{RF}}$. The time-evolution of the spin-wave amplitude $m(t)$, i.e. the cone angle of the precession motion, is given by [15]

$$m(t) \propto \exp(-\Gamma t + \kappa P^{1/2} t) \quad . \tag{2}$$

Here, the relaxation rate Γ represents the effective damping and, therefore, depends on the Gilbert damping, the damping-like term caused by the spin-transfer torque and propagation losses. The coupling constant κ can depend on a variety of parameters but can be estimated as a constant for a given structure, fixed external field, spin-wave frequency and spin-wave mode. The threshold character of the parametric amplification can immediately be seen from Eq. (2): Amplification only takes place if the exponent becomes positive. The corresponding threshold power P_{Th} is given by

$$P_{Th} = \Gamma / \kappa \tag{3}$$

and, in our experiment, only depends on the relaxation rate and is, therefore, a very sensitive measure for any manipulation of the effective magnon damping.

All presented results were obtained using Brillouin light scattering (BLS) microscopy [16]. BLS is the inelastic scattering of photons at magnons. By investigating the frequency and the intensity of the inelastically scattered light, the frequency and the density of the corresponding magnon states can be obtained. Using a microfocussed laser allows for a spatial resolution of about 300 nm.

In order to avoid excessive strong sample heating, the DC- as well as the RF currents are applied in 500 ns long pulses with a repetition time of 1 µs. Providing that the current density is maximal in the center between the contacts, the effects in the center position should be most pronounced. However, as the laser heats the sample significantly, the additional heating due to the RF- and DC currents can easily break the contact if the laserspot is probing the center position. Therefore, the response of the spin-wave system is probed with the BLS laser not being in the center between the contacts but in a distance of approximately 700 nm away from the center (see Fig. 1).

Figure 2 shows the excitation spectra of the CMS layer at different applied external magnetic fields and DC currents. The RF frequency is kept constant at $f_{RF} = 14.2$ GHz, resulting in a spin-wave frequency of $f_{SW} = 7.1$ GHz. The RF power is set to $P_{RF} = 30$ dBm. In Fig. 2 one can clearly see the influence of the applied DC current on the measured spin-wave intensity as well as on the position of the excitation spectra. The change of the position of the spectra in terms of the applied magnetic field can easily be attributed to the Oersted-field generated by the DC current. This field contributes to the effective field in the magnetic layer and has to be compensated by the external applied magnetic field. However, the large change in the spin-wave intensities of more than a factor of 4 for the peak values is mainly contributed to a significant change in the effective damping due to the applied DC current. As expected from the theory, the effective damping, and, thus, the spin-wave intensities show an asymmetric dependence on changing the sign of the DC current (see also Eq. (2)).

The experimentally obtained results for the determination of the parallel parametric amplification threshold power are shown in Fig. 3a-c. Here, BLS intensity maps depending on the applied RF power and the external magnetic field for varying DC currents are shown. In Fig. 3b,c, i.e. for 0 mA and +40 mA, respectively, one can clearly see the onset of the amplification of spin waves for increasing applied RF powers. In the case of an applied current of −40 mA (Fig. 3a), no clear

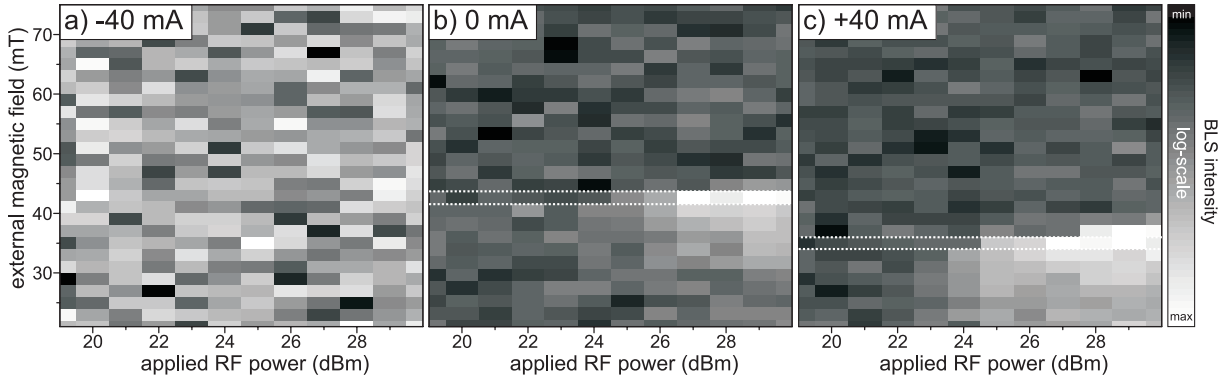

Fig. 3: Normalized BLS intensity maps depending on the applied RF power and external magnetic field for different applied DC currents of a) $-40\,\mathrm{mA}$, b) $0\,\mathrm{mA}$ and c) $+40\,\mathrm{mA}$. Brighter spots show a higher BLS intensity and therefore a higher magnon density. The dashed lines in b) and c) indicate the spin-wave mode showing the lowest threshold power for parametric amplification.

spin-wave signal is observed as the effective damping is strongly increased by the spin-transfer torque effect and the treshold power for parametric amplification is not overcome anymore. Again, this is in agreement with the theoretically predicted torque of the pure spin current. Here, positive (negative) DC currents lead to a decrease (increase) of the effective damping in the CMS layer and an according change of P_{Th}. One should also note that the applied RF power in Fig. 3 is the power applied to the microwave equipment, not the power running through the sample stack. Due to absorptions and reflections of the RF signal in the cables, etc., the power in the microstructure is much lower. However, the relative change of P_{Th} is not affected by this as the microwave transmission characteristics only depend on the applied frequency which is fixed to $f_{RF} = 14.2\,\mathrm{GHz}$ in all experiments presented in this Report.

To visualize and investigate the change of P_{Th} in more detail, Fig. 4 shows the spin-wave intensity depending on the applied RF power for the spin-wave mode with the lowest P_{Th}. This mode can be attributed to the quasi-uniform mode in the system showing the highest possible coupling. As the coupling factor κ depends on the amplified spin-wave mode, only by choosing the same mode for the different applied DC currents, the results can be compared. The modes shown in Fig. 4 for an applied DC current of $0\,\mathrm{mA}$ and $+40\,\mathrm{mA}$ are marked in Fig. 3b,c by the dashed lines. The data in Fig. 4 shows again a clear influence of the applied DC current on the threshold power P_{Th} if the parametric amplification takes place.

In conclusion, the obtained results show the feasibility of using a DC current in a Pt layer to control the effective damping in the adjacent Heusler compound CMS. By exploiting the threshold character of the parametric amplification process, a change in the effective damping of the CMS layer could be shown. The observed effects agree with the expected influence of the DC current due to the spin-Hall effect and spin-transfer torque, making these effects a convenient approach to change the effective damping in Heusler compound microstructures. To further investigate these effects in Heusler-Pt bilayers, and to investigate the influence of a possible pure spin current arising from the Cr layer, additional sets of samples need to be prepared. Also, a separation of the RF current from the DC current line will give a better insight in the underlying effects. Nevertheless, in this Report, the control, i.e., the possibility to further decrease the damping in Heusler materials could be proven. This offers a tool for future investigations on strongly nonlinear processes in magnetic systems on the microscale.

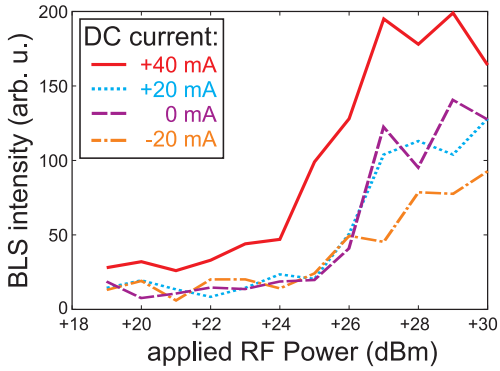

Fig. 4: Measured BLS intensity for a single spin-wave mode depending on the applied RF power and applied DC current. The spin-wave mode was selected as the one with the lowest threshold power from measurements as shown in Fig. 3

We gratefully acknowledge Financial support by the DFG Research Unit 1464 and the Strategic Japanese-German Joint Research Program from JST: ASPIMATT. We thank our colleagues from the Nanostructuring-Center of the TU Kaiserslautern for their assistance in sample preparation.

References

[1] T. Sebastian, Y. Ohdaira, T. Kubota, P. Pirro, T. Brächer, K. Vogt, A.A. Serga, H. Naganuma, M. Oogane, Y. Ando, B. Hillebrands, *Low-damping spin-wave propagation in a micro-structured $Co_2Mn_{0.6}Fe_{0.4}Si$ Heusler waveguide*, Appl. Phys. Lett. **100**, 112402 (2012).

[2] T. Sebastian, T. Brächer, P. Pirro, A.A. Serga, T. Kubota, H. Naganuma, M. Oogane, Y. Ando, B. Hillebrands, *Nonlinear emission of spin-wave caustics from an edge mode of a microstructured $Co_2Mn_{0.6}Fe_{0.4}Si$ waveguide*, Phys. Rev. Lett. **110**, 067201 (2013).

[3] T. Brächer, P. Pirro, A.A. Serga, B. Hillebrands, *Localized parametric generation of spin waves in a longitudinally magnetized $Ni_{81}Fe_{19}$ waveguide*, Appl. Phys. Lett. **103**, 142415 (2013).

[4] J.C. Slonczewski, *Current-driven excitation of magnetic multilayers*, J. Magn. Magn. Mater. **159** (1996).

[5] J. Hirsch, *Spin Hall effect*, Phys. Rev. Lett. **83**, 1834 (1999).

[6] V.E. Demidov, S. Urazhdin, E.R.J. Edwards, S.O. Demokritov, *Wide-range control of ferromagnetic resonance by spin Hall effect*, Appl. Phys. Lett. **99**, 172501 (2011).

[7] E.R.J. Edwards, H. Ulrichs, V.E. Demidov, S.O. Demokritov, S. Urazhdin, *Parametric excitation of magnetization oscillations controlled by pure spin current*, Phys. Rev. B **86**, 134420 (2012).

[8] L. Liu, T. Moriyama, D.C. Ralph, R.A. Buhrman, *Spin-torque ferromagnetic resonance induced by the spin Hall effect*, Phys. Rev. Lett. **106**, 036601 (2011).

[9] K. Ando, S. Takahashi, K. Harii, K. Sasage, J. Ieda, S. Maekawa, E. Saitoh, *Electric manipulation of spin relaxation using the spin Hall effect*, Phys. Rev. Lett. **101**, 036601 (2008).

[10] O. Rousseau, M. Viret, *Interaction between ferromagnetic resonance and spin currents in nanostructures*, Phys. Rev. B **85**, 144413 (2012).

[11] V.E. Demidov, S. Urazhdin, H. Ulrichs, V. Tiberkevich, A. Slavin, D. Baither, G. Schmitz, S.O. Demokritov, *Magnetic nano-oscillator driven by pure spin current*, Nat. mater. **11** (2012).

[12] S. Takahashi, S. Maekawa, *Spin current, spin accumulation and spin Hall effect*, Sci. Technol. Adv. Mater. **9**, 014105 (2008).

[13] M. Schreier, G.E.W. Bauer, V. Vasyuchka, J. Flipse, K. Uchida, J. Lotze, V. Lauer, A. Chumak, A.A. Serga, S. Daimon, T. Kikkawa, E. Saitoh, B.J. van Wees, B. Hillebrands, R. Gross, S.T.B. Goennenwein, *Sign of inverse spin Hall voltages generated by ferromagnetic resonance and temperature gradients in yttrium iron garnet\platinum bilayers*, arXiv:1404.3490v1 (2014).

[14] C. Du, H. Wang, F. Yang, P.C. Hammel, *Systematic variation of spin-orbit coupling with d-orbital filling: Large inverse spin Hall effect in 3d transition metals*, Phys. Rev. B **90**, 140407 (2014).

[15] V.S. L'vov, *Wave turbulence under parametric excitation application to magnets*, (Springer-Verlag Berlin-Heidelberg, 1994).

[16] V.E. Demidov, S.O. Demokritov, B. Hillebrands, M. Laufenberg, P.P. Freitas, *Radiation of spin waves by a single micrometer-sized magnetic element*, Appl. Phys. Lett. **85**, 2866 (2004).

4.19 Influence of a non-Gilbert damping mechanism on the nonlinear spin dynamics in a ferromagnetic Heusler compound

P. Pirro, T. Sebastian, T. Brächer, A.A. Serga, and B. Hillebrands*

In collaboration with T. Kubota, Institute for Materials Research, Tohoku University, Katahira 2-1-1, Aoba-ku, Sendai 980-8577, Japan and H. Naganuma, M. Oogane and Y. Ando, Department of Applied Physics, Graduate School of Engineering, Tohoku University, Aoba-yama 6-6-05, Sendai 980-8579, Japan

**Current affiliation: Institut für Ionenstrahlphysik und Materialforschung, Helmholtz-Zentrum Dresden-Rossendorf, 01328 Dresden, Germany*

The field of spintronics has attracted huge interest in recent years due to a multitude of physical phenomena and applications related to the spin degree of freedom [1, 2]. To develop this area further, intensive theoretical and experimental research efforts are devoted to design new materials with outstanding properties, e.g., high spin polarization. The class of ferromagnetic Heusler materials [3] is of special interest since these materials potentially combine high spin-polarization and Curie temperature with low magnetic Gilbert damping [4–6]. Thus, these materials allow for a long-distance spin transport by magnons—the quanta of spin waves. Alongside with the decrease of the Gilbert-type relaxation, which results in this case from the reduced interaction of the magnetic excitations with the electron bath, other damping mechanisms, caused by, for example, nonlinear magnon-magnon scattering, can play an important role [7–11]. Thus, the development of new ferromagnetic Heusler materials calls for a comprehensive study of the occurring nonlinear spin-wave phenomena since these will dominate the energy redistribution in magnetization dynamics. For example, the high impact of nonlinear phenomena on spin dynamics in Heusler compounds has been already demonstrated by the generation of spin-wave beams via nonlinear emission [12].

In this article, we report on the experimental observation and theoretical analysis of the second-order instability [10, 13–17] of propagating spin waves in a micro-scaled magnonic waveguide structured from the Heusler compound $Co_2Mn_{0.6}Fe_{0.4}Si$ (CMFS) [4,5,12,18]. In this four-magnon scattering process, two initial magnons of frequency f_0 scatter into two magnons with frequencies f_1 and f_2, named the unstable modes.

We observe that the mode f_1 is a dominant unstable mode whose frequency is independent of the frequency f_0 of the initially excited spin waves. Such a dominant mode has not been reported previously for metallic ferromagnetic thin films. It can be understood as a specific feature of the low Gilbert damping Heusler film. We show that its occurrence is caused by the combination of several characteristic material properties: Due to the high saturation magnetization M_s non-resonant three-magnon processes start to play an important role for the nonlinear four-magnon coupling [8, 16]. More importantly, due to the small Gilbert damping contribution, the total relaxation rate η of the individual spin-wave modes is strongly influenced by magnon-magnon relaxation, which in the end determines the frequencies of the unstable modes.

The sample scheme is presented in Fig. 1a: A 5 µm wide CMFS waveguide (30 nm thick, 70 µm long, capped with a layer of Ta (5 nm)) grown on a MgO substrate with a 40 nm Cr buffer layer was

This work has been accepted for publication in Physical Review Letters.

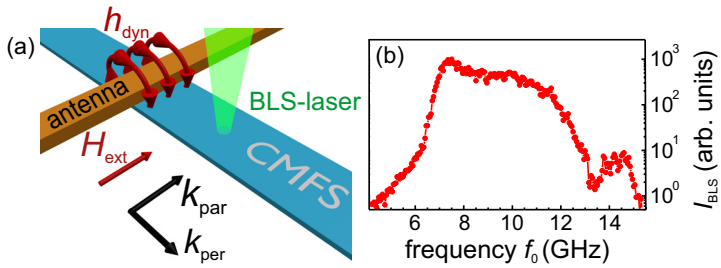

Fig. 1: (a) Schematic view of the investigated sample: Spin waves are excited in a 5 µm wide waveguide of CMFS by means of a 1 µm wide Ti/Cu antenna. A bias field $\mu_0 H_{ext} = 48\,\mathrm{mT}$ is applied perpendicular to the waveguide's long axis. (b) Normalized Brillouin light scattering intensity I_{BLS} in the linear regime as a function of the microwave excitation frequency f_0.

patterned by electron beam lithography and argon ion milling. Then, a 1 µm wide antenna (made of Ti/Cu) was produced on top of the CMFS waveguide by electron beam evaporation and lift off. A microwave current with variable frequency f_0 is passed through the antenna to create a dynamic Oersted field h_{dyn} which leads to a torque on the magnetization exciting coherent propagating spin waves. If not stated differently, a static external magnetic field $\mu_0 H_{ext} = 48\,\mathrm{mT}$ is applied perpendicular to the waveguide's long axis (as depicted in Fig. 1). Hence, an efficient excitation of spin waves propagating perpendicularly to H_{ext} is realized. The spin waves are detected at a distance of about 2 µm from the antenna in the center of the waveguide using Brillouin light scattering microscopy (BLS) [19]. Figure 1b shows the BLS intensity I_{BLS}, which is proportional to the total spin-wave intensity, as a function of the applied microwave frequency f_0 for a microwave power of 0 dBm. As expected from earlier investigations [20, 21], an efficient excitation of different spin-wave modes with wavelengths in the micrometer range in a frequency interval of several Gigahertz is realized. Let us now turn to the frequency composition of the individual spin-wave spectra. Figure 2a exemplarily shows BLS spectra for a fixed microwave frequency $f_0 = 10.5\,\mathrm{GHz}$. For a power of $P = 5\,\mathrm{dBm}$ (squares), only the directly excited, *initial* spin-wave mode with frequency f_0 is visible. At $P = 9\,\mathrm{dBm}$ (circles), the amplitude of the initial spin waves exceeds the instability threshold and the spectrum shows two additional peaks at f_1 and f_2, corresponding to the unstable spin-wave modes, which are also referred to as critical modes. The clear threshold character of this process is demonstrated in Fig. 2b: If the threshold power is exceeded, I_{BLS} at f_1 and f_2 abruptly increases. Simultaneously, the slope of the intensity increase at the excitation frequency f_{MW} strongly drops below the linear increase (dotted line) observed for small microwave powers. For even higher powers (diamonds in Fig. 2a), a continuum of spin-wave frequencies between f_1 and f_2 is found, whereas the intensities of the former peaks at f_1 and f_2 saturate. This supercritical regime, where a large number of modes is populated above the thermal level, has already been observed in [11]. However, the further discussion will concentrate on the unstable modes f_1 and f_2 with the lowest threshold for the four-magnon instability process, since these modes provide information about intrinsic properties of the system.

Figure 2c shows the evolution of the frequencies f_1 and f_2 as a function of the frequency f_0 of the initial spin waves. For each shown f_0 in the range from 8.25 GHz to 11.25 GHz, the microwave power is increased until the first satellites of the four-magnon scattering appear in the BLS spectrum, hence f_1 and f_2 are always recorded close to the threshold power. For $f_0 > 11.25$ GHz, the instability threshold amplitude of the initial spin waves was not reached anymore due to the decreased excitation efficiency [11, 20, 21], which can also be seen in Fig. 1b. Remarkably, f_1 is practically independent of f_0. This indicates that the mode f_1 features a reduced relaxation rate or an enhanced coupling for the four-magnon interaction compared to competing modes. Concerning f_2, a linear increase with f_0 is observed, which is necessary to conserve the total energy. Quantitatively, the energy conservation ($2f_0 = f_1 + f_2$) is demonstrated by comparing the energy of the

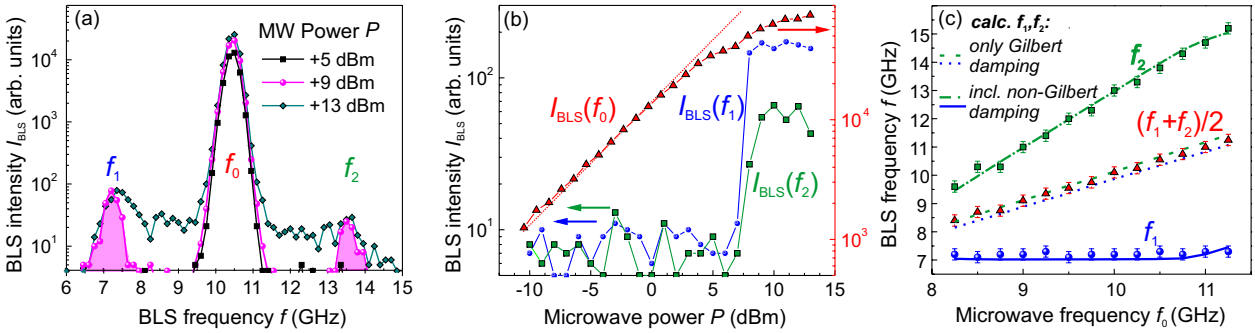

Fig. 2: (a) BLS spectra for $f_{\mathrm{MW}} = 10.5\,\mathrm{GHz}$ at different microwave powers. The spectrum at the threshold power ($P = 9\,\mathrm{dBm}$) shows the two unstable mode frequencies f_1 and f_2 (shaded). The different BLS intensities at f_1 and f_2 are caused by different detection efficiencies. For supercritical powers ($P > 9\,\mathrm{dBm}$), the intensities at f_1 and f_2 do not increase further, instead the spectrum becomes continuously broadened. (b) BLS intensity I_{BLS} for the modes f_1, f_2 and f_0 as a function of the microwave power P. Above the threshold power, I_{BLS} of the unstable modes at f_1, f_2 rises sharply. (c) Unstable mode frequencies f_1 and f_2 (circles and squares, respectively) as a function of the microwave frequency f_0. f_1 is independent of f_0 and constant at $f_1 \approx 7.1\,\mathrm{GHz}$, while f_2 increases linearly with f_0. The lines indicate the calculated values for f_1 and f_2 according to Eq. (1), which show no match with the experiment for pure Gilbert-damping (dashed lines) but good agreement if a additional non-Gilbert damping term (Eq. (5)) is included (solid line for f_1, dashed dotted line for f_2).

initial magnons (black line) with the mean energy of the pair of the unstable magnons (triangles). The perfect agreement for all f_0 proves that energy conservation is fulfilled in all cases. In order to identify the mechanism which leads to the observed frequencies of the unstable modes, an appropriate theoretical description of the nonlinear interaction of propagating spin waves in thin films is needed. A general way to perform this analysis is to consider the critical amplitude of the initial wave for a second order instability [15, 16]:

$$|c_{\mathrm{crit}}| = \min_{(\mathbf{k}_1,\mathbf{k}_2)} \left(\sqrt{\frac{\eta_{\mathrm{eff}}}{|\widetilde{W}_{\mathbf{k}_0\mathbf{k}_0,\mathbf{k}_1\mathbf{k}_2}|}} \right), \tag{1}$$

where the minimization is carried out over all resonant spin-wave modes fulfilling energy and momentum conservation. From Eq. (1) it can be seen that the unstable modes have the lowest ratio of their effective relaxation frequency η_{eff} over their four-magnon coupling strength $|\widetilde{W}_{\mathbf{k}_0\mathbf{k}_0,\mathbf{k}_1\mathbf{k}_2}|$. To evaluate Eq. (1), the resonant modes need to be determined first. Energy conservation can be accounted for by choosing the frequencies of the *potentially* unstable modes f_1', f_2' to fulfill $2f_0 = f_1' + f_2'$. Subsequently, momentum conservation can be analyzed by calculating the isofrequency curves $\{\mathbf{k}_1'\}$ and $\{\mathbf{k}_2'\}$ for a magnetic thin film, which include all wave vectors with $f(\mathbf{k}_i') = f_i'$, $i = 1, 2$. Hereby, only the in-plane components of the wave vector are considered, since for this film thickness, the modes with finite out-of-plane wave vector have frequencies above 20 GHz due to the exchange interaction. Thus, these modes can be neglected in the investigated frequency range ($f(\mathbf{k})$ calculated using Ref. [22], parameters see [23]). From the set of in-plane wave vectors, all wave-vector pairs $(\mathbf{k}_1', \mathbf{k}_2')$ which fulfill the wave-vector conservation

$$2\mathbf{k}_0 = \mathbf{k}_1' + \mathbf{k}_2' \tag{2}$$

can be numerically selected [24]. In Fig. 3, this approach is demonstrated exemplarily for the experimental data of Fig. 2a ($f_1 = 7.1\,\mathrm{GHz}$, $f_2 = 13.9\,\mathrm{GHz}$). The wave vector $\mathbf{k}_0$ of the initial spin waves is calculated assuming that the microwave antenna excites predominantly the first waveguide mode (see Ref. [20, 21]). For the potentially unstable modes, the quantization of the wave vector

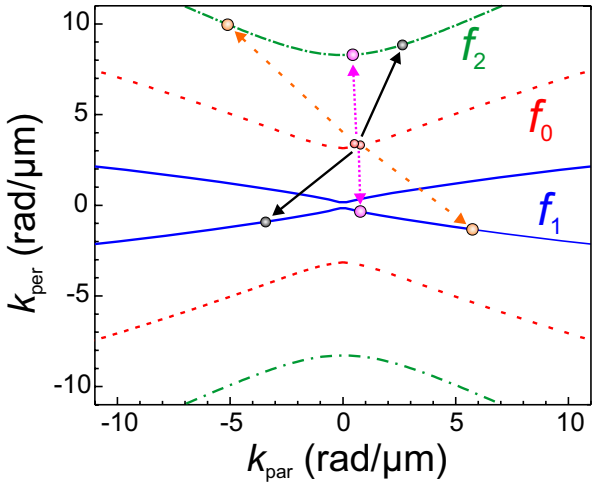

Fig. 3: Isofrequency curves for the experimental conditions of Fig. 2a: $f_1 = 7.1\,\mathrm{GHz}$ (straight line), $f_0 = 10.5\,\mathrm{GHz}$ (dashed line), $f_2 = 13.9\,\mathrm{GHz}$ (dashed-dotted line). Three possible four-magnon scattering processes are schematically illustrated with arrows.

due to the finite waveguide width can be neglected in this geometry since the different quantized modes have only small frequency differences compared to the separation between the observed mode frequencies f_1, f_0 and f_2. With the resonant modes being identified, let us evaluate if the coupling $\widetilde{W}$ can provide an explanation for the observed f_1 and f_2. To calculate $\widetilde{W}$, the expression deduced in Ref. [16] for the case of spin waves with a finite, in-plane wave vector in a magnetic thin film is used. Besides the direct four-magnon coupling W, also the contribution T [8, 16] due to non-resonant three-magnon processes has to be included:

$$\widetilde{W}_{\mathbf{k}_0\mathbf{k}_0,\mathbf{k}_1\mathbf{k}_2} = W_{\mathbf{k}_0\mathbf{k}_0,\mathbf{k}_1\mathbf{k}_2} + T_{\mathbf{k}_0\mathbf{k}_0,\mathbf{k}_1\mathbf{k}_2}. \tag{3}$$

In the particle picture, T describes two subsequent three-magnon scattering processes which involve a common virtual magnon state. Since three-magnon processes are purely dipolar, T is proportional to the saturation magnetization M_s [16] which leads to an important contribution for CMFS ($M_s \approx 1000$ kA/m). It has been neglected in the explanation of many classical experiments with the ultra-low damping insulator YIG (Yttrium Iron Garnet) [13–16], since its influence vanishes in the high field limit where $f_0 \gg f_M = \gamma\mu_0 M_S$. However, due to the comparably high saturation magnetization of CMFS ($M_s \approx 1000\,\mathrm{kA/m}$, $M_s^{\mathrm{CMFS}}/M_s^{\mathrm{YIG}} \approx 7.5$), the experimental situation in our studies corresponds to the low field limit in which all spin-wave frequencies are much smaller than $f_M(\mathrm{CMFS}) \approx 37\,\mathrm{GHz}$.

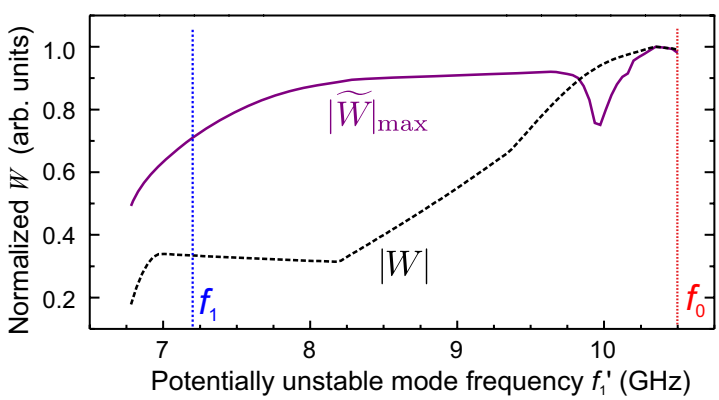

Fig. 4: Normalized maximal four-magnon coupling strength $\widetilde{W}_{\max}$ [25] as function of the frequency f_1' of the lower potentially unstable mode (parameters see Fig. 2). The dotted line represents the bare four-magnon coupling W without the incorporation of the non-resonant three-magnon contribution.

From all the resonant wave vector pairs $(\mathbf{k}_1', \mathbf{k}_2')$, the one with the maximal $|\widetilde{W}|$ has been selected. Figure 4 exemplarily shows this maximum coupling strength $|\widetilde{W}|_{\max}$ as a function of the lower

unstable mode frequency f_1' (f_2' is given by $2f_0 - f_1'$) for the experimental parameters of Fig. 2a [25]. For comparison, the maximum of $|W|$ calculated without taking into account the three-magnon correction T is also shown. From Fig. 4, two important conclusions can be deduced. Firstly, the three-magnon correction T enhances the coupling for wave pairs with frequencies f_1' significantly lower than f_0 (in the range $\approx$ 6.7 - 9.5 GHz) compared to the uncorrected four-magnon coupling $|W|$. Secondly, even with the incorporation of the non-resonant three-magnon effects, the complete coupling $|\widetilde{W}|$ exhibits no maximum for the observed unstable mode frequency f_1. The calculations show a similar behavior for all f_0 in the experimentally probed range of Fig. 2c. Nevertheless, since the coupling value for f_1 is not too far from its maximum, a reasonable variation of the effective relaxation rate η_{eff} might explain the experimental observations.

Therefore, the effective relaxation frequency η_{eff} of the potentially unstable spin waves has to be considered in more detail. A particular spin-wave mode can relax via a large number of different processes, which involve the interaction with electrons, phonons and other magnons [14, 15, 26]. Let us first analyze the part of these damping processes which can be described as "viscous" processes and which are taken into account by the Gilbert damping constant α in the Landau-Lifshitz-Gilbert equation [15]. In this case, the dissipated energy is proportional to the time derivative of the magnetization. For CMFS, this Gilbert damping contribution is mainly due to the electron-magnon interaction [6] and was measured to be $\alpha^{\text{CMFS}} \approx 0.003$ [4, 5]. Applying the approach presented in Ref. [27] to the used dispersion relations, the Gilbert relaxation rate $\eta^{\text{Gilb}} = \eta^{\text{Gilb}}(f, \alpha)$ is calculated for finite wave-vector, dipolar-dominated spin waves:

$$\eta^{\text{Gilb}} = \alpha \frac{(\gamma\mu_0 H)^2 + f(\mathbf{k})^2}{2\gamma\mu_0 H} \tag{4}$$

with γ =28 GHz/T.

Next, the resulting threshold $c_{\text{crit}}^{\text{Gilb}}$ given by Eq. (1) with $\eta_{\text{eff}}(\mathbf{k}_1', \mathbf{k}_2') = \sqrt{\eta(\mathbf{k}_1')\eta(\mathbf{k}_2')}$ [15] is derived for each potentially unstable magnon pair. Figure 5 shows this normalized threshold $|c_{\text{crit}}^{\text{Gilb}}|$ for pure Gilbert damping as a function of f_1' (dark blue curve). In contradiction to the experimental results, the minimal threshold in this case is predicted for almost degenerated modes with $f_1 \approx f_0 \approx f_2$. As the dashed blue and green lines in Fig. 2, which show this predicted unstable mode frequencies f_1, f_2 for pure Gilbert damping as a function of f_0, demonstrate, this pronounced mismatch between experiment and theoretical prediction is present in the whole investigated range. Since the curve for the normalized $|c_{\text{crit}}^{\text{Gilb}}|$, and therefore the predicted f_1 and f_2, are independent of the absolute value of α, the experimental observations can neither be explained if a different Gilbert damping strength is assumed. Thus, additional, non-Gilbert damping mechanisms have to play a significant role for the unstable modes in CMFS.

In this context, a non-viscous relaxation contribution for spin waves which has to be considered is the interaction with the thermal magnon bath, since it is an intrinsic damping mechanism which is known to be important in high quality, low Gilbert damping materials [7, 28–31]. For example, the relaxation of a mode with wave vector $\mathbf{k}$ can occur due to the confluence with a thermal magnon $\mathbf{k}_{\text{t}}$. The relaxation rate η^{Mag} due to this magnon-magnon scattering processes depends on the nonlinear coupling in the magnon system, the thermal population of the magnon spectrum, and the shape of the dispersion relation. In a first approximation, η^{Mag} is usually described as [28–30]:

$$\eta^{\text{Mag}}(\mathbf{k}) = \frac{A}{f(\mathbf{k})}|\mathbf{k}|. \tag{5}$$

Here, $f(\mathbf{k})$ is the frequency of the spin wave under consideration and A is a parameter which depends on temperature, saturation magnetization, exchange constant, geometry and applied field

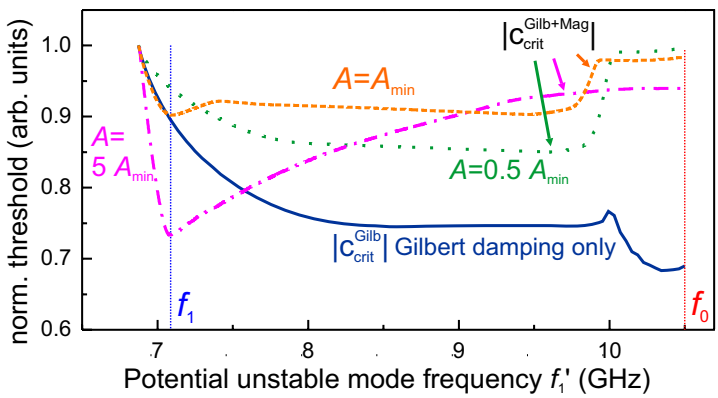

Fig. 5: Individually normalized critical threshold amplitudes c_{crit} as a function of f_1' for pure Gilbert damping (straight curve) and for different values of the parameter A. For $A > A_{\mathrm{min}} \approx 10^{-7}\,\mathrm{m}\cdot\mathrm{GHz}^2/\mathrm{rad}$ (dashed line), the threshold is minimal for the experimentally observed unstable mode frequency $f_1 \approx 7.1\,\mathrm{GHz}$. With increasing A, this minimum becomes increasingly pronounced.

[15, 26]. The damping mechanism described by Eq. (5) does not contribute to the damping at $|\mathbf{k}| = 0$ and, thus, does not influence the ferromagnetic resonance measurements [4, 5] used to extract the Gilbert damping.

A precise theoretical calculation of A for the CMFS thin film in the low field limit is rather involved and beyond the scope of this Letter. However, based on the general theory for nonlinear spin waves [16] and numerical evaluation of the magnon-magnon relaxation for thin films [7], we can conclude that the latter can be of the same order of magnitude as the Gilbert damping in CMFS and thus, it should be included in our analysis. Since the theoretical value of A is unknown, the normalized threshold $|c_{\mathrm{crit}}^{\mathrm{Gilb+Mag}}|$ with $\eta(\mathbf{k}) = \eta^{\mathrm{Gilb}}(\mathbf{k}) + \eta^{\mathrm{Mag}}(\mathbf{k})$ is shown in Fig. 5 for several values of A as a function of f_1'. The relaxation rate η^{Mag} for these A is in the same order of magnitude or smaller as the Gilbert relaxation rate for the wave-vector range considered here. It is evident that for $A \geq A_{\mathrm{min}} \approx 10^{-7}\,\mathrm{m}\cdot\mathrm{GHz}^2/\mathrm{rad}$ (dashed line), the threshold is minimal for the dominant unstable mode frequency $f_1 \approx 7.1\,\mathrm{GHz}$ observed in the experiment. Thus, the inclusion of a damping term in the form of Eq. (5) explains the position of the unstable modes in Fig. 2a. The transition of the critical modes at A_{min} occurs because of the change in the ratio of η^{Gilb} to η^{Mag}; thus A_{min} is a function of the Gilbert damping parameter: $A_{\mathrm{min}} = A_{\mathrm{min}}(\alpha)$.

In Fig. 2c, the same analysis is applied to all values of f_0: the solid line and dashed-dotted green line show the calculated values for f_1 and f_2, respectively, as a function of f_0 if a constant value of $A = 3\cdot 10^{-7}\,\mathrm{m}\cdot\mathrm{GHz}^2/\mathrm{rad}$ is assumed. The explicit $|\mathbf{k}|$-dependence of η^{Mag} fixes the calculated f_1 close to 7.1 GHz, in excellent agreement with the experiment. Thus, the fact that a *dominant* unstable mode exists in the system can be confidently attributed to the influence of the non-Gilbert damping process discussed above.

Additional measurements presented in Fig. 6 for a varying external field with a fixed excitation frequency $f_0 = 11\,\mathrm{GHz}$ show that the dominant critical mode frequency f_1 depends on the dispersion relation $f(\mathbf{k})$: f_1 increases for higher magnetic fields (and f_2 decreases consequently to fulfill energy conservation). Also in this situation, where the dispersion relations are continuously changed, a good agreement between the calculated unstable mode frequencies (solid lines) and the experimentally observed f_1 and f_2 (circles and squares) is found. Remarkably, the theoretically predicted unstable modes nicely reproduce the experimental observation that f_1 gets close to the frequency of the ferromagnetic resonance f_{FMR} (dotted line) for fields higher than 50 mT, but lies significantly above f_{FMR} for lower fields.

Thus, the inclusion of a rather simple, explicitly wave vector dependent damping term reproduces the critical unstable modes in CMFS which cannot be understood if only Gilbert-damping is assumed. However, if the ratio of $\eta^{\mathrm{Mag}}/\eta^{\mathrm{Gilb}}$ is too small, the Gilbert damping dominates and

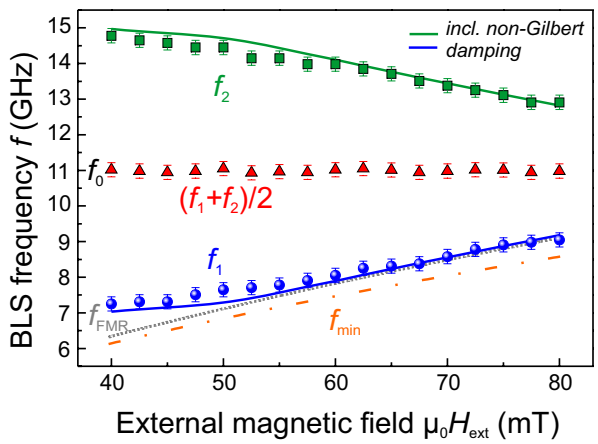

Fig. 6: Unstable modes f_1 and f_2 as a function of the external field H_{ext}. The theoretically predicted unstable modes (solid lines) which have been calculated including the magnon-magnon damping show a good agreement with the experiment. As an additional information, the frequency of the ferromagnetic resonance f_{FMR} (dotted line) and the lowest frequency of the spin-wave manifold f_{min} (dashed-dotted line) are indicated.

modes close to f_0 are predicted to get unstable first (compare Fig. 5). Indeed, such a behavior with a continuously broadened spectrum was observed in Permalloy [11], where the Gilbert damping is significantly larger than in CMFS.

To conclude, by using four-magnon instabilities as a probing tool, we have demonstrated that non-Gilbert damping plays an important role for the spin dynamics in the Heusler compound CMFS. By including a non-viscous, explicitly wave vector dependent relaxation contribution, all characteristics of the instabilities have been explained using one constant parameter A for the entire investigated range. This non-Gilbert relaxation mechanism can be attributed to the interaction of the considered magnon with the thermal magnon bath. Since this intrinsic damping cannot be reduced without changing elementary material parameters like the saturation magnetization or the exchange constant, it constitutes a lower limit for the total damping of spin waves in general. Thus, for a further development of low damping ferromagnetic compounds, magnon-magnon interactions can be anticipated to play an decisive role.

We thank G.A. Melkov for fruitful discussions and our colleagues from the *Nano Structuring Center* of the TU Kaiserslautern for their assistance in sample preparation. We gratefully acknowledge financial support by the DFG Research Unit 1464 and the Strategic Japanese-German Joint Research from JST: ASPIMATT. Thomas Brächer was supported by a fellowship of the Graduate School Materials Science in Mainz (MAINZ) through DFG-funding of the Excellence Initiative (GSC 266).

References

[1] N. Locatelli, V. Cros, J. Grollier, *Spin-torque building blocks*, Nature Mat. **13**, 11 (2014).
[2] S.A. Wolf, D.D. Awschalom, R.A. Buhrman, J.M. Daughton, S. von Molnár, M.L. Roukes, A.Y. Chtchelkanova, D.M. Treger, *Spintronics: A spin-based electronics vision for the future*, Science **294**, 1488 (2001).
[3] T. Graf, J. Winterlik, L. Müchler, G.H. Fecher, C. Felser, S.S.P. Parkin, *Magnetic Heusler compounds* in *Handbook of magnetic materials* edited by K.H.J. Buschow, North Holland, Amsterdam (2013).
[4] M. Oogane, T. Kubota, Y. Kota, S. Mizukami, H. Naganuma, A. Sakuma, Y. Ando, *Gilbert magnetic damping constant of epitaxially grown Co-based Heusler alloy thin films*, Appl. Phys. Lett. **96**, 252501 (2010).
[5] T. Kubota, S. Tsunegi, M. Oogane, S. Mizukami, T. Miyazaki, H. Naganuma, Y. Ando, *Half-metallicity and Gilbert damping constant in $Co_2Fe_xMn_{1-x}Si$ Heusler alloys depending on the film composition*, Appl. Phys. Lett. **94**, 122504 (2009).
[6] C. Liu, C.K.A. Mewes, M. Chshiev, T. Mewes, W.H. Butler, *Origin of low Gilbert damping in half metals*, Appl. Phys. Lett. **95**, 022509 (2009).
[7] A.Yu. Dobin, R.H. Victora, *Intrinsic nonlinear ferromagnetic relaxation in thin metallic films*, Phys. Rev. Lett. **90**, 167203 (2003).

[8] K.L. Livesey, M.P. Kostylev, R.L. Stamps, *Parametric spin wave excitation and cascaded processes during switching in thin films*, Phys. Rev. B **75**, 174427 (2007).

[9] S.Y. An, P. Krivosik, M.A. Kraemer, H.M. Olson, A.V. Nazarov, C.E. Patton, *High power ferromagnetic resonance and spin wave instability processes in permalloy thin films*, J. Appl. Phys. **96**, 1572 (2004).

[10] H.M. Olson, P. Krivosik, K. Srinivasan, C.E. Patton, *Ferromagnetic resonance saturation and second order Suhl spin wave instability processes in thin permalloy films*, J. Appl. Phys. **102**, 023904 (2007).

[11] H. Schultheiss, K. Vogt, B. Hillebrands, *Direct observation of nonlinear four-magnon scattering in spin-wave microconduits*, Phys. Rev. B **86**, 054414 (2012).

[12] T. Sebastian, P. Pirro, T. Brächer, A.A. Serga, T. Kubota, H. Naganuma, M. Oogane, Y. Ando, B. Hillebrands, *Nonlinear emission of spin-wave caustics from an edge mode of a microstructured* $Co_2Mn_0.6Fe_0.4Si$ *waveguide*, Phys. Rev. Lett. **110**, 067201 (2013).

[13] H. Suhl, *The theory of ferromagnetic resonance at hight signal powers*, Phys. Chem. Solids. **1**, 209-227 (1957).

[14] R.M. White, M. Sparks, *Ferromagnetic relaxation. III. Theory of instabilities*, Phys. Rev. **130**, 632 (1963).

[15] A.G. Gurevich, G.A. Melkov, *Magnetization oscillations and waves*, CRC Press, New York, (1996).

[16] P. Krivosik, C.E. Patton, *Hamiltonian formulation of nonlinear spin-wave dynamics: Theory and application* Phys. Rev. B **82**, 184428 (2010).

[17] P. Kabos, C.E. Patton, G. Wiese, A.D. Sullins, E.S. Wright, L. Chen, *Butterfly curves and critical modes for second-order spin-wave instability processes in yttrium iron garnet films*, J. Appl. Phys. **89**, 3962 (1996).

[18] T. Sebastian, Y. Ohdaira, T. Kubota, P. Pirro, T. Brächer, K. Vogt, A.A. Serga, H. Naganuma, M. Oogane, Y. Ando, B. Hillebrands, *Low-damping spin-wave propagation in a micro-structured* $Co_2Mn_{0.6}Fe_{0.4}Si$ *Heusler waveguide*, Appl. Phys. Lett. **100**, 112402 (2012).

[19] V.E. Demidov, S.O. Demokritov, B. Hillebrands, M. Laufenberg, P.P. Freitas, *Radiation of spin waves by a single micrometer-sized magnetic element*, Appl. Phys. Lett. **85**, 2866 (2004).

[20] V.E. Demidov, M.P. Kostylev, K. Rott, P. Krzysteczko, G. Reiss, S.O. Demokritov, *Radiation of spin waves from the open end of a microscopic magnetic-film waveguide*, Appl. Phys. Lett. **95**, 112509 (2009).

[21] P. Pirro, T. Brächer, K. Vogt, B. Obry, H. Schultheiss, B. Leven, B. Hillebrands, *Interference of coherent spin waves in micron-sized ferromagnetic waveguides*, Phys. Status Solidi B **248**, 2404 (2011).

[22] B. Kalinikos, A. Slavin, *Theory of dipole-exchange spin wave spectrum for ferromagnetic films with mixed exchange boundary conditions*, J. Phys. C: Solid State **19**, 7013 (1986).

[23] Parameters of calculation: Saturation magnetization $M_s = 1003$ kA/m (from ferromagnetic resonance), exchange constant $A_{ex} = 13\,\mathrm{pJ/m}$ (from thermal BLS spectra of quantized thickness modes).

[24] Due to the finite size of the microstructure, the wave-vector conservation has to be fulfilled only within a uncertainty of about Radiation of spin waves from the open end of a microscopic magnetic-film waveguide $3\,\mathrm{rad/\mu m}$.

[25] The local minimum of $\widetilde{W}$ near 10 GHz arises from the interplay between W and T. At frequencies below this minimum, $\widetilde{W}$ is dominated by the contribution of T, whereas the contribution by W dominates for higher frequencies close to f_0.

[26] C.E. Patton, *Microwave resonance and relaxation* in *Magnetic oxides*, John Wiley, London, 575 (1975).

[27] D.D. Stancil, A. Prabhakar, *Spin Waves: Theory and applications*, Spinger, New York (2009).

[28] M. Sparks, *Ferromagnetic relaxation theory*, Mc Gray-Hill, New York (1964).

[29] E. Schlömann, *Ferromagnetic relaxation caused by interaction with thermally excited magnons*, Phys. Rev. **121**, 1312 (1961).

[30] T. Kasuya and R.C. LeCraw, *Relaxation mechanisms in ferromagnetic resonance*, Phys. Rev. Lett. **6**, 223 (1961).

[31] C.T. Boone, J.A. Katine, J.R. Childress, V. Tiberkevich, A. Slavin, J. Zhu, X. Cheng, I.N. Krivorotov, *Resonant nonlinear damping of quantized spin waves in ferromagnetic nanowires: A spin torque ferromagnetic resonance study*, Phys. Rev. Lett. **103**, 167601 (2009).

E. Applied Spintronics

A substantial part of our research is devoted to fields that have a close relation to applications. Our group is aiming to intensify the communication flow between the academic and the industrial world in order to promote the necessary transfer of technology and *know-how*. Since beginning of the year 2012 we are taking part in the industrial collaboration project STeP (Spintronic Technology Platform) funded by the Ministerium für Bildung, Wissenschaft, Weiterbildung und Kultur in Rhineland-Palatinate in the frame of the European EFRE-Program. The Platform is built jointly with the industrial partner Sensitec, Mainz, and the Johannes Gutenberg University Mainz. Among its main goals, one can cite the generation of new capabilities in the field of spintronics, the construction of a R&D infrastructure directed to small and medium enterprises in Rhineland-Palatinate together with the innovation in GMR and TMR technologies with a strong emphasis on the use of industrial production lines for the creation and testing of new sensor concepts. In this project we contribute to the design and testing of new sensor concepts, the material characterization, especially of Heusler thin films and in other subjects.

Also in 2012 the Greater Region Magnetism Network (GRMN) has been established in the framework of the University of the Greater Region. Here, the universities of Lorraine, Saarrebruck and Kaiserslautern joined their forces to explore magnetic phenomena and their novel application potential. As main aim of the GRMN the synergy of expertise and activities to develop concerted teaching strategies as well as highly innovative technology transfer concepts has been identified.

In Report 4.20 a systematic study of the magnetic properties of the FM materials $Ni_{81}Fe_{19}$ and $Co_{40}Fe_{40}B_{20}$ in FM/NM/Pt layer systems where the feasibility of different non-magnetic materials (NM) as interlayers for spin pumping applications is presented.

In Report 4.21 the influence of the MgO barrier thickness on the lifetime characteristics of CoFeB/MgO/CoFeB tunneling junctions for magnetic sensor applications is described. These investigations follow industrial requirements and are part of the STeP project.

In Report 4.22 a study of the enhancement of the polar magneto-optic Kerr effect in hexagonally patterned Co/Au multilayers is presented. It can be shown that the efficiency of the magneto-plasmonic interaction can be drastically enhanced by multilayers and by surface modifications.

In Report 4.23 some of our activities aiming at bringing magnetism closer to industrial application awareness as well as clarifying the physics behind magnetic applications in our today's life to the open public is presented.

E. Angewandte Spindynamik

Ein Teil unserer Aktivitäten ist auf anwendungsorientierte Forschung gerichtet. Unsere Gruppe versucht Brücken zwischen der akademischen und der industriellen Welt zu bauen, um den Technologietransfer und den Ideenaustausch zu fördern. Seit Anfang 2012 nehmen wir an der Spintronik-Technologie-Plattform (STeP) teil, finanziert vom Ministerium für Bildung, Wissenschaft, Weiterbildung und Kultur in Rheinland-Pfalz im Rahmen des europäischen EFRE-Programms. Dieses Projekt ist eine Zusammenarbeit zwischen der TU Kaiserslautern, der Universität Mainz und dem Industriepartner Sensitec, der große Erfahrung in der Sensorik und in den praktischen Anwendungen der Spintronik gesammelt hat. Als Hauptziele der Plattform kann man unter anderem folgende erwähnen: den Aufbau neuer Kompetenzen auf dem Gebiet der Spintronik, die Bereitstellung der Forschungsinfrastruktur und des anwendungsorientiertem universitären *Know-How* besonders für

kleine und mittlere Unternehmen (KMU) in Rheinland-Pfalz und die Förderung von Innovation im Bereich der GMR und TMR-Technologien. Unsere Aufgabe besteht unter anderen darin, das Design neuer Sensoren mit mikromagnetischen Simulationen zu unterstützen und die Charakterisierung von Heusler-Dünnschichtsystemen vorzunehmen.

Als weitere prominente Initiative auf dem Gebiet der anwendungsorientierten Forschung wurde ebenfalls im Jahre 2012 das Magnetismusnetzwerk der Großregion (GRMN) im Rahmen der Universität der Großregion etabliert. Hier bündeln die Universitäten von Lothringen, Saarbrücken und Kaiserslautern ihr *know-how* und ihre *Netzwerkstrukturen*, um magnetische Phänomene und ihr Anwendungspotential auszuloten. Ein Hauptziel dieser Initiative ist es, die Synergie der Expertisen und Aktivitäten zu nutzen um ein konzertiertes Lehrkonzept auf dem Gebiet des Magnetismus und innovative *Technologietransfer-Konzepte* zu entwickeln.

Im Bericht 4.20 ist eine systematische Studie der magnetischen Eigenschaften der ferromagnetischen Materialien $Ni_{81}Fe_{19}$ und $Co_{40}Fe_{40}B_{20}$ in FM/NM/Pt Schichtsystemen präsentiert, in denen die verschiedenen Grenzflächeneigenschaften eine wesentliche Rolle für Anwendungen des Spinpumpens spielen.

Im Bericht 4.21 werden die Ergebnisse zu Untersuchungen des Einflusses der Barrierendicke in CoFeB/MgO/CoFeB Tunnelstrukturen für magnetische Sensoranwendungen vorgestellt. Diese Untersuchungen erfolgten gemäßindustriellen Standards und wurden im Rahmen des STeP-Projektes durchgeführt.

Im Bericht 4.22 wird eine Studie der Verstärkung des polaren magneto-optischen Kerr-Effekts in hexagonal strukturierten Co/Au-Multilagen präsentiert. Es kann gezeigt werden, dass die Effizienz der magneto-plasmonischen Wechselwirkung durch die Nutzung von Multilagen und durch die Modifikation der Oberflächen drastisch gesteigert werden kann.

Im Bericht 4.23 sind einige erfolgreiche Beispiele unserer Aktivitäten zum Technologietransfer und der Öffentlichkeitsarbeit vorgestellt. Eine Zielgruppe ist die Industrie, in deren Bewusstsein das mögliche Anwendungsspektrum des Magnetismus gerückt werden soll. Eine weitere Zielgruppe ist die allgemeine Öffentlichkeit, der das Thema Magnetismus und dessen Nutzung im täglichen Leben erläutert werden soll.

4.20 Influence of the non-magnetic material (NM) layer on the magnetic properties and spin pumping in NiFe/NM/Pt and CoFeB/NM/Pt layer systems

A. Ruiz-Calaforra, T. Brächer, V. Lauer, P. Pirro, B. Heinz, M. Geilen, A.V. Chumak, A. Conca, B. Leven, and B. Hillebrands

Over the last years, investigations on the influence of a normal metal layer adjacent to a thin layer of a soft ferromagnetic material (FM) have gained large interest due to their impact on spintronic applications. The use of these layer systems in spin-transport devices stresses the importance of understanding the magnetic dynamics and the control of the relaxation processes which take place in these systems. More specifically, FM/Pt layer systems have attracted attention. This is due to the fact that in these systems a drastic increase of the damping, which is commonly associated with spin pumping, and a large inverse spin Hall effect (ISHE) are observed [1, 2]. However, in many experiments a discrepancy between the measured damping increase and the increase expected due to spin pumping occurs [3, 4]. It was shown that the introduction of a normal metal spacer layer reduces the damping increase [5–7]. In most of these studies, Cu is used as spacer due to its long spin diffusion length. This allows for a spin diffusion throughout the Cu into the Pt without the presence of a FM/Pt interface. However, whether this works specifically well for a Cu spacer and the origin of the enhanced damping if Pt is in direct contact to the FM remain unclear.

Here, we present a study of the magnetic dynamic properties of the FM materials $Ni_{81}Fe_{19}$ (hereafter NiFe) and $Co_{40}Fe_{40}B_{20}$ (hereafter CoFeB) in FM/NM/Pt layer systems where the feasibility of different non-magnetic materials (NM) as interlayers for spin pumping applications is investigated. The NM materials commonly used in spintronics Cr and Al, which feature a large spin diffusion length [8–10], as well as Ru, which features a small spin diffusion length [11], and MgO, which blocks spin diffusion, are studied employing ferromagnetic resonance (FMR) spectroscopy. The effective magnetization M_{eff} and the effective damping parameter α_{eff} are studied for different NiFe/NM/Pt and CoFeB/NM/Pt systems. Moreover, a study on the thickness dependence of M_{eff} and α_{eff} for the systems NiFe/Pt, NiFe/Ru/Pt and NiFe/Ru is presented and compared to NiFe/MgO, NiFe/Al and NiFe/Cr. The results show that NiFe/Pt present a large enhancement of the α_{eff} and that this enhancement is reduced by the addition of the NM interlayer. Furthermore, for NiFe/NM layer systems, an adjacent layer of Ru, Pt or MgO induces a certain change in M_{eff} and α_{eff}, while this is not the case for Cr and Al adjacent layers. The enhancement of α_{eff} in CoFeB/Pt systems is not so pronounced, neither are the changes of the magnetic properties with any other NM adjacent layer. Additionally, the spin pumping in NiFe/NM/Pt systems is studied by means of inverse spin Hall effect (ISHE) measurements and the symmetry of the measured voltage is analyzed. Here, an enhancement of the symmetric voltage contribution is associated with the presence of spin pumping [12, 13]. We observe that NiFe/Pt presents the largest symmetric part, while the symmetry decreases with the introduction of a spacer layer. Still, differences of symmetry are observed when comparing NiFe/NM/Pt to the respective NiFe/NM, indicating the existence of ISHE in NiFe/NM/Pt systems.

The films have been fabricated by magnetron rf sputter deposition on SiO_2 substrates in a HV chamber with a base pressure of 5×10^{-7} mbar. Systems which do not feature Pt as top layer have been capped with an additional layer of MgO/Pt. During the film deposition, the substrate is rotated and a magnetic field is applied with permanent magnets that provide a nominal in-plane field $\mu_0 H_{\mathrm{deposition}} = 30\,\mathrm{mT}$. This gives rise to a weak and direction-defined magnetic uniaxial

anisotropy. Within the study, the thickness of the interlayers have been kept fixed to 5 nm for MgO, 8 nm for Ru and Al and 15 nm for Cr. In all films the Pt layer is 2 nm thick. Atomic force microscopy (AFM) analysis determined that the layer systems present a root-mean-square roughness of $Sq \leq 0.55$ nm for all NM materials.

The FMR technique used for the dynamic magnetic characterization of the films is described by Kalarickal *et al.* [14]. The film is placed face-down on a stripline and oriented with the uniaxial anisotropy easy axis parallel to the line. A vector network analyzer (VNA) provides the microwave field which excites the magnetization precession, while a set of coils provide an in-plane static magnetic field. Field dependent FMR spectra are recorded by the measurement of the complex transmission parameter S_{12} with the VNA as the frequency is swept. For a proper calibration, for each data point a reference measurement at a field value of about 20 mT lower than the measured field is taken. The inset of Fig. 1a shows exemplarily the real and imaginary components of a FMR spectra for a NiFe(9 nm)/Al(8 nm)/Pt(2 nm) film at a resonance field $\mu_0 H_{\mathrm{FMR}} = 35.40$ mT. From the spectra, the resonance frequency f_{FMR} and the frequency-swept linewidth Δf are determined following the procedure discussed in Ref. [14].

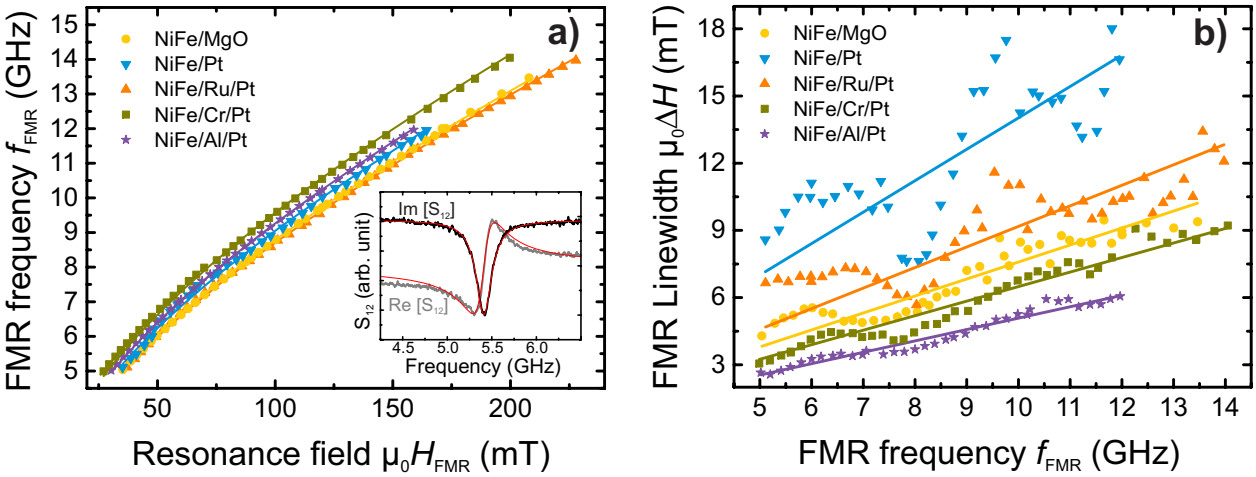

Fig. 1: a) Resonance frequency f_{FMR} versus the resonance field $\mu_0 H_{\mathrm{FMR}}$ for 9 nm thick NiFe films with Pt adjacent layer (NiFe/Pt), and with MgO, Ru, Cr and Al as interlayers. Solid lines represent the fits to the experimental data using Eq. (1) for the determination of M_{eff}. *Inset:* Example of the real and imaginary vector network analyzer - ferromagnetic resonance (VNA-FMR) spectrum and fits for the determination of f_{FMR} and the frequency-swept linewidth Δf of a NiFe(9 nm)/Al(8 nm)/Pt(2 nm) film at a resonance field $\mu_0 H_{\mathrm{FMR}} = 35.40$ mT. b) Resonance field linewidth $\mu_0 \Delta H$ versus the resonance frequency f_{FMR} for 9 nm thick NiFe films with Pt adjacent layer (NiFe/Pt), and with MgO, Ru, Cr and Al as interlayers. Solid lines represent the fits to the experimental data using Eq. (3) for the determination of α_{eff}.

Figure 1a shows the dependence of the resonance frequency f_{FMR} on the resonance field $\mu_0 H_{\mathrm{FMR}}$ for 9 nm thick NiFe films with adjacent Pt layer (NiFe/Pt), and with MgO, Ru, Cr and Al as interlayers. The effective magnetization M_{eff} has been determined by fitting the data to the Kittel formula [15]

$$f_{\mathrm{FMR}} = \gamma \mu_0 \sqrt{(H_{\mathrm{FMR}} + H_{\mathrm{k}})(H_{\mathrm{FMR}} + H_{\mathrm{k}} + M_{\mathrm{eff}})} \tag{1}$$

where H_{FMR} is the applied resonance magnetic field, H_{k} the in-plane anisotropy field and γ the gyromagnetic ratio. Since it has been observed that the determination of γ at low frequencies

can give rise to significant errors in the fitted values [16], the used values for γ are taken from Refs. [16, 17], which have been obtained by broadband ferromagnetic resonance spectroscopy. Hence, $\gamma_{\mathrm{NiFe}} = 29.5\,\mathrm{GHz/T}$ and $\gamma_{\mathrm{CoFeB}} = 29\,\mathrm{GHz/T}$. The anisotropy field H_{k} has been determined by measurements of the resonance field at $\varphi = 0^\circ$ and $\varphi = 90^\circ$, i.e., along the easy and hard axis, respectively, using the relationship for a film with a weak uniaxial in-plane anisotropy ($M_{\mathrm{S}} >> H_{\mathrm{k}}$) [18, 19]:

$$H_{\mathrm{FMR}} = H_0 - H_{\mathrm{k}} \cos(2\varphi) \tag{2}$$

being H_0 the in-plane resonance field in absence of an in-plane anisotropy. It was determined that H_{k} slightly varies depending on the adjacent layer material, resulting in values which range from $\mu_0 H_{\mathrm{k}} = 0.5 - 0.7\,\mathrm{mT}$ for NiFe and $\mu_0 H_{\mathrm{k}} = 2.8 - 4.9\,\mathrm{mT}$ for CoFeB.

Following the procedure described in Ref. [14] the resonance field linewidth $\mu_0 \Delta H$ is determined and plotted against the resonance frequency f_{FMR} as shown in Fig. 1b. The oscillations around the straight line are due to the microwave transmission characteristics of our setup. Their period is practically independent of the investigated sample. However, their relative amplitude depends on the overall absorption in the film. The frequency dependence of $\mu_0 \Delta H$ is used to determine the effective damping parameter α_{eff} by fitting the data to [14, 20]

$$\mu_0 \Delta H = \mu_0 \Delta H_0 + \frac{2\alpha_{\mathrm{eff}} f}{\gamma} \quad , \tag{3}$$

with

$$\alpha_{\mathrm{eff}} = \alpha_0 + \Delta\alpha \tag{4}$$

where α_0 is the bulk damping parameter and $\Delta\alpha$ is the enhancement of the damping parameter due to spin pumping and other interface effects. The inhomogeneous linewidth broadening ΔH_0 was determined to be very small and, consequently, its influence on the slopes and, thus, α_{eff} is negligible. The results for M_{eff} and α_{eff} obtained from the fittings have been summarized in Table 1. For a comparison, the results for the layer systems NiFe/Ru, NiFe/Cr and NiFe/Al (i.e., without adjacent Pt layer) have been included. The error accounts for the dispersion of the results between several samples.

The reduction of M_{eff} with respect to the saturation magnetization M_{S} is caused by the out-of-plane anisotropy, which depends on the exact nature of the interface (e.g., interface/surface roughness, adjacent materials). These effects are summarized in the perpendicular surface anisotropy field $H_{\mathrm{K}}^{\perp}$. Hence, $M_{\mathrm{eff}} = M_{\mathrm{S}} - H_{\mathrm{K}}^{\perp}$ and, therefore, it is expected that M_{eff} depends drastically on the adjacent layers. In our results it is observed that the films with Cr and Al feature a large M_{eff} while films with MgO, Pt or Ru adjacent layer show a rather low M_{eff}. This means that there is a larger contribution of the mentioned interface effects for these last adjacent layers. Furthermore, in NiFe/Cr/Pt and NiFe/Cr films, as well as for NiFe/Al/Pt and NiFe/Al films, a comparable M_{eff} is observed, as it is expected. However, this is not the case for NiFe/Ru/Pt and NiFe/Ru films. M_{eff} of NiFe/Ru systems is much lower, implying that such layer systems present larger interface effects.

The fact that some interfaces affect the magnetic properties of the FM layer is not only visible in a decrease of M_{eff} but also in a change of α_{eff}. In particular, this is seen in the difference of α_{eff} between NiFe/MgO and NiFe/Al or NiFe/Cr layer systems, where a smaller α_{eff} is obtained

	M_{eff} kA/m	α_{eff} 10^{-3}	M_{S} kA/m	$K_{\mathrm{S}}^{\perp}$ mJ/m^2	c 10^{-2}nm	$V_{\mathrm{S}}/V_{\mathrm{A}}$
NiFe/MgO	620 ± 20	12 ± 1	800 ± 20	0.7 ± 0.1	4.7 ± 0.8	3.5 ± 0.3
NiFe/Pt	630 ± 20	21 ± 1	810 ± 20	0.9 ± 0.1	14 ± 1	5.2 ± 0.3
NiFe/Ru/Pt	600 ± 20	14 ± 1	820 ± 30	1.1 ± 0.1	6.9 ± 0.7	2.8 ± 0.1
NiFe/Ru	540 ± 20	15 ± 2	800 ± 20	1.2 ± 0.1	7.4 ± 0.6	2.2 ± 0.1
NiFe/Cr/Pt	750 ± 20	10 ± 1				4.4 ± 0.1
NiFe/Cr	750 ± 20	9 ± 1	842 ± 7	0.4 ± 0.1	2.5 ± 0.1	3.6 ± 0.1
NiFe/Al/Pt	700 ± 20	8 ± 1				4.1 ± 0.1
NiFe/Al	690 ± 20	8 ± 1	850 ± 20	0.6 ± 0.1	1.1 ± 0.3	3.3 ± 0.1

Table 1: Summary of the results for M_{eff}, α_{eff}, $K_{\mathrm{S}}^{\perp}$, c, and $V_{\mathrm{S}}/V_{\mathrm{A}}$ obtained from the fittings of Eq. (1), Eq. (3), Eq. (5), Eq. (4) and Eq. (8), respectively, for NiFe layer systems. The results of M_{eff}, α_{eff} and $V_{\mathrm{S}}/V_{\mathrm{A}}$ correspond to a 9 nm thick NiFe film. The non-magnetic layer thicknesses are: MgO (5 nm), Ru (8 nm), Cr (15 nm), Al (8 nm) and Pt (2 nm).

for systems which present a higher M_{eff} and therefore, less contributions of interface effects. On the other hand NiFe/Pt films present a very large α_{eff} compared to NiFe/MgO, although both systems present a similar M_{eff}. Furthermore, if an interlayer is added (Ru, Cr or Al), α_{eff} decreases. However, in the case of NiFe/Ru/Pt layer systems, the value of α_{eff} is larger than for NiFe/MgO. Due to the fact that the spin diffusion length of Ru is of the order of the thickness [11], there is a possibility that the increase of α_{eff} is due to spin flip scattering within the Ru thickness. On the other hand, this increase can also be connected to the decrease of M_{eff} observed in both NiFe/Ru/Pt and NiFe/Ru layer systems. Furthermore, materials with a large spin diffusion length such as Cr and Al should allow for spin pumping into the Pt in NiFe/NM/Pt layer systems and, hence, such systems should present a certain increase of α_{eff}. The comparison between NiFe/Pt and NiFe/Cr/Pt (NiFe/Al/Pt) layer systems and the lack of difference of α_{eff} between NiFe/Cr/Pt (NiFe/Al/Pt) and NiFe/Cr (NiFe/Al) layer systems leads to the conclusion that either the contribution of spin pumping to α_{eff} is very small or that spin pumping is blocked by these spacer materials.

The same study has been carried out for 9 nm thick CoFeB films. The results for this material are shown in Table 2. In the case of CoFeB the differences in M_{eff} due to the interface effects are much less pronounced than for NiFe. In this case, the addition of a NM such as Ru, Cr or Al decreases M_{eff} slightly with respect to CoFeB/MgO. Consequently, these differences are reflected in the small differences of α_{eff}, although all values oscillate around a common value of $\alpha_{\mathrm{eff}} = 0.011$. An enhancement of α_{eff} is only present in CoFeB/Pt layer systems; however, this enhancement is smaller than for NiFe/Pt. Moreover, M_{eff} for CoFeB/Pt layer systems shows a low value with respect to the other studied systems, while Ru has no strong influence on the adjacent CoFeB.

For a deeper study of the influence of the interface on the magnetic properties of the NiFe layer, a thickness dependence study of M_{eff} and α_{eff} for the different adjacent material layers has been carried out. In Fig. 2a the results corresponding to M_{eff} are shown. As mentioned before, M_{eff} will decrease by the contribution of $H_{\mathrm{K}}^{\perp}$ as a function of the thickness of the FM layer [21, 22]:

$$M_{\mathrm{eff}} = M_{\mathrm{S}} - H_{\mathrm{K}}^{\perp} = M_{\mathrm{S}} - \frac{2K_{\mathrm{S}}^{\perp}}{\mu_0 M_{\mathrm{S}} d_{\mathrm{FM}}} \quad . \tag{5}$$

Here, $K_{\mathrm{S}}^{\perp}$ is the perpendicular surface anisotropy constant and can be determined from the linear

	M_{eff} kA/m	α_{eff} 10^{-3}
CoFeB/MgO	1080 ± 20	11 ± 1
CoFeB/Pt	1000 ± 20	16 ± 1
CoFeB/Ru/Pt	1050 ± 20	10 ± 1
CoFeB/Ru	1020 ± 20	11 ± 2
CoFeB/Cr/Pt	1020 ± 20	9 ± 1
CoFeB/Cr	1070 ± 20	12 ± 1
CoFeB/Al/Pt	1030 ± 20	11 ± 1
CoFeB/Al	1060 ± 20	12 ± 1

Table 2: Summary of the results for M_{eff} and α_{eff} obtained from the fittings of Eq. (1) and Eq. (3) for CoFeB (9 nm) layer systems. The layer thicknesses are: MgO (5 nm), Ru (8 nm), Cr (15 nm), Al (8 nm) and Pt (2 nm). The error accounts for the dispersion of the results between several samples.

fits together with M_{S}. The results for both parameters have been summarized in Table 1. It is observed that M_{S} varies for the different adjacent layers, being larger for films with Cr and Al as adjacent layer and smaller for films with Ru. Nevertheless, this variation is small and stays within the experimental error. $\overline{M_{\mathrm{S}}}$ averaged over all studied layer systems was determined to be $\overline{M_{\mathrm{S}}} = 820 \pm 20\,\mathrm{kA/m}$. The results of $K_{\mathrm{S}}^{\perp}$ show that a Ru adjacent layer causes a large out-of-plane surface anisotropy, certifying the results obtained for the 9 nm thick NiFe films and corroborating the presence of interface effects in NiFe-Ru layer systems. On the other hand, a very low out-of-plane surface anisotropy is observed in films with Cr as adjacent material, much lower than for NiFe/MgO. The presence of perpendicular surface anisotropy in NiFe/MgO layer systems has been observed before and it has been related to the hybridization of Fe $3d$ and O $4p$ orbits at the Fe/MgO interfaces [23, 24]. NiFe/Pt layer systems also present a relatively large $K_{\mathrm{S}}^{\perp}$.

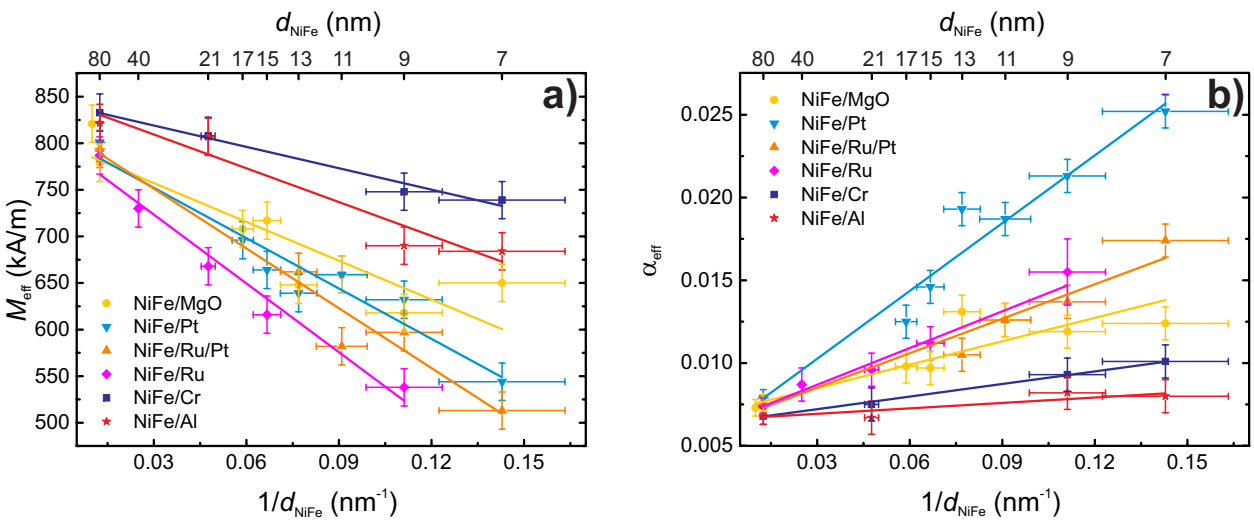

Fig. 2: Thickness dependence of a) M_{eff} and b) α_{eff} for NiFe films with MgO, Pt, Ru/Pt, Ru, Cr and Al adjacent layers. In a) solid lines represent the linear fits to the experimental data using Eq. (5) for the determination of M_{S} and $K_{\mathrm{S}}^{\perp}$. In b) solid lines represent the linear fits to the experimental data using Eq. (4) for the determination of α_0 and c.

The results of the dependence of α_{eff} on the thickness of NiFe for the studied layer systems are shown in Fig. 2b. If the enhanced damping is purely caused at the interface, $\Delta\alpha$ should scale with with the thickness of the FM layer as $1/d_{\text{FM}}$ [1]. Consequently, a fit of α_{eff} versus $1/d_{\text{FM}}$ yields the strength of the interface effects in the form of the slope $c = \Delta(\alpha_{\text{eff}})/\Delta(1/d_{\text{FM}})$.

From the fitting the averaged value of the bulk damping parameter is found to be $\overline{\alpha_0} = (6.5 \pm 0.5) \times 10^{-3}$. The results for c (shown in Table 1) confirm the large strength of the interface effects in NiFe/Pt systems which lead to a large damping enhancement with decreasing NiFe thickness. A decrease of the damping enhancement is obtained by the addition of a Ru spacer layer. Still, both NiFe/Ru/Pt and NiFe/Ru present a rather large c, although no difference is seen between them within the error bar. Additionally, it is observed that, even in the absence of spin pumping (NiFe/MgO), interface effects influence the increase of the damping parameter. Moreover, NiFe/Al and NiFe/Cr layer systems show practically no enhancement.

For pure spin pumping, the slope c is connected to the spin mixing conductance $g_{\text{eff}}^{\uparrow\downarrow}$ via [12, 25]

$$g_{\text{eff}}^{\uparrow\downarrow} = \frac{4\pi\overline{M_{\text{S}}}}{g\mu_{\text{B}}} c \quad . \tag{6}$$

In order to determine the spin mixing conductance it is important to note that the enhancement of the damping given by c will not necessarily only be due to spin pumping but also due to other interface effects. Therefore, it is necessary to subtract this contribution to the enhancement in a reference sample where no spin pumping occurs. Hence, the effective spin mixing conductance for NiFe/Pt layer systems can be determined from the resulting slopes c obtained from the thickness dependence of α_{eff}

$$g_{\text{eff,NiFe/Pt}}^{\uparrow\downarrow} = \frac{4\pi\overline{M_{\text{S}}}}{g_{\text{NiFe}}\mu_{\text{B}}} (c_{\text{NiFe/Pt}} - c_{\text{ref}}) \quad . \tag{7}$$

Using NiFe/MgO, where the spin pumping is blocked, a spin mixing conductance of $g_{\text{eff,NiFe/Pt}}^{\uparrow\downarrow} = (4.7 \pm 0.2) \times 10^{19}\,\text{m}^{-2}$ is obtained for NiFe/Pt. However, using NiFe/MgO as reference for the calculation potentially leads to an underestimation of $g_{\text{eff,NiFe/Pt}}^{\uparrow\downarrow}$, as NiFe/MgO presents a relatively large enhancement of α_{eff} by itself. If NiFe/Al, which presents the lowest enhancement of α_{eff} and which should not contain additional losses from spin pumping due to the large spin diffusion length in Al, is taken as a reference the spin mixing conductance is determined to $g_{\text{eff,NiFe/Pt}}^{\uparrow\downarrow} = (6.6 \pm 0.1) \times 10^{19}\,\text{m}^{-2}$. For both reference layers, the obtained values are larger than some of the reported values [12, 13, 26]. This discrepancy can be due to additional effects that influence the Gilbert damping at the NiFe/Pt interface such as spin memory loss or induced ferromagnetism in the Pt [7, 27] which do not occur in the reference samples.

In the case of CoFeB/Pt the spin mixing conductance is determined for the fixed thickness of 9 nm and the difference between α_{eff} for CoFeB/Pt and CoFeB/MgO. In this case, the spin mixing conductance is $g_{\text{eff,CoFeB/Pt}}^{\uparrow\downarrow} = (3 \pm 1) \times 10^{19}\,\text{m}^{-2}$. The difference in $g_{\text{eff,CoFeB/Pt}}^{\uparrow\downarrow}$ if CoFeB/Al is taken as reference is within the error. These value is slightly smaller than the one presented in Ref. [28].

Furthermore, ISHE measurements have been performed on the 9 nm thick NiFe samples listed in Table 1. These results allow for the quantification of spin pumping depending on the layer system.

In order to perform the measurements, the sample is magnetized in-plane along the easy axis direction by an external magnetic field H_{ext}. The magnetization dynamics are excited by an alternating Oersted field $\tilde{h}$ oriented perpendicular to H_{ext} (see inset Fig. 3). For this purpose a modulated microwave signal of a fixed frequency of $f = 6.8\,\text{GHz}$, an amplitude modulation frequency of $f_{\text{mod}} = 500\,\text{Hz}$ and a peak power level of $P = 10\,\text{mW}$ is applied to a 600 µm wide 50 Ohm-matched Cu microstrip antenna by means of an Agilent E8257D microwave source. During the measurements H_{ext} is swept and the voltage drop is modulated by $f_{\text{mod}} = 500\,\text{Hz}$ due to the modulation of the microwave signal amplitude. A low pass filter eliminates the higher AC currents induced directly by the microwave signal at $f = 6.8\,\text{GHz}$. Getting close to the FMR condition by sweeping the field, the voltage drop signal changes significantly [29] (see Fig. 3).

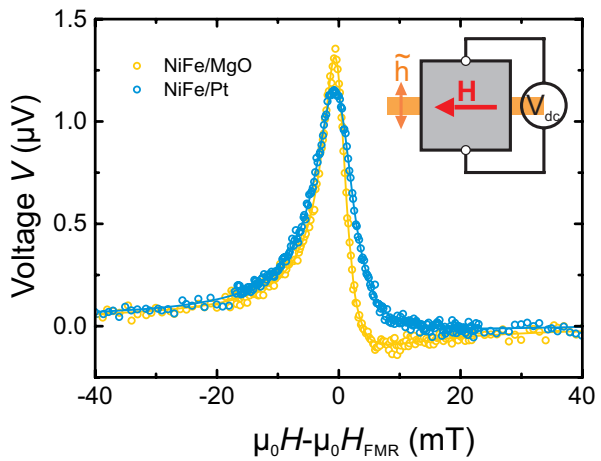

Fig. 3: Field-swept voltage measurements for positive fields for NiFe/MgO and NiFe/Pt layer systems. The solid lines represent the fit of Eq. (8).

The Voltage V measured in the vicinity of the FMR as a function of the applied field has a symmetric and an asymmetric contribution and can be fitted according to [13]

$$V(H) = V_0 + V_{\text{S}} \frac{\Delta H^2}{(H - H_{\text{FMR}})^2 + \Delta H^2} + V_{\text{A}} \frac{-\Delta H (H - H_{\text{FMR}})}{(H - H_{\text{FMR}})^2 + \Delta H^2} \tag{8}$$

in order to separate both contributions. While the ISHE gives a symmetric contribution only, other effects, which are commonly summarized under the term *spin rectification*, can contribute to both the symmetric and asymmetric parts of the measured voltage in a layer system incorporating a ferromagnetic metal [13, 30]. Here, as a quantification of the spin pumping, the ratio $V_{\text{S}}/V_{\text{A}}$ is compared for the different NiFe layer systems, where a direct comparison is only performed for layer systems with identical metallic layers with and without MgO layer between the top FM/NM layer and the Pt layer, which has always been used as capping layer. This ensures that the difference in the symmetry of the measured voltage is connected to the ISHE in the NM since the spin rectification contributions are not changed.

Figure 3 shows exemplarily the experimental data of the voltage V for positive fields obtained for NiFe/MgO (i.e., NiFe with MgO/Pt cap layer) and NiFe/Pt. NiFe/MgO presents both symmetric and asymmetric contributions. Even though there is no spin pumping into the Pt layer because of the MgO interlayer the symmetric contribution is dominant ($V_{\text{S}}/V_{\text{A}} = 3.5$). In addition to the spin rectification effects mentioned above, this symmetric voltage can be influenced by an ISHE from the NiFe layer itself [31, 32]. However, if the MgO barrier between the Py and the Pt is removed, spin pumping into the Pt and, consequently, ISHE inside the Pt can occur, which give rise an additional symmetric voltage contribution ($V_{\text{S}}/V_{\text{A}} = 5.2$).

Similar results are obtained if the NM spacer is introduced, cf. Table 1. For all NM spacer the removal of the MgO barrier increases the symmetry of the measured voltage which can be attributed to the ISHE in Pt. Moreover, for Al and Cr spacer, the symmetry of the voltage for NiFe/Al and NiFe/Cr is very similar to NiFe/MgO which is consistent with the assumption that no strong ISHE should occur in those metal layers. Only for NiFe/Ru a change of symmetry is observed. This can be caused by the spin pumping and consequent ISHE in Ru. However, this would imply that the ISHE voltage in Ru opposes the other voltage contributions. Another possible reason is the decreased quality of the NiFe in this layer system, as discussed above. This is a further hint that a detailed study of the NiFe/Ru layer system is needed. Comparing the increase of the symmetric part of the voltage for the different systems, we find that NiFe/Pt has the largest contribution from ISHE. The increase of the symmetric part when introducing a spacer layer is lower and very similar for all spacers. This is a strong hint that spin pumping is still present in the systems with NM spacer. For all studied layer systems, a change in the direction of the applied field changes the voltage peak polarity, but no difference in the ratio V_S/V_A is observed. Furthermore, the field linewidths obtained are in agreement with the field linewidths obtained by FMR spin pumping.

To summarize, we have studied the influence of the interface on the dynamic magnetic properties of NiFe/Pt, NiFe/NM and NiFe/NM/Pt layer systems by FMR and ISHE technique. As spacer materials Ru, Cr, Al and MgO are used. We observe that NiFe/Pt presents the largest enhancement of the damping parameter, as well as the largest voltage ratio V_S/V_A in the ISHE measurements due to the presence of spin pumping and consequent ISHE in the Pt layer. Additionally, an adjacent Pt layer decreases the M_{eff}. While Al and Cr by themselves induce no major change of the magnetic properties of NiFe, an adjacent Ru layer reduces M_{eff} and enhances α_{eff} significantly. In comparison to NiFe/Pt, the introduction of any of the studied spacer layers strongly decreases the damping enhancement in NiFe/Pt systems while the ratio V_S/V_A still indicates that spin pumping and ISHE into Pt occurs through all metallic spacer layers. For these spacer materials we find an increase of the voltage ratio V_S/V_A if Pt is in direct contact to the spacer material. Still, the presence of an adjacent Ru layer decreases V_S/V_A by itself, which is either caused by the spin pumping and ISHE in Ru or a general reduction of the magnetic properties of the NiFe layer in NiFe/Ru systems. Additionally, we find that in NiFe/MgO/Pt systems, M_{eff} is decreased and α_{eff} is enhanced. This indicates that even in the absence of spin pumping, other interface effects can influence the magnetic properties and the derivation of parameters like the spin-mixing conductance, from spin pumping measurements.

For comparison, an FMR study on CoFeB/NM/Pt systems was performed using the same NM materials. This reveals that interface effects are much less pronounced in these systems, and only for CoFeB/Pt an enhancement of the damping parameter is evident. In particular, no strong influence of Ru on CoFeB is found, meaning that this is a peculiarity of NiFe-Ru interfaces which needs to be studied further.

Financial support by the state Rhineland-Palatinate (MBWWK and MWKEL) and the European Regional development Fund (ERDF) in the frame of the Spintronic Technology Platform (STeP), as well as by Deutsche Forschungsgemeinschaft (CH 1037/1-1) is gratefully acknowledged. T. B. was supported by the DFG within the Graduate School of Excellence "Materials Science in Mainz (MAINZ)" (GSC266).

References

[1] S. Mizukami, Y. Ando, T. Miyazaki, *The study on ferromagnetic resonance linewidth for NM/80NiFe/NM (NM = Cu, Ta, Pd and Pt) films*, Jpn. J. Appl. Phy. **40**, 580 (2001).

[2] E. Saitoh, M. Ueda, H. Miyajima, G. Tatara, *Conversion of spin current into charge current at room temperature: Inverse spin-Hall effect*, Appl. Phys. Lett. **88**, 182509 (2006).

[3] S.M. Rezende, R.L. Rodríguez-Suárez, M.M. Soares, L.H. Vilela-Leão, D. Ley Domínguez, A. Azevedo, *Enhanced spin pumping damping in yttrium iron garnet/Pt bilayers*, Appl. Phys. Lett. **102**, 012402 (2013).

[4] P. Pirro, T. Brächer, A.V. Chumak, B. Lägel, C. Dubs, O. Surzhenko, P. Görnert, B. Leven, B. Hillebrands *Spin-wave excitation and propagation in microstructured waveguides of yttrium iron garnet/Pt bilayers*, Appl. Phys. Lett. **104**, 012402 (2014).

[5] S. Mizukami, Y. Ando, T. Miyazaki, *Effect of spin diffusion on Gilbert damping for a very thin permalloy layer in Cu/permalloy/Cu/Pt films*, Phys. Rev. B **66**, 104413 (2002).

[6] A. Ghosh, S. Auffret, U. Ebels, W.E. Bailey, *Penetration depth of transverse spin current in ultrathin ferromagnets*, Phys. Rev. Lett. **109**, 127202 (2012).

[7] J.-C. Rojas-Sánchez, N. Reyren, P. Laczkowski, W. Savero, J.-P. Attané, C. Deranlot, M. Jamet, J.-M. George, L. Vila, H. Jaffrès, *Spin pumping and inverse spin Hall effect in Platinum: The essential role of spin-memory loss at metallic interfaces*, Phys. Rev. Lett. **112**, 106602 (2014).

[8] A. Zambano, K. Eid, R. Loloee, W.P. Pratt, Jr., J. Bass, *Interfacial properties of Fe/Cr multilayers in the current-perpendicular-to-plane geometry*, J. Magn. Magn. Mater. **51**, 253 (2002).

[9] F.J. Jedema, M.S. Nijboer, A.T. Filip, B.J. van Wees, *Spin injection and spin accumulation in all-metal mesoscopic spin valves*, Phys. Rev. B **67**, 085319 (2003).

[10] N. Poli, M. Urech, V. Korenivski, D.B. Haviland, *Spin-flip scattering at Al surfaces*, J. Appl. Phys. **99**, 08H701 (2006).

[11] K. Eid, R. Fonck, M. AlHaj Darwish, W.P. Pratt, Jr., J. Bass, *Current-perpendicular-to-plane-magnetoresistance properties of Ru and Co/Ru interfaces*, J. Appl. Phys. **91**, 8102 (2002).

[12] O. Mosendz, V. Vlaminck, J.E. Pearson, F.Y. Fradin, G.E.W. Bauer, S.D. Bader, A. Hoffmann, *Detection and quantification of inverse spin Hall effect from spin pumping in permalloy/normal metal bilayers*, Phys. Rev. B **82**, 214403 (2010).

[13] A. Azevedo, L.H. Vilela-Leão, R. L. Rodríguez-Suárez, A.F. Lacerda Santos, S.M. Rezende, *Spin pumping and anisotropic magnetoresistance voltages in magnetic bilayers: Theory and experiment*, Phys. Rev. B **83**, 144402 (2011).

[14] S.S. Kalarickal, P. Krivosik, M. Wu, C.E. Patton, M.L. Schneider, P. Kabos, T.J. Silva, J.P. Nibarger, *Ferromagnetic resonance linewidth in metallic thin films: Comparison of measurement methods*, J. Appl. Phys. **99**, 093909 (2006).

[15] C. Kittel, *On the theory of ferromagnetic resonance absorption*, Phys. Rev. **73**, 155 (1948).

[16] J.M. Shaw, H.T. Nembach, T.J. Silva, C.T. Boone, *Precise determination of the spectroscopic g-factor by use of broadband ferromagnetic resonance spectroscopy*, J. Appl. Phys. **114**, 243906 (2013).

[17] X. Liu, W. Zhang, M.J. Carter, G. Xiao, *Ferromagnetic resonance and damping properties of CoFeB thin films as free layers in MgO-based magnetic tunneling junctions*, J. Appl. Phys. **110**, 033910 (2011).

[18] A. Layadi, W.C. Cain, J.-W. Lee, J.O. Artman, *Investigation of anisotropy by ferromagnetic resonance (FMR) in exchange-coupled bilayer films*, IEEE Trans. Magn. Magn. **23**, 2993 (1987)

[19] M. Rubinstein, P. Lubitz, S.-F. Cheng, *Ferromagnetic-resonance field shift in an exchange-biased CoO/$Ni_{80}Fe_{20}$ bilayer*, J. Magn. Magn. Mater. **195**, 299 (1999).

[20] B. Heinrich, J.F. Cochran, R. Hasegawa, *FMR linebroadening in metals due to two-magnon scattering*, J. Appl. Phys. **57**, 3690 (1985).

[21] J.-M.L. Beaujour, W. Chen, A.D. Kent, J.Z. Sun, *Ferromagnetic resonance study of polycrystalline cobalt ultrathin films*, J. Appl. Phys. **99**, 08N503 (2006).

[22] Y.K. Kim, T.J. Silva, *Magnetostriction characteristics of ultrathin permalloy films*, Appl. Phys. Lett. **68**, 2885 (1996).

[23] R. Shimabukuro, K. Nakamura, T. Akiyama, T. Ito, *Electric field effects on magnetocrystalline anisotropy in ferromagnetic Fe monolayers*, Physica E **42**, 1014 (2010).

[24] J. Okabayashi, J.W. Koo, H. Sukegawa, S. Mitani, Y. Takagi, T. Yokoyama, *Perpendicular magnetic anisotropy at the interface between ultrathin Fe film and MgO studied by angular-dependent x-ray magnetic circular dichroism*, Appl. Phys. Lett. **105**, 122408 (2014).

[25] Y. Tserkovnyak, A. Brataas, G.E.W. Bauer, B.I. Halperin, *Nonlocal magnetization dynamics in ferromagnetic heterostructures*, Rev. Mod. Phys. **77**, 1375 (2005).

[26] M. Obstbaum, M. Härtinger, H.G. Bauer, T. Meier, F. Swientek, C.H. Back, G. Woltersdorf, *Inverse spin Hall effect in $Ni_{81}Fe_{19}$/normal-metal bilayers*, Phys. Rev. B **89**, 060407(R) (2014).

[27] Y. Sun, H. Chang, M. Kabatek, Y.-Y. Song, Z. Wang, M. Jantz, W. Schneider, M. Wu, E. Montoya, B. Kardasz, B. Heinrich, S.G.E. te Velthuis, H. Schultheiss, A. Hoffmann, *Damping in Yttrium Iron Garnet nanoscale films capped by Platinum*, Phys. Rev. Lett. **111**, 106601 (2013).

[28] D.-J. Kim, S.-I. Kim, S.-Y. Park, K.-D. Lee, B.-G. Park, *Ferromagnetic resonance spin pumping in CoFeB with highly resistive non-magnetic electrodes*, Current Applied Physics **14**, 1344 (2014).

[29] K. Ando, S. Takahashi, J. Ieda, Y. Kajiwara, H. Nakayama, T. Yoshino, K. Harii, Y. Fujikawa, M. Matsuo, S. Maekawa, E. Saitoh, *Inverse spin-Hall effect induced by spin pumping in metallic system*, J. Appl. Phys. **109**, 103913 (2011).

[30] M. Harder, Z.X. Cao, Y.S. Gui, X.L. Fan, C.-M. Hu, *Analysis of the line shape of electrically detected ferromagnetic resonance*, Phys. Rev. B **84**, 054423 (2011).

[31] B.F. Miao, S.Y. Huang, D. Qu, C.L. Chien, *Inverse spin Hall effect in a ferromagnetic metal*, Phys. Rev. Lett. **111**, 066602 (2013).

[32] A. Tsukahara, Y. Ando, Y. Kitamura, H. Emoto, E. Shikoh, M.P. Delmo, T. Shinjo, M. Shiraishi, *Self-induced inverse spin Hall effect in permalloy at room temperature*, Phys. Rev. B **89**, 235317 (2014).

4.21 Influence of the MgO barrier thickness on the lifetime characteristics of magnetic tunneling junctions for sensors

A. Conca, B. Hillebrands, and B. Leven

In collaboration with F. Casper, Institute of Inorg. Chemistry and Anal. Chemistry, Johannes Gutenberg Universität, Mainz, Germany,
J. Paul, R. Lehndorff, Sensitec GmbH, Mainz, Germany,
G. Jakob and M. Kläui, Institute of Physics, Johannes Gutenberg-Universität, Mainz, Germany.

Magnetic tunneling junctions (MTJs) are commonly used in hard disc read heads. As magnetic field sensors they are entering the field of industrial applications in the automotive branch, in robotics and in machine automation in general. Due to the higher tunneling magnetoresistance values in comparison with AMR and GMR technologies (anisotropic and giant magnetoresistance, respectively), MTJs can provide higher sensitivity in sensors. This eliminates the need of a signal preamplifier with the subsequent simplification of the chip design. Additionally, their typically larger resistance values make them promising candidates for green energy applications with low-consumption requirements, due to the reduction of the current needed to obtain a voltage signal. For these reasons, it is no wonder that the main sensors producers are developing new prototypes and products based on MTJs [1–3].

One of the main criticism points that prevents a faster adoption of the MTJs for sensors is their long-time stability against failure. The thin insulating layer responsible for the tunneling effect is the weakest point. During working conditions the voltage drops over the few nanometer thick tunneling barrier resulting in a large electrical field (10^7 V/m). This field represents a strong stress agent beeing able, after a certain time, to produce an electric breakdown of the barrier and a device failure. This process is independent on electrostatic discharge (ESD) events which can also destroy the barrier. While the latter can be prevented with diverting on-chip circuits or by training of the mounting employees, the former cannot be avoided since the stress agent is present any time that the sensor/device is in use.

For a given junction, the time to a breakdown event cannot be predicted since we are handling here a stochastic process analog to metal failure under mechanical stress. However, the failure rate for a given sensor population and its time evolution characteristics can be measured and analyzed using

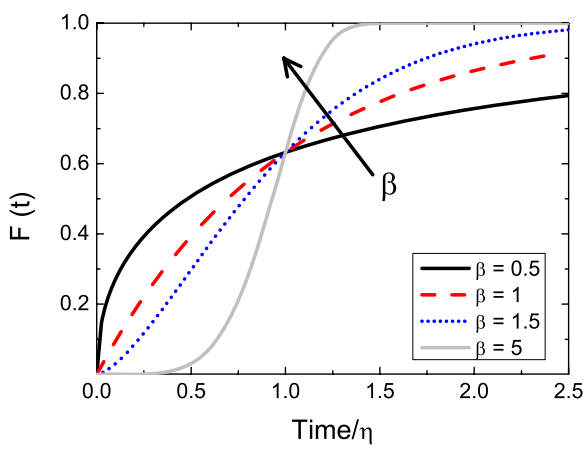

Fig. 1: Weibull cumulative function $F(t)$, describing the total fraction of broken elements after a time t, calculated for different values of the shape parameter β. Time is given in units of the characteristic lifetime η.

statistical methods. Here we report on a systematic study of the barrier thickness influence on the lifetime characteristics for CoFeB/MgO/CoFeB tunneling junctions. For this purpose, the Weibull distribution is used. This approach can be used in any study of failure events caused by a single stress agent (in our case the electrical field). The distribution does not take into account thermal or current-induced electromigration effects for which other statistical models are more appropiate. For this reason, the current density must be kept low which may complicate measurements for MTJ with very low resistance×area (RA) values. The suitability of the Weibull distribution for the description of breakdown processes in thin oxide layers [4] and, more concretely, of MTJ has been already proven for MTJs with Al_2O_3 [5,6] and MgO [7] barriers.

The Weibull cumulative function describes the total fraction F of broken elements after a certain time t:

$$F(t) = 1 - \exp\left(-\left[\frac{t}{\eta}\right]^{\beta}\right) \quad . \tag{1}$$

Here, η is the characteristic lifetime of the junction population (for $t = \eta$, 63.2% of the elements are broken) and β is the shape parameter. Its influence can be better understood using Fig. 1. Three cases are discussed in general:

- $\beta < 1$: Failure rate decreases with time. The population shows a large *infant mortality*, i.e. a significant fraction of the elements breaks shortly after the application of the stress agent (black line in Fig. 1). In general, this regime is not desired since a large part of an hypothetical sensor production will fail in an early stage.
- $\beta > 1$ Failure rate increases with time. The behavior is dominated by *aging* (dotted data and gray line) and there is a time window for which the failure rate is negligible. This is the desired situation since it allows the introduction of a guaranty time.
- $\beta = 1$ Constant failure rate. This represents the transition between the two previous cases but it must be handled with care since it may point to an external random agent dominating the behavior (e.g. a defective measurement setup generating peak voltages).

For better comparison between different data sets, the use of Weibull plots is recommended. Applying the logarithmic function to Eq. (1) results in:

$$\ln[-\ln(1 - F(t))] = \beta \cdot \ln(t) - \beta \cdot \ln(\eta) \quad . \tag{2}$$

The use of Weibull plots is more convenient than plotting $F(t)$ since they allow an easier comparison of all measurements at different voltages and time scales. Additionally, the slope in the graph is directly related to the β parameter allowing for a fast optical check of measurement validity. If the failure mechanism is voltage-independent, the slope should not be very different. The opposite case is not well described by the Weibull distribution.

The characterization of the breakdown processes was carried on for circular CoFeB/MgO/CoFeB junctions with a diameter of 10 µm. The barrier is deposited directly from a MgO target by rf-sputtering and synthetic antiferromagnet layer structure is used. The deposition and the lithography process to create the structures were carried on in the facilities of our industrial partner Sensitec GmbH. [10]

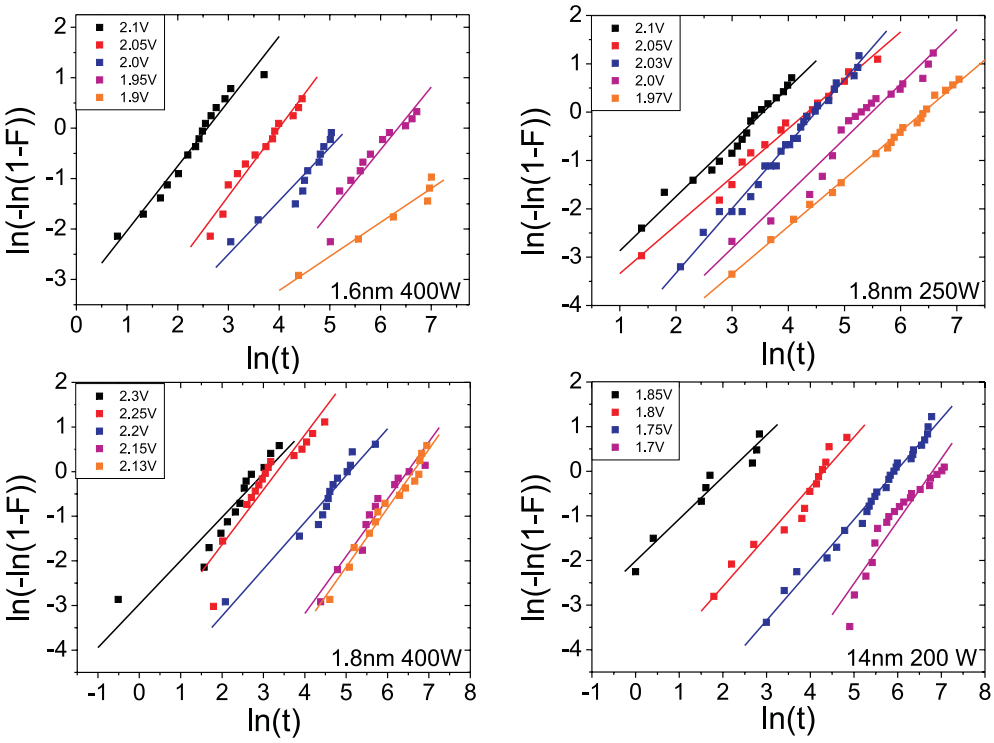

Fig. 2: Weibull plots for different barrier thicknesses and rf deposition power. The scaling of the lifetime with the applied voltage is immediately recognized in the Weibull plots by a shift of the data sets for different values. The lines are a fit of Eq. (2).

Figure 2 shows exemplarily Weibull plots corresponding to different barrier thicknesses and rf deposition power. The scaling of the lifetime with the applied voltage is immediately recognized in the Weibull plots by a shift of the data sets for different values. The lines are a fit of Eq. (2) to the experimental data. The estimated slopes are similar for each plot although a certain scatter is unavoidable due to the finite size of the measured population.

Typical working condition voltages for MTJs are much lower than the voltages used here (below 0.5 V). Since the lifetimes in the low voltage region can reach values well above 10^6 years, it is impossible then to get enough statistics in a reasonable measurement time. For this reason, the stress processes are accelerated by measuring at larger voltages. The open question now is the relation between the measured lifetimes at large voltages and the expected lifetimes at working conditions. In the literature several models are chosen, going from an inverse power law model to a more or less complicated exponential law [2,5,6,8]. In our case, we choose a simple exponential dependence, which has been proven for Al_2O_3 [5,6,8] and MgO [9] tunneling barriers:

$$\eta = A\ \exp(-BV) \quad . \tag{3}$$

Figure 3 shows exemplarily the measured dependence of the lifetime η on the applied voltage for a MTJ population with a 1.4 nm thick barrier. The line represents a fit to the exponential law shown in Eq. (3).

The obtained data is now summarized in Fig. 4. The top panels shows the dependence of the shape parameter β on the barrier thickness and the RA product for three wafer sets deposited with different ac power. Two main features can be recognized: first, the deposition power seems to have no influence on β, and, secondly, this parameter decreases continuously with the thickness (or RA

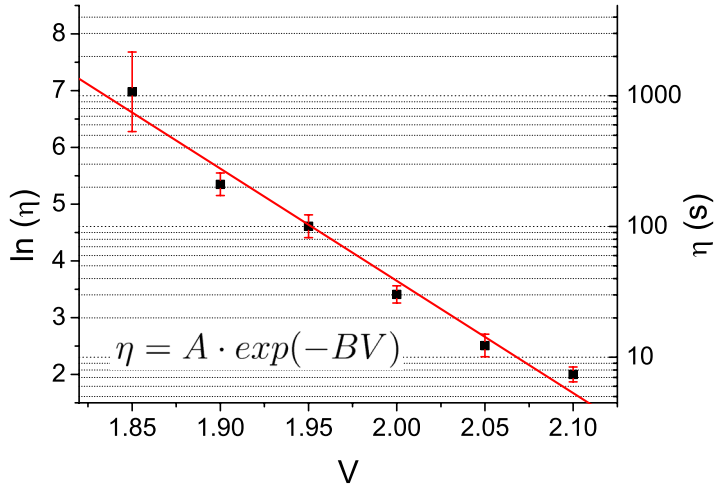

Fig. 3: Dependence of the characteristic lifetime η of the tunneling junctions and $\ln(\eta)$ on the stress voltage. The line is a fit to Eq. (3) for the estimation of the lifetime in the low voltage regime.

product) of the MgO barrier. An important point has to be remarked here: with the exception of the case with 2.2 nm, all the values are larger than unity, i.e. we are in the situation with a low infant mortality and consequently high device reliability during the first operation stage. The bottom panels show now the dependence for the lifetime η in the low voltage regime. Here again the deposition power seems to have no influence. The lifetime increases with increasing barrier thickness. This is somehow intuitive since thicker barriers are more robust against breakdown processes. The overall absolute values for η are very large, pointing again to a very high reliability. In fact, using the obtained values and Eq. (1) it is possible to calculate failure rates below 1 ppm for most of the measured wafers after 10 years operation.

In summary, a highly automatized procedure to determine long-time characteristics of magnetic tunneling junctions have been established in the production line of our industrial partner Sensitec GmbH. The results confirm the high quality of the MgO junctions by showing β and lifetime values compatible with low infant mortality and large endurability and reliability. Further developments are being carried one in order to speed up the measurement procedure and also to study the influence of other preparation parameters.

Financial support by the state of Rhineland-Palatinate (MBWWK and MWKEL) and by the European Regional Development Fund (ERDF) in the frame of the Spintronic Technology Platform (STeP) is acknowledged. The authors thank Stefan Eilers and Matthias Bürkle for their technical support at Sensitec.

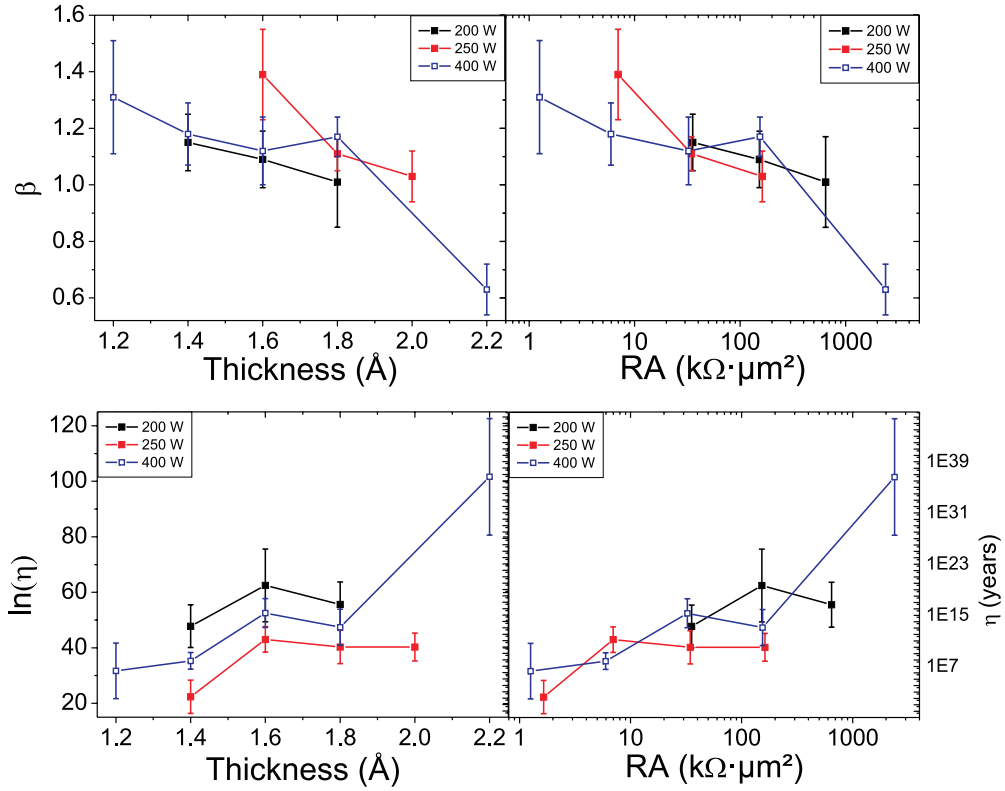

Fig. 4: Dependence of the shape parameter β and the characteristic lifetime η in the low voltage regime (0.4 V) on the nominal thickness and the resistance×area (RA) product.

References

[1] SensorKosmos **11**, 2013 (in german).

[2] H. Yamazaki, H. Hirabayashi, N. Oyama, M. Sakai, *Characteristics of TMR angle sensors*, Proc. SENSOR+TEST Conferences 2011.

[3] Data sheet AAT001-10E TMR Angle Sensor, NVE Corporation.

[4] Kin P. Cheung, *Plasma charging damage*, Springer Verlag, p. 14 (2000).

[5] J. Das, R. Degraeve, P. Roussel, G. Groeseneken, G. Borghs, J. De Boeck, *Area scaling and voltage dependence of time-to-breakdown in magnetic tunnel junctions*, J. Appl. Phys. **91**, 7712 (2002).

[6] H. Kim, J. Sok, B.K. Cho, J.R. Rhee, W. Parkand, T. Kim, *Dielectric characteristics of magnetic tunnel junctions using amorphous CoNbZr layers*, J. of the Korean Physical Society, **46**, No. 6,1425 (2005).

[7] T. Min, Q. Chen, R. Beach, G. Jan, C. Horng, W. Kula, T. Torng, R. Tong, T. Zhong, D. Tang, P. Wang, M. Chen, J.Z. Sun, J.K. Debrosse, D.C. Worledge, T.M. Maffitt, W.J. Gallagher, *A Study of write margin of spin torque transfer magnetic random access memory technology*, IEEE Trans. Magn. **46**, 2322 (2010).

[8] M. Gibbons, K. Sin, S. Funada X. Shi, *Lifetime of magnetic tunnel junction under voltage stress*, Proc. of INTERMAG Europe 2002.

[9] C. Yoshida, M. Kurasawa, Y. Min Lee, K. Tsunoda, M. Aoki Y. Sugiyama, *A study of dielectric breakdown mechanism in CoFeB/MgO/CoFeB magnetic tunnel junction*, Proc. Reliability Physics Symposium (IRPS), 2009 IEEE International Conferences.

[10] www.sensitec.com

4.22 Magneto-optical enhancement in Co | Au patterned nanostructures

E.Th. Papaioannou, T. Meyer, and B. Hillebrands

The field of plasmonics is growing rapidly nowadays due to the progress in the fabrication of nanostructures. The latter, together with a deeper understanding of the underlying physics have led to a variety of possible applications ranging from physics to photonics and from chemistry to biology, from sensing [2] to microscopy [3] and to telecommunications [4]. Ag and Au are traditionally the noble metals that are used by the plasmonic community due to their low losses in the visible range. Previous investigations have avoided the use of magnetic materials due to the presence of absorptive losses for the plasmons. However, due to the advances in nano-patterning the last decade, combined structures composed of plasmonic and ferromagnetic materials allowed the coupling between plasmonic and magnetic states through the utilization of magneto-optic (MO) effects [5, 6]. Such a coupling has shown that MO effects like polar MO and transverse MO Kerr effect can be largely enhanced in the presence of plasmonic resonances [7–9].

In this Report we focus on the enhancement of the polar magneto-optic Kerr effect (P-MOKE) in hexagonal patterned structures of Co | Au multilayers. The multilayer is grown on top of a mask of with polystyrene spheres with diameter $d = 220\,\text{nm}$ and pitch size $a = 470\,\text{nm}$. We show that the efficiency of the magneto-plasmonic interaction can be drastically enhanced by multilayers and by using curved surfaces.

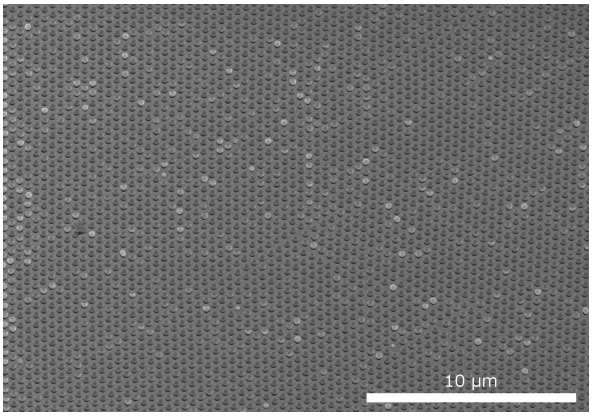

Fig. 1: Scanning electron microscopy image of polystyrene spheres arranged in a hexagonal pattern. The distance between the center of the spheres is $a = 470\,\text{nm}$ while the size of the diameter of the spheres $d = 220\,\text{nm}$. In between the spheres and on top of them a Co | Au multilayer is deposited. Some spheres appear brighter than others due to charging effects in the electron microscope.

P-MOKE refers to the change of the polarization state of the incident linear polarized light, when the latter reflects from the surface of a magnetic material. In this particular geometry, an external magnetic field (or the presence of spontaneous magnetization) points perpendicular to the sample's surface. The reflected light in such geometry is elliptically polarized, giving rise to the experimentally measured quantity η_K (polar Kerr ellipticity) and its polarization plane is tilted with respect to the incident light with the corresponding experimental quantity θ_K (polar Kerr rotation).

The Kerr rotation θ_K is influenced by two factors: the intrinsic MO active electronic transitions (related to the optical conductivity tensor) and the extrinsic reflectivity (related to the refractive index η and extinction coefficient k). Therefore, a proper adjustment of η can lead to an enhance-

This work has been recently published in Journal of Surfaces and Interfaces of Materials [1].

ment of θ_K. In particular, three main effects can enhance θ_K without increasing the intrinsic Kerr effect in the MO material: the interface, interference, and plasma edge effects [11].

A new type of P-MOKE enhancement has been revealed in recent years with the development of nanostructured hybrid magneto-plasmonic crystals: the localized (LSPs) and/ or propagating surface plasmons (SPPs) assisted enhancement. In contrast to the aforementioned pure optical enhancement effects, the surface plasmons enhancement includes both factors to increase in θ_K, the intrinsic magneto-optically active electronic transitions and the extrinsic reflectivity. By using either localized surface plasmons excited in magnetic wires of nanoparticles [12] or propagating surface plasmon resonances excited in combined structures of noble and magnetic metals/dielectrics, such as Co | Au or Iron garnets and in patterned magnetic Fe, Co, Ni films, [7, 8, 10] a P-MOKE signal enhancement has been observed. Localized or propagating plasmon excitation modes induce an increase of the intensity of the electromagnetic field inside the ferromagnetic materials that leads to a higher polarization conversion. At plasmonic resonances one observes that the reflectivity (or transmission) exhibits minima (or maxima), and a MO enhancement appears at the corresponding energies.

Multilayer structures composed of ferromagnetic and plasmonic layers offer unique possibilities to manipulate the magneto-plasmonic response. A multilayer possesses more interfaces were SPPs can be introduced. Furthermore, the appropriate choice of the thicknesses of the ferromagnetic and plasmonic layers allow for the control of the P-MOKE signal strength [13]. In our work, we sue the Co | Au multilayer system in the form of [Co (1nm) | Au (2.5 nm)] $\times 10$. This system is known to present very sharp interfaces, a very important factor for the plasmonic response of the samples. The thicknesses of the individual layers were chosen in order that the system possesses perpendicular anisotropy. The multilayers were fabricated with electron beam evaporation in ultra high vacuum on top of polystyrene spheres on Si substrates. The spheres where initially etched in order to form a hexagonal lattice with characteristic dimensions of: sphere diameter $d = 220\,\text{nm}$ and pitch size $a = 470\,\text{nm}$. The evaporation filled the space between the spheres and the outer surface of the spheres. The resulting final structure is composed of a continuous film decorated with spherically curved caps as shown in Fig. 1. A continuous multilayer of the same composition was also prepared, acting as a reference sample. MO and magnetic measurements were performed before the removal of the mask.

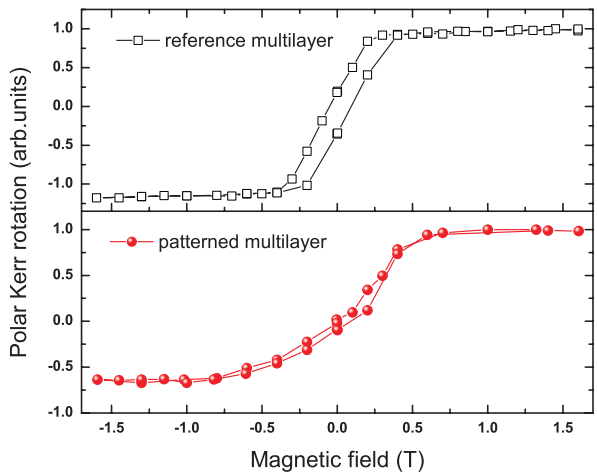

Fig. 2: Magnetization curves for the continuous and the patterned [Co (1nm) | Au (2.5 nm)] $\times 10$ multilayer. The loops were recorded in the polar configuration (magnetic field perpendicular to the sample plane) using P-MOKE.

Magnetization curves for the continuous and the patterned sample are presented in Fig. 2. The

P-MOKE hysteresis loop of the reference continuous multilayer reveals the presence of a relative strong perpendicular anisotropy. The shape of the curve, the relative small saturation field of 0.4 T, and a remanence ratio of 24% are indicative of the presence of perpendicular anisotropy. On the other side, the patterned multilayer exhibits no such characteristics, proving the strong influence of the patterning. No clear hysteresis is present while the saturation field is close to 0.75 T. Due to the multilayer structure of our samples it is expected that observables like reflectivity and polar Kerr rotation are dependent on several factors like absorption, interface reflectivity and interference phenomena [14, 17]. Furthermore, the size of the P-MOKE signal is not any more directly proportional to the measured magnetization in Fig. 2 but to the ratio of magnetization in the different layers and the thicknesses of the layers [16, 17].

The optical reflectivity and Kerr spectra presented in Fig. 3 were obtained at 4° angle of incidence measured against the sample normal. The reflectivity of the continuous multilayer displays no specific features. The patterned sample, on the other hand, presents a broad dip at 2.4 eV while the reflectivity is almost close to zero for energies above 3 eV. The presence of curved surfaces and multiple interfaces of Co and Au can drastically change the reflectivity and influence the resonances. A possible factor that contributes to this behaviour is the additional roughness that the presence of the polystyrene spheres cause. Rougher surfaces have been shown to cause displacement of plasmonic dips in reflectivity to longer wavelengths [15], while the curves are becoming broader due to the additional damping. Furthermore, the resonance at 2.4 eV is close to the plasmonic resonance of Au, an indication that Au plays a significant role in the case of multilayers. Furthermore, excitation of localized plasmon resonances at the curved surfaces should be also taken into account.

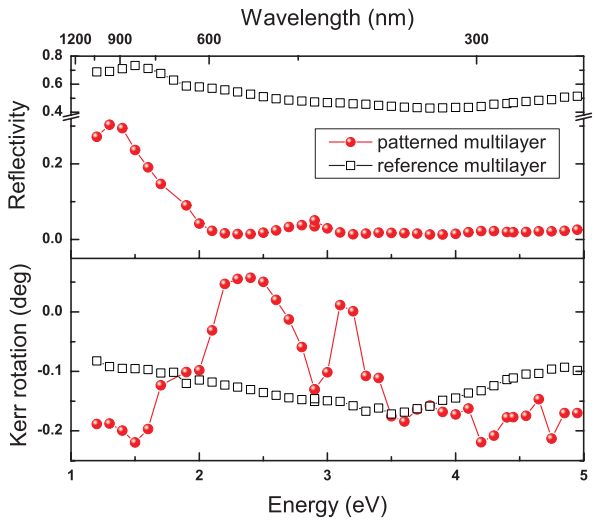

Fig. 3: Reflectivity and PMOKE spectra as a function of the light energy for the continuous and the patterned [Co (1nm) | Au (2.5 nm)] ×10 multilayer. The reflectivity curve is measured relative to an aluminum mirror. The Kerr spectra are recorded at the saturation state of the samples at magnetic field of 1.64 T

The P-MOKE spectra of both samples were obtained with the samples being in the saturation state (applied magnetic field $B = 1.64$ T). The reference film exhibits a maximum Kerr rotation of 0.18 deg at 3.6 eV. The magnitude of the Kerr rotation is in the range of similar Co | Au multilayers [13] but lower compared to a Co film. Due to the limited penetration depth of about 15 nm at the photon energy range of the experiment, the magnetically active thickness of Co, that contributes to the Kerr rotation is less that the half of the total film thickness. The latter, together with the relatively thicker Au layers result in a reduction of the polar Kerr rotation. On the other side, the patterned multilayer displays remarkable characteristics. The polar Kerr rotation exhibits a large modulation with change of sign at energies where the dip in reflectivity appears. This remarkable

change of the Kerr curve into an S-shaped curve is indicative of an intrinsic pure MO enhancement [11]. Although further investigations and theoretical work is needed to reveal the origin of the effects, the presented data show the big perspective in manipulating the MO response with such hybrid patterns and the use of multilayers.

In summary, we have presented the effect of strong MO enhancement in the presence of surface plasmons polaritons in patterned Co | Au multilayers. Despite the complicated geometry, strong enhancement is observed due to the pattern and the multilayer structure. The manipulation of the MO enhancement with a patterned and multilayered structure provides new directions for further developments in magneto-plasmonic research.

Financial support by Carl Zeiss Stiftung is gratefully acknowledged.

References

[1] E.Th. Papaioannou, T. Meyer, B. Hillebrands, *Magneto-optical enhancement in Co/Au patterned nanostructures*, Journal of Surfaces and Interfaces of Materials **2**, 40-45 (2014).

[2] J.N. Anker, W.P. Hall, O. Lyandres, N.C. Shah, J. Zhao, R.P. van Duyne, *Biosensing with plasmonic nanosensors*, Nature Mater **7**, 442 (2008).

[3] D. van Oosten, M. Spacenovic, L. Kuipers, *Nanohole chains for directional and localized surface plasmon excitation*, Nano Lett. **10**, 286 (2010).

[4] V.V. Temnov, G. Armelles, U. Woggon, D. Guzatov, A. Cebollada, A. Garcia-Martin, J.M. Garcia-Martin, T. Thomay, A. Leitenstorfer, R. Bratschitsch, *Active magneto-plasmonics in hybrid metal/ferromagnet structures*, Nature Photon. **4**, 107 (2010).

[5] I. Pimenov, V. Kurin, *Theory of magneto-optical effects in nanostructured ferromagnetics*, J. Opt. Soc. Am. B **29**,1815 (2012).

[6] A.A. Grunin, A.V. Chetvertukhin, T.V. Dolgova, A.A. Ezhov, A.A. Fedyanin, *Magnetoplasmonic crystals based on commercial digital discs*, J. Appl. Phys. **113**, 17A946 (2013).

[7] E. Melander, E. Ostman, J. Keller, J. Schmidt, E.T. Papaioannou, V. Kapaklis, U.B. Arnalds, B. Caballero, A. Garcia-Martin, J.C. Cuevas, B. Hjörvarsson, *Influence of the magnetic field on the plasmonic properties of transparent Ni anti-dot arrays* Appl. Phys. Lett. **101**, 063107 (2012).

[8] E.T. Papaioannou, V. Kapaklis, E. Melander, B. Hjövarsson, S.D. Pappas, P. Patoka, M. Giersig, P. Fumagalli, A. Garcia-Martin, G. Ctistis, *Surface plasmons and magneto-optic activity in hexagonal Ni anti-dot arrays*, Opt. Express **19**, 23867 (2011).

[9] E.T. Papaioannou, V. Kapaklis, P. Patoka, M. Giersig, P. Fumagalli, A. Garcia Martin, E. Ferreiro-Vila, G. Ctistis, *Magneto-optic enhancement and magnetic properties in Fe antidot films with hexagonal symmetry*, Phys. Rev. B **81**, 054424 (2010).

[10] D. Martin-Becerra, J.B. Gonzalez-Diaz, V.V. Temnov, A. Cebollada, G. Armelles, T. Thomay, A. Leitenstorfer, R. Bratschitsch, A. Garcia-Martin, M.U. Gonzalez, *Enhancement of the magnetic modulation of surface plasmon polaritons in Au/Co/Au films*, Appl. Phys. Lett. **97**, 183114 (2010).

[11] P. Fumagalli, H. Munekata, *Magneto-optic properties and ferromagnetism of (In,Mn)As/(In,Al)As/(Ga,Al)Sb heterostructures*, Phys. Rev. B **53**, 15045 (1996).

[12] V. Bonanni, S. Bonetti, T. Pakizeh, Z. Pirzadeh, J. Chen, J. Nogues, P. Vavassori, R. Hillenbrand, J. Akerman, A. Dmitriev, *Design magnetoplasmonics with Nickel nanoferromagnets*, Nano Lett.**11**, 5333 (2011).

[13] E.Th. Papaioannou, V. Karoutsos, M. Angelakeris, O. Valassiades, P. Fumagalli, N. Flevaris, P. Poulopoulos, *Magnetic, magneto-optic and magnetotransport properties of nanocrystalline Co/Au multilayers with ultrathin Au interlayers*, Journal of Nanoscience and Nanotechnology **8**, 4323 (2008).

[14] J. Hamrle, J. Pistora, B. Hillebrands, B. Lenk, M. Münzenberg, *Analytical expression of the magneto-optical Kerr effect and Brillouin light scattering intensity arising from dynamic magnetization*, Journal of Physics D: Applied Physics **43**, 325004 (2010).

[15] H. Raether, *Surface plasmons*, Vol. **111**, Springer Tracts in Modern Physics, Springer, Berlin,(1988).

[16] E.T. Papaioannou, M. Angelakeris, N.K. Flevaris, P. Fumagalli, C. Mueller, A. Troupis, A. Spanou, V. Karoutsos, P. Poulopoulos, V. Kapaklis, C. Politis, *Magnetism and magneto-optics of nanocrystalline Ni/Pt multilayers grown by e-beam evaporation at room temperature*, J. Appl. Phys. **101**, 023913 (2007).

[17] J. Hamrle, J. Ferré, M. Nývlt, Š. Višňovský, *In-depth resolution of the magneto-optical Kerr effect in ferromagnetic multilayers*, Phys. Rev. B **66**, 224423 (2002).

4.23 Promoting Magnetism

B. Leven, I. Sattler, A. Conca, E.Th. Papaioannou, A.A. Serga, and B. Hillebrands

In the recent years magnetism continues to enter increasingly the application fields of our daily life, e.g. various sensors in cars or in data storage. However, for the broad field of industrial customers as well as in the people's awareness magnetism often remains an unclear or even *magic* environment. To overcome those prejudices of magnetism is one of the key aims of the Greater Region Magnetism Network (GRMN) in the frame of the University of the Greater Region (UNIGR) which we already introduced in last year's Report (page 138). GRMN is operated by groups at the University of the Saarland (*coordination*), the University of Lorraine at Nancy and at the University of Kaiserslautern (next to us, the groups Aeschlimann and Kuhn are involved, too). In this article we report on some of our activities aiming at bringing magnetism closer to industrial application awareness as well as clarifying the physics behind magnetic applications in our today's life to the open public.

The *Taipei Tower 101* (see last year's Annual Report, page 138) continues to be a most valuable demonstrator and eye catcher at all our dissemination activities. Last year we complemented our exhibition collection with a *MagView* table top microscope for visualizing information encoded in the magnetic stripe of swipe cards. During the exhibitions we also encode for our visitors individual information on sample cards. Future concepts of GRMN aim at widening dissemination towards the fine arts. So-called NanoArt objects are designed so that they attract the attention of people in a completely different environment and thus brings magnetism to their minds. One example is shown in Fig. 1.

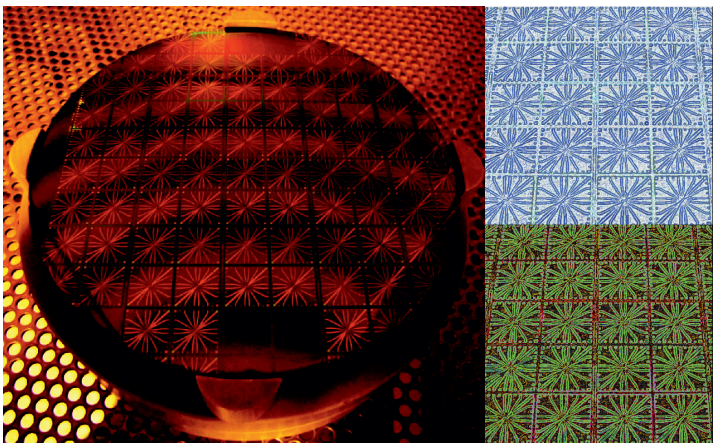

Fig. 1: Examples of the magnetism NanoArt project: Graphically modified images of a magnetic sensor wafer (overview) as well as an enlarged area of few sensor fields. For more examples please visit http://greater-magnetism.eu/galerie/bilder-galeriemagnetismus/

"Transfer to future", this was the title of the *21. Technologie- und Innovationsforum Pfalz*, taking place on March 19th 2014 at the University of Kaiserslautern. The fair is the largest event for the exchange between science and commerce in the state of Rhineland-Palatinate and provides an excellent platform for technology and knowledge transfer. Lectures, discussions, workshops and an exhibition provide insights into collaborations between companies and academia. Best practice examples show how both partners can profit from each other in such projects. The auditory mainly comprises representatives of small and medium size enterprises. The participants are particularly interested in the potential of new technologies for industrial and consumer applications.

In a presentation titled *Magnetsensoren sind überAll* we presented jointly with Dr. Rolf Slatter, the CEO of Sensitec GmbH, our well established university-industry collaboration project Spintronics Technology Platform of Rhineland-Palatinate (STeP). We also contributed to the accompanying exhibition, which provided an excellent opportunity for individual discussions with experts.

Another event with respect to "Promoting Magnetism"was the visit by representatives of Hydac Electronic GmbH, Saarbrücken, at our group in April 2014. Hydac is a member of the industrial advisory board of GRMN. In presentations and a round table discussion we evaluated together with our guests, Dr. Horst Mannebach (Manager R&D) and Dr. Matthias Wolff, the potential of magnetic applications in hydraulic systems. During a laboratory tour we provided our guests with insights into magnetic thin film deposition and magnetic analysis systems. Figure 2 provides some impressions of the fruitful exchange.

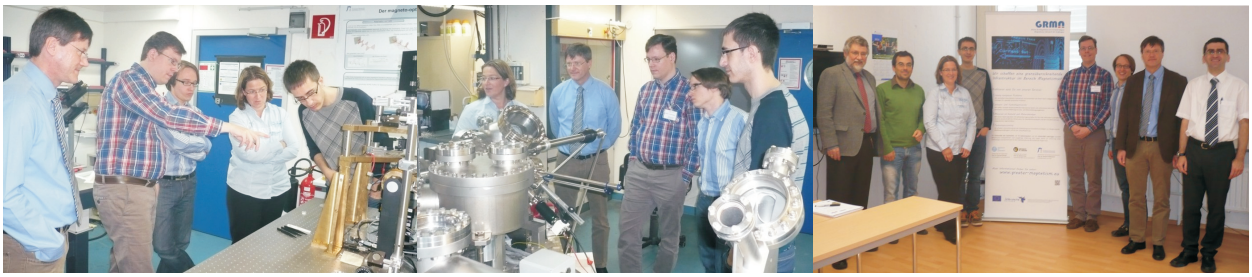

Fig. 2: Impressions of the visit of representatives of Hydac Electronic GmbH, Saarbrücken, at the magnetism group at Kaiserslautern. Left: MOKE lab, Middle: MBE lab, Right: group picture (From left to right: Prof. Dr. Burkard Hillebrands, JP Dr. Evangelos Papaioannou, Dr. Britta Leven, Dr. Andres Conca (UNI KL), Dr. Matthias Wolff (Hydac), Dr. Philipp Pirro (Uni KL), Dr. Horst Mannebach (Hydac), Minko Kostov (EU office at Uni KL).

On April 25th 2014, we took part in the exhibition of the department of Physics during the Kaiserslautern's *Nacht, die Wissen schafft* (Night of Science). In this well perceived event for the general public our group presented many hands-on examples of magnetic effects, e.g. a levitating globe, several magnetic toys, and a compass array for visualizing magnetic domains. Our exhibition also included the *Taipei Tower 101* and the *MagView* microscope as demonstrators for modern applications. As shown in Fig. 3 we attracted the attention of visitors of all ages. The visitors enjoyed testing the demonstrators and satisfying their curiosity in intense discussions with members of our group almost until midnight.

Fig. 3: Snapshots of our activities at the Night of Science at the University of Kaiserslautern 2014.

Once again, we took part in the *Hannover Messe der Industrie*, the world-leading fair for industrial technology (2014). Jointly with the Johannes Gutenberg University Mainz, we presented, the Spintronic Technology Platform of Rhineland-Palatinate (STeP), our R&D project on magnetic sensors for industrial automation, automotive industry or robotics. The project is focused on magnetoresistive technologies for the development of new sensor designs. The main activities are performed at the facilities of Sensitec GmbH in Mainz. STeP is also associated with the Service Center for New Materials (TT-DINEMA) of the Johannes Gutenberg University Mainz which was also presented at the fair. Additionally, we presented the Magnetism Network of the Greater Region (GRMN).

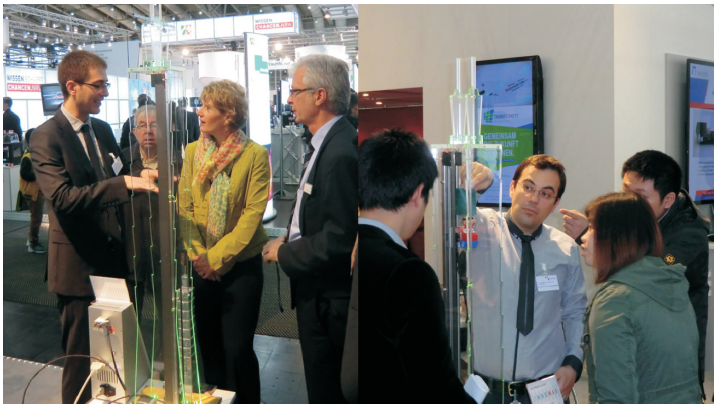

Fig. 4: Left: (From left to right) Dr. A. Conca (AG Magnetismus), Ministerin E. Lemke (Commerce, Climate Protection, Energy and Regional Development, Rhineland-Palatinate), Dr. J. Gerber INNOMAG) Right: Dr. Evangelos Papaioannou (AG Magnetismus) explains to visitors magnetic sensors.

As can be seen in Fig. 4 we not only received the awareness of regular fair visitors (on the right), but also gladly hosted *Ministerin Evelyn Lemke* (Commerce, Climate Protection, Energy and Regional Development) as top-ranking politician of the State of Rhineland-Palatinate. She was accompanied by Dr. Jürgen Gerber, CEO of the INNOMAG association (Innovationsplattform Magnetische Mikrosysteme e.V.).

Financial support by the state Rhineland-Palatinate (MBWWK and MWKEL) and by the European Regional Development Fund (ERDF) in case of STeP and by the European Regional Development Fund (ERDF) in the framework of the INTERREG IVA Greater region in case of GRMN is gratefully acknowledged.

Chapter 5: Publications

Most publications can be downloaded from http://www.physik.uni-kl.de/hillebrands.

5.1 submitted

1. *A micro-sized parametric spin-wave amplifier*
   T. Brächer, F. Heussner, P. Pirro, T. Fischer, M. Geilen, B. Heinz, B. Lägel, A.A. Serga, B. Hillebrands
   submitted, arXiv:1411.0830

2. *Optically-reconfigurable dynamic magnetic materials*
   M. Vogel, A.V. Chumak, E.H. Waller, T. Langner, V.I. Vasyuchka, B. Hillebrands, G. von Freymann
   submitted

3. *All-optical characterisation of the spintronic Heusler compound* $Co_2Mn_{0.6}Fe_{0.4}Si$
   T. Sebastian, Y. Kawada, B. Obry, T. Brächer, P. Pirro, D.A. Bozhko, A.A. Serga, H. Naganuma, M. Oogane, Y. Ando, B. Hillebrands
   submitted

4. *Sign of inverse spin Hall voltages generated by ferromagnetic resonance and temperature gradients in yttrium iron garnet | platinum bilayers*
   M. Schreier, G.E.W. Bauer, V.I. Vasyuchka, J. Flipse, K. Uchida, J. Lotze, V. Lauer, A.V. Chumak, A.A. Serga, S. Daimon, T. Kikkawa, E. Saitoh, B.J. van Wees, B. Hillebrands, R. Gross, S.T.B. Goennenwein
   submitted, arXiv:1404.3490

5. *Thickness and power dependence of the spin-pumping effect in* $Y_3Fe_5O_{12}$*/Pt heterostructures measured by the inverse spin Hall effect*
   M.B. Jungfleisch, A.V. Chumak, A. Kehlberger, V. Lauer, D.H. Kim, M.C. Onbasli, C.A. Ross, M. Kläui, B. Hillebrands
   submitted, arXiv:1308.3787

5.2 in press

1. *Measurements of the exchange stiffness of YIG films by microwave resonance techniques*
   S. Klingler, A.V. Chumak, T. Mewes, B. Khodadadi, C. Mewes, C. Dubs, O. Surzhenko, B. Hillebrands, A. Conca
   accepted in J. Phys. D: Appl. Phys., arXiv:1408.5772

2. *Influence of a non-Gilbert damping mechanism on the nonlinear spin dynamics in a ferromagnetic Heusler compound*
   P. Pirro, T. Sebastian, T. Brächer, A.A. Serga, T. Kubota, H. Naganuma, M. Oogane, Y. Ando, B. Hillebrands
   accepted in Phys. Rev. Lett.

3. *Magnonen für den Computer von übermorgen*
   B. Leven, A.V. Chumak, B. Hillebrands
   accepted in Physik in unserer Zeit

5.3 published

1. *Design of a spin-wave majority gate employing mode selection*
   S. Klingler, P. Pirro, T. Brächer, B. Leven, B. Hillebrands, A.V. Chumak
   Appl. Phys. Lett. **105**, 152410 (2014)

2. *Pulsed laser deposition of epitaxial yttrium iron garnet films with low Gilbert damping and bulk-like magnetization*
   M.C. Onbasli, A. Kehlberger, D.H. Kim, G. Jakob, M. Kläui, A.V. Chumak, B. Hillebrands, C.A. Ross
   APL Mater. **2**, 106102 (2014)

3. *Microwave-induced spin currents in ferromagnetic-insulator | normal-metal bilayer system*
   M. Agrawal, A.A. Serga, V. Lauer, E.Th. Papaioannou, B. Hillebrands, V.I. Vasyuchka
   Appl. Phys. Lett. **105**, 092404 (2014)

4. *Magneto-optical enhancement in Co/Au patterned nanostructures*
   E.Th. Papaioannou, T. Meyer, B. Hillebrands
   J. Surf. Interfac. Mater. **2**, 1, 40-45 (2014)

5. *Magnon transistor for all-magnon data processing*
   A.V. Chumak, A.A. Serga, B. Hillebrands
   Nature Communications **5**, 4700 (2014)

6. *Topical Review: The 2014 Magnetism Roadmap*
   R.L. Stamps, S. Breitkreutz, J. Åkerman, A.V. Chumak, Y. Otani, G.E.W. Bauer, J.-U. Thiele, M. Bowen, S.A. Majetich, M. Kläui, I.L. Prejbeanu, B. Dieny, N.M. Dempsey, B. Hillebrands
   J. Phys. D: Appl. Phys. **47**, 333001 (2014)

7. *Ultrafast magnetization dynamics in Co-based Heusler compounds with tuned chemical ordering*
   D. Steil, O. Schmitt, R. Fetzer, T. Kubota, H. Naganuma, M. Oogane, Y. Ando, A.K. Suszka, O. Idigoras, G. Wolf, B. Hillebrands, A. Berger, M. Aeschlimann, M. Cinchetti
   New Journal of Physics **16**, 063068 (2014)

8. *Role of bulk-magnon transport in temporal evolution of the longitudinal spin Seebeck effect*
   M. Agrawal, V.I. Vasyuchka, A.A Serga, A. Kirihara, P. Pirro, T. Langner, M.B. Jungfleisch, A.V. Chumak, E.Th. Papaioannou, B. Hillebrands
   Phys. Rev. B **89**, 224414 (2014)

9. *Magnetoelastic modes and lifetime of magnons in thin yttrium iron garnet films*
   A. Rückriegel, P. Kopietz, D.A. Bozhko, A.A. Serga, B. Hillebrands
   Phys. Rev. B **89**, 184413 (2014)

10. *Parallel parametric amplification of coherently excited propagating spin waves in a microscopic $Ni_{81}Fe_{19}$ waveguide*
T. Brächer, P. Pirro, T. Meyer, F. Heussner, B. Lägel, A.A. Serga, B. Hillebrands
Appl. Phys. Lett. **104**, 202408 (2014)

11. *Annealing influence on the Gilbert damping parameter and the exchange constant of CoFeB thin films*
A. Conca, E.Th. Papaioannou, S. Klingler, J. Greser, T. Sebastian, B. Leven, J. Lösch, B. Hillebrands
Appl. Phys. Lett. **104**, 182407 (2014)

12. *Realization of a spin-wave multiplexer*
K. Vogt, F.Y. Fradin, J.E. Pearson, T. Sebastian, S.D. Bader, B. Hillebrands, A. Hoffmann, H. Schultheiss
Nature Communications **5**, 3727 (2014)

13. *Bose-Einstein condensation in an ultra-hot gas of pumped magnons*
A.A. Serga, V.S. Tiberkevich, C.W. Sandweg, V.I. Vasyuchka, D.A. Bozhko, A.V. Chumak, T. Neumann, B. Obry, G.A. Melkov, A.N. Slavin, B. Hillebrands
Nature Communications **5**, 3452 (2014)

14. *Localized parallel parametric generation of spin waves in a $Ni_{81}Fe_{19}$ waveguide by spatial variation of the pumping field*
T. Brächer, P. Pirro, F. Heussner, A.A. Serga, B. Hillebrands
Appl. Phys. Lett. **104**, 092418 (2014)

15. *Magnetization reversal of in-plane uniaxial Co films and its dependence on epitaxial alignment*
O. Idigoras, A.K. Suszka, P. Vavassori, B. Obry, B. Hillebrands, P. Landeros, A. Berger
J. Appl. Phys. **115**, 083912 (2014)

16. *Spin-wave excitation and propagation in microstructured waveguides of yttrium iron garnet/Pt bilayers*
P. Pirro, T. Brächer, A.V. Chumak, B. Lägel, C. Dubs, O. Surzhenko, P. Görnert, B. Leven, B. Hillebrands
Appl. Phys. Lett. **104**, 012402 (2014)

5.4 Ph.D. theses

1. *Lineare und nichtlineare Spinwelleninteraktionen in magnetischen Mikrostrukturen*
Philipp Pirro, TU Kaiserslautern, July 2014

2. *Thermally driven magnon transport in the magnetic insulator Yttrium Iron Garnet*
Milan Agrawal, TU Kaiserslautern, February 2014

3. *Herstellung potentieller magnetischer Speichermedien durch Ionenbeschuss antiferromagnetisch gekoppelter Trilagen*
Roland Neb, TU Kaiserslautern, February 2014

Chapter 6: Conferences, Workshops, Schools, Seminars

(shown in chronological order)

6.1 Conferences and workshops

6.1.1 Invited talks

B. Hillebrands:
Smart magnon spintronics
Kavli Conference "Spintronics: Progress in theory, materials and devices", Santa Barbara, California, USA, November 2013

B. Hillebrands:
Spin Caloric Transport
Seminar talk, Kavli Conference "Spintronics: Progress in theory, materials and devices", Santa Barbara, California, USA, November 2013

B. Hillebrands:
Smart magnon spintronics
Plenary talk, The 8th international Conference on Advanced Materials and Devices (ICAMD 2013), Jeju, Korea, December 2013

B. Hillebrands:
Magnonic spin currents
14th REIMEI workshop on spin currents and related phenomena (REIMEI 2014), Grenoble, France, February 2014

E.Th. Papaioannou:
Use of magnetic materials in the direction of active plasmonics
Workshop on Magnetoplasmonics, Uppsala, Sweden, February 2014

A.A. Serga:
Magnon gases and condensates
4th International Conference on Superconductivity and Magnetism (ICSM 2014), Antalya, Turkey, April 2014

V.I. Vasyuchka:
Bulk magnon contribution to the spin Seebeck effect
IEEE International Magnetics Conference (INTERMAG Europe 2014), Dresden, Germany, May 2014

A.A. Serga:
Observation of condensed magnon phases in yttrium iron garnet films
4th International Conference on Oxide Materials for Electronic Engineering (OMEE-2014), Lviv, Ukraine, May 2014

B. Hillebrands:
Phonon mediated magnon condensate
ICC-IMR / 20th REIMEI International Workshop "Spin Mechanics 2", Sendai, Japan, June 2014

V.I. Vasyuchka:
Magnon mediated caloritronic effects in a magnetic insulator
IEEE International Conference on Microwave Magnetics (ICMM 2014), Sendai, Japan, June 2014

A.A. Serga:
Nonlinear dynamics of micro-sized Heusler structures
IEEE International Conference on Microwave Magnetics (ICMM 2014), Sendai, Japan, June 2014

B. Hillebrands:
Magnon-based spin-caloric effects
Plenary talk, IEEE International Conference on Microwave Magnetics (ICMM 2014), Sendai, Japan, July 2014

A.V. Chumak:
Magnonics: current status and outlook
The 10th AIMS Conference on Dynamical Systems, Differential Equations and Applications, Madrid, Spain, July 2014

V.I. Vasyuchka:
Thermally reconfigurable spin-wave waveguides
Spin Caloritronics VI School & Conference 2014, Irsee, Germany, July 2014

B. Hillebrands:
Condensation of mixed magnon-phonon states in gas of pumped magnons
International workshop on Brillouin and Microwave Spectroscopy of Magnetic Micro- and Nanostructures (BrilMicS 2014), Saratov, Russia, August 2014

E.Th. Papaioannou:
Interface engineering of the spin-pumping induced inverse spin Hall effect
3rd German-Russian-Swedish Workshop on Ordering and Dynamics in Magnetic Nanostructures, Schloß Maurach, Germany, September 2014

B. Hillebrands:
Magnonics: Trends and Challenges
3rd German-Russian-Swedish Workshop on Ordering and Dynamics in Magnetic Nanostructures, Schloß Maurach, Germany, September 2014

A.V. Chumak:
Magnonics - Trends and Challenges in view applications in logic
Workshop beyond CMOS, IMEC, Leuven, Belgium, October 2014

6.1.2 Contributed talks and posters

P. Clausen, D.A. Bozhko, V.I. Vasyuchka, A.V. Chumak, A.A. Serga, G.A. Melkov, B. Hillebrands:
Influence of laser power on Bose-Einstein condensate and magneto-elastic magnon mode in a magnon gas
58th Annual Conference on Magnetism and Magnetic Materials (MMM), Denver, Colorado, USA, November 2013

A.A. Serga, P. Pirro, T. Brächer, T. Sebastian, T. Kubota, Y. Ohdaira, H. Naganuma, M. Oogane, Y. Ando, B. Hillebrands:
Four-magnon instabilities in a micro-structured $Co_2Mn_{0.6}Fe_{0.4}Si$ spin-wave conduit
58th Annual Conference on Magnetism and Magnetic Materials (MMM), Denver, Colorado, USA, November 2013

M. Kläui, A. Kehlberger, R. Röser, G. Jakob, U. Ritzmann, D. Hinzke, U. Nowak, M.C. Onbasli, D. Kim, C.A. Ross, M.B. Jungfleisch, B. Hillebrands:
Determination of the origin of the spin Seebeck effect - bulk vs. interface effects
58th Annual Conference on Magnetism and Magnetic Materials (MMM), Denver, Colorado, USA, November 2013

E.Th. Papaioannou, P. Fuhrmann, T. Brächer, M.B. Jungfleisch, B. Hillebrands:
Manipulating the spin-pumping induced inverse spin Hall voltage by crystal growth in Fe/Pt bilayers
58th Annual Conference on Magnetism and Magnetic Materials (MMM), Denver, Colorado, USA, November 2013

V.I. Vasyuchka, F. Ciubotaru, A.V. Chumak, T. Langner, A.A. Serga, B. Hillebrands:
Magnon transport in a temperature gradient
550. WE-Heraeus-Seminar “Spin transport beyond Boltzmann”, Bad Honnef, Germany, January 2014

A.A. Serga, M. Agrawal, V.I. Vasyuchka, A. Kirihara, P. Pirro, T. Langner, M.B. Jungfleisch, A.V. Chumak, E.Th. Papaioannou, B. Hillebrands:
Time-dependent magnon Seebeck effect
550. WE-Heraeus-Seminar “Spin transport beyond Boltzmann”, Bad Honnef, Germany, January 2014

T. Langner, M. Vogel, V.I. Vasyuchka, A.V. Chumak, A.A. Serga, G. von Freymann, B. Hillebrands:
Spin wave control by thermal gradients
550. WE-Heraeus-Seminar “Spin transport beyond Boltzmann”, Bad Honnef, Germany, January 2014

A.A. Serga, D.A. Bozhko, P. Clausen, V.I. Vasyuchka, A.V. Chumak, G.A. Melkov, B. Hillebrands:
Bose-Einstein magnon condensate in thermal gradient
2nd International Symposium of the SFB/TR 49 on “Novel states in correlated condensed matter-from model systems to real materials”, Königstein, Germany, April 2014

D.A. Bozhko, A.A. Serga, P. Clausen, V.I. Vasyuchka, A.V. Chumak, G.A. Melkov, B. Hillebrands:
Kinetic instability and Bose-Einstein condensation of mixed magnon-phonon states at the bottom of the magnon spectrum
2nd International Symposium of the SFB/TR 49 on "Novel states in correlated condensed matter-from model systems to real materials", Königstein, Germany, April 2014

F. Ciubotaru, V.I. Vasyuchka, A.V. Chumak, T. Langner, A.A. Serga, B. Hillebrands:
Spin wave reflection and magnon-phonon energy transfer
IEEE International Magnetics Conference (INTERMAG Europe 2014), Dresden, Germany, May 2014

T. Brächer, P. Pirro, T. Meyer, F. Heussner, A.A. Serga, B. Hillebrands:
Parallel parametric amplification of externally excited spin waves in a microstructured magnonic waveguide
IEEE International Magnetics Conference (INTERMAG Europe 2014), Dresden, Germany, May 2014

A.A. Serga, P. Clausen, D.A. Bozhko, V.I. Vasyuchka, A.V. Chumak, G.A. Melkov, B. Hillebrands:
Bose-Einstein magnon condensation in thermal gradient
IEEE International Magnetics Conference (INTERMAG Europe 2014), Dresden, Germany, May 2014

M. Agrawal, V.I. Vasyuchka, A.A. Serga, A. Kirihara, P. Pirro, T. Langner, M.B. Jungfleisch, A.V. Chumak, E.Th. Papaioannou, B. Hillebrands:
Temporal evolution of the longitudinal spin Seebeck effect
IEEE International Magnetics Conference (INTERMAG Europe 2014), Dresden, Germany, May 2014

T. Meyer, T. Brächer, T. Sebastian, P. Pirro, T. Fischer, A.A. Serga, H. Naganuma, K. Mukaiyama, M. Oogane, Y. Ando, B. Hillebrands:
Control of parametric amplification via spin-transfer torque of a pure spin current in a Co_2MnSi disc
IEEE International Magnetics Conference (INTERMAG Europe 2014), Dresden, Germany, May 2014

P. Pirro, T. Brächer, T. Sebastian, B. Leven, A.A. Serga, T. Koyama, H. Naganuma, M. Oogane, Y. Ando, B. Hillebrands:
Propagating spin waves trapped in magnetic domains
IEEE International Magnetics Conference (INTERMAG Europe 2014), Dresden, Germany, May 2014

A. Conca, E.Th. Papaioannou, S. Klingler, J. Greser, T. Sebastian, B. Leven, J. Lösch, B. Hillebrands:
Annealing influence on the Gilbert damping parameter and the exchange constant of CoFeB thin films
IEEE International Magnetics Conference (INTERMAG Europe 2014), Dresden, Germany, May 2014

A.V. Chumak, P. Pirro, T. Brächer, B. Lägel, C. Dubs, O. Surzhenko, P. Görnert, B. Leven, B. Hillebrands:
Spin waves in micro-structured waveguides of yttrium iron garnet/Pt bi-layers
IEEE International Magnetics Conference (INTERMAG Europe 2014), Dresden, Germany, May 2014

P. Clausen, D.A. Bozhko, V.I. Vasyuchka, A.A. Serga, G.A. Melkov, B. Hillebrands:
Bose-Einstein condensation of dipolar-exchange magnons
IEEE International Magnetics Conference (INTERMAG Europe 2014), Dresden, Germany, May 2014

A.A. Nikitin, A.B. Ustinov, A.A. Semenov, B.A. Kalinikos, A.V. Chumak, A.A. Serga, V.I. Vasyuchka, B. Hillebrands:
Single-element logic gates based on width-modulated magnonic crystals
IEEE International Magnetics Conference (INTERMAG Europe 2014), Dresden, Germany, May 2014

M. Vogel, T. Langner, V.I. Vasyuchka, A.V. Chumak, A.A. Serga, B. Hillebrands, G. von Freymann:
Spin-wave control in thermal landscapes
IEEE International Magnetics Conference (INTERMAG Europe 2014), Dresden, Germany, May 2014

D.A. Bozhko, A.A. Serga, P. Clausen, V.I. Vasyuchka, A.V. Chumak, G.A. Melkov, B. Hillebrands:
Condensation of mixed magnon-phonon states below the bottom of the magnon spectrum
IEEE International Magnetics Conference (INTERMAG Europe 2014), Dresden, Germany, May 2014

T. Sebastian, P. Pirro, T. Brächer, T. Kubota, A.A. Serga, H. Naganuma, M. Oogane, B. Hillebrands:
Spin-wave caustic formation by higher-harmonic radiation from a localized spin-wave mode in a Heusler waveguide
IEEE International Magnetics Conference (INTERMAG Europe 2014), Dresden, Germany, May 2014

V. Lauer, M.B. Jungfleisch, R. Neb, A.V. Chumak, B. Hillebrands:
Improvement of the YIG/Pt interface for spin pumping-based applications
4th International Conference on Oxide Materials for Electronic Engineering (OMEE-2014), Lviv, Ukraine, May 2014

T. Meyer, T. Brächer, T. Sebastian, P. Pirro, T. Fischer, A.A. Serga, H. Naganuma, K. Mukaiyama, M. Oogane, Y. Ando, B. Hillebrands:
Control of parametric amplification via spin-transfer torque of a pure spin current in Heusler-Pt bilayers
ICC-IMR / 20th REIMEI International Workshop “Spin Mechanics 2”, Sendai, Japan, June 2014

M. Agrawal, V.I. Vasyuchka, A.A. Serga, A. Kirihara, P. Pirro, T. Langner, M.B. Jungfleisch, A.V. Chumak, E.Th. Papaioannou, B. Hillebrands:

Temporal evolution of the longitudinal spin Seebeck effect
ICC-IMR / 20th REIMEI International Workshop "Spin Mechanics 2", Sendai, Japan, June 2014

T. Meyer, T. Brächer, T. Sebastian, P. Pirro, T. Fischer, A.A. Serga, H. Naganuma, K. Mukaiyama, M. Oogane, Y. Ando, B. Hillebrands:

Control of parametric amplification via spin-transfer torque of a pure spin current in Heusler-Pt bilayers
12th RIEC International Workshop on Spintronics, Sendai, Japan, June 2014

T. Meyer, T. Brächer, T. Sebastian, P. Pirro, T. Fischer, A.A. Serga, H. Naganuma, K. Mukaiyama, M. Oogane, Y. Ando, B. Hillebrands:

Control of the effective damping in Heusler-Pt microstructures via spin-transfer torque
IEEE International Conference on Microwave Magnetics (ICMM 2014), Sendai, Japan, July 2014

A. Ruiz-Calaforra, T. Brächer, P. Pirro, B. Heinz, M. Geilen, L. Gareis, B. Hillebrands:

FMR study of $Ni_{81}Fe_{19}$/Ru/Pt and $Co_{40}Fe_{40}B_{20}$/Ru/Pt layer systems
IEEE International Conference on Microwave Magnetics (ICMM 2014), Sendai, Japan, July 2014

T. Brächer, P. Pirro, T. Meyer, F. Heussner, A.A. Serga, B. Hillebrands:

Parallel parametric amplification of externally excited spin waves in a microstructured magnonic waveguide
IEEE International Conference on Microwave Magnetics (ICMM 2014), Sendai, Japan, July 2014

A. Conca, F. Casper, J. Paul, R. Lehndorff, B. Leven, M. Kläui, B. Hillebrands:

Lifetime measurements for CoFeB/MgO/CoFeB tunneling junctions
10th European Conference on Magnetic Sensors and Actuators (EMSA 2014), Wien, Austria, July 2014

M. Vogel, T. Langner, V.I. Vasyuchka, A.V. Chumak, A.A. Serga, B. Hillebrands, G. von Freymann:

Spin-wave control in thermal landscapes
Spin Caloritronics VI School & Conference 2014, Irsee, Germany, July 2014

D.A. Bozhko, A. Kirihara, A.V. Chumak, B. Hillebrands, A.A. Serga:

Spin pumping by Bose-Einstein condensate of magnons in YIG/Pt bilayers
Spin Caloritronics VI School & Conference 2014, Irsee, Germany, July 2014

D.A. Bozhko, A.A. Serga, P. Clausen, V.I. Vasyuchka, A.V. Chumak, G.A. Melkov, B. Hillebrands:

Condensation of mixed magnon-phonon states below the bottom of the magnon spectrum
5th MAINZ student seminar, Prague, Czech Republic, July 2014

T. Meyer, T. Brächer, T. Sebastian, P. Pirro, T. Fischer, A.A. Serga, H. Naganuma, K. Mukaiyama, M. Oogane, Y. Ando, B. Hillebrands:

Control of the effective Damping in Heusler/Pt microstructures via spin-transfer torque
International workshop on Brillouin and Microwave Spectroscopy of Magnetic Micro- and Nanostructures (BrilMicS 2014), Saratov, Russia, August 2014

A. Conca, F. Casper, J. Paul, R. Lehndorff, B. Leven, M. Kläui, B. Hillebrands:

Lifetime measurements for CoFeB/MgO/CoFeB tunneling junctions
Magnetic Single Nano-Object Workshop & School (MSNOWS Lorraine 2014), Nancy, France, September 2014

E.Th. Papaioannou:

Influence of magnetic field on the plasmonic excitations in patterned magnetic films
Magnetic Single Nano-Object Workshop & School (MSNOWS Lorraine 2014), Nancy, France, September 2014

T. Brächer, F. Heussner, P. Pirro, T. Meyer, A.A. Serga, B. Hillebrands:

Parallel parametric amplification of propagating spin waves in microstructured $Ni_{81}Fe_{19}$ waveguides
Magnetic Single Nano-Object Workshop & School (MSNOWS Lorraine 2014), Nancy, France, September 2014

S. Klingler, P. Pirro, T. Brächer, B. Leven, B. Hillebrands, A.V. Chumak:

Design of a spin-wave majority gate employing mode selection
Magnetic Single Nano-Object Workshop & School (MSNOWS Lorraine 2014), Nancy, France, September 2014

M. Agrawal, V.I. Vasyuchka, A.A. Serga, A. Kirihara, P. Pirro, T. Langner, M.B. Jungfleisch, A.V. Chumak, E.Th. Papaioannou, B. Hillebrands:

Temporal evolution of the longitudinal spin Seebeck effect
Magnetic Single Nano-Object Workshop & School (MSNOWS Lorraine 2014), Nancy, France, September 2014

A. Ruiz-Calaforra, T. Brächer, P. Pirro, B. Heinz, M. Geilen, L. Gareis, B. Hillebrands:

FMR study of $Ni_{81}Fe_{19}$/NM/Pt and $Co_{40}Fe_{40}B_{20}$/NM/Pt layer systems
Magnetic Single Nano-Object Workshop & School (MSNOWS Lorraine 2014), Nancy, France, September 2014

D.A. Bozhko, A.A. Serga, P. Clausen, V.I. Vasyuchka, A.V. Chumak, G.A. Melkov, B. Hillebrands:

Condensation of mixed magnon-phonon states below the bottom of the magnon spectrum
Magnetic Single Nano-Object Workshop & School (MSNOWS Lorraine 2014), Nancy, France, September 2014

T. Brächer, F. Heussner, P. Pirro, T. Meyer, A.A. Serga, B. Hillebrands:

Phase-to-amplitude conversion by parallel parametric amplification of propagating spin waves in microstructured $Ni_{81}Fe_{19}$ waveguides
Magnetic Single Nano-Object Workshop & School (MSNOWS Lorraine 2014), Nancy, France, September 2014

T. Meyer, T. Brächer, T. Sebastian, P. Pirro, T. Fischer, A.A. Serga, H. Naganuma, K. Mukaiyama, M. Oogane, Y. Ando, B. Hillebrands:

Control of the effective damping in Heusler/Pt microstructures via spin-transfer torque
Magnetic Single Nano-Object Workshop & School (MSNOWS Lorraine 2014), Nancy, France, September 2014

D.A. Bozhko, A. Kirihara, A.V. Chumak, B. Hillebrands, A.A. Serga:

Spin pumping by Bose-Einstein condensate of magnons in YIG/Pt bilayers
8th Annual retreat of the SFB/TR49, Höhr-Grenzhausen, Germany, September 2014

T. Langner, V.I. Vasyuchka, A.V. Chumak, A.A. Serga, B. Hillebrands:

Spin-wave propagation through a magnonic crystal in thermal gradients
4th DFG SPP 1538 "Spin Caloric Transport" PhD workshop, Bielefeld, Germany, October 2014

T. Meyer, T. Brächer, T. Sebastian, P. Pirro, T. Fischer, A.A. Serga, H. Naganuma, K. Mukaiyama, M. Oogane, Y. Ando, B. Hillebrands:

Control of the effective damping in Heusler-Pt microstructures via spin-transfer torque
Annual meeting of ASPIMATT JST-DFG Research Unit, Sendai, Japan, October 2014

T. Fischer, T. Meyer, T. Brächer, P. Pirro, A.A. Serga, H. Naganuma, K. Mukaiyama, M. Oogane, Y. Ando, B. Hillebrands:

Spin-wave propagation in Heusler-Pt waveguides
Annual meeting of ASPIMATT JST-DFG Research Unit, Sendai, Japan, October 2014

A.A. Serga, B. Hillebrands:

Nonlinear spin-wave dynamics and radiation properties of small Heusler devices
Annual meeting of ASPIMATT JST-DFG Research Unit, Sendai, Japan, October 2014

6.1.3 Contributions to the DPG Frühjahrstagung

16 contributions: DPG Frühjahrstagung, Dresden, Germany, April 2014

6.2 Schools

6.2.1 Invited lectures

B. Hillebrands:

Role of bulk magnons in the spin Seebeck effect
Tutorial lecture, Spin Caloritronics VI School & Conference 2014, Irsee, Germany, July 2014

B. Hillebrands:

Magnetization dynamics I: Fundamentals of spin dynamics and Brillouin light scattering
Magnetization dynamics II: Magnonics: Trends and Challenges
The 7th IEEE Magnetics Society Summer School, Rio de Janeiro, Brazil, August 2014

B. Hillebrands:
Magnetization dynamics
Magnetic Single Nano-Object Workshop & School (MSNOWS Lorraine 2014), Nancy, France, September 2014

B. Hillebrands:
Introduction into magnonics
Annual meeting of ASPIMATT JST-DFG Research Unit, Sendai, Japan, October 2014

6.3 Invited seminar talks and colloquia

A.V. Chumak:
Magnons as an alternative to a charge current
IFW Dresden, Dresden, Germany, November 2013

A.V. Chumak:
Magnonen als eine Alternative zum Ladungsstrom
OPTIMAS Laser- und Quantenoptikseminar, TU Kaiserslautern, Germany, December 2013

E.Th. Papaioannou:
Oberflächenplasmonen und Magnetismus in Metamaterialien
Physics Special Colloquium, TU Kaiserslautern, Germany, February 2014

A.V. Chumak:
Magnons as an alternative to a charge current
University of Bialystok, Bialystok, Poland, May 2014

A.V. Chumak:
Magnons as an alternative to a charge current
Adam Mickiewicz University, Poznan, Poland, May 2014

V.I. Vasyuchka:
Magnon caloritronics
Bielefeld University, Bielefeld, Germany, May 2014

B. Hillebrands:
Magnonics - Trends and Challenges
RIKEN Colloquium, Wako, Saitama, Japan, October 2014

6.4 Seminars

T. Meyer, T. Brächer, T. Sebastian, P. Pirro, T. Fischer, A.A. Serga, H. Naganuma, K. Mukaiyama, M. Oogane, Y. Ando, B. Hillebrands:
Control of the effective damping in Heusler-Pt microstructures via spin-transfer torque
Seminar at Tohoku University, Sendai, Japan, June 2014

F. Heussner, T. Brächer, P. Pirro, T. Meyer, A.A. Serga, B. Hillebrands:
Localized parallel parametric amplification of propagating spin waves in microstructured $Ni_{81}Fe_{19}$ waveguides
Helmholtz-Zentrum Dresden-Rossendorf, Dresden, Germany, October 2014

6.5 Annual group retreat

In 2014 our group organized a three-day retreat at the Kurhaus am Trifels, Annweiler. We had three days of intense scientific discussion and 18 presentations by our group members. Roland Paul, director of the *Institut für pfälzische Geschichte und Volkskunde* in Kaiserslautern, gave a fascinating evening talk on *Nationalsozialismus in der Pfalz*. On the first day, Dr. Sebastian Hermsdörfer, a former group member and now a patent attorney at *Pfenning, Meinig & Partner GbR* in Dresden, Germany, held an afternoon session about patents and their filing processes. In the frame of the session about magnon gases and condensates Prof. Arthur Widera from TU Kaiserslautern gave a talk on *Investigating solid state quasi-particles with controlled impurities in a quantum gas*. Furthermore we organized a hiking trip to Trifels castle where we had an excellent view over the Palatinate Forest.

6.6 Other meetings and trade fairs

B. Leven, R. Slatter:
Magnetsensoren sind überALL
21. Technologie- und InnovationsFORUM Pfalz, Kaiserslautern, Germany, February 2014

B. Hillebrands:
Magnon spintronics in Kaiserslautern
InSpin kick-off meeting, Trondheim, Norway, March 2014

A.V. Chumak:
InSpin: What do we have already?
InSpin kick-off meeting, Trondheim, Norway, March 2014

A.A. Serga:
Magnon Bose Einstein condensation
InSpin kick-off meeting, Trondheim, Norway, March 2014

A. Conca, B. Leven, B. Hillebrands:
Presentation of the Spintronic Technology Platform
Hannover Messe 2014, Hannover, Germany, April 2014

A.V. Chumak, S. Klingler, V. Lauer, D.A. Bozhko, A.A. Serga, B. Leven, B. Hillebrands:
Experimental control of generation of magnons and/or ferromagnetic resonance via the spin Hall effect or spin accumulation
InSpin project meeting, Mainz, Germany, August 2014

B. Hillebrands:
Magnetwiderstandseffekte für die Sensorik
Micronas R&D Konferenz, Waldhof-Akademie für Weiterbildung, Mannheim, Germany, October 2014

A. Conca:
Der Tunnelmagnetwiderstandseffekt für die Sensorik
Micronas R&D Konferenz, Waldhof-Akademie für Weiterbildung, Mannheim, Germany, October 2014

6.7 Awards and Fellowships

D.A. Bozhko:
Fellowship of Graduate School "Materials Science in Mainz" (MAINZ)
Mainz and Kaiserslautern, Germany, March 2014

M.B. Jungfleisch:
Preis der Kreissparkassen-Stiftung
Kaiserslautern, Germany, May 2014

T. Meyer, T. Brächer, T. Sebastian, P. Pirro, T. Fischer, A.A. Serga, H. Naganuma, K. Mukaiyama, M. Oogane, Y. Ando, B. Hillebrands:
Poster award for "Control of the effective damping in Heusler-Pt microstructures via spin-transfer torque"
IEEE International Conference on Microwave Magnetics (ICMM 2014), Sendai, Japan, July 2014

Appendix: Magnetism goes App

B. Leven and B. Hillebrands

In collaboration with Jean-Francois Pautex, Hélène Fischer, Michel Hehn, Philippe Lambert, Stéphane Mangin, Institut Jean Lamour, UMR 7198 CNRS - Université de Lorraine, Faculté des Sciences et Technologies, F-54506 VANDŒUVRE-lès-NANCY cedex

Magnetism is everywhere - especially in our daily life. However, we cannot see or sense it in any way! To increase the awareness the general public - and especially to the younger community, Jean-Francois Pautex and the team of the Greater Region Magnetism Network (GRMN) at the Université de Lorraine developed an App for mobile applications which allows to visualize magnetic fields anywhere. This GRMagNeto-App is free of charge and can be downloaded in the iTunes-store. Once installed, one can easily detect all three components of the magnetic field independently, record and save them. One can even send those data saved as CSV-file via e-mail. One can visualize a local magnetic field, either natural fields or generated by other sources, such as magnets, machines, etc.- with a compass application or even express the field orientation acoustically: the higher and louder the acoustic signal, the better the alignment of the magnetic sensors of your smart phone to the orientation of the field. Thus, one is directly able e.g. to demonstrate the Earth magnetic field. Or detect the magnetic fields of machines in the surrounding! But be careful: don't expose it to large magnetic fields - you might destroy the sensors in your smart-phone!

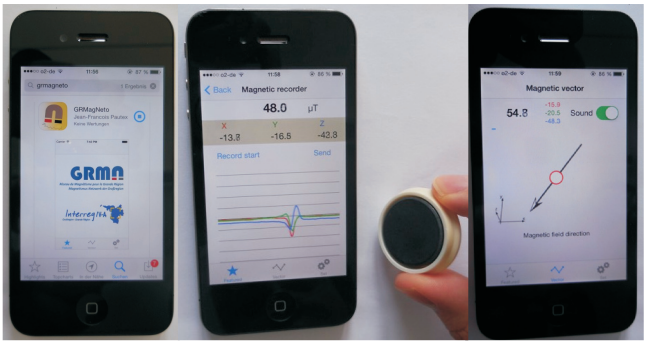

Fig. 1: Snapshots of the GRMagNeto-App: Left: Appearance in the iTunes-store. Middle: Recording of all three components of the applied magnetic field. Right: Compass needle shows the orientation of the local magnetic field.

The current version of the App works on Apple devices, it is suitable for users starting from the school age.

Financial support by the European Regional Development Fund (ERDF) in the framework of the INTERREG IVA Greater region in case of GRMN is gratefully acknowledged.

Appendix: Impressions from 2014

Ph.D. defense Dr. Roland Neb, 17.02.2014

Ph.D. defense Dr. Milan Agrawal, 18.02.2014

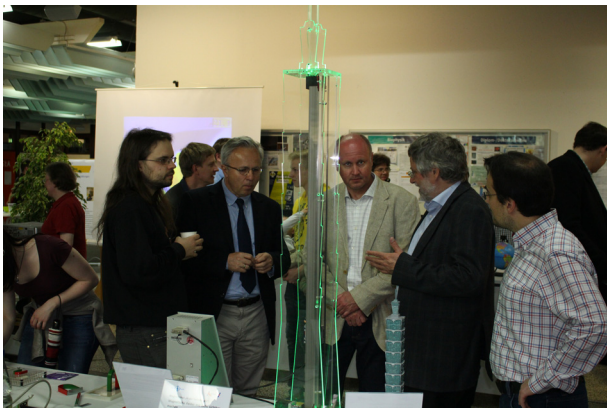

Nacht, die Wissen schafft, 25.04.2014

Ph.D. defense Dr. Philipp Pirro, 28.07.2014

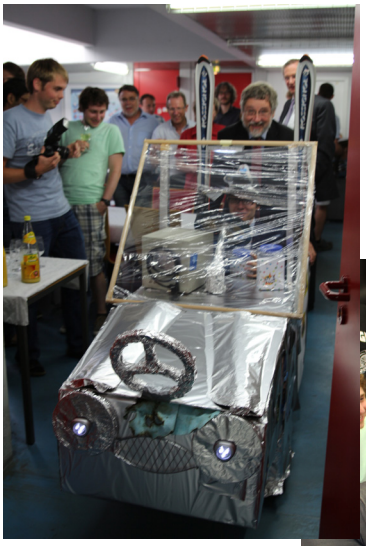

Group excursion to the chalk mine in Wolfstein, 29.07.2014

Prof. Dr. Burkard Hillebrands
Fachbereich Physik
Landesforschungszentrum OPTIMAS
Technische Universität Kaiserslautern, Germany
P.O. Box 3049
67653 Kaiserslautern
Phone: +49 631 205-4228
Fax: +49 631 205-4095
hilleb@physik.uni-kl.de
www.physik.uni-kl.de/hillebrands/

TECHNISCHE UNIVERSITÄT
KAISERSLAUTERN